Modeling the Evolution and Impact of Space Weather Drivers

Ph.D. Thesis

By

Prateek Mayank

Department of Astronomy, Astrophysics and Space Engineering

Indian Institute of Technology Indore

Simrol, Indore, Madhya Pradesh - 453552, India

Modeling the Evolution and Impact of Space Weather Drivers

A THESIS

Submitted in partial fulfillment of the
requirements for the award of the degree

of

DOCTOR OF PHILOSOPHY

by

Prateek Mayank

Department of Astronomy, Astrophysics
and Space Engineering

Indian Institute of Technology Indore
Simrol, Indore, Madhya Pradesh - 453552, India

INDIAN INSTITUTE OF TECHNOLOGY INDORE

I hereby certify that the work which is being presented in the thesis entitled **MODELING THE EVOLUTION AND IMPACT OF SPACE WEATHER DRIVERS** in the partial fulfillment of the requirements for the award of the degree of **DOCTOR OF PHILOSOPHY** and submitted in the **DEPARTMENT OF ASTRONOMY, ASTROPHYSICS AND SPACE ENGINEERING, INDIAN INSTITUTE OF TECHNOLOGY INDORE**, is an authentic record of my own work carried out during the time period from August 21, 2020 to August 16, 2024 under the supervision of Dr. Bhargav Vaidya, Associate Professor, Indian Institute of Technology Indore.

The matter presented in this thesis has not been submitted by me for the award of any other degree of this or any other institute.

11/10/2024

signature of the student with date
(PRATEEK MAYANK)

This is to certify that the above statement made by the candidate is correct to the best of my knowledge.

Signature of Thesis Supervisor with date
(DR. BHARGAV VAIDYA)

Prateek Mayank has successfully given his Ph.D. Oral Examination held on **October 11, 2024**.

Signature of Thesis Supervisor with date
(DR. BHARGAV VAIDYA)

Dedicated
to
Mother Nature!

“ Nature has a great simplicity and therefore a great beauty. ”

— *Richard Feynman*

Acknowledgements

This PhD thesis represents the culmination of several years of hard work, learning, and personal growth. However, none of this would have been possible without the unwavering support, guidance, and encouragement of numerous individuals and institutions. The journey has been challenging yet fulfilling, and I would like to acknowledge those who have made this work possible.

First and foremost, I would like to express my deep gratitude to my PhD supervisor, Dr. Bhargav Vaidya, for his invaluable guidance throughout my PhD journey. His constant encouragement and insightful feedback have been instrumental in pushing me to achieve greater heights, and I am immensely thankful for his mentorship.

I am also grateful to the members of my PG Student's Progress Committee (PSPC): Dr. Ankhi Roy, Dr. Amit Shukla and Dr. Saurabh Das, for their constructive feedback and suggestions, which enhanced the quality of my research work. Their insights have been crucial to my development as a researcher.

A heartfelt thanks goes to the Department of Astronomy, Astrophysics, and Space Engineering at the Indian Institute of Technology Indore, India, for providing me with the resources and a stimulating academic environment. I also wish to acknowledge the Council of Scientific and Industrial Research (CSIR) for the initial funding through the Junior Research Fellowship (JRF), as well as the Prime Minister's Research Fellowship (PMRF), which provided not only a generous stipend but also a contingency fund that allowed me to travel and attend conferences, supporting my research without the worry of financial constraints.

I must also acknowledge the critical role of the computation cluster 'THOR', which has been a reliable workhorse for my research. Without its power and dependability, completing this thesis would not have been possible.

I have been fortunate to work with several outstanding collaborators. Prof. Dibyendu Chakrabarty from PRL, Ahmedabad deserves a special mention, not only for enhancing the quality of our collaborative research but also for his mentorship, which has guided me through many phases of my PhD. I would also like to extend my thanks to Dr. Wageesh Mishra from IIA, Bangalore and Dr. Stefan Lotz from SANSA, South Africa, for their fruitful and engaging collaborations, which enriched my work in several ways.

On a personal note, I owe a deep debt of gratitude to my dear wife and parents for their steadfast support, patience, and understanding throughout this rollercoaster journey. Their encouragement has been a constant source of strength for me.

I would also like to acknowledge the emotional support I received from my seniors in the lab — Dr. Sayan, Dr. Sriyasriti, Dr. Arghyadeep, and especially Dr. Gourab — who always treated me as a peer and never as a junior. Their comradeship and guidance made my time in the lab both enjoyable and enriching. A heartfelt thanks to my batchmates, friends in the department, and juniors in the lab for the friendship and support that sustained me through the long hours of research.

Finally, I would like to give special thanks to my close friends — Arpit and Sumit, who are also navigating their own PhD journeys — for sharing in both the challenges and triumphs along the way. A special shout-out goes to my cherished friends Shashwat and Manish, whose enduring friendship and encouragement have been invaluable to me.

Abstract

Space weather has gained increasing significance due to its potential impact on power grids, navigation systems, satellite operations, and astronaut safety. As nations, including India, prepare for upcoming space missions, the development of reliable space weather prediction models has become essential to safeguard these assets. Solar wind, coronal mass ejections (CMEs), and solar flares are the primary space weather drivers that can cause disturbances on Earth. This thesis presents a numerical approach to study these space weather drivers, focusing on their origins, evolution, and interactions, with the goal of enhancing forecasting capabilities.

The first phase of this thesis introduces an indigenous three-dimensional (3D) solar wind model (SWASTi-SW), developed to forecast the ambient solar wind properties in the heliosphere. This model leverages a semi-empirical coronal model combined with a physics-based inner heliospheric model. The study refines the widely used Wang-Sheeley-Arge (WSA) relation, offering a more generalized version that estimates the solar wind speed at 0.1 AU. Validated against in-situ observations across multiple Carrington rotations, the SWASTi-SW model effectively simulates solar wind properties in the inner-heliosphere. The work also explores the multi-directional features of stream interaction regions (SIRs), providing synthetic measurements for the Solar Wind Ion Spectrometer (SWIS) aboard ISRO's Aditya-L1 mission, showcasing the model's potential for operational space weather forecasting.

The next phase of the thesis focuses on the evolution of CMEs within the heliosphere. This newly developed CME module, integrated into the SWASTi framework, models both non-magnetized elliptic cone and magnetized flux rope CMEs. The study highlights the significant influence of ambient solar wind conditions on CME propagation, revealing that these conditions can alter CME properties such as internal

pressure distribution and density throughout their journey. The model's validation against in-situ observations and the analysis of CME-solar wind interactions emphasize the complex dynamics involved, including asymmetric deformation of the CME leading edge and a non-fractal power-law expansion of CME volume as it reaches a balanced state with the ambient solar wind.

Solar flares, another primary space weather driver, are addressed in the third part of the thesis. A solar flare prediction model using the Light Gradient Boosting Machine (LightGBM) algorithm has been developed, utilizing nine years of data from the Space-weather Helioseismic and Magnetic Imager Active Region Patches (SHARP). The model has been trained on a comprehensive dataset of 37 features, including active region parameters and flare history. Through feature selection and addressing class imbalance, the model has achieved high predictive performance, surpassing the performance of most existing solar flare models. The findings demonstrate that a limited set of significant features can enhance prediction accuracy, offering a robust tool for operational purposes.

The final part of the thesis explores the geo-effectiveness of one of the most energetic space weather phenomena: CME-CME interactions, an area that still remains less understood. Using the SWASTi framework, 3D MHD simulations have been conducted across various scenarios within realistic solar wind conditions. The study reveals that inhomogeneous ambient solar wind leads to non-uniform CME-CME interactions along different longitudes, significantly affecting the dynamics of the leading CME. Key findings include significant increases in the momentum and kinetic energy of the leading CME due to collision, the formation of reverse shocks, and the resultant complex wave patterns that can prolong geomagnetic storm recovery phases. The study also shows that the geo-effectiveness, as measured by the disturbance storm time (Dst) index, is significantly influenced by the initial properties of the trailing CME, particularly their relative tilt, density, and speed.

List of Publications

1. "SWASTi-SW: Space Weather Adaptive Simulation Framework for Solar Wind and Its Relevance to the Aditya-L1 Mission", **Prateek Mayank**, Bhargav Vaidya, Dibyendu Chakrabarty, 2022, *The Astrophysical Journal Supplement Series*, 262, 23, DOI: 10.3847/1538-4365/ac8551

2. "SWASTi-CME: A physics-based model to study CME evolution and its interaction with Ambient Solar Wind", **Prateek Mayank**, Bhargav Vaidya, Wageesh Mishra, Dibyendu Chakrabarty, 2023, *The Astrophysical Journal Supplement Series*, 270, 10, DOI: 10.3847/1538-4365/ad08c7

3. "Solar flare prediction and feature selection using Light Gradient Boosting Machine Algorithm", P A Vysakh, **Prateek Mayank**, 2023, *Solar Physics*, 298, 137, DOI: 10.1007/s11207-023-02223-5

4. "Study of Evolution and Geo-effectiveness of CME-CME Interactions Using MHD Simulations with SWASTi Framework", **Prateek Mayank**, Stefan Lotz, Bhargav Vaidya, Wageesh Mishra, Dibyendu Chakrabarty, *Accepted for publication in The Astrophysical Journal*, DOI: 10.3847/1538-4357/ad8084

NB: All the above entries are parts of my thesis.

Table of Contents

List of Figures

List of Tables

Chapter 1

Introduction

1.1 Space Weather and Society

Our nearest star, the Sun, is a hot ball of plasma with dynamic magnetic activity that influences inter-planetary space. The changing conditions in space caused by the Sun's activity and their effects on Earth's environment and technology are referred to as space weather. These events can lead to geomagnetic storms, which are disturbances in Earth's magnetic field caused by interactions with charged particles. They can disrupt satellite operations, power grids, and communication systems, and pose risks to astronauts and high-altitude flights [Schwenn, 2006; Webb & Howard, 2012]. Hence, the importance of space weather research has grown with society's increasing reliance on technology. Therefore, comprehensive understanding and accurate forecasting are crucial for mitigating its impacts.

One dramatic illustration of space weather's impact occurred during the geomagnetic storm of March 1989, which caused the Hydro-Quebec power grid to collapse, leaving millions without electricity for up to nine hours [Allen et al., 1989]. This

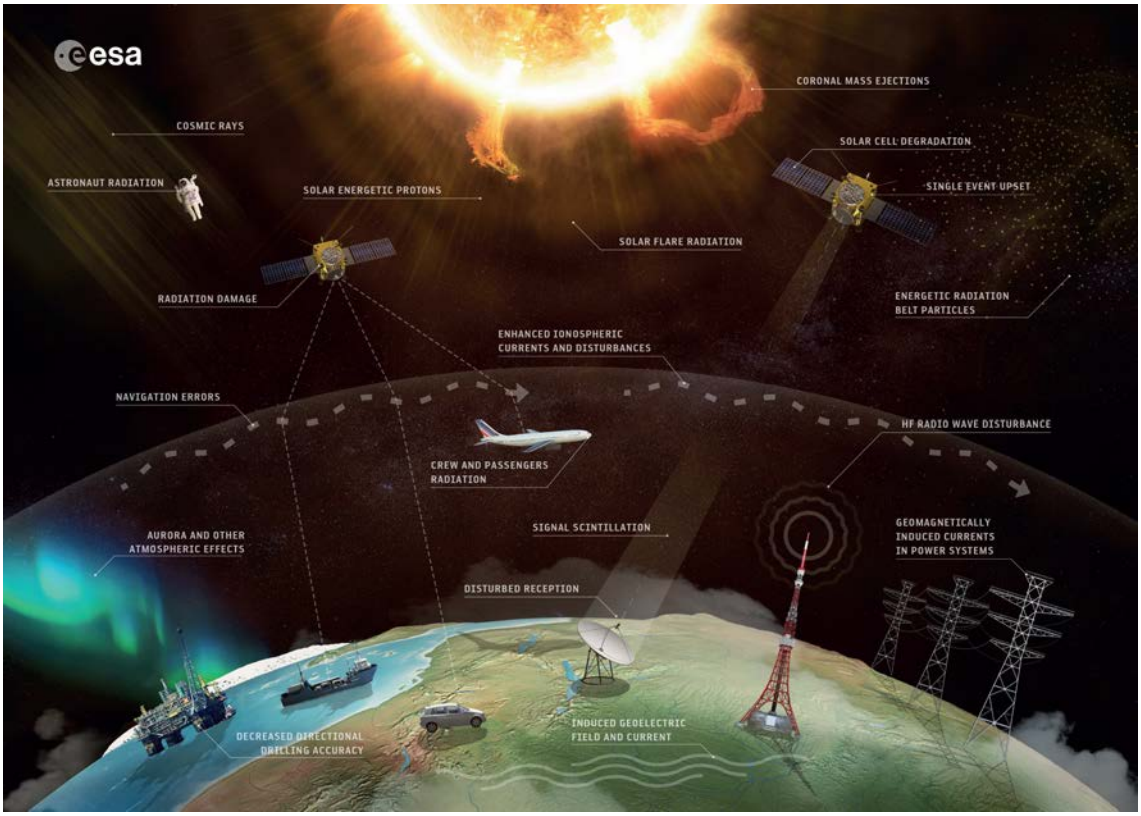

Figure 1.1: An illustration highlighting the effects of space weather on our society. Image credit: ESA.

blackout highlighted the vulnerability of our power infrastructure to geomagnetic disturbances, which can induce damaging currents in transmission lines and transformers, leading to widespread outages and long-term damage.

Telecommunications are also at risk from space weather. For instance, in January 1994, two Canadian satellites experienced outages during heightened solar activity, causing nationwide communication disruptions. The first satellite recovered in a few hours, but the second took six months and cost up to $70 million to restore, illustrating the high stakes involved [Council, 2008].

The aviation industry faces significant challenges from space weather. Increased radiation during space weather events can force airlines to reroute flights, avoiding

communication blackouts and protecting passengers and crew from heightened radiation exposure. These reroutes increase flight times and operational costs, causing economic impact, disruption in connecting flights, and inconvenience.

Spacecraft operations are also not immune to space weather events. Energetic particles can cause temporary operational anomalies, damage critical electronics, degrade solar arrays, and impair optical systems. The loss of the $640 million ADEOS-2 spacecraft in 2003 during a severe solar storm highlights the severity of space weather impacts on space missions [Council, 2008]. More recently, in February 2022, a geomagnetic storm caused the loss of 40 out of 49 newly launched Starlink satellites, underscoring the vulnerability of modern satellite constellations to space weather [Hapgood et al., 2022].

The interconnected nature of modern society means that the effects of space weather can ripple across various sectors, amplifying their impact. A power grid failure can disrupt transportation, communication, banking, and emergency services, leading to significant economic and social consequences. The 1989 Quebec blackout affected numerous sectors, demonstrating the need for comprehensive risk management strategies to mitigate such risks.

Understanding the full scope of space weather's impact involves recognizing its direct effects on technology and considering the cascading effects on societal infrastructure. The economic cost of severe space weather events can be staggering, with estimates suggesting losses ranging from $1 trillion to $2 trillion in the first year alone, and recovery times of up to a decade [Council, 2008].

To address these vulnerabilities, it is crucial to deepen our knowledge of space weather events and improve forecasting capabilities. A coordinated approach is essential for advancing space weather research and developing effective mitigation strategies. This involves a clear comprehension of the origins and evolution of space

weather drivers, as well as reliable forecasting of their arrival using observational and modeling techniques.

1.2 Space Weather Drivers

Like terrestrial weather, space weather manifests itself as a variety of distinct phenomena, ranging from benign to extremely severe. These solar phenomena, which lead to space weather events, are generally referred to as space weather drivers. Understanding these drivers is essential for comprehending their effects. Primary space weather drivers include the solar wind, coronal mass ejections (CMEs), and solar flares. Each of these drivers can influence Earth's magnetosphere, ionosphere, and technological systems in unique ways. For instance, solar wind stream interaction regions (SIRs) can lead to moderate geomagnetic activity and auroras. Meanwhile, CMEs are among the most impactful, capable of causing significant geomagnetic storms that disrupt power grids and satellite operations. Solar flares, on the other hand, can cause immediate radio communication disruptions. These major space weather drivers are described in more details in the following subsections.

1.2.1 Solar Wind

The solar wind is a continuous outflow of charged particles from the Sun's outer atmosphere, known as the corona. This stream of plasma is propelled by the high temperatures and magnetic fields of the corona, primarily composed of protons and electrons, with an admixture of a few percent alpha particles and much less abundant heavy ions in different ionization stages. As it flows outward, the solar wind carries with it the Sun's magnetic field, which permeates the entire solar system and forms a vast bubble called the heliosphere.

As the solar wind travels outward, it carries the Sun's magnetic field, which spirals outward due to the Sun's rotation. This interplanetary magnetic field (IMF)

influences the entire heliosphere and interacts with the magnetic fields of planets, including Earth. The solar wind plasma properties, such as its speed, magnetic field strength, density, and temperature, are influenced by the solar cycle, typically intensifying during periods of high solar activity [Hundhausen, 1979; McComas et al., 2003]. These variations can cause significant fluctuations in space weather, influencing geomagnetic activity and the behavior of cosmic rays [Belov et al., 2001].

1.2.1.1 Solar Wind Streams

As the solar wind streams move outward from the corona, they pass through several critical points where significant changes occur [Matthaeus, 2021; Parker, 1958]. Around 2 to 5 solar radii ($R_\odot$) from the Sun (transonic region), the solar wind reaches the sonic point, where its speed surpasses the local sound speed, transitioning to a super-sonic flow. Further out, approximately 10 to 20 $R_\odot$, it becomes super-Alfvénic, exceeding the Alfvén speed. This transition marks the point where the solar wind speed becomes greater than the speed at which magnetic disturbances can propagate. This means that changes in the coronal magnetic field cannot propagate upstream against the flow of the solar wind. The solar wind continues to expand as it travels through interplanetary space, forming a complex and dynamic medium that interacts with planetary magnetospheres.

Originating from different regions of the Sun, the solar wind varies significantly in its characteristics. It is generally categorized into two main types: a steady, fast solar wind and a more sporadic, slow solar wind (see Fig. 1.2). Understanding the origins, propagation, and interactions of these different solar wind streams is essential for forecasting the heliospheric state.

Fast solar wind streams originate from coronal holes, which are regions of the Sun's corona with open magnetic field lines. These regions allow the plasma to escape more easily, resulting in higher-speed winds. Fast solar wind travels roughly at speeds of

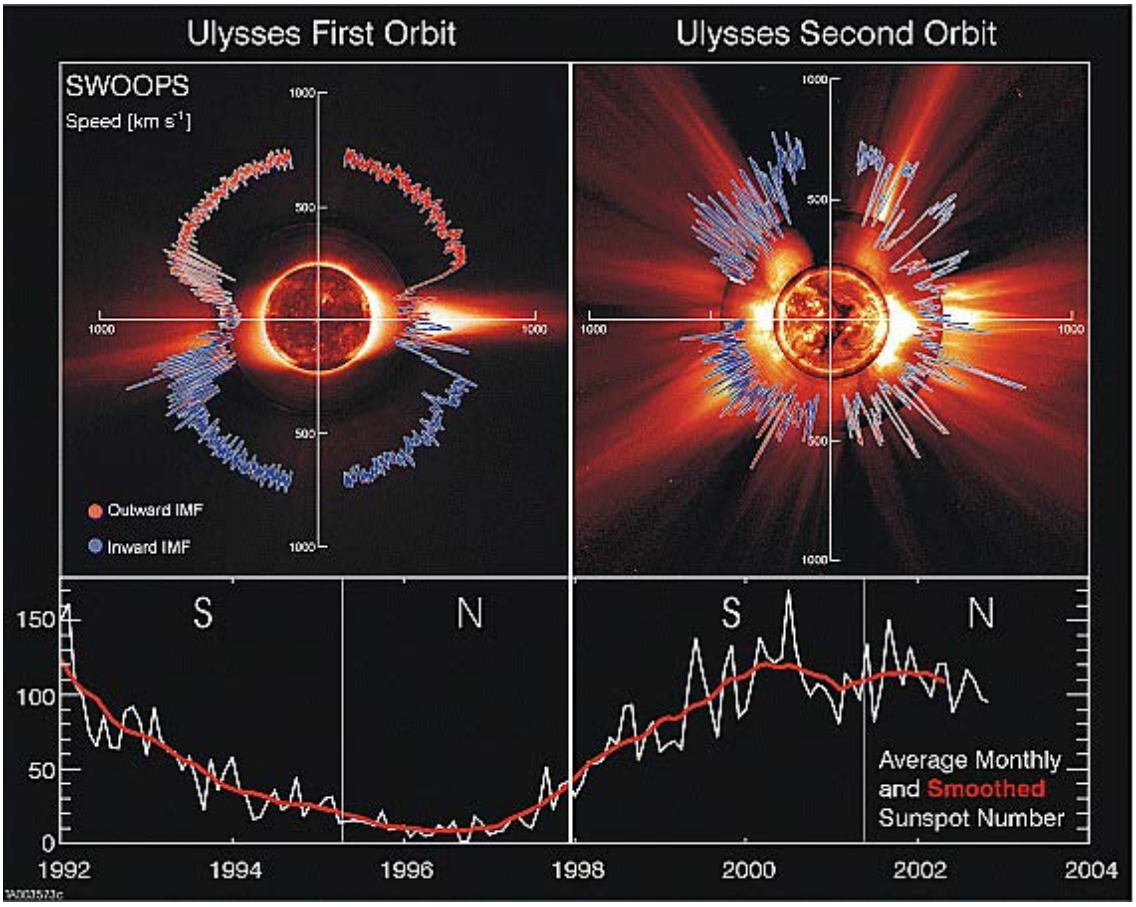

Figure 1.2: Figure shows the polar plot of the Ulysses's observation of solar wind speed in its first two orbits. In the top panel, these data are overlaid on solar images representative of solar minimum (August 17, 1996) and solar maximum (December 7, 2000). The bottom panel shows the sunspot numbers, indicating that first orbit took place during the declining phase and solar minima, while the second orbit occurred during the solar maxima [McComas et al., 2003].

>500 km/s and is characterized by lower density and higher temperature compared to slow solar wind. Its composition is relatively uniform, with less variation in particle density and temperature as it moves outward through the heliosphere.

On the other hand, the origin of slow solar wind streams is not fully understood. The prevailing scenario is that it comes from closed-field regions such as coronal streamers or active regions as well as from the edges of coronal holes [Wang, 2024].

These regions have more complex magnetic field configurations, which can trap the plasma and release it more sporadically. Slow solar wind travels roughly at speeds of <500km/s and is denser and cooler than fast solar wind. It exhibits more significant fluctuations in density, temperature, and composition, often containing a higher proportion of heavy ions and a greater variability in its plasma properties.

The primary differences between fast and slow solar wind streams lie in their speed, density, temperature, and composition. Fast solar wind, with its higher speed and lower density, tends to be more homogeneous. In contrast, slow solar wind is more variable, with greater fluctuations in its properties. The interaction between fast and slow solar wind streams plays a crucial role in shaping the heliosphere.

1.2.1.2 Stream Interaction Regions

When faster solar wind streams overtake the preceding slower solar wind streams, a region of compressed plasma with enhanced magnetic fields forms. These regions are called stream interaction regions (SIRs; see Fig. 1.3). They are characterized by a sharp increase in plasma density, temperature, and magnetic field strength [Wilcox & Ness, 1965]. The leading edge of an SIR often shows a region of compressed and heated slow wind, while the trailing edge features decelerated fast wind. These compressed regions form corotating interaction regions (CIRs) that persist over multiple solar rotations.

As SIRs travel outward from the Sun, their structure evolves. Near the Sun, the interaction regions have sharp speed gradients and distinct boundaries between the fast and slow streams. Additionally, shock formations are less frequent. With heliospheric distance, the sharpness of gradient decreases due to momentum transfer between the slow and fast streams. However, the likelihood of shock formation increases [Gosling et al., 1978]. The reason being that magnetosonic speed in the solar wind decreases with increasing distance from the Sun.

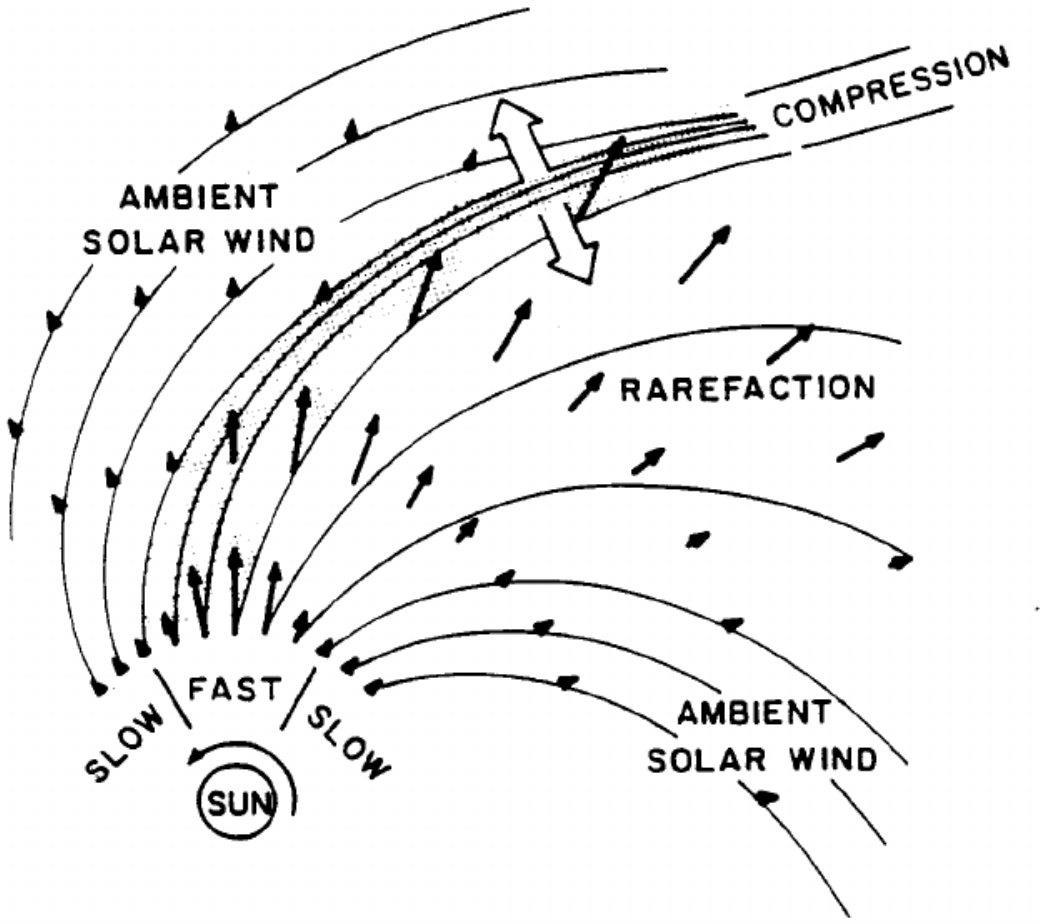

Figure 1.3: 2D schematic diagram of stream interaction region, showcasing the compressed region between fast and slow solar wind streams Pizzo [1978].

The difference in the composition of slow (have higher proportion of heavy ions) and fast solar wind also reflects in the vicinity of SIRs. For instance, Richardson et al. [2006] have shown that the ratios of oxygen ions (O^7/O^6) decrease in the vicinity of the stream interface, indicating a compositional shift. Several statistical studies (e.g., [Alves et al., 2006; Tsurutani et al., 2006; Zhang et al., 2008b]) have found the correlation these characteristic features at the stream interface, and the associated geomagnetic activity. They have shown that SIRs are chiefly responsible for most of the weak to moderate geomagnetic storms.

1.2.1.3 Modes of Study

Understanding and forecasting the solar wind, particularly SIRs, rely on three primary methods: in-situ measurements, remote sensing observations, and computational modeling. In-situ data collection is a cornerstone of solar wind studies. Most of our understanding has come from in-situ data collected in the interplanetary space (e.g., Voyager, Ulysses, Parker Solar Probe) and at Sun-Earth Lagrangian points (e.g., ACE, Wind, STEREO). These spacecrafts directly measure solar wind properties such as particle density, temperature, speed, and magnetic field as they pass through the solar wind. Some of them provide near real-time data on the local conditions of the solar wind and SIRs, offering detailed insights into their physical characteristics. However, in-situ measurements have limited spatial coverage, which impedes the acquisition of a complete picture of the spatial and temporal distribution of properties.

Remote sensing techniques are also used for observing the large-scale structure and evolution of the solar wind. Two primary methods are interplanetary scintillation (IPS) and white-light imaging. The IPS technique involves observing the scintillation of radio signals from distant astronomical sources caused by solar wind plasma. IPS data, collected by networks of radio telescopes, can infer solar wind speed and density variations, offering a broad view of the solar wind's three-dimensional structure. However, the plasma properties inferred from IPS can lack the resolution and reliability needed for comprehensive analysis, especially in the inner heliosphere where the solar wind density is low. White-light imaging instruments, such as the Heliospheric Imagers (HI) on the STEREO spacecraft, capture sunlight scattered by electrons in the solar wind. Despite their utility, white-light observations alone cannot provide complete plasma property measurements, limiting their effectiveness in fully characterizing SIRs.

Magnetohydrodynamic (MHD) modeling is another essential tool for studying and

forecasting solar wind behavior. These models simulate the dynamics of the solar wind by solving the MHD equations, which describe the behavior of a plasma influenced by magnetic fields. MHD models provide a comprehensive framework for understanding the complex interactions within the solar wind. One of the main advantages of MHD modeling is its ability to offer a global perspective on solar wind dynamics, overcoming the limitations of in-situ and remote sensing observations. A detailed description of different numerical models is discussed in Section 1.3.

1.2.2 Coronal Mass Ejection

CMEs are large-scale expulsions of plasma from the solar corona, capable of releasing billions of tons of coronal material into space at high velocities. These powerful eruptions are among the most significant space weather events. They originate from regions of intense magnetic activity on the Sun, such as active regions, and are often associated with solar flares. The eruption is driven by the release of magnetic energy stored in the Sun's corona, which propels the coronal material outward. One of the key reasons CMEs are of great interest to space weather researchers is their ability to carry strong magnetic fields that can reconnect with Earth's magnetic field, leading to intense geomagnetic storms.

1.2.2.1 Initial Properties of CMEs

After eruption, CMEs propagate through the corona exhibiting distinct initial properties: magnetic structure, speed, density, and temperature. CMEs are typically characterized by large-scale magnetic flux ropes, which are twisted helical structures composed of magnetic field lines. These flux ropes can vary in size and complexity, often spanning several solar radii.

In the corona, CMEs can be observed using white light coronagraph images, which provide critical information about their initial speed, width, and mass. The initial speeds of CMEs can vary significantly, from a few hundred kilometers per second

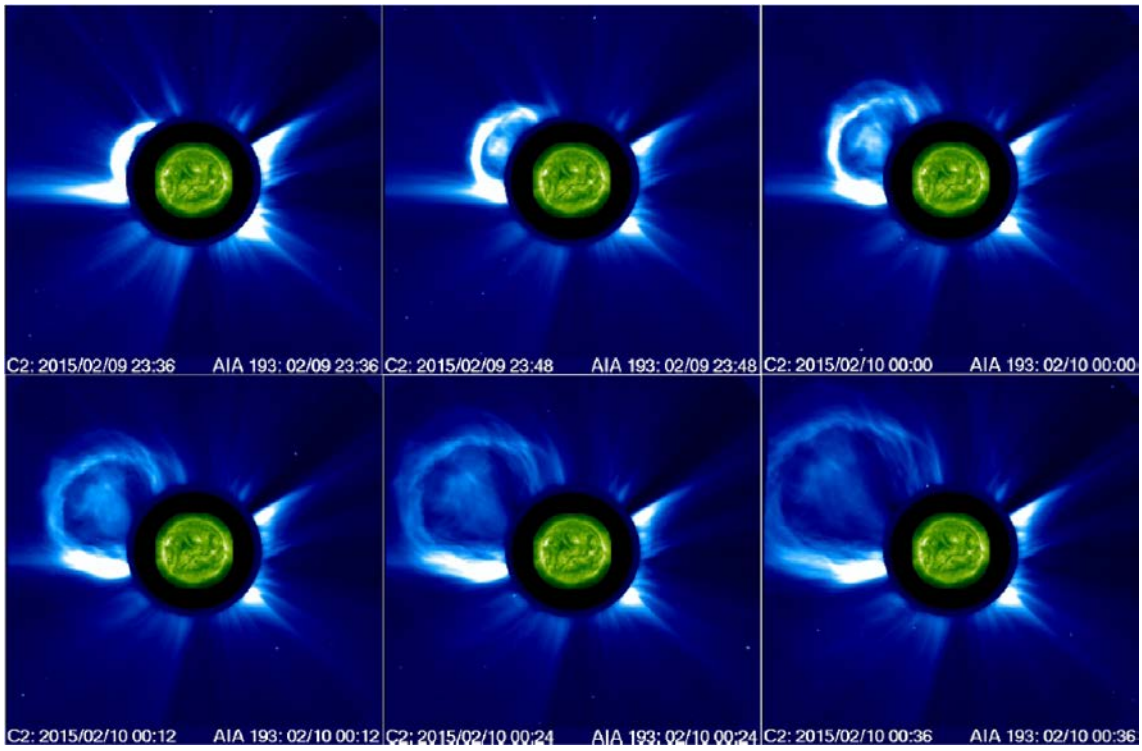

Figure 1.4: Progression of a CME as observed within the SOHO/LASCO C2 coronagraph's field of view. In each subplot, the CME is visible in the top-left quadrant [Georgoulis et al., 2019].

to over 2,000 kilometers per second. The mass density of a typical CME can be around 10^{-18} kg/m^3 [Temmer et al., 2021], and their kinetic energy can be as high as 10^{24} joules [Gopalswamy et al., 2015]. The magnetic flux of CME is also a key parameter, with typical values ranging around 10^{13} Wb [Gopalswamy et al., 2017].

The magnetic structure of CMEs is often modeled as a flux rope, which can be detected in white light coronagraph images as a bright leading edge, followed by a dark cavity and a bright core. This three-part structure is indicative of the magnetic field configuration within the CME, with the bright leading edge corresponding to the compressed plasma and magnetic field, the dark cavity representing the flux rope, and the bright core indicating the prominence material carried by the CME (see Fig. 1.4). These coronagraph images provide insights into the size, shape,

orientation, and dynamics of CMEs in the corona.

The primary forces acting on the CME are the Lorentz force, aerodynamic drag, and gravity. The Lorentz force is dominant at low heights, particularly in the inner corona [Vršnak, 2006], driving the initial CME acceleration as it moves outward from the Sun. Additionally, the magnetic pressure within the CME and the magnetic tension force play crucial roles in shaping its structure and dynamics. The balance between these forces determines the evolution of the CME in the corona and its eventual interaction with the interplanetary medium.

1.2.2.2 Heliospheric Evolution

As Coronal Mass Ejections (CMEs) propagate from the outer corona into the heliosphere, interactions with the ambient solar wind play a significant role in their evolution. These interactions have an impact on the kinematic and structural evolution of CMEs. For example, fast CMEs tend to deflect eastward during their propagation in the inner-heliosphere, and this deflection is further enhanced in the presence of a CIR [Heinemann et al., 2019; Liu et al., 2019b]. Furthermore, when a CME propagates within an high speed stream (HSS), it experiences a lesser drag force compared to when it encounters the boundary of an HSS [Kay et al., 2022]. Some studies have also reported the pancaking of the CME structure [Raghav & Shaikh, 2020; Riley & Crooker, 2004] and the deformation of the leading edge of CMEs [Hinterreiter et al., 2021; Sudar et al., 2022].

Additionally, the ambient solar wind conditions also effect the internal magnetic and thermodynamic properties of CMEs [Davies et al., 2022; Winslow et al., 2021]. However, quantification of such impacts is not very well studied. Few studies [e.g., Scolini et al., 2021, 2022] have estimated some effects but the primary challenge in exploring the 3D properties of CMEs lies in accurately separating the CME structure from the surrounding solar wind.

As CME evolves in the inner-heliosphere and goes beyond a distance of ∼15 $R_\odot$, the aerodynamic drag force becomes the dominant force governing CME dynamics [Sachdeva et al., 2015; Vršnak et al., 2008]. This drag force acts in the opposite direction of the CME's motion, slowing it down as it propagates through the heliosphere. The drag force depends on the relative speed between the CME and the solar wind, as well as the density and cross-sectional area of the CME. However, tracking CMEs in the inner-heliosphere becomes increasingly difficult with distances. Heliospheric imagers provide valuable data, but their observations can be limited by line-of-sight effects, making it hard to accurately determine the CME's three-dimensional structure and trajectory. Given these challenges, numerical modeling becomes the most reliable and efficient tool for investigation of CME evolution in the heliosphere.

1.2.2.3 In-situ Signatures

In-situ observations are conducted by spacecraft equipped with instruments designed to measure local magnetic fields, plasma density, temperature, velocity, and other parameters. The current in-situ fleet includes the Parker Solar Probe, Solar Orbiter, Wind, ACE, STEREO, DSCOVR, and BepiColombo, all of which provide high-resolution data on CME properties as they travel through the heliosphere before reaching 1 AU. These spacecraft offer detailed insights into the internal structure and composition of CMEs, which are essential for understanding their interactions with the solar wind and their impact on the magnetosphere.

One of the most distinctive in-situ signatures of a CME is the presence of a magnetic flux rope, which often shows a characteristic rotation in the magnetic field components, commonly referred to as the B_z flipping. This rotation is a key indicator of the CME's internal magnetic structure and can provide valuable information about its orientation and potential geo-effectiveness. Additionally, CMEs are characterized by leading shock and sheath regions, magnetic clouds (with relatively smooth and

coherent magnetic fields), high charge states of oxygen and iron, elevated helium abundance, and lower proton temperatures.

1.2.3 Solar Flare

Solar flares are sudden, intense bursts of radiation emanating from the Sun's atmosphere. These powerful events release a tremendous amount of energy, equivalent to millions of hydrogen bombs exploding simultaneously. Solar flares are among the most significant manifestations of solar activity, impacting space weather and various technological systems on Earth. They are characterized by a rapid increase in brightness across a broad spectrum of electromagnetic radiation, from radio waves to gamma rays. Typically lasting from minutes to hours, they are often associated with active regions on the Sun. The peak emission of a solar flare usually occurs in the X-ray wavelengths.

Solar flares form when magnetic energy stored in the Sun's atmosphere is suddenly released. This process is driven by magnetic reconnection, where oppositely directed magnetic field lines near active regions reconfigure and release energy. The released energy heats the surrounding plasma, accelerates particles, and produces the observed radiation. They are classified based on their peak X-ray flux in the 1 to 8 Angstrom range, as measured by the Geostationary Operational Environmental Satellites (GOES). The classification system includes: A (weakest), B, C, M (moderate), and X (strongest) class flares with subclasses 1 to 10 (e.g., X1 to X10).

What makes solar flares unique is their rapid onset and the broad range of emitted radiation. Unlike CMEs and solar wind, which involve the ejection of solar material, solar flares primarily involve the release of electromagnetic energy. Additionally, they take only about 8 minutes to reach Earth's location. In contrast, CMEs typically take around 1-3 days, and SIRs take around 3-4 days to reach Earth. They can affect Earth's ionosphere almost instantaneously, disrupting radio communications

and navigation systems. It has been observed that M-class solar flares can result in small radiation storms and brief radio interruptions, particularly in the polar regions [Echer et al., 2005]. X-class solar flares, which are more powerful than M-class flares, can cause radiation storms with extended durations and more severe impacts.

1.2.4 CME-CME Interaction

When multiple CMEs are erupted in quick succession, their interactions—termed CME-CME interactions—can dramatically enhance their space weather impact. CME-CME interactions occur when a faster CME overtakes a slower one, leading to a complex interplay of their shocks, magnetic fields and plasma structures. Studying these interactions is crucial as they can significantly amplify geomagnetic storms, particle acceleration, and other space weather phenomena [Gopalswamy et al., 2001; Lugaz et al., 2017; Scolini et al., 2020].

The complexity of CME-CME interactions arises from the already intricate dynamics present in individual CME and solar wind (SW) interactions. In single CME-SW interactions, ambient solar wind conditions can effect the CME's trajectory, speed, internal properties, and structure [Shen et al., 2012b; Temmer et al., 2011; Wu et al., 2016]. When a trailing CME catches up and collides with a leading CME, resulting in a CME-CME-SW interaction, the scenario becomes even more complex. Studies have reported a wide range of collision types between CMEs, from inelastic [Mishra et al., 2014a], nearly elastic [Mishra et al., 2015], superelastic collisions [Shen et al., 2012a], to merging-like processes [Temmer et al., 2012].

Multiple observational and simulation studies have made significant progress in understanding the evolution of CMEs during interactions. Shen et al. [2016] showed that the final speeds depend on the relative masses of the CMEs as well as their relative speeds. Through 2.5D simulations, Poedts et al. [2003] noted that the acceleration of the leading CME increases as the mass of the trailing CME increases. In

addition to speed, CME-CME interactions can also lead to deflection of the CMEs [Lugaz et al., 2012; Shen et al., 2012a]. Observational and simulation-based studies have also demonstrated that the expansion of the radial width of the leading CME decreases as the trailing CME impacts and compresses its rear [Lugaz et al., 2005; Xiong et al., 2006].

Several studies have observed that CME-CME interactions are a common source of double-dip and multiple-dip geomagnetic storms [Richardson & Zhang, 2008; Zhang et al., 2008a]. Much of the understanding about the impact of CME's initial properties – that is, right after eruption, measured at around 0.1 AU – on their geo-effectiveness has come from MHD simulations. Scolini et al. [2020] quantified the impact of interactions on the geo-effectiveness of individual CMEs using the EUHFORIA spheromak CME model. They found that the time interval between the CME eruptions and their relative speeds are critical factors in determining the resulting impact of the CME-CME structure. Additionally, Koehn et al. [2022] conducted MHD simulations of spheromak CMEs with a uniform outflowing solar wind and found that the orientation and handedness of a given CME can significantly impact the conservation and loss of magnetic flux in the CME.

Although several observational studies have shown the consequences of CME-CME interactions, they have not been very successful in elucidating the interaction process itself. Most studies have primarily focused on different aspects of the interaction without attempting to explore a global view. While multiple numerical studies have provided great insights into these interaction processes, particularly shock evolution, there have been very few studies on CME-CME interactions occurring within realistic dynamic ambient solar wind conditions [e.g., Scolini et al., 2020]. Given the complexities and limitations in observational and simplified simulation studies, MHD ensemble simulations with realistic solar wind backgrounds offer a powerful tool to obtain a global view.

1.3 Space Weather Modeling

Considering the observational challenges in the inner-heliosphere, several numerical models have been developed for their study as well as forecasting. The method of solar wind modeling can be broadly classified into three categories: empirical, semi-empirical, and MHD based simulation. Empirical models (e.g., PDF [Bussy-Virat & Ridley, 2014], PROJECTZED [Riley et al., 2017], AnEn [Owens et al., 2017b], etc.) use a probabilistic forecasting approach, which is framed by analyzing solar wind observations at Sun-Earth L1 Lagrangian point. The semi-empirical models (e.g., ESWF [Reiss et al., 2016], WSA [Arge & Pizzo, 2000], etc.) employ an empirical relation of solar wind speed based on the observation of coronal holes. On the other hand, simulation models (e.g., MAS [Riley et al., 2001], ENLIL [Odstrcil, 2003], SWMF [Tóth et al., 2005], SWIM [Feng et al., 2010], SUSANOO [Shiota et al., 2014], EUHFORIA [Pomoell & Poedts, 2018a], Narechania et al. [2021] etc.) are physics-based models which use photospheric magnetograms to determine plasma properties in the heliosphere. According to MacNeice et al. [2018], empirical models are more accurate and less computationally intensive than semi-empirical and simulation models. However, they offer a limited range of plasma properties, providing only tome series data at one location. While simulation models are computationally expensive, they provide a deeper understanding of fundamental physics, which is crucial for developing effective responses to space weather effects.

Numerous studies have also been conducted to develop inner-heliospheric models that aim to continuously track the evolution of CMEs in the interplanetary space. These approaches can be broadly classified into two categories: magneto-hydrodynamic (MHD) simulations and analytical modeling. Additionally, some of these models simulate CMEs with a realistic background solar wind, while others do not, assuming the solar wind has an insignificant effect on the CME properties being studied. Table 1.1 presents a list of physics-based heliospheric models, categorizing

Table 1.1: List of physics-based CME models with their model type and modules.

Model Name	**Type**	**Modules**
MAS	MHD	Solar Wind
ENLIL	WSA+MHD	Solar Wind + cone CME
SWMF	MHD	Solar Wind + flux rope CME
SWIM	MHD	Solar Wind
SUSANOO	WSA+MHD	Solar Wind + spheromak CME
EUHFORIA	WSA+MHD	Solar Wind + cone, flux rope, spheromak CMEs
CORHEL	WSA+MHD	Solar Wind
DBM	Analytical	cone CME
ELEvoHI	Analytical	Solar Wind + cone CME
ANTEATR-PARADE	Analytical	Solar Wind + flux rope CME
3D-CORE	Analytical	flux rope CME

them by model type and the usage of background solar wind. However, despite the availability of global models, they are typically accessible only on a run-on-request basis and are not open source.

In the category of MHD models, the WSA-ENLIL+Cone model [Odstrcil et al., 2004] has been widely used, which implements a non-magnetized CME with a simple cone geometry [Xie, 2004]. Another MHD model, SUSANOO-CME [Shiota & Kataoka, 2016], utilizes a spheromak-type magnetic CME. EEGGL+AWSoM_R [Jin et al., 2017] combines the Gibson-Low flux rope model [Gibson & Low, 1998] with the AWSoM MHD solar wind model to compute CME plasma properties in the inner-heliosphere. Similarly, EUHFORIA [Pomoell & Poedts, 2018b] also utilizes the MHD approach by incorporating a non-magnetized cone [Pomoell & Poedts, 2018b], magnetized spheromak [Verbeke et al., 2019], and magnetized flux rope CME [Maharana et al., 2022].

Among the analytical models, the drag-based model [Vršnak et al., 2013] exclusively accounts for the effect of solar wind drag to determine the CME arrival time. This model presumes that the CME evolution is primarily governed by its interaction with ambient solar wind within the inner-heliosphere. Its updated version, the DBEM [Dumbović et al., 2018], carries out multiple runs to yield an ensemble of arrival time and speed results by taking into account the uncertainty in input values obtained from coronagraph images. The ELEvoHI [Rollett et al., 2016] model further incorporates heliospheric imager observations to estimate CME properties, while its upgraded version [Hinterreiter et al., 2021] also considers the deformation of the CME front due to ambient solar wind conditions. Likewise, the newly developed ANTEATR-PARADE [Kay & Nieves-Chinchilla, 2021] drag-based model accounts for changes in CME size and shape while it propagates in the inner-heliosphere.

However, when it comes to predicting solar flares, probabilistic methods stand out as the only efficient option. This is due to their ability to provide results promptly, which is crucial considering the rapid travel time of solar flares. Over the past decade, significant progress has been made in probabilistic methods for solar flare prediction, leading to the emergence of various techniques. Huang & Wang [2013]; Nishizuka et al. [2017] utilised the Decision Tree algorithm in their solar flare model, while Li & Zhu [2013] employed Neural Networks and Learning Vector Quantisation models. The Support Vector Machine algorithm has been widely employed in solar flare prediction, with studies conducted by Bobra & Couvidat [2015]; Florios et al. [2018]; Nishizuka et al. [2017]; Ribeiro & Gradvohl [2021]. The other machine learning based solar flare model includes the k-NN method [Nishizuka et al., 2017], Multi-Models [Liu et al., 2017], the Random Forest [Florios et al., 2018; Liu et al., 2017; Ribeiro & Gradvohl, 2021], Multi-layer Perceptrons [Florios et al., 2018], Long-Short Term Memory (LSTM) [Chen et al., 2019; Jiao et al., 2020; Liu et al., 2019a; Wang et al., 2020]. Additionally, Deep Learning Neural Networks have been

used for solar flare prediction [Nishizuka et al., 2018]. Despite substantial advancements in diverse prediction models for solar flares, a definitive consensus regarding the optimal performing model is currently lacking.

1.4 Objective of the Thesis

The primary goal of this thesis has been to develop a comprehensive indigenous space weather model that can be used both as an operational forecasting tool and for studying space weather drivers. This thesis is centered around two main objectives: creating a functional space weather forecasting model and utilizing it to explore and understand space weather phenomena. To achieve these goals, we have developed the SWASTi (***S****pace* ***W****eather* ***A****daptive* ***S****imula****Ti****on*) framework, which includes modules for SW and CMEs, as well as a ML model for solar flare prediction. These models have been rigorously validated with observational data. Additionally, we have used these models to conduct numerical studies addressing unresolved problems in the field, leading to new insights into the evolution and geo-effectiveness of space weather drivers.

In this regard, the following objectives were adopted in the projects:

i. Developing a global SW model to compute plasma properties at 1 AU using the solar magnetogram as input, and validating it with in-situ observations.

ii. Simulating potential solar wind observations of ADITYA L1 to comprehend its multi-directional observational capability and study the peculiar 3D features of SIRs.

iii. Developing a fast and realistic CME model to study the evolution of its properties as it propagates through the inner heliosphere, interacting with the ambient SW.

iv. Investigating the LightGBM technique for solar flare prediction compared to

other existing ML techniques and examining the relative significance of flare features.

v. Understanding the evolution of CME-CME interactions in the inner heliosphere and the role of initial CME properties in their effective geo-effectiveness.

The thesis work is organised in the following order: ***Chapter 2*** provides a detailed description of the numerical techniques and observational tools used to achieve the scientific goals of the thesis. ***Chapter 3*** describes and validates the SWASTi-SW model and its relevance to the ADITYA-L1 mission. ***Chapter 4*** provides a description and validation of the SWASTi-CME model and studies the evolution of CMEs in the inner heliosphere and the impact of ambient SW on them. ***Chapter 5*** discusses solar flare prediction using the LightGBM machine learning algorithm and the importance of solar flare features. ***Chapter 6*** presents an ensemble study quantifying the evolution of CME-CME interactions and their geo-effectiveness. Finally, ***Chapter 7*** summarizes the key conclusions of this PhD thesis work.

Chapter 2

Data and Techniques

In this chapter, an overview of several key observational datasets and numerical techniques are discussed that are imperative to comprehend prior to assessing the methodologies highlighted in Section 1.4. The purpose is to establish an understanding of these data and techniques, which will serve as a foundation for evaluating the methodologies employed in the thesis.

2.1 Observational Data

Observational data serves several critical functions in this thesis work. It is indispensable for data-driven simulations, acting as essential inputs for the models, which enhances the fidelity of the simulations by aligning them more closely with real-world conditions. Additionally, observational data is used to validate the developed models and perform accuracy analysis, ensuring the reliability and robustness of the simulations. Consequently, both remote sensing and in-situ observations become highly relevant, which are discussed in detail in the following subsections.

2.1.1 Remote Sensing

Remote sensing data is crucial for capturing large-scale and detailed observations of solar phenomena. It provides comprehensive imagery and measurements of the Sun's

surface and outer atmosphere. Instruments like magnetograms and coronagraphs offer continuous monitoring and high-resolution data, enabling the study of dynamic solar processes over time. The vital remote sensing data used in this thesis work for initializing models and simulations is described here.

2.1.1.1 Magnetogram

Magnetograms provide detailed maps of the solar surface magnetic field. They capture the magnetic field strength and direction on the solar surface, allowing for the study of solar activity and its influence on space weather. Two prominent sources of magnetogram data are the Global Oscillation Network Group (GONG) and the Helioseismic and Magnetic Imager (HMI) on the Solar Dynamics Observatory (SDO).

GONG is a network of six ground-based observatories strategically located around the globe to provide nearly continuous observations of the Sun [Harvey et al., 1996]. The six sites (see Fig. 2.1) that comprise the GONG network are: Big Bear Solar Observatory, California, USA; Mauna Loa Solar Observatory, Hawaii, USA; Learmonth Solar Observatory, Australia; Udaipur Solar Observatory, India; Observatorio del Roque de los Muchachos, Canary Islands, Spain, and Cerro Tololo Interamerican Observatory, Chile. The main instrument of GONG is known as a Fourier Tachometer that comprises a polarizing Michelson interferometer, narrow-band prefilters, and a rotating half-wave plate that sweeps the interference fringes of the Michelson across the solar spectral line in wavelength. The Doppler shift of the Ni I 676.8 nm line used by GONG is determined by comparing the intensity in three segments of the rotation of the waveplate to measure the phase shift of the spectral line, from which the Doppler velocity can be determined. The full-disk 1024×1024 velocity images are the prime helioseismology input data.

A useful aspect of the Fourier Tachometer measurement principle is that magnetograms can be simply created by obtaining the velocity images in two opposite

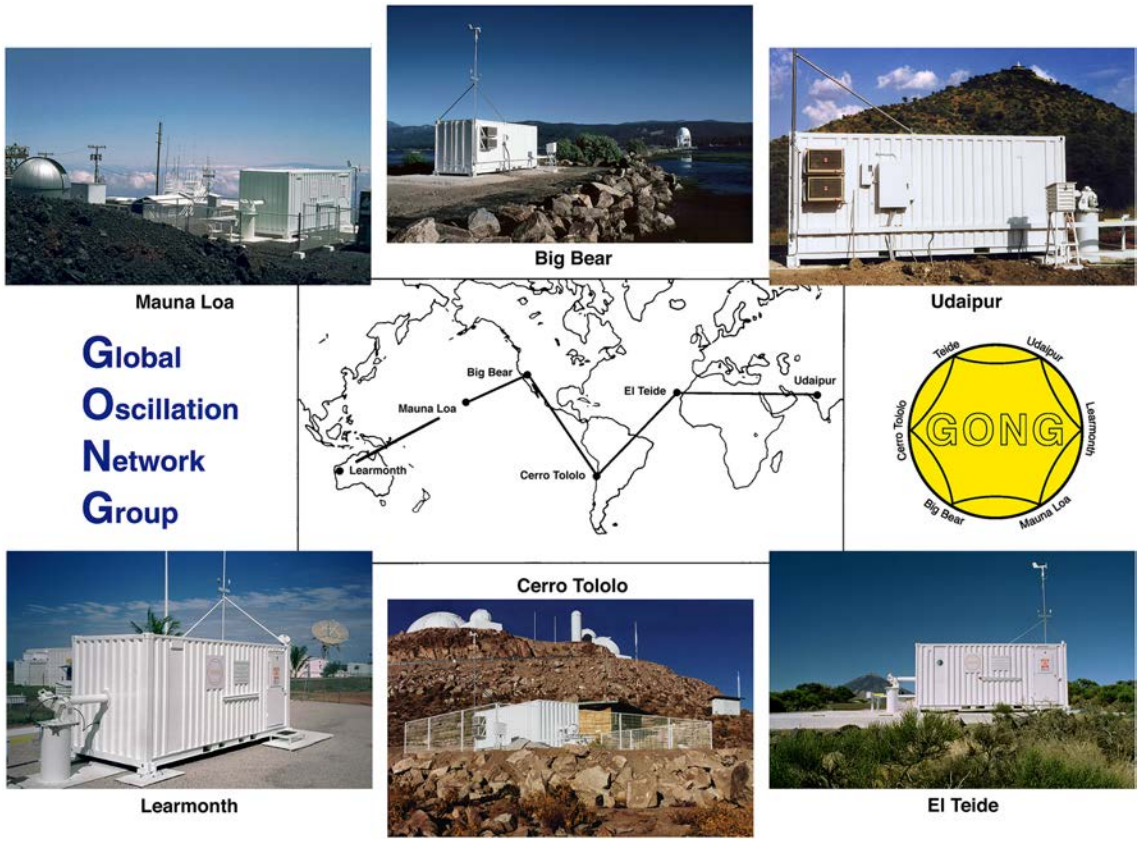

Figure 2.1: The locations of the six GONG sites and images of the instruments at each location [Hill, 2018].

states of circular polarization and then differencing them to produce a line-of-sight full-disk magnetogram. Both the Doppler velocity and magnetic field images are obtained with a cadence of 1 min. The magnetograms are averaged over 10 min at the remote sites after removal of bad images, and the average and variance of the magnetic field are returned to the Boulder data center shortly after acquisition. These data are then used to create a synoptic map every hour for input into models that produce forecasts of geomagnetic storms.

HMI aboard SDO offers high-resolution magnetograms with a spatial resolution of about 1 arcsecond. HMI provides full-disk Doppler velocity, line-of-sight magnetic flux, and continuum proxy images every 45 seconds, and vector magnetic field maps

every 90 or 135 seconds depending on the image frame sequence selected [Scherrer et al., 2012]. HMI uses Fe I 617.3 nm emission line and the magnetic field is derived from the Stokes parameters (I,Q,U,V) using a Milne–Eddington-based inversion model. The solar image nearly fills the 4096 × 4096 pixel CCD camera allowing 0.5 arcsecond per pixel. The HMI instrument was developed at the Lockheed Martin Solar and Astrophysics Laboratory (LMSAL) in collaboration with Stanford University as part of the Stanford Lockheed Institute for Space Research collaboration.

2.1.1.2 Coronagraph Images

Coronagraphs are pivotal instruments for studying solar corona, designed to block out the direct light from the Sun's photosphere, allowing the faint corona to be observed in detail. This is a very important tool for studying CMEs and other phenomena of solar corona. Two key space-based coronagraph missions are the Large Angle and Spectrometric Coronagraph (LASCO) [Brueckner et al., 1995] on the Solar and Heliospheric Observatory (SOHO) and the COR instruments on the Solar Terrestrial Relations Observatory (STEREO) [Howard et al., 2008].

The LASCO instrument on SOHO have two working coronagraphs: C2 and C3. C2 covers a field of view from 1.5 to 6 solar radii, while C3 extends this to 30 solar radii. LASCO images are vital for detecting and tracking CMEs from their origin near the solar surface out into the heliosphere. The data provided by LASCO allows for detailed analysis of the speed, direction, and structure of CMEs, which are essential parameters for space weather forecasting.

The COR1 and COR2 instruments on the STEREO spacecraft provide stereoscopic views of the Sun's corona. COR1 has a field of view from 1.5 to 4 solar radii, while COR2 extends from 2 to 15 solar radii. By observing the corona from different vantage points, STEREO's COR instruments offer a three-dimensional perspective

of CMEs. This stereoscopic capability is crucial for accurately determining the three-dimensional structure, speed, and trajectory of CMEs, improving our understanding of their propagation through the heliosphere.

Coronagraph images from LASCO and STEREO are extensively used to estimate the properties of CMEs. These images allow for the calculation of CME speed by tracking the motion of the leading edge over time. The acceleration or deceleration of a CME can also be determined, which is critical for predicting its arrival time at Earth. Additionally, coronagraph images help estimate the mass of CMEs by measuring the amount of scattered light, which is proportional to the density of the ejected material.

The three-dimensional reconstruction of CMEs using STEREO's COR images enables a more accurate determination of their direction and angular width. This information is essential for assessing the trajectory, heliospheric evolution and potential impact of a CME on Earth's magnetosphere. Furthermore, the polarization measurements from coronagraphs can provide insights into the density and temperature of the coronal plasma, offering a deeper understanding of the physical conditions in the corona during a CME.

2.1.1.3 SHARP data

The Space-weather HMI Active Region Patches (SHARP) data, provided by the Helioseismic and Magnetic Imager (HMI) on the Solar Dynamics Observatory (SDO), is a pivotal dataset for studying solar flares and active regions. Released in 2014, the SHARP data series includes maps of magnetic concentrations that are automatically tracked throughout their lifetime. These patches identify active regions (ARs) and continuously calculate various summary parameters at a 12-minute cadence, providing a comprehensive dataset for solar flare modeling and analysis [Bobra et al., 2014].

The SHARP data series is particularly valuable for its detailed characterization of active regions. A total of 25 summary parameters are provided, based on the work by Bobra et al. [2014], which include indices such as magnetic flux, spatial field gradients, vertical current density characteristics, current helicity, and proxy for integrated free magnetic energy. These parameters are critical for understanding the magnetic structure and dynamics of active regions, which are linked to increased flare activity. The initial list of parameters and their corresponding equations, along with brief descriptions, are presented in Table 5.1.

For the solar flare model used in this thesis, SHARP data was collected using the SunPy Python module with the JSOC client. The data products used included *hmi.sharp.720s* and *cgem.lorentz*. The *hmi.sharp.720s* data series provides vector magnetogram patches at a 12-minute cadence, while the *cgem.lorentz* data series, as described by Sun [2019], estimates the Lorentz force in active regions. These high-cadence observations are essential for capturing the rapid changes in the magnetic field that can lead to solar flares.

The SHARP dataset's ability to automatically track and analyze active regions over time makes it an invaluable resource for solar physics research. By providing detailed, high-cadence measurements of magnetic fields in active regions, SHARP data enables the development of accurate models for predicting solar flares and understanding the underlying physical processes.

2.1.1.4 GOES data

The Geostationary Operational Environmental Satellite (GOES) series, operated by the National Oceanic and Atmospheric Administration (NOAA), provides vital X-ray data that is widely utilized in the study of solar flares. Equipped with Solar X-ray Sensors (XRS), these satellites continuously monitor the Sun's X-ray emissions, capturing data in two key wavelength bands: 0.5-4.0 Å and 1.0-8.0 Å. This data

is invaluable for detecting and classifying solar flares based on their X-ray output, using a system that categorizes flares into A, B, C, M, and X classes according to their peak flux in the 1.0-8.0 Å band. This classification is fundamental for assessing the potential impacts of these energetic events on Earth's space environment and technological systems.

GOES X-ray data is also helpful in analyzing the thermal properties of solar flares. The fluxes in the two X-ray bands provide critical parameters such as the temperature and emission measure of the flare plasma. Calculating the ratio of these fluxes, under the assumption of an isothermal plasma, yields insights into the energy release mechanisms and the physical characteristics of the flaring region [Garcia, 1994]. These parameters are crucial for studying the heating processes in the solar corona and the overall energy dynamics of solar flares, making thermal analysis based on GOES data a standard approach in solar physics.

The long-term archive of GOES X-ray data, spanning multiple solar cycles, offers a rich resource for examining trends in solar activity. The high temporal resolution of this data, with measurements taken as frequently as every second, allows for precise tracking of both short-lived and prolonged solar flare events. This continuous monitoring capability is fundamental for studying the influence of the solar cycle on flare activity and understanding the broader context of solar and heliospheric dynamics. Beyond its scientific value, GOES X-ray data is integral to operational space weather forecasting, providing real-time assessments of flare activity and issuing alerts to mitigate potential impacts on Earth. The extensive application of GOES data in both research and operational contexts underscores its significance in advancing the understanding of solar flares and their effects on the near-Earth environment.

2.1.2 In-situ Observation

While remote sensing observations provide comprehensive imagery and measurements of the Sun's surface and outer atmosphere, in-situ observations are necessary for directly measuring the properties of the solar wind and interplanetary magnetic field (IMF) as they reach 1 AU. These direct measurements are essential for understanding the solar wind's interactions with Earth's magnetosphere and for predicting space weather events that can affect technological systems and human activities.

The OMNI dataset, maintained by NASA's Space Physics Data Facility, offers a rich collection of solar wind and IMF parameters measured by various spacecraft positioned near 1 AU, such as ACE, Wind, and IMP-8. This dataset is invaluable for space weather research and modeling, providing high-resolution, continuous data that spans several solar cycles. OMNI data includes key solar wind parameters such as proton density, velocity, temperature, and IMF components, typically taken at a 1-minute or hourly cadence. This detailed temporal resolution captures the dynamic nature of the solar wind and allows for the identification of transient solar wind structures, such as corotating interaction regions (CIRs), shocks, and CMEs.

The accurate measurements of the IMF components, particularly the B_z component, are vital for predicting geomagnetic activity. The southward orientation of the B_z component can lead to geomagnetic storms by enabling magnetic reconnection with Earth's magnetosphere. Continuous monitoring of the IMF and solar wind parameters at 1 AU helps forecast space weather events and mitigate their impacts on technological systems and human activities.

OMNI data also facilitates the validation and calibration of space weather models. By providing a reliable benchmark of solar wind conditions at 1 AU, it enables the comparison of model outputs with observed data, ensuring the models' accuracy and robustness. This is particularly important for models that aim to predict the

propagation of solar wind disturbances from the Sun to Earth, such as CMEs and high-speed solar wind streams.

2.2 Numerical Techniques

Numerical techniques are fundamental for simulating and understanding the complex dynamics of space weather phenomena. These methods enable the modeling of physical processes in the heliosphere, from the propagation of solar wind to the interactions between CMEs. In this thesis, magnetohydrodynamic (MHD) simulations and machine learning algorithms have been employed to model and analyze the behavior of space weather drivers. Specifically, the PLUTO code and LightGBM algorithm have been utilized for these purposes, with detailed descriptions provided in the subsequent sections.

2.2.1 PLUTO Code

The astrophysical computational code PLUTO [Mignone et al., 2007a] is a highly versatile and powerful computational tool designed for astrophysical fluid dynamics and MHD simulations. Developed to address a wide range of astrophysical phenomena, PLUTO is capable of solving complex problems involving compressible and incompressible fluids, as well as ideal and non-ideal MHD. Its modular and flexible framework allows researchers to customize the code for specific scientific needs, making it an invaluable resource in the field of computational astrophysics.

PLUTO code can be used to simulate a variety of astrophysical environments and processes, from the dynamics of interstellar medium to the behavior of accretion disks around black holes. It supports multiple geometries (cartesian, cylindrical, and spherical coordinates), which are essential for accurately modeling different astrophysical systems. The modular structure of the code is based on a robust framework that incorporates a system of conservation laws based on modern Godunov-type

shock-capturing algorithms.

One of the key strengths of PLUTO is its extensive suite of numerical solvers. These include Riemann solvers for handling discontinuities, as well as algorithms for solving the MHD equations, both in their ideal and resistive forms. The high-order accuracy of these solvers ensures that PLUTO can simulate complex fluid behaviors with great precision. Additionally, PLUTO offers several limiters and reconstruction methods to maintain numerical stability and reduce computational errors.

To handle the computational demands of large-scale simulations, PLUTO is designed with parallel computing capabilities. It supports Message Passing Interface (MPI) for distributed memory systems, allowing it to efficiently utilize modern supercomputers and high-performance computing clusters. This parallelization is critical for running large simulations that require significant computational resources, enabling the study of large-scale astrophysical phenomena over extended periods. The code integrates a system of conservation laws defined as follows:

$$\frac{\partial U}{\partial t} + \nabla \cdot T_h = \nabla \cdot T_p + S(U) \tag{2.1}$$

where, U denotes a collection of conservative quantities. The hyperbolic flux tensor $T_h(U)$ and the diffusion parabolic flux tensor $T_p(U)$ capture the transport of these quantities. Additionally, $S(U)$ specifies the source terms that influence the evolution of the system. The precise mathematical formulation of these variables relies on the specific physics employed for the simulation, as the explicit expressions may vary accordingly. Additionally, the code helps introduce a passive scalar tracer that obeys the simple advection equation as follows:

$$\frac{\partial \rho Q_k}{\partial t} + \nabla \cdot (\rho Q_k \mathbf{v}) = 0 \tag{2.2}$$

where, Q_k is the passive scalars or "color". This equation is showcased in a conser-

vative form which the code actually solves.

PLUTO has been widely used in various areas of astrophysics, including the study of astrophysical jets [Mukherjee et al., 2018], the dynamics of galaxies [Giri et al., 2022], interstellar medium [Wagner et al., 2013], stellar evolution [Hosokawa et al., 2016] and heliospheric plasma [Biondo et al., 2022]. Its ability to model both hydrodynamic and magnetohydrodynamic processes makes it particularly valuable for understanding the interactions between magnetic fields and fluid flows in space. Several studies have leveraged PLUTO's capabilities to gain insights into the fundamental processes that shape the universe, from the behavior of plasma in star-forming regions to the mechanics of black hole accretion disks. In this thesis, this versatile code has been used for the modeling of space weather drivers, particularly solar wind and CME.

2.2.2 Light GBM

Machine learning algorithms have become indispensable tools in data analysis and predictive modeling, with LightGBM [Light Gradient Boosting Machine, Ke et al., 2017] being a relatively new and powerful addition to this domain. LightGBM is specifically designed for efficiency and high performance, making it suitable for large-scale data and high-dimensional feature spaces. At its core, LightGBM builds upon the decision tree algorithm, which is a non-parametric supervised learning method. Decision trees work by recursively splitting the data into subsets based on the value of input features. While decision trees are easy to interpret and implement, they can suffer from overfitting and are often not as powerful as ensemble methods.

LightGBM enhances the basic decision tree by using gradient boosting. Gradient boosting is an ensemble technique that builds models sequentially, with each new model attempting to correct the errors of the previous ones. In gradient boosting, each new tree is trained on the residuals of the predictions made by the ensemble

of all previous trees, gradually improving the model's accuracy. This approach can produce highly accurate models but can also be computationally expensive and slow to train, especially with large datasets.

LightGBM introduces an optimized histogram-building method to address the computational inefficiencies of traditional gradient boosting. Instead of evaluating all possible splits for each feature at each node, LightGBM discretizes (or bins) continuous feature values into a limited number of bins (or histograms). This reduces the number of possible split points, significantly speeding up the training process while maintaining high accuracy.

To further enhance efficiency, LightGBM employs Gradient-Based One-Side Sampling (GOSS). In GOSS, instead of using all the data points for each iteration, the algorithm selectively samples data points based on their gradients. Specifically, it keeps all data points with large gradients (which are harder to predict and thus more important) and randomly samples from data points with small gradients. This downsampling approach reduces the amount of data processed in each iteration, speeding up training without significantly compromising accuracy.

Another optimization in LightGBM is Exclusive Feature Bundling (EFB). EFB is designed to reduce the dimensionality of high-dimensional feature spaces. It exploits the sparsity of the data by bundling mutually exclusive features (features that rarely take non-zero values simultaneously) into a single feature. This bundling reduces the number of effective features that the algorithm needs to evaluate, further speeding up the training process.

Conclusively, LightGBM enhances traditional decision tree-based methods through several key innovations: the optimized histogram-building method, Gradient-Based One-Side Sampling (GOSS), and Exclusive Feature Bundling (EFB). These techniques make LightGBM comparatively faster and more efficient, capable of handling

large-scale datasets and high-dimensional feature spaces, making it a powerful tool for machine learning tasks in this thesis.

Chapter 3

SWASTi-SW and ADITYA L1

This chapter is structured based on the paper titled "SWASTi-SW: Space Weather Adaptive Simulation Framework for Solar Wind and Its Relevance to the Aditya-L1 Mission" by Prateek Mayank, Bhargav Vaidya, and D. Chakrabarty [Mayank et al., 2022].

3.1 SWASTi-SW

This numerical framework for forecasting and assessing the ambient solar wind is based on a well-established scheme which uses semi-empirical coronal model and physics-based inner heliospheric model. Figure 3.1 shows the processes involved in SWASTi-SW, from photospheric magnetogram input to computing plasma properties in the inner-heliosphere. The spatial range of coronal domain goes from 1.0 $R_\odot$ to 21.5 $R_\odot$ (0.1 AU) and that of inner heliosphere from 0.1 AU to 2.1 AU. The mentioned scheme is now commonly used for the simulation of Sun-Earth connection, for example in ENLIL, SUSANOO, EUHFORIA, etc. Though a similar scheme is followed by these existing models, they differ in defining crucial parameters in both the subdomains. The details of sub domains of SWASTi-SW have been described in the following sub sections.

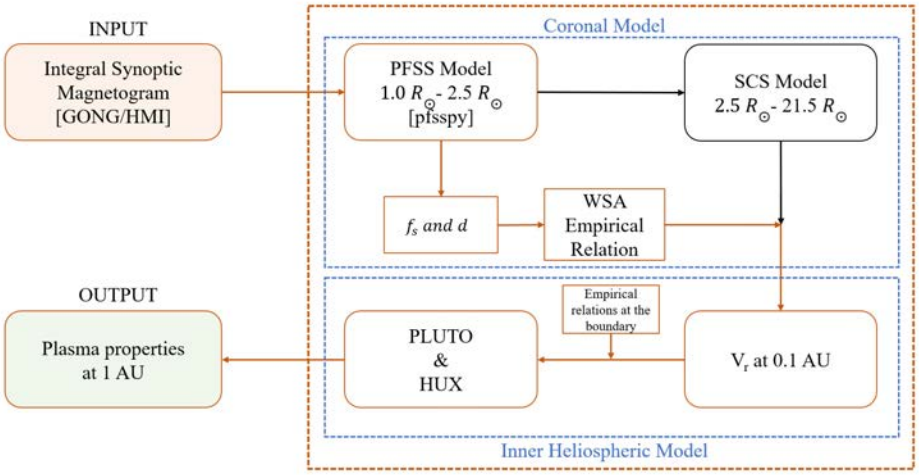

Figure 3.1: Process flow diagram of the proposed solar wind model showing the range of numerical models involved in the subdomains.

3.1.1 Submodel for Corona

The primary aim of coronal domain is to provide inner boundary condition for the inner-heliospheric model, thereby the radial distance of this boundary (R_{in}), from the centre of the Sun, decides the range of coronal model. R_{in} should essentially lie in the region where solar wind plasma becomes supersonic as well as super-Alfvenic. Goelzer et al. [2014] showed that this distance is correlated with the sunspot number and varies from 15 $R_\odot$ at solar minima to 30 $R_\odot$ at solar maxima. As in this work we have mainly focused around the solar minima regime, taking this distance to be 21.5 $R_\odot$ (i.e. 0.1 AU) is a physically suitable estimate. Therefore, the coronal domain's radial coverage extends to 0.1 AU, while its latitudinal and longitudinal coverage range from -90° to 90° and from 0° to 360°, respectively, in heliographic Carrington frame.

SWASTi-SW uses synoptic magnetogram as input and a modular approach for coupling Potential Field Source Surface (PFSS) [Altschuler & Newkirk, 1969a] and

Schatten Current Sheet (SCS) [Schatten, 1971] codes. This modular method facilitates an option of using PFSS alone or a coupled PFSS+SCS. Both versions rely on empirical relation of WSA model to calculate the solar wind speed profile at R_{in}.

3.1.1.1 Input Magnetogram

The only observational input in our model is full-disk photospheric magnetogram. Therefore it becomes important to carefully choose the suitable type of input magnetogram. In this work, we have used integral Carrington rotation (CR) synoptic maps provided by NSO-GONG (filename prefix: *mrmqs*) and SDO-HMI (JSOC series: *hmi.synoptic_mr_polfil_720s*). The integral synoptic maps are calibrated by merging standard line-of-sight (LOS) maps and remapping into appropriate longitude in the Carrington frame. For each Carrington longitude of synoptic map, standard magnetograms near the central meridian, of that longitude, is averaged using a weighting factor (for example, GONG uses cosine^4(longitude)), for more details see Hill [2018] and Scherrer et al. [2012]. The advantage of using integral CR synoptic maps is that each point along the X-axis (longitude) represents the location of Earth during that CR period, thereby providing the required input for studying the ambient solar wind at 1 AU in lesser computational time.

Both GONG and HMI magnetograms provide magnetic fields at solar surface over linearly spaced grid points in longitude (X-axis) and equally spaced in sine(latitude) grid points in latitude (Y-axis). The used GONG magnetogram has resolution of 360×180 points whereas that of HMI is 720×360 points in phi-theta plane.

3.1.1.2 Potential Field Source Surface Model

In the lower solar corona, we have used PFSS model to solve for the global magnetic fields. It is based on a simple approach which exercises the uniqueness theorem of Laplace equation by assuming the electric current to be negligible. This approximation is reasonable in lower corona where plasma is force-free [Gary, 2001] and most

of the trans-equatorial fields lines are current-free [Tadesse et al., 2014], specially in quiet and weak active regions. Though more realistic, but complex, models exist see [Wiegelmann et al., 2017, and references therein], observational tests [Liu & Lin, 2008; Schrijver & Derosa, 2003] and comparative studies e.g., [Riley et al., 2006] depict that PFSS model is adequate for examining large-scale solar and heliospheric fields.

PFSS solves Laplace equation from the solar surface (boundary condition provided by input magnetogram) to source surface (from where field is prescribed to be radial). Traditionally, a spherical harmonic expansion approach is implemented (e.g., Altschuler et al. [1977]; Hakamada [1995]; Nikolić [2019], WSA-ENLIL, EUHFORIA). However, this technique gives rise to ring-like patterns and is also sensitive to the choice of number of spherical harmonics [Asvestari et al., 2019; Tóth et al., 2011]. An iterative finite difference scheme has also been applied to solve PFSS [Caplan et al., 2021; van der Holst et al., 2010] and it shows no signature of ringing effect and can be favoured over harmonic approach, specially near strong magnetic field regions. In this work, we have used PFSSPY which is based on the method of van Ballegooijen et al. [2000]. PFSSPY code is a finite difference solver and hence allows the model to escape the ringing effect disadvantage occurring in spherical harmonic approach.

PFSSPY is solved on a rectilinear grid which is equally spaced in ln(r), $\cos\theta$ and ϕ in spherical coordinates (r, θ, ϕ). We have used grid resolution of $100 \times 181 \times 361$ to solve for fieldlines from 1 $R_\odot$ to source surface radius (R_{ss}), which is 2.5 $R_\odot$ in our case. The magnetic fieldlines is traced in two sets. First, from inner boundary (1 $R_\odot$) to outer boundary (2.5 $R_\odot$) at the mentioned resolution, which gives coronal hole perimeter as both open and closed fieldlines are traced. Second, from source to solar surface at higher resolution of $100 \times 181 \times N$ where N is the number of hours in CR. In the later set, there are only open fieldlines originating from inside

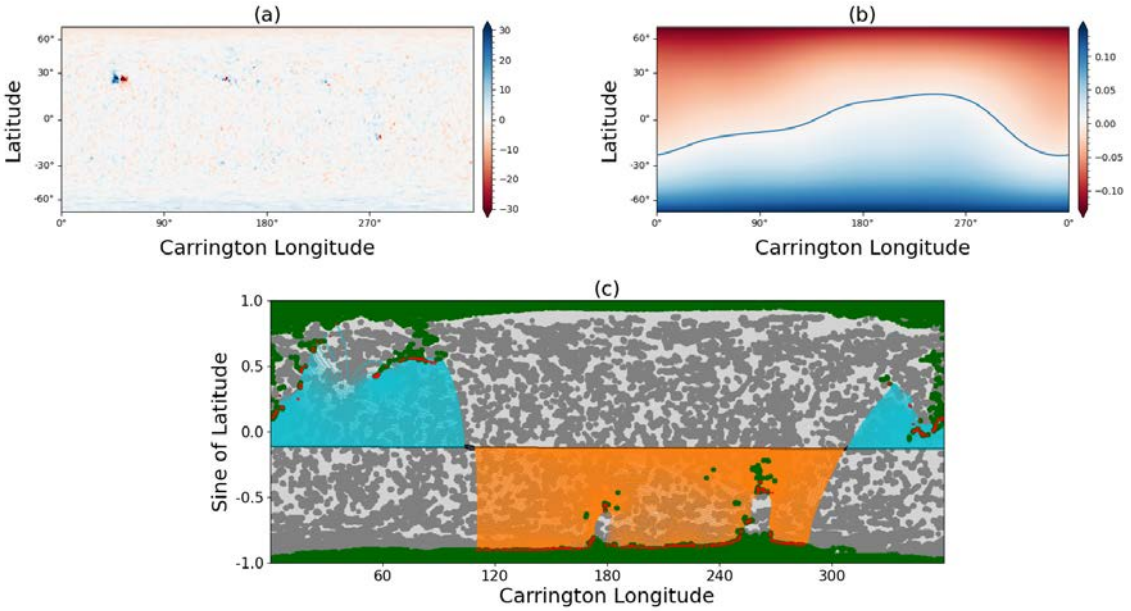

Figure 3.2: PFSS model results for CR2081. Here, (a) is computed radial magnetic field (Gauss) at 1 $R_\odot$, (b) is radial magnetic field (Gauss) output at 2.5 $R_\odot$ and, (c) is tracing of fieldlines from solar to source surface that will reach sub-Earth points. Here, cyan-orange and light-dark grey shows the open and closed fieldlines of opposite polarity. The green coloured area is coronal hole and red dots are the footpoint of open fieldlines. The horizontal black line is the location of Earth in heliographic coordinates for CR2081.

the coronal hole, whose perimeter is traced by the first set. This two set tracing approach provides greater resolution of fieldlines at the source surface.

Figure 3.2 shows the results of PFSS model, projected in $\theta - \phi$ plane. Subplot (a) shows the computed input radial magnetic field from the GONG magnetogram and (b) shows the radial magnetic field at the source surface (R_{ss}). In subplot (b), the blue line in the middle represents the magnetic polarity inversion line which effectively shapes the current sheet in heliosphere. Subplot (c) depicts the two set tracing approach of magnetic fieldlines. The tracing from 1 $R_\odot$ to R_{ss} gives the region of closed fieldlines (light and dark grey) and the coronal hole boundary (the green area) at solar surface. Further, the tracing of open fieldlines (cyan and orange)

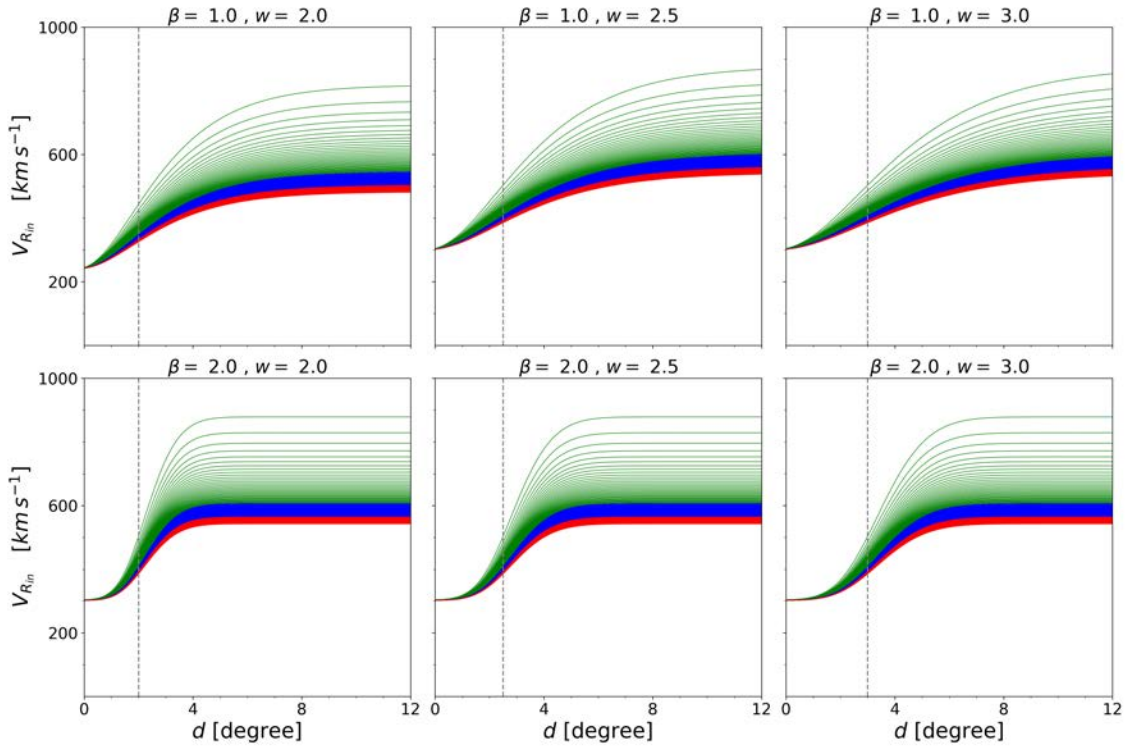

Figure 3.3: Variation of solar wind speed for the range of values of d and f_s based on different set of values of β and w while keeping the V_{min} and V_{max} constant (240 km/s and 725 km/s). d varies from 0° to 12° and value of f_s goes from 1 to 99 (equally distributed in green (1-33), blue (34-66), and red (67-99) colors) with increment of 1. The dotted vertical lines are placed corresponding to values of w. For $\beta = 2$, $V_{R_{in}}$ becomes independent of d for much smaller as compared to $\beta = 1$.

from R_{ss} to $R_\odot$ provides their foot points (red dots) inside the coronal hole area. The black line in the middle is the location of Earth for the CR2081. Hence, the figure illustrates the origin points of the fieldlines that will reach the Earth.

3.1.1.3 Schatten Current Sheet Model

In the upper corona (i.e. beyond R_{ss}), plasma beta becomes greater than unity [Gary, 2001] and most of the fieldlines become almost radial, as plasma pressure starts dominating the dynamics. To incorporate the non-zero current region near the polarity inversion territory, Schatten [1971] proposed SCS model. It requires

solving another Laplace equation with inner boundary conditions given by PFSS and outer boundary extending to infinity, leading the fields to vanish. The inner boundary distance of SCS (R_{scs}) is usually taken less than R_{ss} to avoid the kink formation at the interface. This technique results in improved solar wind structures at 1 AU sometimes, but most of the time it doesn't affect solar wind predictions [McGregor et al., 2008]. In SWASTi-SW, the default setup is $R_{scs} = R_{ss}$, but it can be changed by the user at the run-time.

There are two main advantages in using coupled PFSS+SCS over PFSS alone. It provides more realistic magnetic field values in the upper corona, and it facilitates more accurate fieldline tracing (by considering non-zero current region) in slightly more computational time.

3.1.1.4 Adapted WSA Model

To provide the inner boundary conditions to MHD-based inner-heliospheric domain, we have used WSA model [Arge et al., 2003], which provides velocity profile at 0.1 AU for a given magnetic flux tube. Though there are many different forms of WSA solar wind relations, in SWASTi-SW we have used the following:

$$V_{R_{in}} = V_{min} + \frac{V_{max}}{(1+f_s)^{\frac{2}{9}}} \times \left[\left(1.0 - 0.8\, exp\left(-\left(\frac{d}{w} \right)^{\beta} \right) \right)^{3} \right] \quad km\, s^{-1} \tag{3.1}$$

where,

$$f_s = \frac{R_{\odot}^2 \times B_r(R_{\odot}, \theta, \phi)}{R_{ss}^2 \times B_r(R_{ss}, \theta, \phi)} \tag{3.2}$$

which is similar to equation (2) of McGregor et al. [2011]. In equation (3.1), V_{min}, V_{max}, β and w are independent parameters whereas, f_s and d are areal expansion factor of flux tube and minimum angular separation of the foot-point from coronal hole boundary, respectively. A similar form of WSA velocity relation is also being used by other models (e.g., WSA-ENLIL, EUHFORIA, Narechania et al.

[2021]) but each uses different set of values of independent parameters.

The role of w is to normalize the minimum angular distance of the flux tube footpoint from the open flux boundary (d) and β controls the affect of this distance on solar wind relation ($V_{R_{in}}$). Whereas, V_{min} and V_{max} regulate the minimum and maximum value of $V_{R_{in}}$. Figure 3.3 shows the graphical representation of the functional form of $V_{R_{in}}$. Two main features are to be observed here. As the value of d increases from 0° (i.e., fieldlines originating from close to the edge of coronal hole) the value of $V_{R_{in}}$ doesn't change much, regardless the value of f_s and after a threshold value of d, $V_{R_{in}}$ depends only on f_s. Additionally, in between these two values, both d and f_s increases monotonically and contribute to $V_{R_{in}}$. And to properly use the capability of WSA model, speed empirical relation has to be dependent on both d and f_s. Parameter w regulates the value of d from which second feature starts and β determines the threshold value of d. The increase (decrease) in V_{min} shifts the graphs upward (downward) and the variation in V_{max} shifts the peak. Therefore, these four independent parameters in the empirical relation are critical in getting an accurate solar wind speed estimation at 0.1 AU.

Out of four free parameters, the optimal value of w is the most volatile, as for different grid resolutions the value of d changes and so will w, to effectively normalize it. With an attempt to take a more generalized approach, we replaced the value of w with the median of d. Keeping the focus on the fieldlines that reaches the location of Earth, we calculated d and f_s (now d_E and f_{s_E} for this case) values for only those flux tubes and checked the variability features in solar wind. As shown in Figure 3.4, this adapted method displays same kind of features as in Figure 3.3. Moreover, by fixing the values of V_{max} and V_{min} (by default 725 km/s and 240 km/s for HUX run) we can presume, from Figure 3.4, that the optimal value of β should lie near 1.0. But to find the optimal value of β precisely, comparison of speed profile at first Lagrangian point of Sun-Earth system (L1) with observational data is required.

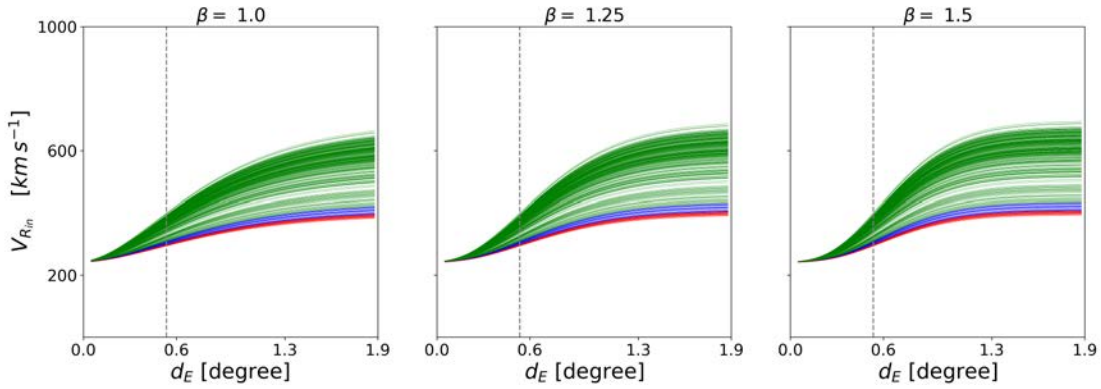

Figure 3.4: Graphical depiction of solar wind speed variation with different values of β at 0.1 AU for CR2081. Speed profiles are of those fieldlines that reaches sub-Earth points (location of Earth in Carrington heliographic coordinates). Here, $V_{min} = 240\,km/s$, $V_{max} = 725\,km/s$ and $w = 0.54$ (median of d_E). For each fieldline, value of d_E and f_{s_E} are calculated from coronal model and the vertical dotted line represents the value of w. f_{s_E} has been distributed in three equal bins (green, blue and red), with green showing the lowest (from top) and red showing the largest values (at bottom).

For comparison with OMNIWeb data, we used Heliospheric Upwind eXtrapolation (HUX) model [Riley & Lionello, 2011], for a range of values of β. HUX is a simple one dimensional upwind extrapolation technique which neglects the effects of magnetic field, gravity and pressure gradient. The HUX model gives very good match for speed results at 1 AU [Riley & Issan, 2021] and that too in very less computational time. To find the optimal value of β for a given CR, we calculated the solar wind profile at 1 AU (V_{HUX}) by varying β from 0.75 to 1.75 in 20 equal steps and compared it with observed data (V_{OBS}). For this initial study we restricted the range to ± 0.5 around the most used value of β i.e., 1.25 e.g., [Narechania et al., 2021; Pomoell & Poedts, 2018a; Riley et al., 2015; van der Holst et al., 2010]. To statistically evaluate the best fit, we used Pearson correlation coefficient (cc), root mean square error ($rmse$) and normalized difference of standard deviation of V_{HUX} and V_{OBS} (nsd). The best match was decided on the basis of a score (Σ in equation 3.3) giving equal weightage to all three, lower Σ value signifies better match.

Table 3.1: Statistical results of selected CRs and their optical value of β.

CR	Optimal value of β	cc	$rmse$	nsd	Σ
2053	1.75	0.85	74.01	0.04	0.57
2077	1.75	0.64	75.20	0.14	0.72
2081	0.75	0.87	41.39	0.03	0.19
2104	1.0	0.85	44.51	0.09	0.23
2202	1.3	0.54	74.35	0.02	0.77

$$\Sigma = (1 - cc)^2 + \left(\frac{rmse}{100}\right)^2 + nsd^2 \tag{3.3}$$

We selected five CRs for comparison, near the solar minima region and in the absence of halo CMEs to properly capture the features of ambient solar wind. Considering that the accuracy of GONG magnetogram has degraded since 2013, specially in polar regions [Nikolić, 2019], we focused more on increasing phase of Solar Cycle 24. The optimal value of β for selected CRs, based on HUX, have been listed in Table 3.1 and variations are shown in Figure 3.5. The subplot 3.5(a) shows the variability of Σ value for all CRs. As β increases from 0.75 to 1.75, the change in Σ value is lesser for CR2077, CR2104 and CR2202 (decline of <0.3) whereas, CR2053 and CR2053 show greater deviation (incline of >0.4). The optimal β value lies in the middle of the chosen range for CR2104 and CR2202, on the contrary, it lies at the boundary for CR2053, CR2077 and CR2081. That means, for the later three CRs the real optimum value can be located outside the chosen range of β. But at their optimum value, the slope of their plots have become almost zero (fig. 3.5(d)). This indicates that no significant reduction in Σ value will occur with further change of β and therefore the chosen range is adequate.

In Figure 3.5, root mean square error (rmse) has monotonically increased with β for CR2104 and CR2081, decreased for CR2053 and remained almost constant for CR2077 and CR2202. The Pearson correlation coefficient (cc) became better with increased value of β for CR2053, CR2077 and CR2202, whereas cc value decreased

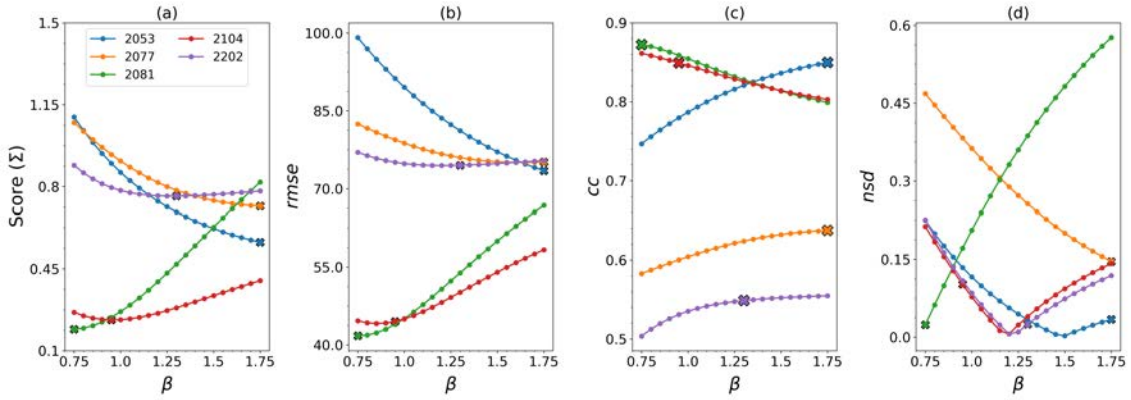

Figure 3.5: Plots showing the statistical results for variation of β from 0.75 to 1.75 in 20 equal steps, for five selected CRs. On the basis of the minimum score value, optimum β value has been deduced. The chosen optimum for each CR, has been marked with 'x', whose values have been mentioned in Table 3.1. All subplots have common plot legend, shown in subplot (a).

for CR2081 and CR2104. The normalized standard deviation (nsd) first increased and then decreased for CR2053, CR2077 and CR2202. And in case of CR2081 (CR2104) the nsd value strictly increased (decreased) with β.

There is no noticeable pattern among the CRs in plots of Figure 3.5, but different optimum β values for different CRs emphasises the influence of d parameter. Higher β value implies greater influence of d on speed profile, as compared to its lower value. Therefore it can be inferred that in the WSA relation (equation 3.1), dominance of d is greater in CR2053 (β=1.75) as compared to CR2081 (β=0.75).

As expected, Figure 3.6 demonstrates that even small variations in β have significant impacts on the speed profile, particularly at peaks, where the value of d is high. As the β value is increased from 0.75 to 1.25 and 1.75, the peak shifts upward and it's fluctuations in that region also increases. The same trend will continue till the threshold value is reached and then no further change will happen, as speed profile becomes independent of d (see fig. 3.4).

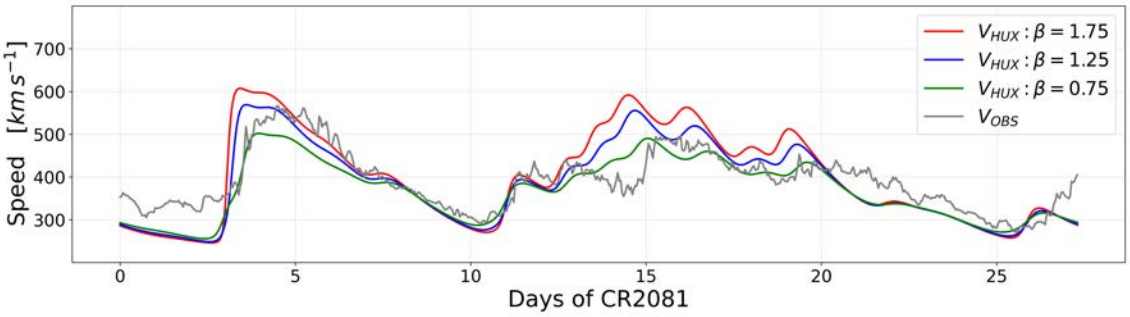

Figure 3.6: Effect of value of β on speed profile at 1 AU. The difference in speed is greater at peaks and lesser at base. The speed profile have smoother peaks for low value of β.

3.1.2 Submodel for Inner Heliosphere

The fundamental purpose of MHD-based inner heliospheric model is to determine plasma properties in inner heliosphere by taking the input from coronal model. The veracity of this domain depends on accurate initial boundary conditions which vastly depends on the speed profile derived from WSA relation. More details has been prescribed in the following subsections.

3.1.2.1 MHD Setup

The inner heliospheric model is based on PLUTO code [Mignone et al., 2007b], which is built on Godunov-type schemes to integrate a set of conservation laws using finite volume or finite difference approach. In the current version of SWASTi-SW, ideal MHD module of PLUTO is used on a uniform static grid in spherical coordinates. The following set of conservative equations are solved using finite volume method:

$$\frac{\partial \rho}{\partial t} + \nabla \cdot (\rho \mathbf{v}) = 0 \quad (3.4)$$

$$\frac{\partial \mathbf{m}}{\partial t} + \nabla \cdot \left[\mathbf{mv} - \mathbf{BB} + \left(p + \frac{\mathbf{B}^2}{2} \right) \right] = \rho \mathbf{g} \quad (3.5)$$

$$\frac{\partial \mathbf{B}}{\partial t} - \nabla \times (\mathbf{v} \times \mathbf{B}) = 0 \quad (3.6)$$

$$\frac{\partial E_t}{\partial t} + \nabla \cdot \left[\left(\frac{\rho \mathbf{v}^2}{2} + \frac{\gamma p}{\gamma - 1} \right) \mathbf{v} + \mathbf{B} \times (\mathbf{v} \times \mathbf{B}) \right] = \mathbf{m.g} \quad (3.7)$$

where ρ is mass density, $\mathbf{v}$ is velocity, $\mathbf{m}$ is momentum density ($\rho\mathbf{v}$), $\mathbf{B}$ is magnetic field, p is isotropic thermal pressure, $\mathbf{g}$ is gravitational acceleration ($-\frac{GM_\odot}{r^2}$), E_t is total energy density and γ (=5/3) is specific heat ratio of solar wind plasma. The above equations are solved in the Stonyhurst Heliographic frame. The coordinates of this frame can be converted to Heliocentric Earth Equatorial (HEEQ) frame by mere spherical to cartesian coordinate transformation [Thompson, 2006]. To incorporate the solar rotation in this frame, inner radial boundary (the whole spherical slice at R_{in}) is rotated with constant angular speed with respect to the computational grid. The rotational time period (TP) remains constant for a specific CR and can have values from 27.21 to 27.34 days [Thompson, 2006], depending on the location of Earth in its orbit. For example, value of TP for CR2053 (starting from February, 2007) is 27.34 days whereas, value of TP for CR2081 (starting from March, 2009) is 27.30 days. And the corresponding centrifugal and Coriolis terms have been neglected due to their trifling share.

The MHD domain range goes from 0.1 AU to 2.1 AU in radial, -60° to 60° in latitudinal and 0° to 360° in longitudinal direction, having $150 \times 120 \times 360$ grid resolution respectively. With the motivation to keep the computational time reasonable, we opted for simple numerical methods involved in a typical time step cycle in PLUTO. For each step we chose RK2 time stepping algorithm, 2^{nd} order TVD linear reconstruction scheme and HLLC Riemann solver. And to ensure the divergence free condition, we selected Powell's 8 wave formulation [Powell, 1994].

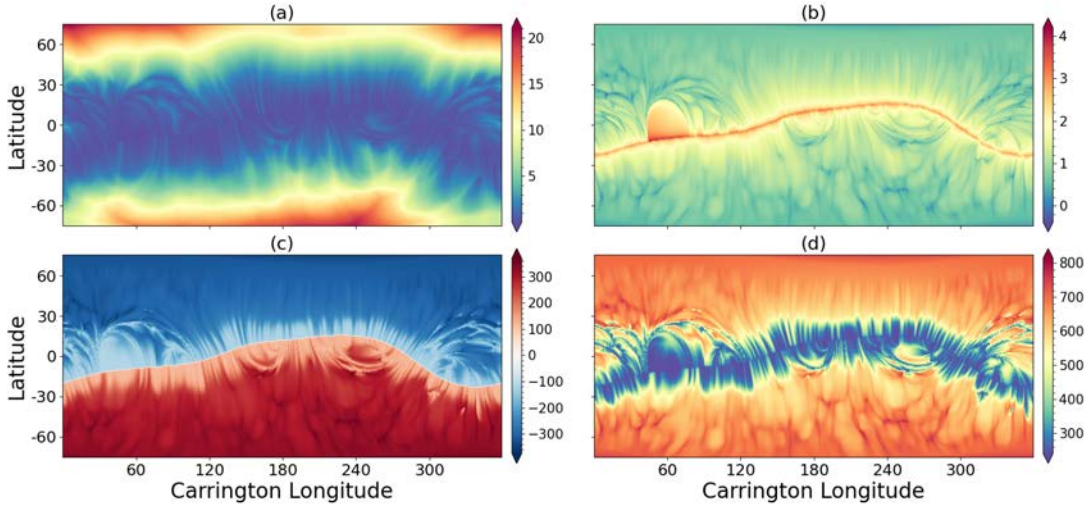

Figure 3.7: Plots for CR2081: (a) d parameter in degree, (b) $\log_{10}(f_s)$, (c) radial magnetic field [nT] at R_{in}, derived from equation 3.10, and (d) solar wind speed [km/s] profile as input for MHD domain.

3.1.2.2 Boundary Specification

The coronal domain provides the speed profile (radial component of $\mathbf{V}$, V_r), for each flux tube, at the inner boundary of MHD domain (R_{in}). For forecasting purpose, the default values of parameters in the adapted WSA relation, for MHD run, are: $V_{min} = 250\,km\,s^{-1}$, $V_{max} = 650\,km\,s^{-1}$, w = median of d_E and $\beta = 1.25$, but in this chapter β values listed in table 3.1 has been taken for assessment. Here, the value of V_{max} is 75 $km\,s^{-1}$ less than the value that was used in HUX. A decreased value of $V_{R_{in}}$ has been applied to retaliate the affect of additional acceleration in MHD domain [McGregor et al., 2011]. As the coronal domain doesn't include solar rotation, the speed profile is rotated in the longitudinal direction by angle α:

$$\alpha = 5^{\circ} + \left(\frac{2\pi}{\mathrm{TP}}\right)\left(\frac{20.5R_{\odot}}{(V_{R_{in}})_{min}}\right) \tag{3.8}$$

where $(V_{R_{in}})_{min}$ is minimum value of $V_{R_{in}}$.

The values of other plasma properties at R_{in} are derived from the following empirical

relations:

$$n = n_0 \left(\frac{V_{max}}{V_r} \right)^2 \tag{3.9}$$

$$B_r = \mathrm{sgn}(B_{corona})\, B_0 \left(\frac{V_r}{V_{max}} \right) \tag{3.10}$$

$$B_\phi = -\, B_r\, \sin\theta \left(\frac{V_{rot}}{V_r} \right) \tag{3.11}$$

where n is plasma number density, $n_0 = 300\ cm^{-3}$, B_r and B_ϕ are radial and azimuthal components of $\mathbf{B}$, $B_0 = 300$ nT, V_{rot} is rotating speed of inner boundary corresponding to TP. Here, n_0 and B_0 refer to number density and magnetic field values of fast solar wind, respectively. The thermal pressure, p has been kept constant at R_{in} at 6.6 nPa. The meridional and azimuthal components of velocity (V_θ and V_ϕ) are assumed to zero at R_{in}. The empirical relations (equation 3.9, 3.10 and 3.11) are similar to those used in Odstrcil [2003] and Pomoell & Poedts [2018a]. The coronal models usually underestimate the heliospheric magnetic flux, i.e., a significant part of magnetic flux goes undiscovered [Linker et al., 2017]. Therefore, implementing an empirical relation, based on properties of fast wind and speed of that flux tube, sidesteps this problem.

Figure 3.7 exhibits the input of MHD model for CR2081 at 0.1 AU. Plots (a) and (b) are of d and f_s (in logarithmic scale) which are used to compute the solar wind speed (plot (d)) using the adapted WSA relation and further, speed profile is used to evaluate radial magnetic field (plot (c)) using equation 3.10. Though the latitudinal range of MHD domain goes from -60° to +60°, the quantities at 0.1 AU are calculated for a wider range.

At the outer boundary, the radial direction is set to outflow condition, i.e., zero gradient across the boundary whereas, latitudinal and longitudinal direction are reflective and periodic, respectively on both sides of the computational domain. In reflective boundary condition, the variables are symmetrized across the boundary.

It is worth mentioning that due to the usage of above empirical relations, the only difference left between coupled PFSS+SCS and PFSS alone is fieldline tracing technique. SCS provides more realistic tracing by incorporating the non-zero current in the current sheet region and as a result latitudinal value at R_{in} differs from pure radial (zero current) extrapolation, which is used in case of PFSS alone approach. Usually, this latitudinal difference is less than 1° for most of the fieldlines and its effect can truly be noticed only when model resolution is better than 1°. Therefore, for lower resolution setup, PFSS+SCS and PFSS alone won't show significant difference. In this work, we have used the PFSS alone procedure by bypassing the SCS model.

3.2 Solar Wind Forecasting and Assessing Capabilities

The motivation of this work is to develop a solar wind forecasting model which could run on a personal workstation in reasonable computational time. The model setup was formulated accordingly and ran on a workstation having 48 cores which computes the final result for mentioned resolution in approximately 6.5 to 9.5 hours. To validate the model output, we introduce the initial results of the current version of SWASTi-SW for selected CRs. The chosen CR number (starting month) are: CR2053 (Feb, 2007), CR2077 (Nov, 2008), CR2081 (March, 2009), CR2104 (Nov, 2010) and CR2202 (March, 2018). The sample CRs are taken in a way to cover regions around the minima of solar cycle. The first CR resides in the minima region of descending phase of solar cycle 23 and the later three CRs belong to the ascending phase of solar cycle 24, starting from its minima whereas, the fifth CR corresponds to minima of descending phase.

The spatial domain of MHD region goes up to 2.1 AU, covering the region of Mercury, Venus, Earth and Mars. A snapshot of the output is shown in Figure 3.8 where, plots (a), (b) and (c) are of radial velocity in different planes and (d), (e) and (f) are

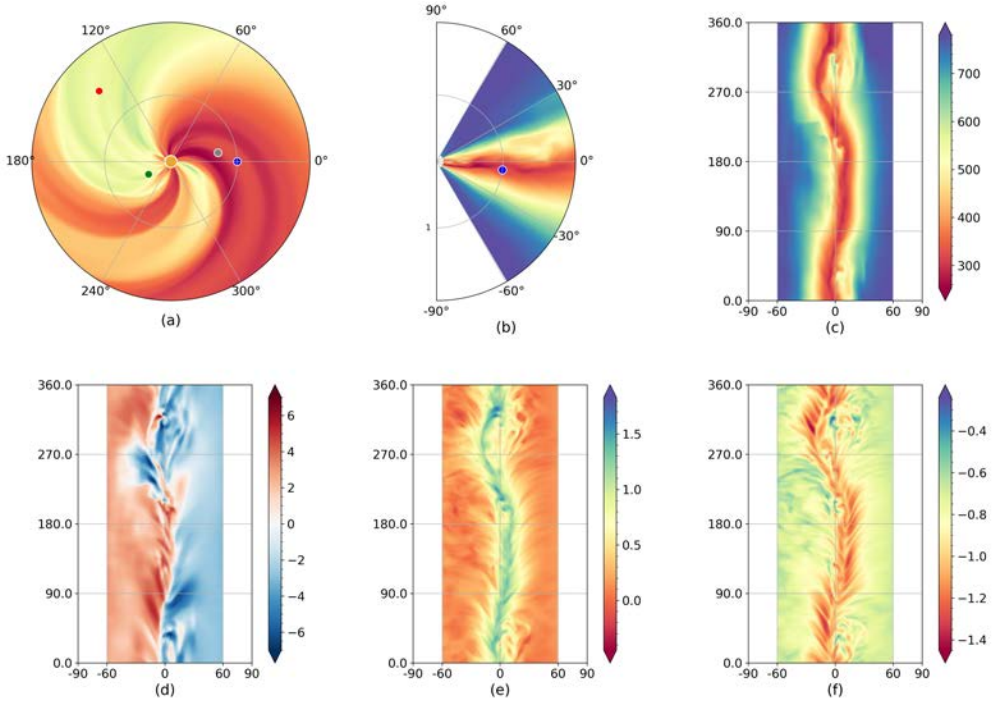

Figure 3.8: Snapshots of output of the inner heliospheric model. The results are for CR2081. Here (a), (b) and (c) are the radial velocity plots whereas, (d) is plot of radial magnetic field (nT), (e) is of proton density ($N_p cm^{-3}$) in logarithmic scale and (f) is of proton temperature (MK) in logarithmic scale. (a) plot is in $r-\phi$ plane at earth's latitude location, (b) is in $r-\theta$ plane at 0° longitude, (c), (d), (e) and (f) are in $\theta-\phi$ plane at 1 AU. The blue dot at 1AU in (a) and (b) is the location of earth at the starting of CR2081. The green, grey and red dots in plot (a) denotes Mercury, Venus and Mars whereas, orange dot at the center highlights the Sun. This figure is available as an animation.

plots of radial magnetic field, proton density and proton temperature, respectively. Plots (c), (d), (e) and (f) are in $\theta - \phi$ plane at 1 AU and density and temperature have been shown in logarithmic scale to display the structure clearly. A heliospheric current sheet, where the polarity of magnetic field changes, can be observed in the middle of plot (d). The fieldlines near the current sheet region originates from the edge of coronal hole, therefore solar wind speed must be low in this region. And slow solar wind have higher density, which in turn leads to lower thermal temperature. As expected, plots (c), (e) and (f) also have current sheet structure with lower values of

speed and temperature whereas, higher value of density near the heliospheric current sheet region.

To compare our model results with observation, we used per hour averaged solar wind magnetic field and plasma data from OMNIWeb database. We interpolated the model output from 360 data points to number of hours in CR (say, N) for comparability. The model output and performance analysis are in the following subsections.

3.2.1 Plasma Properties at L1

Figure 3.9 shows plasma speed for all the selected CRs at L1, using GONG (all CRs) and HMI (one CR) magnetograms. In this Figure, the results of our MHD model and HUX technique has been compared with OMNI one hour averaged data. Since, the observed plasma speed is mainly radial, it has been compared with the radial velocity of the model. The X-axis is flipped Carrington longitude where 0° and 360° signify the start and end time of CR, respectively. Technically, the Carrington longitude starts from 360° and ends at 0° therefore, it has been flipped to keep the CR starting time and 0° as origin on the left side. The comparison with other plasma properties are in Figure 3.10 where additionally, magnetic field magnitude, number density and proton temperature has been shown.

The speed profile output of SWASTi-SW for CR2053 has successfully captured the observed structure ($cc = 0.81$ and $rmse = 80.87$ km/s), which has two local sideward peaks and a global peak at the centre in Figure 3.9. Though the positions of sideward peaks have matched well, the global peak seems to be slightly shifted to the right by a few hours.

In CR2077, the leftmost peak has bifurcated and become broader, but the positions of rest of the structure show a decent match. A considerable difference in the slope of HUX and MHD profiles is visible around 210° Carrington longitude, where physics-

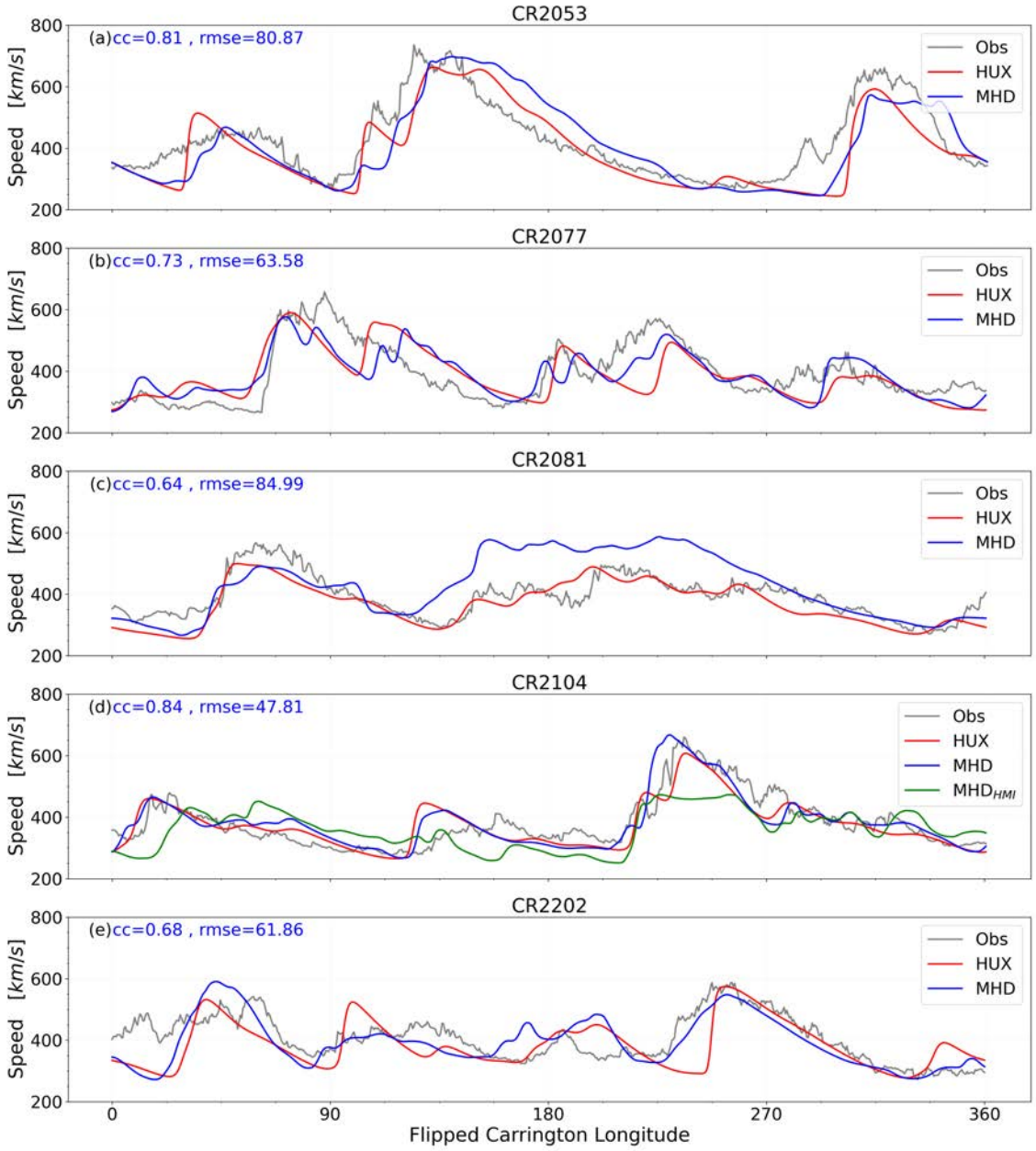

Figure 3.9: Plasma speed profile at L1 for mentioned CRs. For CR2053, CR2077, CR2081 and CR2022 MHD (using GONG magnetogram) and HUX results are plotted along with the per hour averaged OMNI data. For CR2104, additionally MHD_{HMI} (using HMI magnetogram) have been plotted along with MHD (using GONG), HUX and OMNI data. The Pearson correlation coefficient (cc) and root mean square error (rmse) have been shown for MHD_{GONG} results, which are in blue.

based result gives a better match with the observed value. As HUX technique neglects the effects of pressure gradient, the gradual increase in solar wind speed was not manifested which MHD approach successfully produced. Considering the fact that HUX extrapolates in only one direction, latitudinal flow of plasma could also be playing a role.

The speed is higher in the middle region for CR2081, but the overall pattern is the same. The HUX result has a better match in this case. Whereas, in the case of CR2104, GONG magnetogram results are having a good match for both HUX (cc = 0.86) and MHD (cc = 0.84). They have accurately captured the whole structure except for a minor peak in the middle. But HMI result for CR2104, MHD (cc = 0.57) is not matching that well, it has failed to reproduce the global maxima, near 240°, accurately.

For CR2202, the same slope difference feature is visible around 240° as it was in CR2077 at 210°. Again the physics-based result is able to capture the observed form whereas, HUX is showing a very sharp peak at that position. An abrupt fall at the beginning of profile can be noticed, as compared to the observed one. A possible reason could be the cyclic nature of the model input, which enforces the same value at the end and beginning of the cycle.

Figure 3.10 shows the plots of other plasma properties for CR2081. The magnetic field output and observation data has the same order of magnitude as it varies under 20 nT. The overall pattern is also showing the same trend. But, the one hour averaged OMNI data has very rapid fluctuations which is missing in the interpolated model output. On the other hand, density plot is always higher than the observed one, indicating that the model is overestimating the plasma number density at L1. Whereas, the temperature plot's peaks are always lower, implying that the model underestimates the proton temperature. The statistical details of other CRs are mentioned in Table 3.2.

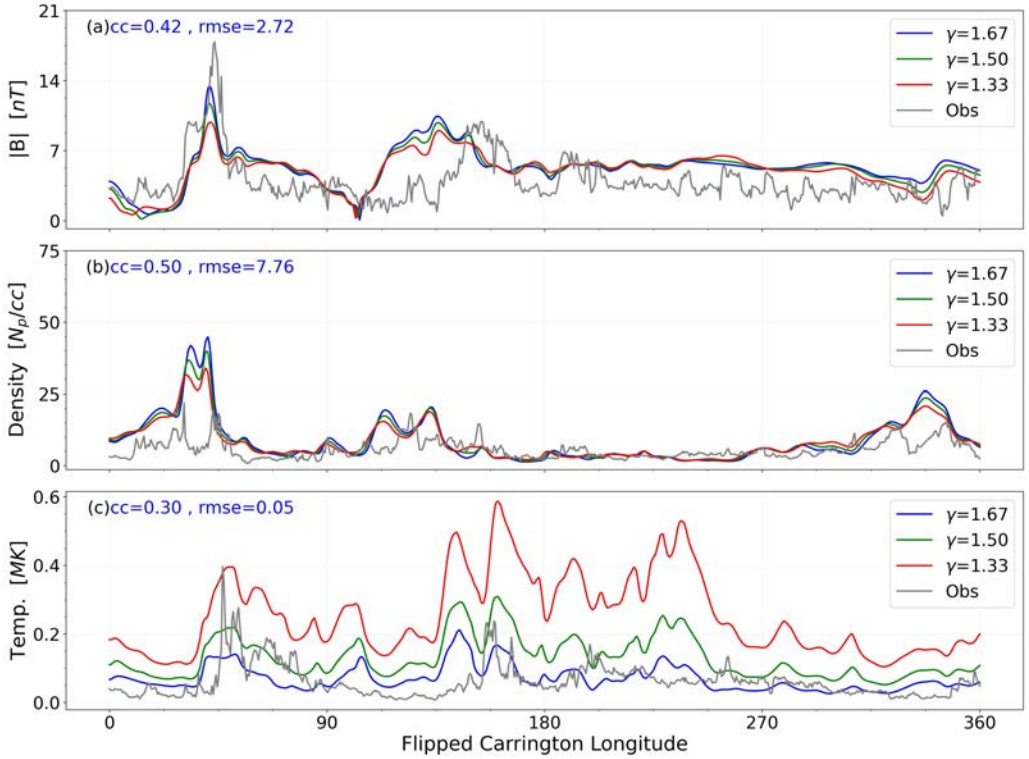

Figure 3.10: Plots showing the comparison of plasma properties with the OMNI data at L1 for different values of specific heat ratio, γ. The results shown here are for CR2081 and the value used in this work is shown in blue ($\gamma = 5/3$). The Pearson correlation coefficient (cc) and root mean square error (rmse) are shown for MHD_{GONG} with γ=5/3.

In addition to used value of γ ($= 5/3$, γ_0), we have also shown the results for $\gamma = 1.50$ (γ_1) and $\gamma = 4/3$ (γ_2) in Figure 3.10. The profile of all three presented properties showed some changes, with temperature varying the most. With the decrease in γ value, the proton temperature increased significantly. γ_1 and γ_2 profiles gave a better match for the peak around 60° as compared to γ_0, but rest of their profile gave high mean error values, specially γ_2. In the density plot, all three showed similar linear correlation but the mean error of γ_0 profile were higher at peaks. For magnetic field, all three profiles have equivalent linear correlation and root mean square error. However, γ_0 profile shows better match than γ_1 and γ_2 at the 60°

Table 3.2: Statistical results of comparison of model output with the OMNI data at L1. Here, *std_model* is standard deviation of model output at 1 AU and *std_obs* is standard deviation of the observed OMNI data at L1.

CR_MAP	Statistical parameter	HUX	MHD			
		Speed (km/s)	Speed (km/s)	|B| (nT)	Density ($N_p cm^{-3}$)	Temperature (MK)
2053_GONG	cc	0.85	0.81	0.46	0.40	0.57
	rmse	74.01	80.87	4.16	20.83	0.09
	std_model	123.97	135.07	4.46	19.93	0.10
	std_obs	119.46		2.03	4.51	0.10
2077_GONG	cc	0.64	0.73	0.20	0.39	0.40
	rmse	75.21	63.58	2.57	14.74	0.07
	std_model	80.12	71.63	1.29	12.41	0.06
	std_obs	93.33		2.30	5.17	0.06
2081_GONG	cc	0.87	0.64	0.42	0.50	0.30
	rmse	41.39	84.99	2.72	7.76	0.05
	std_model	69.75	100.03	2.02	8.12	0.04
	std_obs	67.69		2.33	3.30	0.05
2104_GONG	cc	0.86	0.84	0.21	0.32	0.31
	rmse	43.58	47.81	2.58	14.33	0.06
	std_model	75.48	85.59	1.48	13.27	0.05
	std_obs	82.89		1.96	4.37	0.06
2104_HMI	cc	0.67	0.57	0.29	0.21	0.15
	rmse	68.90	73.14	2.45	16.42	0.08
	std_model	63.63	63.29	1.82	14.11	0.06
	std_obs	82.89		1.96	4.37	0.06
2202_GONG	cc	0.54	0.68	0.40	0.34	0.25
	rmse	74.35	61.86	2.85	13.44	0.06
	std_model	74.37	78.63	3.08	12.25	0.04
	std_obs	73.20		1.39	3.48	0.05

peak. Furthermore, the accuracy of solar wind speed profile also reduced with γ value ($rmse$ for: $\gamma_0 = 84.99\,km/s$, $\gamma_1 = 86.12\,km/s$, $\gamma_2 = 87.10\,km/s$). Therefore, slight decrease in γ value, from 5/3, might give better match for proton temperature and density but the magnetic field and plasma speed accuracy might decrease.

3.2.2 Solar Wind Interaction Region

Apart from determining the plasma properties in the inner heliosphere, SWASTi-SW can also be used to study the high speed solar wind streams (HSSs) and stream interaction regions (SIRs). Additionally, the model can also mimic the observations of in-situ instruments of the upcoming Aditya-L1 mission. For example, Figure 3.11 shows the schematic diagram of Solar Wind Ion Spectrometer (SWIS) which is a

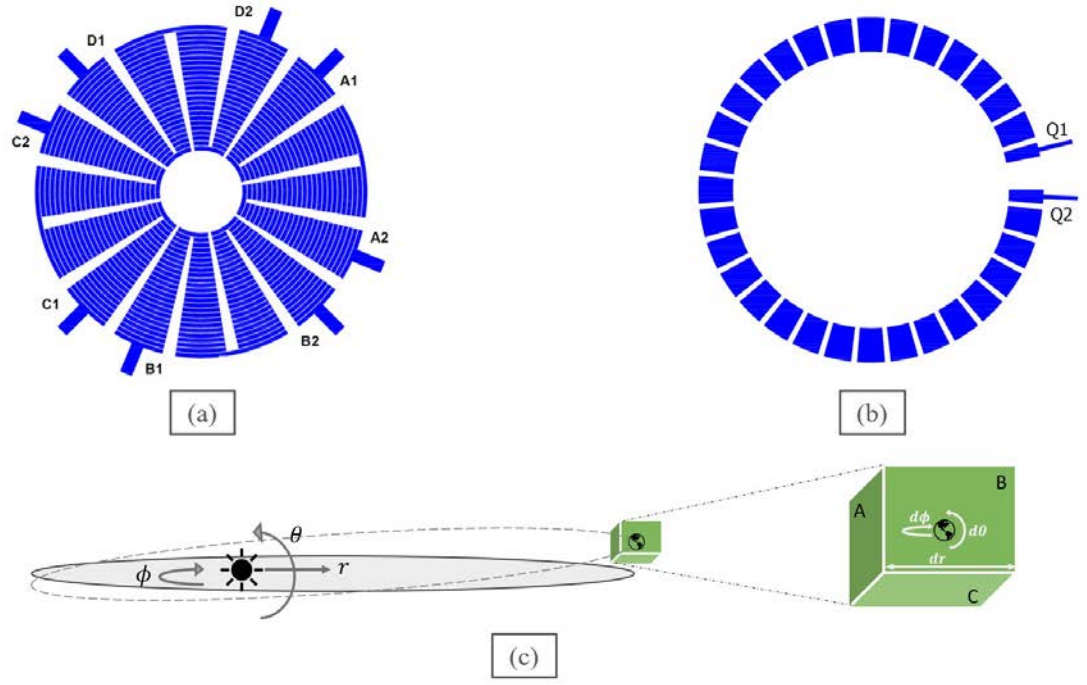

Figure 3.11: Schematic diagrams of RAE of (a) THA-1, (b) THA-2 of SWIS-ASPEX and (c) the computational surfaces (A, B and C) covering the openings of detectors. Computational surfaces A and B covers the THA-1 and C covers the THA-2. In subplot (c), the solid eclipse represents the equatorial plane in Sun centered frame and the dotted eclipse is the ecliptic plane. The direction of unit vectors in ecliptic plane have been shown and dr, $d\theta$ and $d\phi$ are widths of computational surfaces along those directions.

subsystem of Aditya Solarwind Particle EXperiment (ASPEX). The three dimensional physics based model allows us to assess the characteristic of SIRs at L1 which can be used as template for directional dependent data acquired by such in-situ payloads (see Section 3.3 for details).

Belcher & Davis [1971] classified this interaction into four regions S, S$'$, F$'$ and F i.e., the unperturbed slow wind, accelerating slow wind, decelerating fast wind and ambient fast wind regions, respectively. The compressed S$'$ and F$'$ regions form the SIR with enhanced plasma density and magnetic field magnitude. We observed the same kind of structure formation in predicted plasma properties at

L1. Figure 3.12 (a) shows the SIR occurring in the first quarter of the CR2081 simulation. Subplots (a1), (a2) and (a3) show the rise in radial velocity, magnetic field magnitude and density in the interaction region. Subplots (a4) and (a5) display the fluctuation in azimuthal component of velocity and flow angle ($\tan^{-1}\left(\frac{V_y}{V_x}\right)$), where x and y are in HEEQ) during the interaction region. Similar pattern was also predicted for transverse component of velocity vector in Belcher & Davis [1971, Fig. 17]. Furthermore, we observed an additional peculiar trait for plasma flux in the meridional and azimuthal directions which is discussed in detail in Section 3.3.

3.3 ASPEX: ADITYA L1

The Indian solar mission, Aditya L1, has seven payloads — four remote sensing and three in-situ instruments. Aditya Solar wind Particle EXperiment (ASPEX) is one of the three in-situ payloads and have multi-directional measurement capabilities. SWIS and SupraThermal & Energetic Particle Spectrometer (STEPS) are two independent subsystems of ASPEX, which, in turn, have two and six units respectively. The primary scientific objective of SWIS is to study the solar wind plasma particles, whereas that of STEPS is to investigate the suprathermal particles and SEPs [Goyal et al., 2018].

The two independent units of SWIS, Top Hat 1 (THA-1) and Top Hat 2 (THA-2) will measure the particle flux in energy range of 100 eV to 20 keV. THA-1 have a field of view (FOV) of 360° along the ecliptic plane and will be capable in differentiating the major solar wind ion species (proton and alpha particles). On the other hand, THA-2 will measure total particle flux with 360° FOV in plane perpendicular to ecliptic plane. Each THA has an electrostatic analyzer (ESA) section that selects the incoming ions based on their energies. In THA-1, there is an additional Magnetic Mass Analyzer (MMA) section that deflects the major ions as per their masses to eventually get detected by a Micro Channel Plate (MCP). The position information

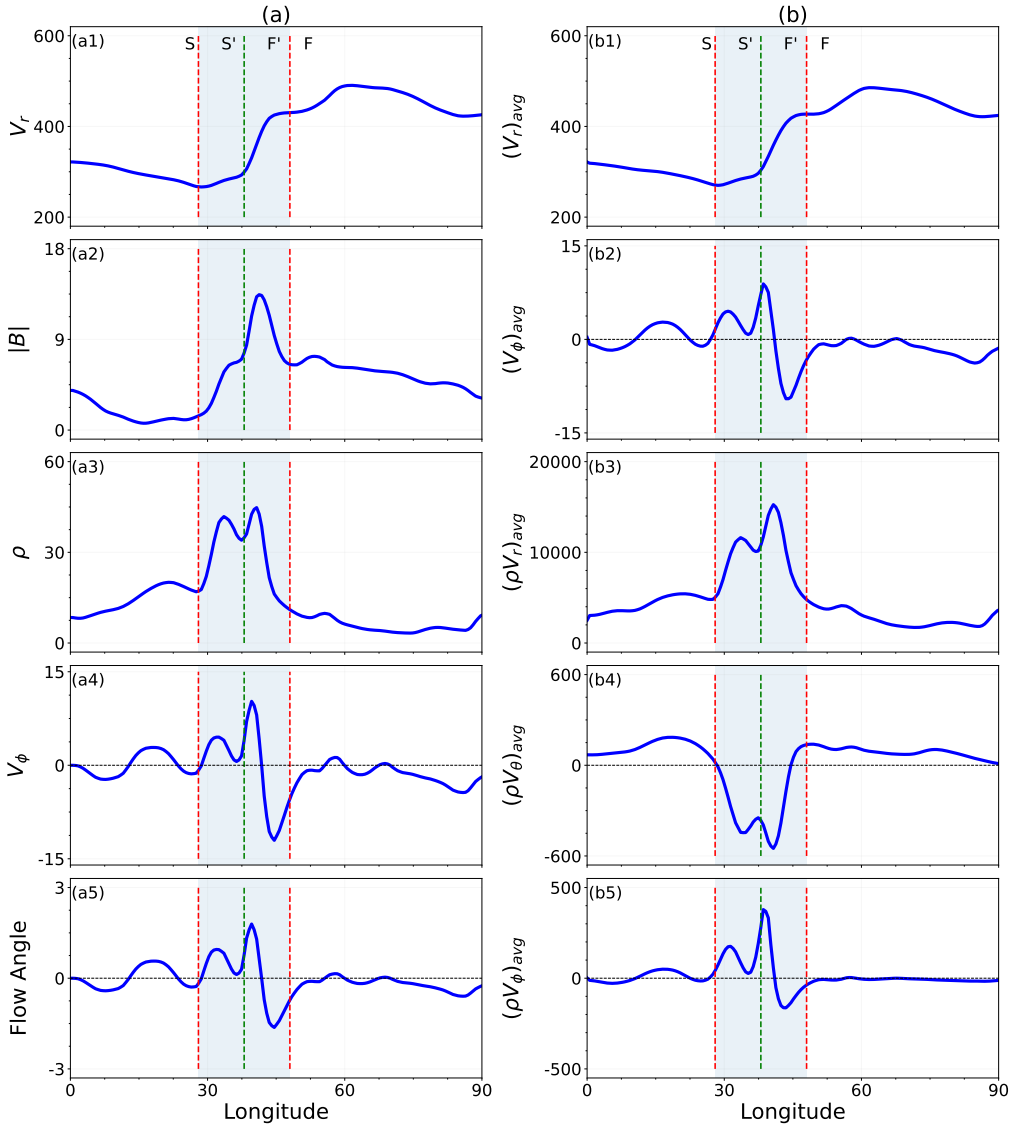

Figure 3.12: Plots showing the features of plasma properties at L1 corresponding to SIR for CR2081. Plot (a) represents the computed plasma properties at L1 location whereas, plot (b) represents the mass averaged properties at L1. The shaded region (S' and F) shows the SIR where in S' region (between red and green dotted vertical lines) solar wind is getting accelerated and in F region (between green and red dotted vertical lines) plasma is getting decelerated. V_r are V_ϕ are plasma velocity in radial and azimuthal direction in km/s. $|B|$ and ρ are IMF magnitude (nT) and proton density ($N_p\ cc^{-1}$). Subplot (a5) shows the variation of flow angle in degree. $(V_r)_{avg}$ and $(V_\phi)_{avg}$ are averaged value of V_r and V_ϕ (km/s). $(\rho V_r)_{avg}$, $(\rho V_\theta)_{avg}$ and $(\rho V_\phi)_{avg}$ are averaged proton flux ($N_p\ cm^{-3}s^{-1}$) in radial, meridional and azimuthal directions. The X-axis, Longitude, is flipped Carrington longitude same as in Figure 3.9 and 3.10.

of the incident charges are derived from the in-house developed Resistive Anode Encoder (RAE). It consists of a number of metallic tracks printed on a PCB material. The position information is derived based on the voltage division across the resistive chains and readout at the end (A1-A2, B1-B2, C1-C2, D1-D2). It is to be noted that RAE of THA-1 consists of four quadrants and each resistive chain in a quadrant consists of four sectors that amounts to an angular resolution of 22.5 degrees (16 sectors). This is shown in Figure 3.11 (a). In addition to the fact that THA-2 is mounted perpendicular to THA-1, there is one more fundamental difference between the THA-1 and THA-2 units. THA-2 does not have any MMA section and hence it is not designed to separate protons and alpha particles. In absence of MMA section, the particles fall on an annular region on RAE that is around the mean radius of the ESA. Therefore, RAE in THA-2 consists of a thin annular strip of a single resistive chain and readouts at the end of the strip. In addition to these differences, THA-2 also has 32 sectors that results in an angular resolution of 11.25 degrees. The schematic of the RAE of THA-2 is shown in Figure 3.11 (b). Therefore, once deployed at L1, SWIS will continuously measure the proton and alpha particles individually in radial and azimuthal directions and integrated flux in the meridional direction.

In this work, we have used our simulation results to synthesize the measurements of SWIS by forming three computational planes (namely A, B and C), each in radial, meridional and azimuthal direction. Each plane is made up of nine grid cells and are at a distance of dr ($\sim 2.8 R_{\odot}$), $d\theta$ (1°) and $d\phi$ (1°) from the L1 grid cell, in their respective unit vector directions. Figure 3.11 (c) displays the computational planes that cover the FOV of SWIS and the L1 grid cell is represented by the Earth's logo. The values at nine grid cells are used to find the averaged value of quantities at L1 which are plotted in Figure 3.12 (b).

We used the above mentioned averaging technique to imitate the observation of

SWIS with the aim to show how its multi-directional measurement capability could lead to more accurate detection of SIRs. For demonstration purpose, we chose a well-defined SIR in the first quarter of CR2081. Figure 3.12 subplots (b1) and (b2) are of averaged radial and azimuthal components of velocity and they are very much similar to their value at the L1 grid cell, implying that the employed technique is satisfactory. Figure 3.12 (b3), (b4) and (b5) are of proton flux density in radial, meridional and azimuthal directions, respectively. In all the three flux plots, there is significant change in $S^{'}$ and $F^{'}$ (shaded) regions. The radial flow has increased, meridional flow has changed its direction and azimuthal flow is fluctuating rapidly in the shaded $S^{'}$ and $F^{'}$ regions. Similar features were also observed for interaction regions at 120° and 300° of CR2053, 60° of CR2077 and 240° of CR2104. This collective feature occurring in proton flux profile in three directions, specially the fluctuations in azimuthal flow and meridional flow, can be called as the characteristic feature of SIRs. The observation of such multi-directional features can be used to detect SIR events at L1, along with rise in density and magnetic field. This will result in a more reliable and precise detection of SIRs at L1.

To observe the above mentioned composite features in plasma flux due to SIR, the spacecraft should have the facility to collect the data continuously in all the three directions. ASPEX has that directional capability and can detect the rise in plasma density, plasma flux in radial as well as fluctuation of flux in azimuthal direction. Along with the on-board magnetometer, Aditya L1 will have the ability to measure the rise in plasma density, IMF magnitude and fluctuations in longitudinal direction. The combined observation of the three specified features will provide a better SIR detection functionality.

3.4 Summary and Discussion

In this work, we presented an indigenous physics-based solar wind forecasting model for inner heliosphere which uses an adapted semi-empirical approach for initial boundary condition. This 3D model has been developed with an intention to run on a personal workstation in reasonable computational time with adequate accuracy. On an average, the coronal domain takes around 2 hours and inner-heliospheric domain takes around 6.5 hours for one complete CR run on a 48 core processor. This computational time is for the resolution and setup mentioned in Section 3.1. To reduce this computational time, user can opt for a lower angular resolution of 2°. However, due to lack of sampling in the longitudinal and latitudinal directions, features of SIR (as depicted in Figure 3.12) would be rather diffused and their identification would be troublesome. Therefore, when SIR assessment is not the objective, then the user can opt for a lower angular resolution.

In this study, two types of magnetograms have been used to validate the results with observation, GONG and HMI. Being the only observational input, accuracy of magnetogram directly effects the veracity of model prediction. Both GONG and HMI measures LOS component and provides radial component of magnetic field on the solar surface. They do so by dividing the observed magnitude by the cosine of the angle from the disk center and assuming that the fields are purely radial at photosphere. But this approximation is sensible only in those regions where the field is not strong enough to resist the fluid forces, like for quiet and weak active regions and not for strong active regions. Therefore, an inevitable discrepancy is always present in the model's input which ultimately gets reflected in final results.

In SWASTi-SW, the initial boundary condition of MHD domain is based on an adapted version of original WSA relation [Arge et al., 2003]. We generalized the empirical relation of plasma speed by successfully reducing one independent parameter. This generic approach makes the WSA model independent of the choice of the

grid resolution in inner-heliospheric domain, specially in latitudinal and longitudinal direction.

An effort to optimize the value of one other independent parameter using HUX algorithm was also demonstrated. Though this method uses observational data and can't be directly used for forecasting purposes, a long term study using this approach would be helpful in finding the optimal set of values of independent parameters. A possible future work would be to use such extensive data set from long term studies to automatize the choice of free parameters for any given Carrington rotation period.

The results from comparison suggests that SWASTi-SW is capable in forecasting the ambient solar wind properties at L1, specially the correlation of plasma speed is high (upto $cc = 0.84$). Model does overestimate (underestimate) the value of plasma density (temperature) and this is something that should be explored in future works. We showcased that a reduced value of specific heat ratio (γ) leads to additional heating, but it also decreases the density and magnetic field intensity. Therefore, a spatially varying relation of γ can be a reasonable alternative for better match. Another rational approach could be the introduction of anisotropic pressure terms in MHD equation to incorporate more insightful physics.

We demonstrated the directional dependent features (e.g., velocity, proton flux, flow angle, etc.) of SIRs using our model and also presented a synthetic measurement to mimic the observations of the SWIS. At this point, we again reiterate that SWIS-THA1 does not have very good latitudinal coverage but exceptional azimuthal coverage. On the other hand, SWIS-THA2 has exceptional latitudinal coverage but limited azimuthal coverage. Therefore, by combining THA-1 and THA-2 measurements, one can pick up the signatures of SIRs in three dimensions. Additionally, Rout et al. [2017] showed that for geoeffectiveness, CIR azimuthal flow angle is mostly within 6 degree. The advantage here is, ASPEX can capture the signatures of the arrival of SIRs/CIRs at the L1 point at all azimuthal and elevation angles -

some of these will turn out to be geoeffective and some will not. In addition, the STEPS subsystem that covers six directions, can detect the energetic particles arriving from the SIR/CIR shock fronts. Therefore, SWIS and STEPS together along with the modeling outputs can be very important for SIR/CIR investigations and can pave the way for the forecasting of their arrival. This framework will therefore complement the upcoming ISRO mission, Aditya-L1. Specifically SWASTi-SW will compliment the in-situ measurements of solar wind properties by ASPEX and MAG.

Chapter 4

SWASTi-CME and CME-SW Interaction

This chapter is structured based on the paper titled "SWASTi-CME: A physics-based model to study CME evolution and its interaction with Solar Wind" by Prateek Mayank, Bhargav Vaidya, Wageesh Mishra, and D. Chakrabarty [Mayank et al., 2023].

4.1 SWASTi-CME

SWASTi (Space Weather Adaptive SimulaTion framework) is a newly developed 3D physics-based heliospheric model designed for space weather research and forecasting [Mayank et al., 2022]. This numerical framework consists of a semi-empirical coronal domain (from 1 $R_\odot$ to 21.5 $R_\odot$) and a magnetohydrodynamic (MHD) based heliospheric domain (from 0.1 AU to 2.1 AU). The CME module of SWASTi comprises two models: the cone model and the flux rope model, which are inserted into the self-consistently propagating background solar wind (SW). The specifics of these CME models are detailed in the following subsections.

4.1.1 Elliptic Cone Model

SWASTi utilizes the cone model to simulate the inner-heliospheric dynamics of CMEs. The cone model has a simple non-magnetic geometry and has been used in numerous studies for forecasting and assessing the CME properties in the inner-heliosphere [EUHFORIA, Odstrcil et al., 2004; Pomoell & Poedts, 2018b]. A common approach in most of the existing MHD models is to describe the CME structure by a constant angular width, propagation direction and speed (e.g., EUHFORIA, ENLIL). They assume the cross-section of CME to be circular with a varying radius. However, from the observations of CMEs in white-light images of the corona, we know that the geometry of CME front is not always circular rather an ellipse. In this work, we propose a more realistic structure for the cone CME model by incorporating the angular height as well. The proposed method allows for the generation of CMEs with elliptical cross-sections, rather than assuming a circular shape. In this manner, the model's geometry better aligns with the observations of CMEs in the corona and enhances the realism of the simulation.

We use the graduated cylindrical shell [GCS; Thernisien, 2011] method to estimate the structural parameters of the CME at 0.1 AU ($\mathrm{R_{in}}$). Afterwards, the CME is inserted in the MHD domain as a homogeneous plasma cloud with uniform radial speed (v_{CME}), density (ρ_{CME}) and temperature (T_{CME}). The time dependent injection at the initial boundary ($\mathrm{R_{in}}, \theta, \phi$) is governed by the following equations:

$$\left(\frac{\phi - \phi_{\mathrm{CME}}}{w(t)}\right)^2 + \left(\frac{\theta - \theta_{\mathrm{CME}}}{h(t)}\right)^2 < 1 \tag{4.1}$$

$$w(t) = \varphi_{\mathrm{hw}} \cdot \sin\left[\frac{\pi}{2}\frac{(t - t_{\mathrm{onset}})}{t_{\mathrm{half}}}\right] \tag{4.2}$$

$$h(t) = \varphi_{\mathrm{hh}} \cdot \sin\left[\frac{\pi}{2}\frac{(t - t_{\mathrm{onset}})}{t_{\mathrm{half}}}\right] \tag{4.3}$$

$$t_{\mathrm{half}} = \mathrm{R_{in}} \cdot \frac{\tan\left(\varphi_{\mathrm{hw}}\right)}{v_{\mathrm{CME}}} \tag{4.4}$$

where, $\phi_{\rm CME}$ and $\theta_{\rm CME}$ are the longitude and latitude of the CME center, $w(t)$ and $h(t)$ are the time dependent width and height of the CME, $\varphi_{\rm hw}$ and $\varphi_{\rm hh}$ are angular half-width and half-height of the CME determined from the coronagraph images, $t_{\rm onset}$ is the injection starting time and $t_{\rm half}$ is the half of the insertion time of the CME. Equation 4.1 ensures the formation of ellipsoidal structure of CME at the boundary of simulation domain, where the ambient solar wind parameters are replaced with CME values. The angular width and height of the elliptic cone CME are modulated sinusoidally with time at $\rm R_{in}$, with the half-time given by equation 4.4, following a similar approach as Pomoell & Poedts [2018b].

4.1.2 Flux Rope Model

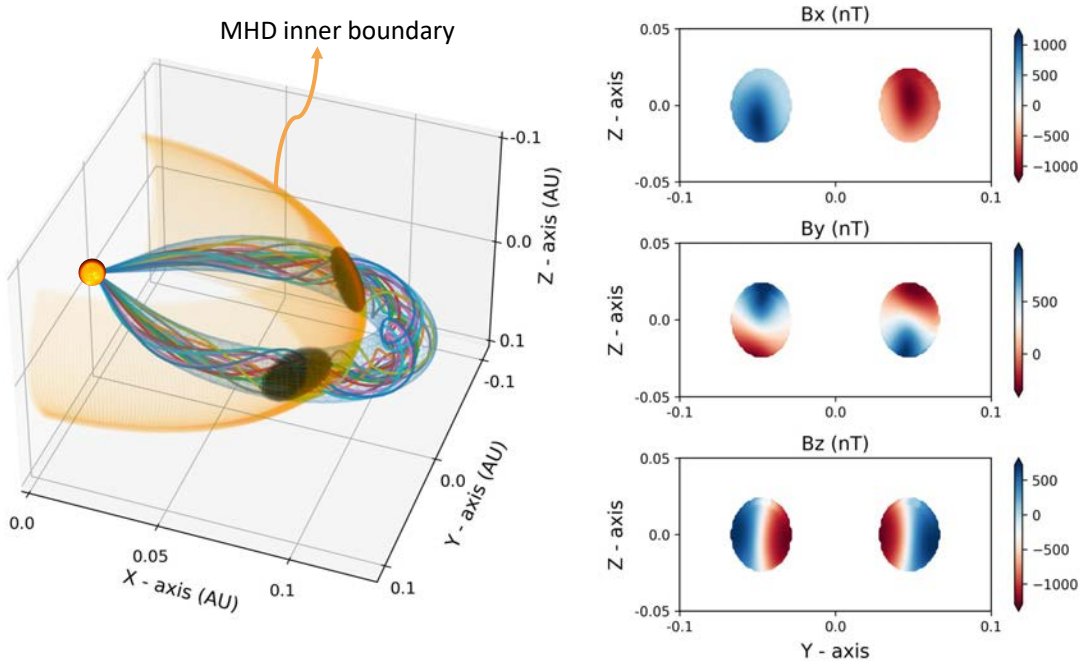

Figure 4.1: Figure illustrates the flux rope model implemented in SWASTi-CME. The left subplot depicts the evolution of the formed flux rope structure as it propagates radially and crosses the inner boundary of the MHD domain. On the right subplot, the magnetic values are displayed for the overlapping region between the flux rope and the MHD boundary, shown as black circle in the left subplot.

To simulate the flux rope CME, SWASTi employs the Flux Rope in 3D [FRi3D; Isavnin, 2016] model. FRi3D is an analytical model that incorporates the 3D magnetic field configuration of CME and is capable of considering the major deformations of CME in reconstructing its global geometrical shape. It has been widely utilized in previous works on CME MHD simulation, such as Maharana et al. [2022] where they implemented this model in EUHFORIA and compared its performance with the spheromak model, and Singh et al. [2022] where they used it to define the geometry of the flux rope CME in their MHD simulation.

In this work, we have used the FRi3D model to construct the 3D magnetized shell of the CME at 0.1 AU, serving as the initial state for the MHD domain. The geometry of the CME forms a classic croissant-like shape that is anchored at both ends to the Sun. The cross-section of CME is assumed to be circular with the radius, $R(\phi)$, varying in proportion to the heliocentric distance, as described below:

$$R(\phi) = \frac{R_t}{R_p} \cdot r(\phi) \tag{4.5}$$

$$R_p = R_t \cdot \tan(\varphi_{hh}) \tag{4.6}$$

$$r(\phi) = R_t \cdot \cos^n\left(\frac{\pi}{2}\frac{\phi}{\varphi_{hw}}\right) \tag{4.7}$$

where R_t is the heliospheric distance of apex of the CME axis (toroidal height), R_p is the radius of cross-section at the apex (poloidal height) which depends on R_t and half-height of CME (φ_{hh}), and $r(\phi)$ is the radial distance of the CME axis at ϕ from the center of the footpoints at the solar surface. This radial distance is defined by the equation 4.7, which depends on the half-width of the CME axis (φ_{hw}) and the parameter n controls the front flattening of the CME structure. See Figure 1 and 2 of Isavnin [2016] for further reference.

The CME structure is populated with magnetic fieldlines that have a low and constant twist, in accordance with the findings of Hu et al. [2015]. The magnetic

fieldlines are twisted based on equation 4.5, and their shape are defined by equation 4.7. Meanwhile the strength of magnetic fields follows a normal distribution in the poloidal plane (perpendicular to the flux rope axis) at each axial point. The analytical form of magnetic field strength at a perpendicular distance $\tilde{r}$ from the flux rope axis is following:

$$B = B_{\text{axis}} \cdot \exp\left(\frac{-1}{2\sigma^2}\left[\frac{R_{\text{t}} \cdot \tilde{r}}{R_{\text{p}} \cdot r(\phi)}\right]^2\right) \tag{4.8}$$

where, B_{axis} is the total magnetic field strength on the flux rope axis at ϕ, which is based on the user defined total flux, conserved along the flux rope cross-section, and σ is the standard deviation coefficient of the distribution. Alternatively, other studies have also used other magnetic profiles to magnetize the FRi3D geometry. For example, Singh et al. [2022] used an analytic form of a constant-turn magnetic field in a torus shape given by Vandas & Romashets [2017].

Figure 4.1 depicts the CME structure with magnetic field modeled using the above described method and its insertion in the MHD domain. Once the FRi3D CME structure is formed, with its leading edge at 0.1 AU, it is allowed to expand radially in a self-similar manner by increasing R_{t}, while keeping everything else constant over time. In this manner, the toroidal and poloidal heights of CME (R_{t} and R_{p}) increases with time as:

$$R_{\text{t}}(t) = R_{\text{t}}(0) + v_{\text{t}} \cdot t \tag{4.9}$$

$$R_{\text{p}}(t) = R_{\text{p}}(0) + v_{\text{p}} \cdot t \tag{4.10}$$

where $R_{\text{t}}(0)$ and $R_{\text{t}}(0)$ are the initial toroidal and poloidal heights when the leading edge is at 0.1 AU. v_{t} and v_{p} are the speeds at which toroidal and poloidal heights increase, respectively. The effective speed of CME apex (v_{CME}) is the summation of v_{t} and v_{p}, as estimated from coronagraphic observations at 0.1 AU. As the leading edge of the CME surpasses 0.1 AU, the initial boundary of the MHD domain is substituted with the values of the overlapping flux rope CME at the intersection region. Similar to cone CME, both density (ρ_{CME}) and temperature (T_{CME}) are

uniform within the flux rope. However, in contrast to cone CME, the local speed inside the flux rope CME varies radially, based on the local toroidal speed of the FRi3D geometry.

The left panel of Figure 4.1 shows the region where the FRi3D CME and MHD domain overlap, indicated by two black circles in the orange plane. The subplots in the right panel of Figure 4.1 display the magnetic field values of this overlapping region. The flux rope CME values corresponding to this intersection region are initialized at the inner-boundary of the MHD domain, and are updated as the leading edge progresses. The insertion process stops when its local speed at boundary matches with the speed of the solar wind stream at the corresponding grid points. Given the variability in solar wind speeds, we use a rounded value of their average for this purpose. This process of leg disconnection ensures that there are no abrupt and significant changes in the pressure gradient, thereby facilitating the smooth insertion of subsequent CMEs.

4.2 Case Study of CR2165 & CR2238

In order to evaluate the performance of SWASTi-CME, we conducted simulations of CME events for two Carrington rotations (CRs) and compared the results with in-situ measurements obtained from the OMNI dataset. The objective was to assess the effectiveness of the model in two different scenarios: one CR with multiple CMEs near solar maxima and another CR with a single isolated CME near solar minima. To achieve this, we specifically chose CR2165, which consisted of five halo CMEs, and CR2238, which featured one halo CME.

4.2.1 3D Reconstruction of CME

To simulate a CME, the foremost step is to reconstruct its 3D geometry in the solar corona using white light images captured by coronagraphs. In this study, we

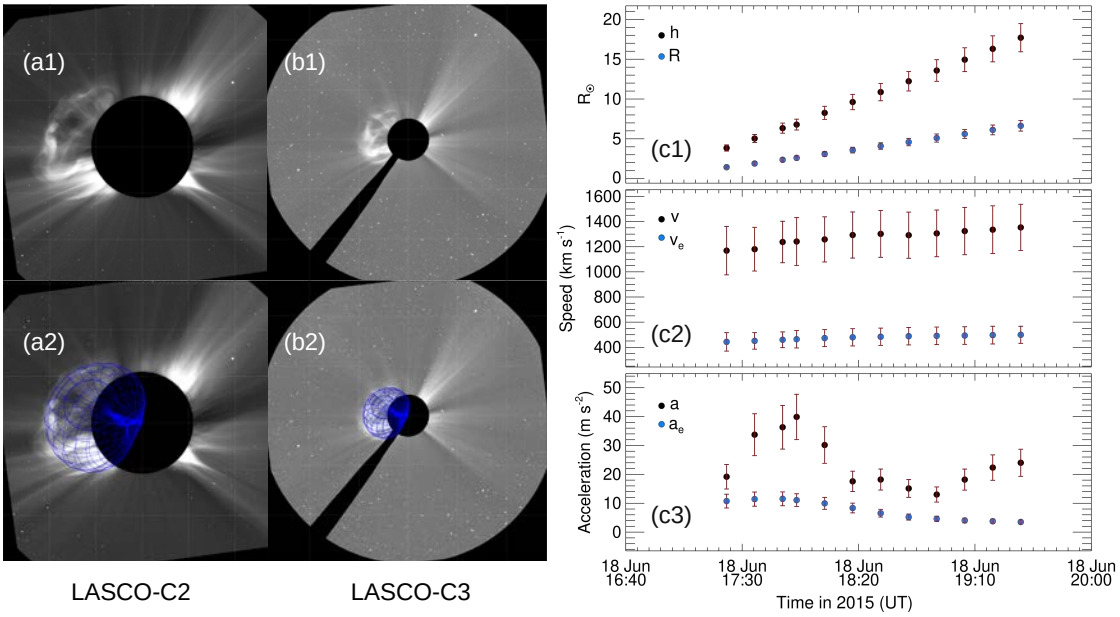

Figure 4.2: The white light images obtained from the SOHO/LASCO coronagraphs on 2015-06-18, capturing the first CME of CR2165. Subplots (a1) and (b1) show the LASCO C2 and C3 images, respectively. The traced GCS structure is superimposed on these images, indicated by the blue overlay in subplots (a2) and (b2). The temporal evolution of the traced CME's propagation distance (h), speed (v), and acceleration (a) can be observed in subplots (c1), (c2), and (c3), respectively. Corresponding expansion properties (R, v_e, a_e) are also shown in the right subplots.

utilized the Graduated Cylindrical Shell [GCS; Thernisien, 2011] forward model for this purpose. Implementing the GCS model requires the manual fitting of a GCS geometry to the white light observations of CMEs to obtain the best model fit parameters. By fitting the model to the temporal sequence of images of CMEs, we could trace the 3D trajectory of the selected CMEs in the corona. This allow us to determine the morphological and kinematic properties of CMEs, such as its de-projected shape, size, and speed. In essence, we employ the GCS technique to obtain the initial properties of the CME at the inner boundary of the MHD domain, specifically at a distance of 21.5 $R_\odot$. These properties include the initial angular width, angular height, tilt, and speed at 21.5 $R_\odot$.

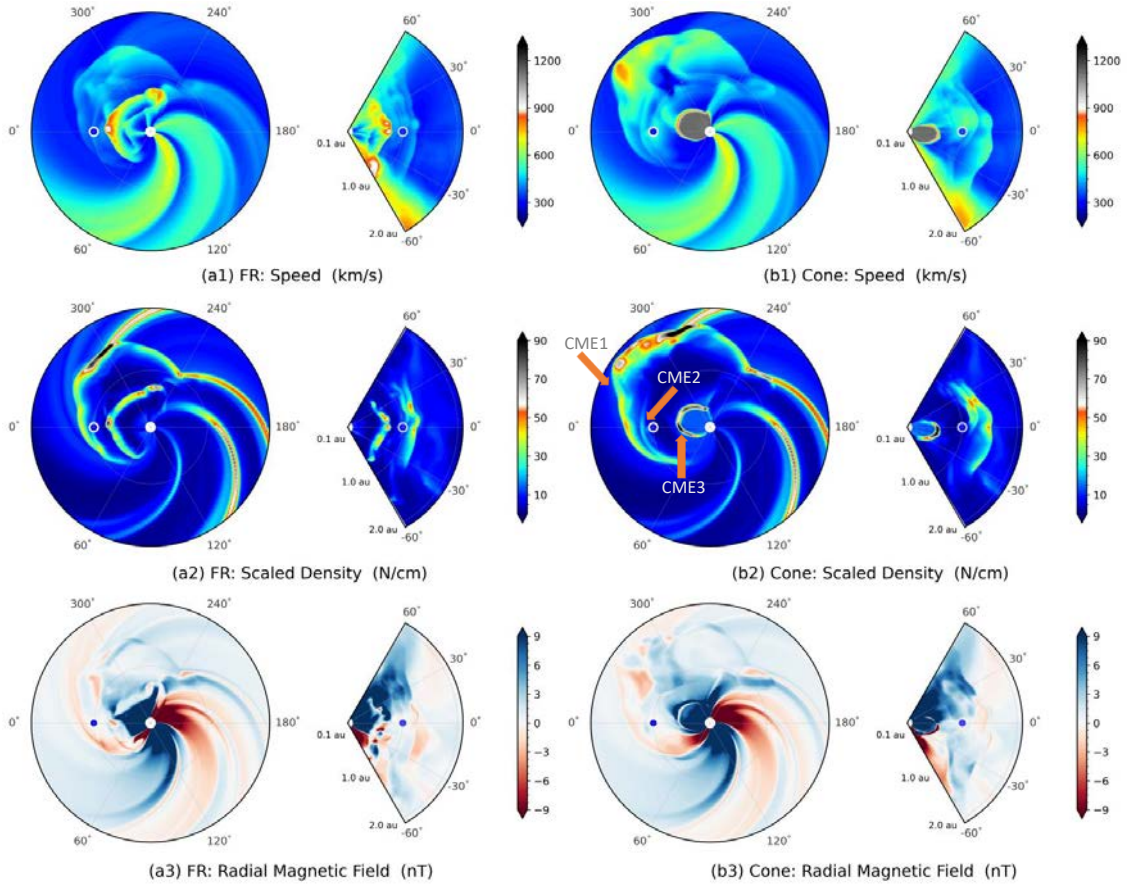

Figure 4.3: Figure displays a time snapshot of the SWASTi-CME results for CR2165 on 2015-06-22 at 10:26 UT. Subplots (a1)-(a3) depict the speed, scaled density, and radial magnetic field results for the flux rope (FR) CMEs, while subplots (b1)-(b3) show the corresponding results for the cone CMEs. At this particular time, three CMEs, namely CME1, CME2, and CME3, are present in the simulation domain.

Figure 4.2 (a1-b2) presents a snapshot of the GCS fitting applied to white light images obtained from LASCO-C2 and LASCO-C3 coronagraphs. Specifically, the figure showcases the results for the first CME observed during CR2165 (CME1). The blue structures in subplots 4.2 (a2) and (b2) represent the GCS model fitted wireframe overlaid on the CME. The estimated kinetic properties of CME1 can be observed in subplots 4.2 (c1), (c2), and (c3), where the three-phase acceleration of the CME [Zhang et al., 2004], is clearly visible. The acceleration of the CME

initially increases until 5 $R_\odot$, followed by a decrease and subsequent gradual increase. The same approach is adopted for the other selected CMEs also. Generally, it is recommended to utilize simultaneous coronagraphic observations from multiple viewpoints for confident results from fitting with the GCS model. However, in this case (CR2165), STEREO/COR observations are not available and therefore we could only use SOHO/LASCO observations. However, for CR2238, both STEREO/COR and SOHO/LASCO observations are available, allowing us to utilize contemporaneous images from multiple viewpoints.

In addition to the properties obtained through the GCS method, the estimation of the magnetic properties, density, and temperature of the CME are required. For simplicity, we have assumed a uniform density and temperature for all CMEs and homogeneous speed for cone CMEs. The temperature for each CME was set at 0.8 MK, while the density was estimated through the optimization of the CME's time of arrival at L1. The estimated density was on the order of 10^{-18} kgm^{-3}, which is consistent with the observations Temmer et al. [2021]. The magnetic properties of the FRi3D CME were modeled using equation 4.8 with a constant twist, and a magnetic flux of 10^{12} Wb was assumed, which is consistent with values used in Isavnin [2016]; Maharana et al. [2022]; Singh et al. [2022]. For the remaining geometric properties of the FRi3D CME, default values were employed. A comprehensive list of all the estimated properties of the CMEs at 21.5 $R_\odot$ is provided in Table 1.

4.2.2 MHD Simulation results

Based on the GCS model results, the first CME of CR2165 (CME1) reached the radial distance of 0.1 AU at 20:03 UT on June 18, 2023, and entered the simulation domain. CME1 was characterized as a fast CME with a speed of 1353 km/s. It had a half angular width of 65.3° and a half angular height of 36.9°. As CME1 started propagating through the interplanetary medium, it encountered a stream interaction

Table 4.1: Initial properties of CMEs associated with CR2165 and CR2238

Parameters with different value for each CME							
	Time of arrival at 21.5 $R_\odot$	v_{CME}	θ_{CME}	ϕ_{CME}	φ_{hw}	φ_{hh}	γ	ρ_{CME}
CME1	20:03 UT 18 June 2015	1353	6.06	-51.18	65.3	36.9	66.6	1e-18
CME2	11:25 UT 19 June 2015	836	-22.5	7.06	40.7	18.7	32	2e-18
CME3	05:09 UT 21 June 2015	1115	11.03	-24.41	84.8	46.8	-85	2e-18
CME4	21:26 UT 22 June 2015	1100	25.11	7.8	55.2	36.1	68.4	1e-18
CME5	10:41 UT 25 June 2015	1330	23.37	31.76	34	16.2	77	3e-17
CME6	19:30 UT 07 Dec. 2020	1250	-24	10	79	44	10	2e-18

Parameters with common value for all CMEs		
T_{CME} = 0.8 MK	$\tau = 2$	φ_p= 0.6
ϕ_B = 1e12 Wb	$n = 0.5$	φ_s= 0.0

Note: (θ_{CME}, ϕ_{CME}) - CME insertion coordinates; φ_{hw} - angular half-width (degree); φ_{hh} - angular half-height (degree); γ - tilt angle (degree); ρ_{CME} - mass density (kgm^{-3}); ϕ_B - magnetic flux (Wb); τ - twist; T_{CME} - temperature (MK); n - flattening; φ_p - pancaking; φ_s - skew.

region (SIR) along its trajectory. This interaction led to the distortion of the arc structure of the CME front, which is evident from the scaled density plot displayed in Figure 4.3. The interaction with the SIR resulted in the formation of a region of elevated density in front of the eastward flank of the CME. Notably, despite both the cone and FR CME initiating simultaneously and propagating through the same medium, they exhibited clear differences in their evolutionary behavior. Specifically, the cone CME exhibited a faster propagation speed compared to the FR CME. This disparity can be attributed to the inherent characteristics of the cone CME, which possessed a homogeneous speed at the onset, while the velocity of the FR CME decreased across its cross-section. Additionally, the cone CME appears to cover a larger area in the $r-\phi$ plane, as shown in Figure 4.3. This difference may be caused by the tilt angle of the FR CME, which is not considered in the cone model. Given that the tilt angle of CME1 is 66.6°, its projection onto the equatorial plane will be smaller compared to a CME with no tilt.

Approximately 18 hours after the insertion of CME1, CME2 started entering the simulation domain. CME2, characterized by weaker attributes including a speed of 836 km/s and a notably smaller size compared to CME1, demonstrated an intriguing

phenomenon. As CME1 propagated through the inner heliosphere, it displaced the surrounding solar wind plasma, creating a less dense interplanetary medium in its path. Due to which, CME2 experienced lesser drag and was able to intercept the westward flank of CME1 nearly at 1.0 AU. However, the relative speed between the two CMEs was not high, resulting in a relatively weak interaction. In Figure 4.3, there aren't very clear signatures of their interaction in $r - \phi$ plane but it can be seen in $r - \theta$ plane, where CME2 has started interacting with CME1. Owing to the less dense medium, CME3 was able to interact with the joint region of CME1 and CME2. This interaction was not as weak as earlier, because CME3 was the largest CME among the five with initial speed of 1115 km/s. This makes it an interesting case, however none of the interaction happened at L1, hence no in-situ signature were recorded in the observations at L1.

CME4 followed a trajectory aligned with the path where the last three CMEs had previously interacted. Despite its initial speed of 1330 km/s, CME4 was unable to catch up with CME3 until reaching a radial distance of 2.0 AU. However, the decreasing distance between CME4 and CME3 indicated an eventual interaction beyond 2.0 AU. In a similar manner, CME5, with a velocity of 1250 km/s, propagated towards the direction of the preceding CME, experiencing less drag. Remarkably, all five CMEs impacted the Earth, with CME3 displaying the highest strength as determined by in-situ measurements. It is worth noting that the successive ejections of CMEs in close proximity led to significant erosion of the SIR, which was located along the trajectory of CME1. This SIR could only regained its heliospheric structure after the transit of CME5.

The CME of CR2238 (CME6) was also a fast one, with initial speed of 1250 km/s, and and significant size, with a half angular width of 79° and a half angular height of 44°. It was the only halo CME observed during this Carrington rotation period, and its trajectory did not encounter any prominent SIR. Unlike the CMEs of

CR2165, CME6 did not have a direct impact on Earth; instead, it merely grazed as it propagated through the inner heliosphere.

4.2.3 Validation with in-situ measurements

To evaluate the precision of the SWASTi-CME model, we conducted a comparative analysis between the simulation results and the OMNI data of CR2165 and CR2238. To ensure a fair comparison with the L1 measurements, a virtual spacecraft was integrated into the simulation, which effectively considered the dynamic changes in the longitudinal and latitudinal position of Earth in the Stonyhurst coordinate system. This virtual spacecraft facilitated the acquisition of plasma properties at 5-minute intervals throughout the computational run, enabling a direct comparison with the 5-minute average data obtained from OMNIWeb.

Figure 4.4 presents the time series plots illustrating the cone and FR CMEs, along with the OMNI data for CR2165 and CR2238. The FR CME results are represented by the blue solid line, the cone CME results are shown in green, and the OMNI data is depicted in brown. The shaded regions indicate the temporal range where the cone and FR CME results differ, highlighting the distinction between the ambient SW and the CME region. The vertical dashed lines in various colors mark the time of arrival of the sheath region for different CMEs.

Time of Arrival. In the case of CR2165, the FR CMEs successfully predicted the arrival time of all five CMEs with good accuracy. However, the cone CMEs, although reaching the Earth's location, exhibited less precise estimations of the time of arrival. The velocity (a1) and density (a2) subplots in Figure 4.4 demonstrate this discrepancy. Cone CME1 arrived much earlier than the observed time (-15.43 hr), along with CME2 (-9.75 hr) and CME3 (-15.84 hr), compared to FR CME1 (-3.85 hr), CME2 (+1.42 hr), and CME5 (+3.67 hr). Conversely, cone CME3 arrived later (+19.4 hr) than FR CME3 (+6.0 hr), while cone CME4 estimated a better

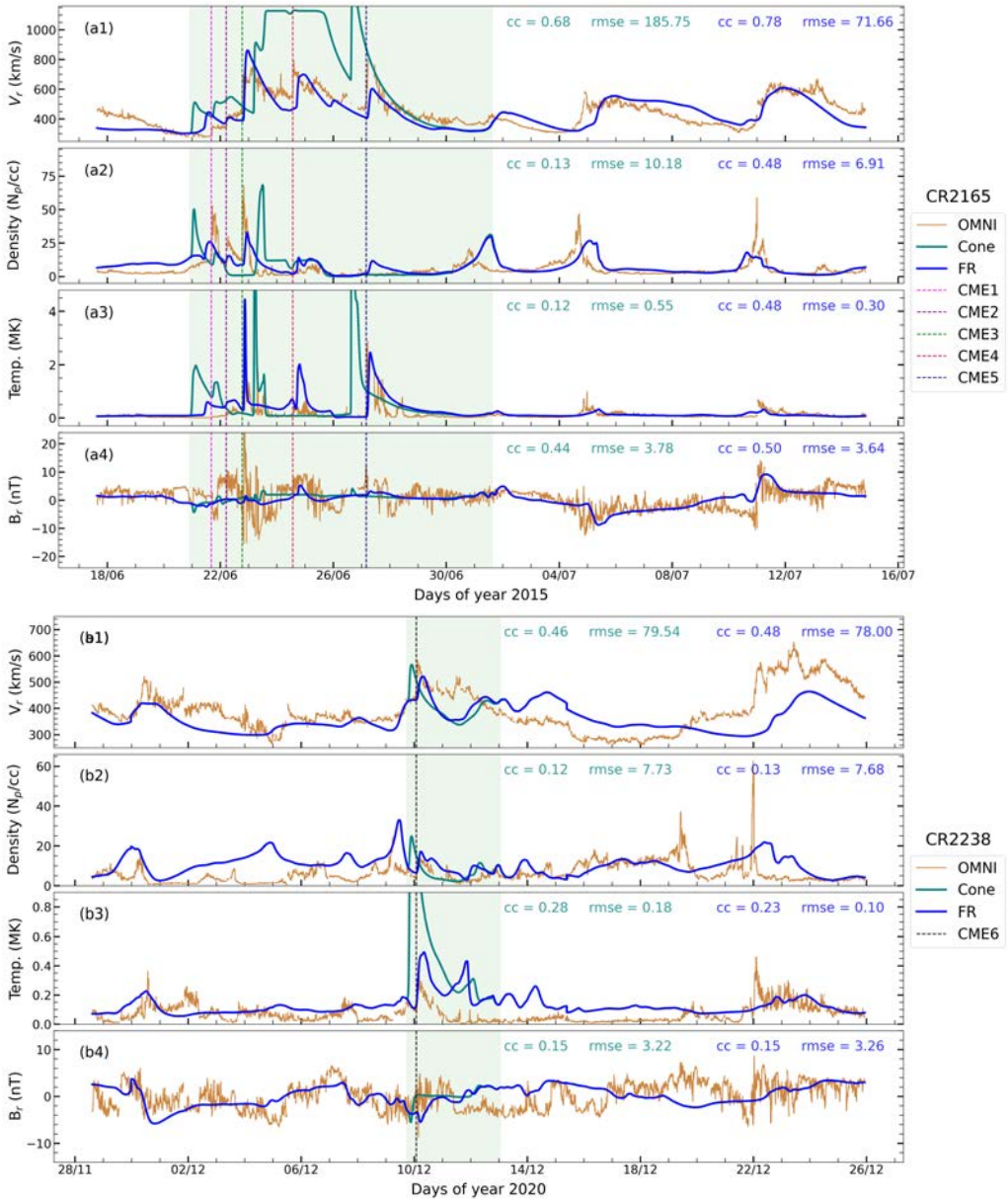

Figure 4.4: Time series plot of in-situ measurements at 1 AU for CR2165 (a1-a4) and CR2238 (b1-b4). The simulated results for the FR and cone CMEs are represented by blue and green colors, respectively, while the observed OMNI data is depicted in brown. Vertical dashed lines of various colors indicate the beginning of the sheath region corresponding to each CME. Both the SWASTi and OMNI data are plotted with a time cadence of 5 minutes.

time of arrival (+3.83 hr) than FR CME4 (+4.92 hr). For CR2238, both FR and cone CMEs provided efficient estimations of the time of arrival, with the cone CME arriving earlier than the observed time and the FR CME arriving later.

Speed. Similar to the time of arrival, the computed CME speed was more accurate for FR CMEs compared to cone CMEs in the case of CR2165. The FR CMEs exhibited a Pearson correlation coefficient (cc) of 0.78 with observations of full CR2165 period and a root mean square error (rmse) of 71.66 km/s. On the other hand, the cone CMEs had a cc of 0.68 and a rmse of 185.75 km/s when compared to the observations. The velocity results from the FR model closely aligned with the observed values for the first four CMEs. However, the simulated speed of CME5 was underestimated by approximately 200 km/s at 1 AU. On the other hand, the cone model overestimated the speed for all CMEs and particularly provided very high values for CME3, CME4, and CME5 compared to the observed values. This discrepancy can be attributed to three factors: homogeneous speed, insertion rate, and the absence of tilt in the cone model. The cone CME, with a constant speed throughout its structure, had a higher effective momentum than the flux rope CME. Moreover, the injection rate of the cone CME, proportional to $\tan(\varphi_{\mathrm{hw}})$, was slower for CMEs with higher angular width ($>75^{\circ}$) compared to a CME with an angular width of 60°. This delay in insertion ultimately impacted the time of arrival at 1 AU. Hence, even with a higher homogeneous speed, CME3 arrived later due to its significantly high angular half-width (84.8°). Additionally, since the cone CME model does not incorporate tilt, the effective trajectory traced by the CME before reaching 1 AU differs from that of the FR CME, which has a higher degree of tilt. For CR2238, both the cone (cc=0.46, rmse=79.54 km/s) and FR (cc=0.48, rmse=78.00 km/s) models provided good estimations of the CME speed at 1 AU. In this case, where CME didn't directly impact the Earth but instead grazed by, the speed estimation in the cone CME was also appropriate.

Density and Temperature. In contrast to FR CMEs, the cone CMEs exhibited higher density and temperature in their sheath regions for all six CMEs. This can be attributed to the homogeneous speed and absence of tilt angle in the cone CME model, which leads to a larger surface area and higher speed in the elliptic plane, consequently resulting in hotter and denser sheath regions as the cone CME propagates in the heliosphere. This pattern is evident in subplots (a2) and (a3) of Figure 4.4. Moreover, CME4 and CME5 presented an interesting scenario where the CME speeds were relatively higher, but the density values were lower. This can be explained by the influence of CME3, which had a very high angular width. The propagation of CME3 likely depleted the density of the interplanetary medium, limiting the aggregation of plasma and resulting in less dense sheath regions for CME4 and CME5.

Magnetic Field. There is noticeable difference in the in-situ magnetic profile between cone and flux rope CMEs. In Figure 4.3 (a4) and (b4), the radial magnetic field remains almost constant with time for cone CMEs, while for flux rope CMEs, it closely matches the feature observed at L1. This indicates that the flux rope CMEs exhibit better agreement with the observed data. However, it is worth noting that the estimated magnitude of the magnetic fields did not always match perfectly with the in-situ data. This suggests that utilizing a constant magnetic flux value for each CME is not the most suitable choice. Adopting different values for different CMEs might lead to improved accuracy in predicting magnetic field variations for the considered cases.

Solar Wind. Regarding the properties of the ambient solar wind, the SWASTi model successfully captured all major features for both CR2165 and CR2238. The simulated speeds, densities, temperatures, and magnetic fields of the solar wind closely aligned with the measurements obtained from the OMNI dataset. This demonstrates the efficacy of the solar wind model in generating a near-realistic ambient

environment for studying the interactions with CMEs even at a high cadence of 5 minutes.

4.3 Method to study CME-SW Interaction

As a CME propagates through the inner heliosphere, it may undergo changes in its dynamics and morphology due to its interaction with the ambient solar wind (SW). Variations in the properties of the ambient SW, such as its speed and density, can result in alterations to the properties of the CME and its shock [Mishra et al., 2021; Winslow et al., 2021]. Investigating the interaction between coronal mass ejections (CMEs) and solar wind (SW), especially in the presence of high-speed streams (HSS) and stream/corotating interaction regions (SIRs/CIRs), can be accomplished by comparing two scenarios in which an identical CME passes in the presence and absence of them. However, to comprehensively evaluate the impact of SW on CME, the entire CME structure must be isolated to measure the differences between the scenarios accurately. In this numerical study, we utilized the SWASTi framework to simulate two different ambient solar wind scenarios. We introduced a flux rope CME into both mediums and employed a novel technique for tracking the 3D CME structure as it propagated through the heliosphere, enabling us to quantify any changes that occurred.

In this section, we discuss the numerical setup that was used to study the effect of SW on CMEs. We implemented this setup on two different Carrington rotation periods, namely CR2165 and CR2238, which were previously validated in Section 4.2.

4.3.1 Numerical setup

To examine the changes in CME properties caused by the ambient SW, we established two setups. The first setup (*real* case) is the default setup of the SWASTi-CME flux rope model and has the realistic SW background. Whereas, the second

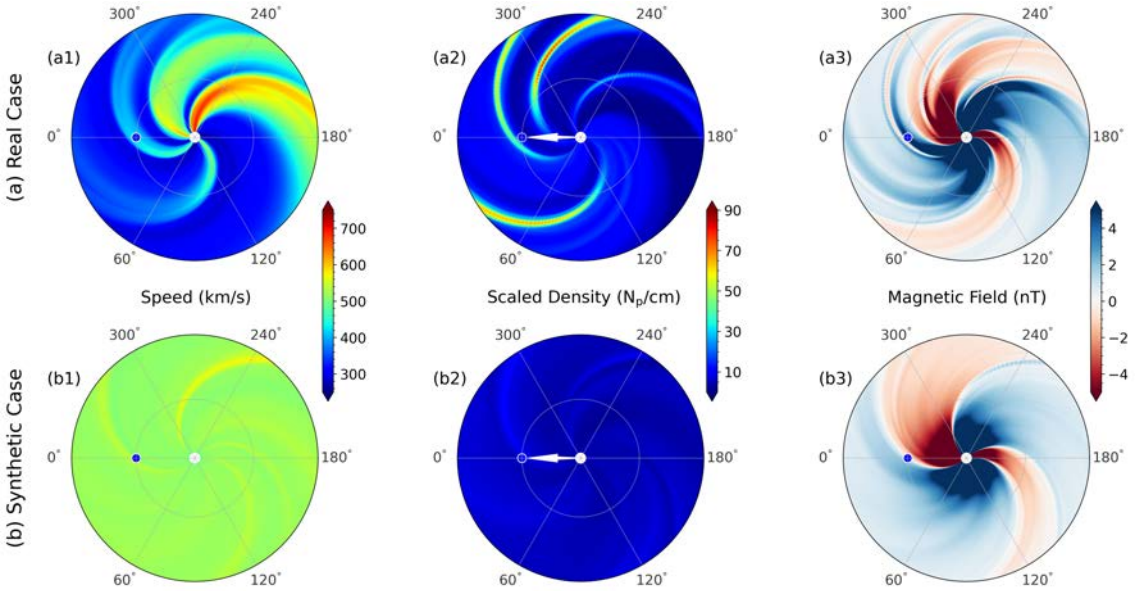

Figure 4.5: The figure showcases the equatorial plane of the numerical setup used to study the influence of ambient solar wind on a coronal mass ejection (CME). Subplots (a1)-(a3) present the speed, scaled density, and radial magnetic field for the real case of CR2165, while subplots (b1)-(b3) depict the results of the synthetic case.

setup (*synthetic* case) is a hypothetical case where solar wind speed is assumed to be almost constant everywhere in the heliosphere. In other words, all the features formed due to the relative speed between different SW streams, for e.g., HSSs and SIRs/CIRs, will be present in the real case but absent in the synthetic case. Further, an identical CME is allowed to propagate in both the cases. Passing through a realistic SW environment, the real case CME will encounter all the variations caused by HSSs and SIRs/CIRs that the synthetic case CME will not. Therefore, the difference in the properties of CMEs corresponding to real and synthetic cases, will directly reflect the impact of HSSs and SIRs/CIRs.

This two setup methodology was carried out for CR2165 and CR2238. The real case SW background simulation, for both CRs, is identical to what is described in Section 3. In the synthetic case, the initial boundary conditions at 0.1 AU are

different, where a constant value of the solar wind speed is provided. In this study, this value is taken to be close to the mean of real case SW speed on the equatorial plane, ensuring similar propagation duration for both real and synthetic CMEs in the simulation domain. At the initial boundary, the density and pressure profiles are also different since they are both dependent on speed, but the magnetic field is kept identical for both the cases. Table 4.2 shows the values of the constant speed taken for the synthetic case of CR2165 and CR2238, which is 500 km/s and 450 km/s respectively.

A flux rope CME structure, with the properties as mentioned in Table 4.2, is injected in both the cases of CR2165 and CR2238. The intention was to deploy a CME with simple structure and symmetry about the equatorial plane, so that the effects can be visualized easily. Therefore, 0° latitude and 0° longitude was taken as the center of CME, with mass density = 10^{-18} kgm^{-3}, front speed = 900 kms^{-1}, temperature = 0.8 MK, and magnetic flux = 10^{12} Wb. Additionally, the half-width, half-height and tilt angle was 45°, 20° and 0°, respectively. Although the above CME features were same for real and synthetic cases of both CRs, the injection time of the CMEs were different. Since, there is significant difference in the SW properties of CR2165 and CR2238, it is important to choose a sensible CME injection time favorable for a significant interaction between CME and ambient SW. The insertion time will determine the local SW surrounding and effective trajectory of CME in the heliosphere, which in turn, will determine the degree of deformation experienced by the CME under the influence of pre-conditioning of the ambient SW structures. CR2165 has a greater variation in SW speed and stronger SIRs than CR2238. Therefore, to encompass a wider range of impacts on the CME, an appropriate injection time was selected to ensure that the CME propagated towards the SIR. Specifically, for CR2165, the direction was towards two high density (strong) SIRs, and for CR2238, it was towards a comparatively lower density (weaker) SIR. The injection location

Table 4.2: Simulation parameters for the synthetic and real cases of CR2165 and CR2238.

CME parameters for Real and synthetic Cases					
$\theta_{\rm CME}$	=	0°	n	=	0.5
$\phi_{\rm CME}$	=	0°	$\varphi_{\rm p}$	=	0.6
$\varphi_{\rm hw}$	=	45°	$\varphi_{\rm s}$	=	0
$\varphi_{\rm hh}$	=	20°	$\phi_{\rm B}$	=	10^{12} Wb
γ	=	0°	τ	=	2
$\rho_{\rm CME}$	=	10^{-18} kg m^{-3}	$T_{\rm CME}$	=	0.8 MK

Solar Wind properties for synthetic case					
CR2165			CR2238		
$v_{\rm in}$	=	500	$v_{\rm in}$	=	450
$P_{\rm in}$	=	6.0 nPa	$P_{\rm in}$	=	6.0 nPa
$\rho_{\rm fsw}$	=	200	$\rho_{\rm fsw}$	=	200

Note: ($\theta_{\rm CME}$, $\phi_{\rm CME}$) - CME center coordinates; $\varphi_{\rm hw}$ - angular half-width; $\varphi_{\rm hh}$ - angular half-height; γ - tilt angle; $\rho_{\rm CME}$ - mass density; n - flattening; $\varphi_{\rm p}$ - pancaking; $\varphi_{\rm s}$ - skew; $\phi_{\rm B}$ - magnetic flux; τ - twist; $T_{\rm CME}$ - temperature; $v_{\rm in}$ and $P_{\rm in}$ - SW speed and pressure at 0.1 AU; $\rho_{\rm fsw}$ - SW number density corresponding to 650 km s^{-1} SW stream.

can be seen in (a2) subplot of Figure 4.5 (marked with white arrow) for CR2165 which corresponds to 10:23 UT 02 July 2015. And similarly, 12:16 UT 20 November 2020 was the CME injection time for CR2238.

Figure 4.5 shows the SW simulation results of real and synthetic cases for CR2165. The figure demonstrates the fundamental differences between the real case (subplots a1, a2 and a3) and synthetic case (subplots b1, b2 and b3) in the equatorial plane. In the synthetic case, the SW speed is almost constant everywhere and hence there's no formation of HSS and SIR/CIR structures. Just like the speed, the scaled density is also relatively uniform in longitudinal direction as compared to the real case. And the magnetic field subplot displays a simple magnetic dipole configuration, whereas for the real case it is more complex due to interaction among solar wind streams of differing characteristics. The spiral features visible in synthetic case subplots (b1) and (b2) are corresponding to the polarity inversion line in (b3). Due to very low

magnetic field strength in those regions, the SW density is lower and hence, speed is slightly higher.

4.3.2 CME structure identification

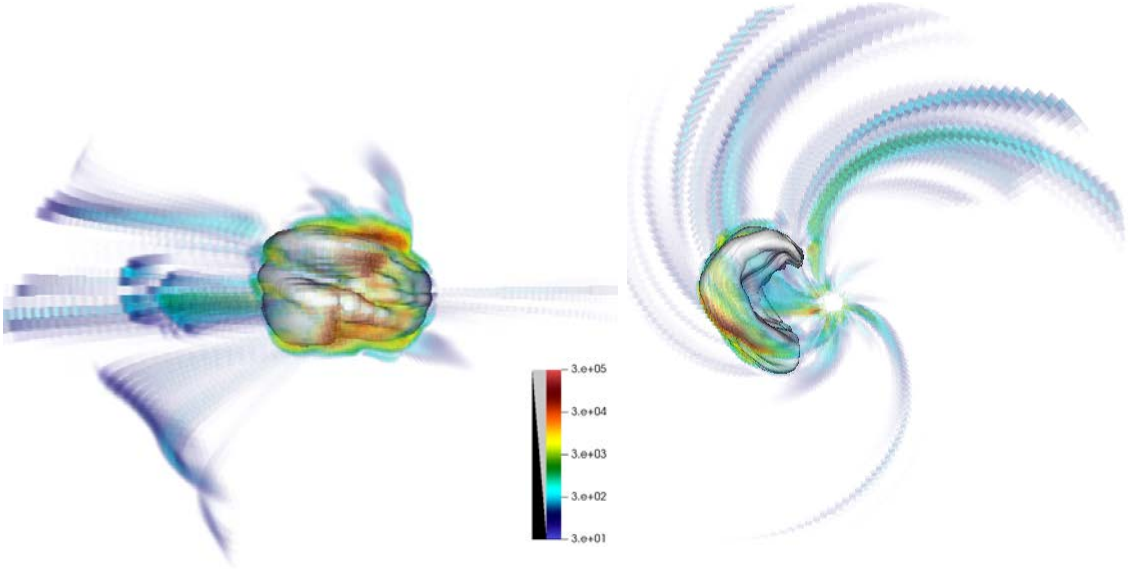

Figure 4.6: Figure demonstrates the tracing of the three-dimensional structure of a CME (denoted by white) in the heliosphere. This volumetric plot showcases the changes in dynamic pressure of the solar wind (denoted by colorbar) caused by the propagation of the CME. The left subplot displays the deformation of the CME front resulting from the interaction with a SIR.

It is expected that structure of CME can be deformed during its propagation in the structured solar wind. Exploration of the heliospheric imagers observations have provided observational evidence that such deformation in CME is significant during its interaction with with SIRs and other preceding CMEs [Heinemann et al., 2019; Liu et al., 2012; Mishra et al., 2014b]. The preceding structures in the background solar wind play a role of density/field obstacles and also cause a steep gradient in the solar wind speed for the following CME. The effect can be more pronounced at large distances from the Sun where the momentum of interacting structures dominates the magnetic force. To identify and track the evolution of whole CME structure

in our simulations, we have adopted a method of tracer. This CME tracer ($\mathcal{T}_r$) is a standard passive scalar that follows a simple advection equation and does not engage in any kind of interaction with any other physical quantities. It is initialized at the time of CME insertion with the value unity inside the CME structure and null elsewhere in the computational domain. This passive scalar can be visualized as a 'color' associated with the CME that follows with its bulk motion and as the CME mixes with the ambient solar wind, the value of this 'color' fades. In this work, the $\mathcal{T}_r$ lower limit to define the CME structure is set to 0.1 and following is the conservative form of the equation that governs it:

$$\frac{\partial(\rho\mathcal{T}_r)}{\partial t} + \nabla\cdot(\mathbf{v}\rho\mathcal{T}_r) = 0 \tag{4.11}$$

Similar CME tracking method was also used by Biondo et al. [2021] to show that CME bubble remains intact even after interaction with multiple solar wind streams.

Figure 4.6 demonstrates the identification of the CME structure using the aforementioned scheme. The CME structure, represented in white color, is traced in the heliosphere, while the volumetric plot displays the ambient solar wind streams, with the color map indicating the dynamic pressure of the solar wind. To enhance visibility, the upper and lower limits of dynamic pressure ($\rho_{sw}v_{sw}^2/2$) have been adjusted to highlight relatively strong SIRs. The left subplot showcases the front view of CME propagation, while the right subplot presents a top view. It is worth emphasizing that the traced CME's front exhibits some deformities rather than being smooth. A better understanding of deviations in the structural front of a CME from its assumed rigid and designated shape due to gradient in the ambient medium properties can help improve its arrival time on Earth. Further analysis of such characteristics is discussed in detail in the subsequent sections.

4.4 CME-Solar Wind Interaction

In this section we present the results of the simulations described in section 4.3, discussing the interaction of CME with structured solar wind (SW) and its impact on the evolution of CME. We focus on investigating the changes in the morphological, dynamic, and physical characteristics of CMEs as they propagate through a non-uniform ambient SW and encounter SIRs.

4.4.1 Evolution of CME structure

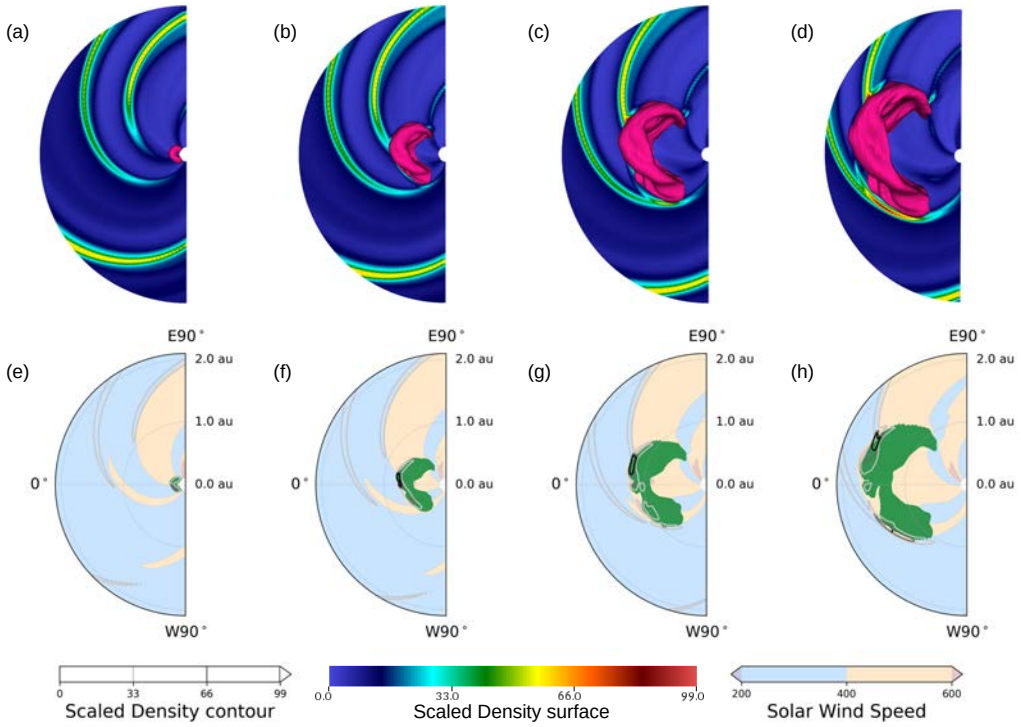

Figure 4.7: The evolution of real case CME in the heliosphere and its interaction with ambient solar wind of CR2165 is depicted in four time steps. Top row (a)-(d): represent the ecliptic plane, showcasing surface plot of the scaled density of the solar wind with the 3D CME (depicted in pink) propagating through it. Bottom row (e)-(f): display a 2D slice of the 3D CME structure (shown in green), along with the surface plot of the solar wind speed, and line contours represent the scaled density.

The interaction of CME with a SIR can result in observable change in the shape of the CME front making it deviate from the self-similar expansion and can also affect

the global trajectory of the CME [Winslow et al., 2021]. An overview of the CME propagation in the presence of HSS and SIR (*real case* of CR2165) is demonstrated in Figure 4.7, where the top row depicts the 3D evolution of the CME structure (pink) and the bottom row shows the 2D slice of same CME (green) in ecliptic plane. Each column represents different time snapshots of the CME evolution in the inner heliosphere. The subplots (a), (b), (c) and (d) have surface plot of scaled density in the background, whereas subplots (e), (f), (g) and (h) have contour plot of scaled density along with the speed of solar wind.

Deflection. Our simulation shows that during the initial stage of CME evolution, the movement of the CME in the $r-\phi$ plane is slightly directed towards the eastward direction, as evident from the Figure 4.7(f). The spiral structure of SW streams in the heliosphere, which propagates from the west to the east, can obstruct the westward motion of CME. This hindrance is more prominent when the CME encounters high-density SIRs. When the SIR is strong enough, it can impel the CME to follow the trajectory of the SIR, resulting in the CME's eastward movement, as illustrated in subplot (f). The extent of deflection experienced by a CME is expected to depend on the relative strength of the SIR and the CME. We could notice that for the real case of CR2165, the SIR was not strong enough to contain the CME for an extended period of time, and thus the deflection is primarily noticeable in the initial phase. Moreover, the interaction between the CME's eastward flank and the SIR has resulted in a coarser CME surface compared to the smoother westward flank, which did not come into contact with the SIR. This asymmetry in CME surface suggests that the interaction with the SIR can have a significant impact on the physical characteristics of the CME.

Expansion. In Figure 4.7, the CME injected into the simulation domain was subjected to faster solar wind streams on its westward flank and slower streams on the eastward flank. The difference in speed also led to a disparity in pressure

gradient and drag experienced by the two flanks of the CME due to the higher density and pressure of the slower streams. Consequently, the expansion rates of the westward and eastward flanks of the CME were significantly different. The westward flank of the CME has been observed to have over-expanded, whereas the eastward flank remained under-expanded due to direct contact with the SIR. This variation in the expansion rates along the CME structure will result in the change of density distribution of CME. In essence, speed variations in the ambient solar wind may introduce substantial changes to the density distribution of the CME.

Leading Edge. The presence of a strong SIR is primarily observed near the equatorial region, as slower or denser solar wind streams are often confined in that region [Gosling & Pizzo, 1999; Richardson, 2018]. As the CME starts propagating in the heliosphere, its sheath region typically displays the highest density, with a nearly symmetric distribution around the CME's axis of propagation. However, as the CME propagates further, it is possible that the flank of the sheath regions that come into contact with the SIR exhibit the highest density values. For instance, in subplots (e) and (f), the density is highest at the front of the CME, while having the CME at larger distance in subplot (h), the density is highest at the sides. Moreover, the regions with the higher density values tend to be slightly pushed behind by the surrounding ambient solar wind, as evident in the eastward flank of subplots (g) and (h). This lagging effect is attributed to the greater effective drag force experienced by these regions compared to other parts of the CME, causing them to be pushed rearward. Consequently, the CME's leading edge exhibits a non-uniform or non-circular shape due to the varying solar wind conditions and the dynamic drag force encountered along its front.

Table 4.3: The values and the range of power law followed by different CME parameters.

Parameters	CR2165		CR2238	
	Real	Synthetic	Real	Synthetic
$\alpha_{\rm th}$	$-2.30^{+0.54}_{-0.37}$	$-3.15^{+0.40}_{-0.36}$	$-2.50^{+0.23}_{-0.1}$	$-3.34^{+0.19}_{-0.34}$
$\alpha_{\rm mag}$	$-2.37^{+0.51}_{-0.24}$	$-2.76^{+0.18}_{-0.26}$	$-2.24^{+0.31}_{-0.28}$	$-2.81^{+0.23}_{-0.34}$
$\alpha_{\rm ram}$	$-2.09^{+0.26}_{-0.21}$	$-2.54^{+0.19}_{-0.15}$	$-2.03^{+0.26}_{-0.18}$	$-2.53^{+0.13}_{-0.19}$
$\alpha_{\rm v}$	$-0.1^{+0.03}_{-0.02}$	$-0.02^{+0.01}_{-0.01}$	$-0.06^{+0.01}_{-0.01}$	$-0.02^{+0.02}_{-0.02}$
α_{ρ}	$-1.88^{+0.21}_{-0.34}$	$-2.59^{+0.29}_{-0.14}$	$-1.92^{+0.18}_{-0.33}$	$-2.55^{+0.12}_{-0.20}$
$\alpha_{\rm T}$	$-0.46^{+0.36}_{-0.15}$	$-1.48^{+0.42}_{-0.31}$	$-0.59^{+0.13}_{-0.09}$	$-1.42^{+0.25}_{-0.55}$

4.4.2 Evolution of CME properties

In past, the evolution of CME has been investigated through observations [Janvier et al., 2019; Liu et al., 2005; Salman et al., 2020] as well as through simulations [Manchester et al., 2017; Scolini et al., 2021]. Typically, the variation of CME properties is investigated through a power law function of radial distance, with an anticipated decrease in the magnitude of CME properties over a certain range of exponent values. However, the influence of ambient solar wind conditions on the evolutionary behavior of CME properties is not yet well understood.

In order to investigate this impact on the evolution of CME properties, we compared the temporal variation of median values between real and synthetic cases using the function given below:

$$\log \tilde{Q}(t) \quad = \quad \alpha_q \cdot \log(t) + \quad \log(Q_0) \tag{4.12}$$

$$slope = \frac{\log \tilde{Q}_{i+1} - \log \tilde{Q}_i}{\log t_{i+1} - \log t_i} \tag{4.13}$$

where, $\tilde{Q}$(t) is the median of CME property Q, t is the time, Q_0 is the typical value of Q at 1.0 AU, α_q is the power law exponent for Q, i is the time step index. As

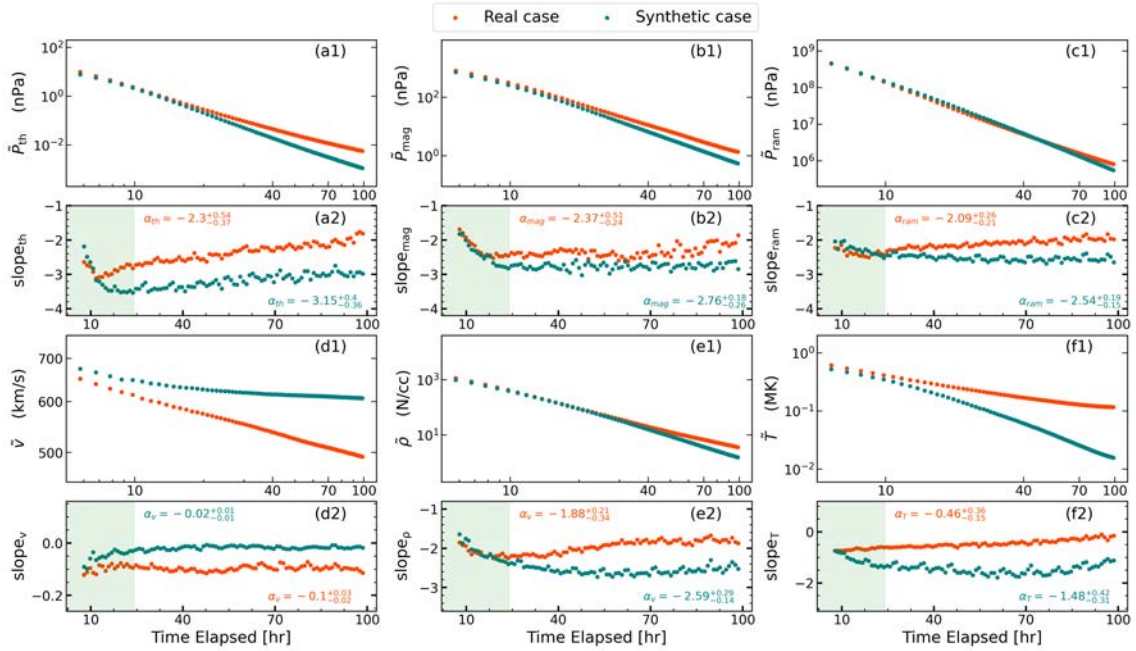

Figure 4.8: Temporal evolution of median of the CME properties for CR2165. The panels (a1) to (f1) represent the temporal profile of median of CME thermal pressure (a1), magnetic pressure (b1), ram pressure (c1), speed (d1), density (e1), and temperature (f1) in log-log scale. In the subplots (a2) to (f2), just below the panels showing variations in the median of CME properties, the change in the gradient of these CME properties in log-log scale at different time steps are shown (see Equation 4.13). The shaded region in slope subplots are corresponding to the initial settling phase of the CME, which has been taken to be 24 hours.

mentioned in last subsection, the location of the CME nose changes continuously as it propagates through the heliosphere, indicating that the rate of change of radial distance is not constant, but rather fluctuating. Additionally, since real and synthetic CMEs have different propagation speeds in the heliosphere, their radial distance profiles will also differ. Therefore, to ensure a fair comparison between the two cases, we opted to fit a power law function of time. While most studies have used mean values with respect to radial distance, for this investigation, examining the time evolution of median values is more appropriate. Scolini et al. [2021] and Janvier et al. [2019] have also emphasised the suitability of using the median to

examine the evolution in their respective studies.

Figure 4.8 displays the outcomes of the real and synthetic cases for CR2165. To have a robust comparison, the slope between two points of the evolution plot in a log-log scale was calculated using equation 4.13. Subsequently, a straight line parallel to X-axis was fitted to the gradient plot to analyze the power law behavior. To prevent any bias in the fitting process, we performed it after the initial settling phase of the CME, as including the points immediately after the CME injection could have affected the fitting results. We considered a settlement time of 24 hours for this purpose. Table 2 reports the range of α_q for both CRs which we got after fitting the slope plots and we found that our results were consistent with the values reported by Liu et al. [2005], Salman et al. [2020] and Scolini et al. [2021].

Pressures. The median values of thermal and magnetic pressure decreases with heliospheric distance for both real and synthetic cases of CR2165 and CR2238. For CR2165 (CR2238), the synthetic case CME was found to show more decrement. The fall of magnetic pressure in the synthetic CME followed a power law of $\alpha_{\rm mag}$ = -2.76 (-2.81), while thermal pressure followed $\alpha_{\rm th}$ = -3.15 (-3.34). For real CME, we noticed that the nature of fall of pressures are almost the same as for synthetic case, but with different values: $\alpha_{\rm mag}$ = -2.37 (-2.24) and $\alpha_{\rm th}$ = -2.3 (-2.5). The similarity in the slope variation between the real and synthetic cases, although with different α values, implies that the ambient solar wind condition does indeed significantly impact the evolution of CME pressures. However, this difference mainly manifests during the early stage of CME propagation, and its impact remains consistent over time. Moreover, the larger difference in $\alpha_{\rm th}$ suggests that the interaction has a greater impact on the thermal pressure as compared to the magnetic pressure of CME.

Speed. The median of CME speed in CR2165 (CR2238) slightly decreases with time with a slope of $\alpha_{\rm v}$ = -0.02 (-0.02) for synthetic case and $\alpha_{\rm v}$ = -0.1 (-0.06) for real

case CME. Unlike all other CME properties, the speed of CMEs in the both CR2165 and CR2238 exhibits a more prominent decline in the real case as compared to the synthetic case. This can be attributed to the increased amount of drag experienced by the real case CMEs, which is a consequence of their interaction with the non-uniform ambient SW. Additionally, it is worth noting that the fall in speed of CME in CR2165 is more pronounced due to the presence of stronger SIRs in the path of the CME compared to that in CR2238. The increased interaction between the CME and the denser SIRs in CR2165 leads to a more significant deceleration effect, resulting in a steeper fall in speed compared to the CME in CR2238. Additionally, the synthetic CME seems to achieve a terminal speed at the end of the plot, i.e., after 100 hours of propagation in inner-heliosphere.

Density. The CME median proton density falls with α_ρ = -2.59 (-2.55) for synthetic case and α_ρ = -1.88 (-1.92) for real case of CR2165 (CR2238). In addition to the different α_ρ values, the real and synthetic case CMEs also exhibit distinct patterns of slope variation in both CRs. This suggests that the ambient SW conditions have a continuing and accumulating impact on the density distribution as CME propagates through the inner-heliosphere. The over-expansion of one flank of CME could lead to such result, which was shown in the Section 4.4.1. Moreover, the fall of median ram pressure (ρv^2) also showed similar trend with $\alpha_{\rm ram}$ = -2.54 (-2.53) for synthetic case and $\alpha_{\rm ram}$ = -2.09 (-2.03) for real case.

Temperature. We note that for CR2165 (CR2238), the median value of CME temperature decreases with time for real case with $\alpha_{\rm T}$ = -0.46 (-0.59), and synthetic case with $\alpha_{\rm T}$ = -1.48 (-1.42). The greater decrease in temperature (panel f1) is also associated with the lower decline in speed (panel d1) and can be attributed to the absence of SIRs and HSS in the uniform ambient through which the synthetic case CMEs propagate. As a result, the retarding force acting on the CME is weaker, allowing for more expansion and subsequent cooling compared to the real

case CMEs. The disparity in the slope variation (α_T) between the real and synthetic cases suggests that the presence of higher density SIRs in the real case CMEs leads to compression, hindering the expansion and cooling process. This highlights that structured background solar wind with larger spatial gradient in density at different distances from the Sun plays an important role in the thermodynamic evolution of CMEs.

4.4.3 CME Volume evolution

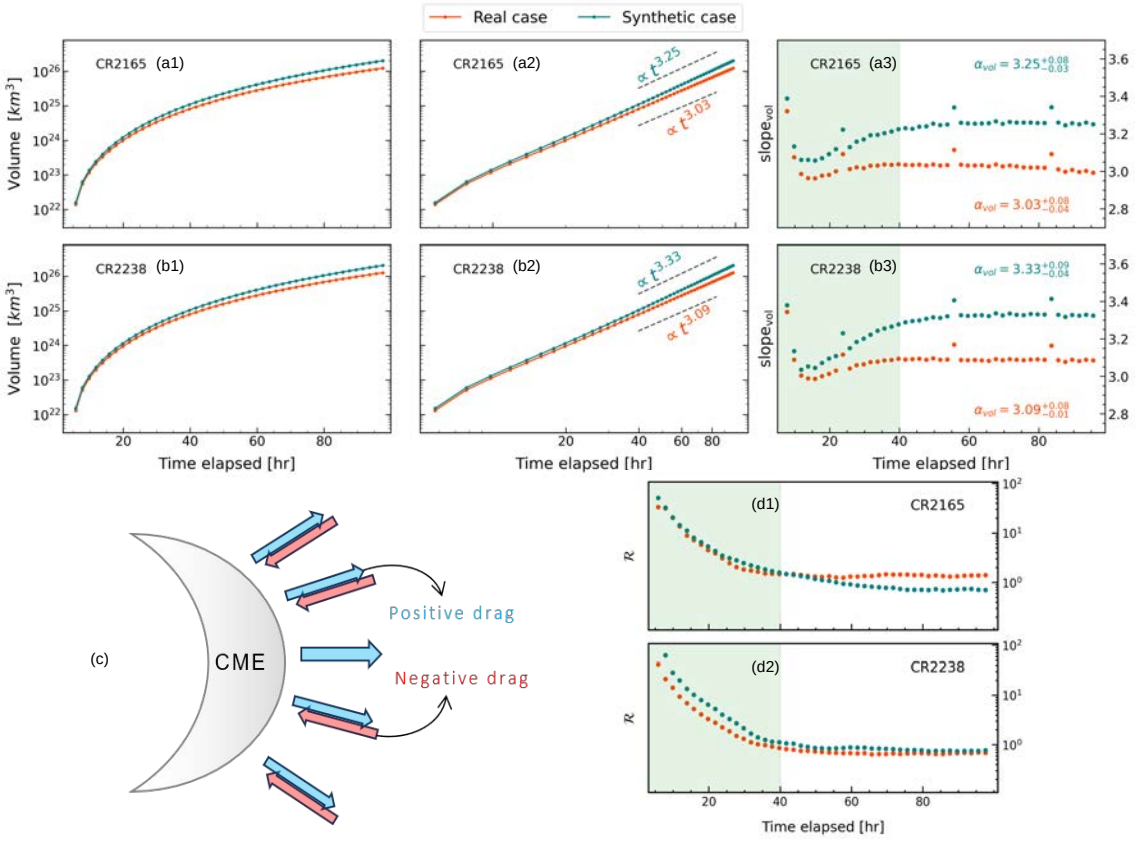

Figure 4.9: The temporal evolution of the total volume of the CME is presented for both the synthetic and real cases of CR2165 (a1, a2 and a3) and CR2238 (b1, b2 and b3). A rough sketch of negative and positive drag has been shown in subplot (c). And the evolution of the ratio of area on which positive and negative drag forces act is shown in the (d1) and (d2).

The evolution of CME volume and its dependence on ambient SW conditions have not been thoroughly investigated in the past. The major challenge in such study, observational or numerical, is the absolute isolation of 3D CME structure from the background medium, specially at large distances from the Sun. In this regard, Majumdar et al. [2022] utilized the GCS model with observations from space and ground-based coronagraphs to study the 3D evolution of CME. However, their work focused on the total volume evolution of CME in the inner corona. In the inner-heliosphere, the density of CMEs is not high enough for unambiguous tracing through remote sensing observations, and thus a self-similar expansion is typically assumed to study the CME volume evolution. Previous studies, such as Holzknecht et al. [2019] and Temmer et al. [2021], employed the GCS fitting and assumed self-similar expansion to investigate CME evolution.

In this work, we employed the structure identification technique detailed in Section 4.3.2 to examine the temporal evolution of total volume of CME and compare the real and synthetic cases to analyze the impact of ambient SW condition. Figure 4.9 demonstrates the time evolution of CME volume for both real and synthetic cases, propagating in the ambient SW of CR2165, which occurred near solar maxima and CR2238, which was near solar minima. The computed values of total volume of CMEs are consistent with the values reported by Holzknecht et al. [2019]. The rate of increase in the total volume of the synthetic case CME is found to be greater than that of the real case CME for both CRs. And as the time progresses, the disparity between the volume evolution of real and synthetic CMEs continues to grow until approximately 40 hours, after which it reaches a near-constant value, following a strict power law. From Figure 4.9 subplot (a3) and (b3) it is evident that in the initial phase (<40 hours), the synthetic case CMEs exhibit a higher expansion rate compared to the real case CMEs. This discrepancy can be attributed to the presence of high density SIRs in the real case CMEs, which result in a greater accumulation

of solar wind at the leading edge of the CME and the formation of a denser sheath region. This accumulation of sheath plasma could impede the expansion of the CME, leading to a slower increase in volume compared to the synthetic case CMEs.

After the initial phase (>40 hours), the rate of increase in volume becomes nearly constant, the total volume of CME rises with $\alpha_{\rm vol} = 3.25$ (3.32) for synthetic case and $\alpha_{\rm vol} = 3.03$ (3.09) for real case of CR2165 (CR2238). It is worth noting that the strength of the SIR in CR2165 was greater than that in CR2238, and the $\alpha_{\rm vol}$ value for the CR2165 real case was lower than that in CR2238. As previously noted, synthetic case CMEs tend to have higher $\alpha_{\rm vol}$ values due to the absence of SIR. Consequently, CMEs that interact with weaker ambient conditions are more likely to have higher $\alpha_{\rm vol}$ values as well.

From our analysis, we can conclude that the temporal evolution of total volume of CME follows a power law beyond a certain propagation time or heliocentric distance from the Sun. We find that all the CMEs, real and synthetic in both CR, were having the power law exponent between 3.03 and 3.32 depending on the state of the background SW. For stronger ambient (presence of SIRs and high anisotropic medium), the exponent's value is smaller while its value is larger for weaker state of the heliosphere. In other words, if a CME is propagating through a dense non-uniform ambient, its total volume will be lesser compared to when it is propagating through a relatively tenuous and uniform ambient.

To identify the underlying factor leading to the power law behavior over time, we examined the drag force acting on the CME's surface. Depending on the specific location and instance, either the CME front pushes solar wind (positive drag) or experiences a pull (negative drag) by the ambient solar wind. By considering the effective areas associated with positive and negative drag forces, we introduced a ratio denoted as $\mathcal{R}$, which represents the number of grid points corresponding to positive and negative drag forces.

The temporal evolution of $\mathcal{R}$ exhibits a similar pattern to that of the volume evolution, characterized by two distinct phases and an asymptotic behavior after approximately 40 hours of propagation. The constant value of $\mathcal{R}$ indicates that the areas of positive and negative drag forces have reached a balanced state. It is important to note that the volume expansion of CMEs in this context is not self-similar. Instead, it is a dynamic process in which any changes are offset by compensating changes, resulting in an overall steady expansion rate. Additionally, as shown in Figure 9, the real case CMEs have achieved asymptotic behavior (in volume and $\mathcal{R}$ subplots) earlier than the ideal case CMEs. This indicates that higher the non-uniformity in the ambient SW, earlier the CME will achieve its steady state with surroundings.

Based on the above findings, we can conclude that the volume of a CME achieves a non-fractal power law state in relation to its surrounding environment after a specific duration of propagation in the inner heliosphere. The duration required to reach this state depends on the prevailing conditions of the ambient solar wind. Specifically, an isolated CME may attain the power law state in a shorter duration during the solar maxima phase, characterized by greater non-uniformity compared to the solar minima phase. These findings provide valuable insights into the intricate dynamics of CMEs and their interactions with the ambient solar wind. They emphasize the significant role played by drag forces in shaping the evolution of CME volume. In the subsequent section, we thoroughly explore the nature and magnitude of the drag force acting on CME.

4.4.4 Drag force analysis

The deceleration of faster CMEs and the acceleration of slower CMEs during their propagation in the inner heliosphere are widely acknowledged phenomena [Gosling & Riley, 1996; Lindsay et al., 1999; Manoharan, 2006]. Beyond a distance of 15 $R_{\odot}$, the dominant force governing CME dynamics is the aerodynamic drag force due to

momentum exchange between CMEs and surrounding solar wind [Kay & Nieves-Chinchilla, 2021; Sachdeva et al., 2015; Vršnak et al., 2008]. Consequently, several drag-based investigations have been conducted to study the dynamics of CMEs and their arrival time at the Earth [Dumbović et al., 2021; Mishra & Srivastava, 2013; Napoletano et al., 2018]. While some research has focused on estimating the structural deformation of the CME front caused by drag, the nature of drag-force variation on the CME front remains unclear. In this study, using the SWASTi-CME model, we attempt to understand the evolution of this force on the CME front and its impact on CME deformation.

In this work, the drag-force ($\mathcal{F}_{\rm drag}$) between CME front and SW has been defined as:

$$\mathcal{F}_{\rm drag} = \frac{1}{2}\, C_d\, A\, \rho_{\rm sw}\, |v_{\rm CME} - v_{\rm sw}|(v_{\rm CME} - v_{\rm sw}) \tag{4.14}$$

where, C_d is dimensionless drag-coefficient, A is the area of contact between CME front and SW, $\rho_{\rm sw}$ is density of the ambient solar wind, $v_{\rm CME}$ and $v_{\rm sw}$ are velocity of CME and ambient SW, respectively [Sachdeva et al., 2015; Vršnak et al., 2013]. A positive value of $\mathcal{F}_{\rm drag}$ indicates that the CME is pushing the ambient medium, while a negative drag implies that the ambient medium is pulling CME because of speed difference. The coefficient C_d represents the level of interaction strength between the CME and the ambient medium, typically assumed to be of the order of unity. In this study, we have made the assumption that the drag coefficient remains constant at different heliocentric distances and set its value to one. The motivation is to explore the influence of density and relative velocity on the temporal evolution of the drag force acting on the CME.

The drag force on the CME front was calculated using Equation 4.14. To identify the entire CME front, we employed the CME isolation technique described in Section 4.3.2. Subsequently, we examined the temporal evolution and distribution of the computed drag force. Figure 4.10 illustrates the evolution of the drag force and its

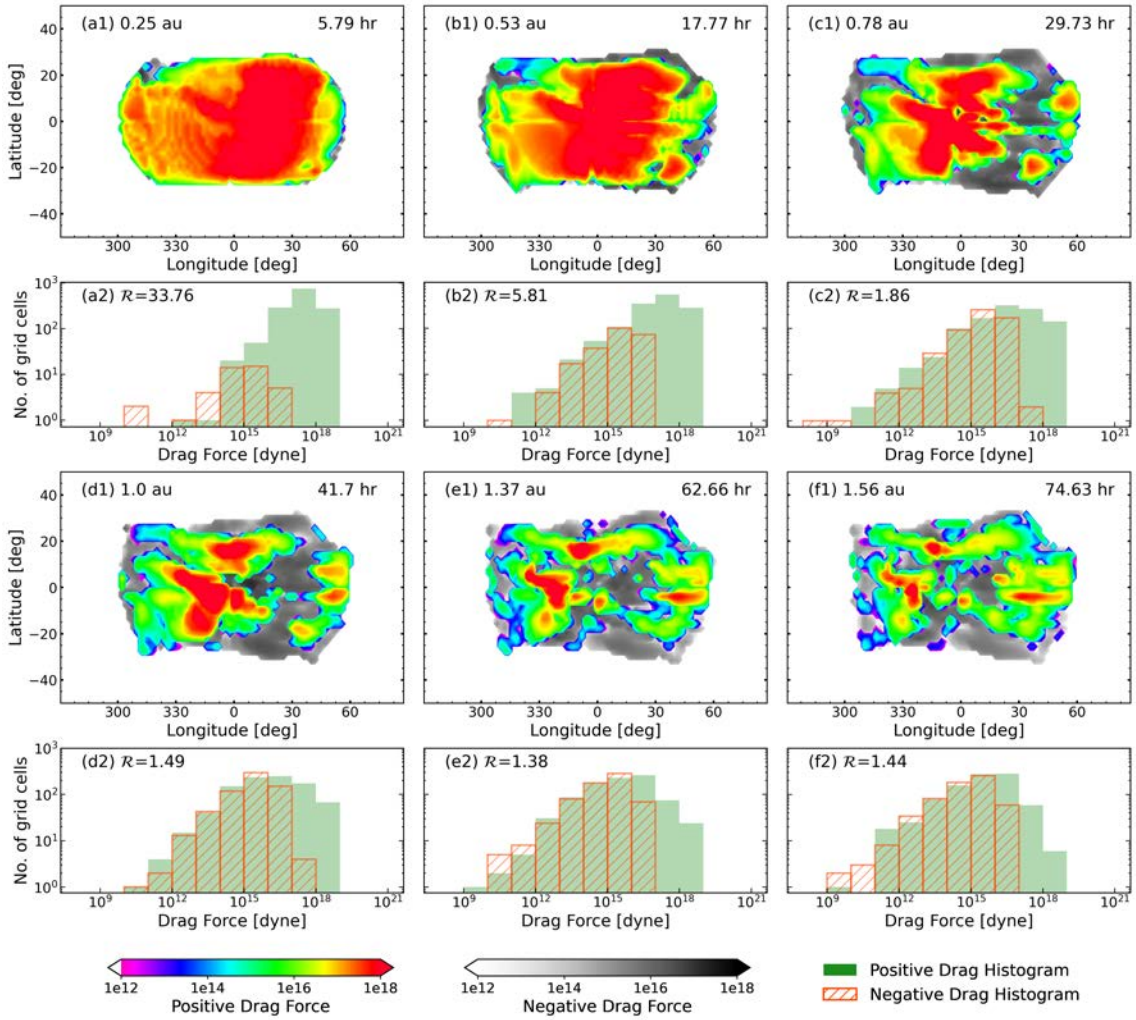

Figure 4.10: Figure showcases the drag force acting on the CME front due to anisotropic ambient conditions. Subplots (a1)-(f1) depicts the evolution of the drag force pattern on the front of real case CME of CR2165 as it advances in the heliosphere. The positive drag has been displayed using color map while, negative drag is in gray scale. Subplots (a2)-(f2) displays the histogram of magnitude of drag force corresponding to (a1)-(f1) subplots.

distribution on the CME front. In subplot 4.10(a1), the CME starts interacting with the ambient SW. We noticed that at a distance of 0.25 AU, the first SIR intercepts the CME's trajectory, leaving its structure imprinted in the drag force profile on the CME front. Furthermore, ripple-like structures are observed on the left side

in subplot 4.10 (a1), indicating the ploughing effect on the SW as the CME exerts drag force on the denser SIR. This implies that near the CME-SIR interaction region, the ambient SW exhibits negative meridional velocity, suggesting a counterflow of some SW plasma against the overall flow. As the CME progresses radially in the inner heliosphere, the negative drag becomes increasingly significant. Regions on the CME front where negative drag is observed indicate that the solar wind speed in those regions exceeds that of the CME. In other words, the presence of negative drag in that region causes the CME to undergo deformation and be pulled forward in relation to the other regions of the CME front. Furthermore, the imprint pattern resulting from the interaction with the SIR is observed to gradually diminish and shift towards the left. This observation aligns with the findings depicted in the subplots of Figure 4.7, where the densest region formed in front of the leading edge is observed to shift eastward over time. And also the regions exhibiting negative drag force correspond to the deformation of the leading edge as illustrated in Figure 4.7.

The presence of negative drag is predominantly observed on the eastward flank of the CME, while it is less pronounced on the westward flank. Initially, due to the higher ram pressure of the CME compared to the ambient solar wind, the CME was able to plow through the ambient medium and the first SIR without significant deformation. However, as the CME progresses and interacts with the second SIR, its effective ram pressure has significantly reduced due to earlier propagation, expansion, and drag. This reduction in ram pressure allows the SIR drag force to become negative, resulting in the deformation of the CME front. The decrease in ram pressure can be observed in Figure 4.8 (c1), where it follows a power law with an exponent of -2.09. This indicates that the deformation of the CME front due to the drag force increases with time and radial distance, illustrating the progressive nature of the deformation process.

The histogram subplots presented in Figure 4.10 illustrate the distribution of positive and negative drag forces acting on the CME front. Both positive and negative drag forces display a left-skewed normal distribution, where the median is greater than the mean. Initially, the distribution of positive drag force exhibits high skewness, which gradually decreases as the CME evolves in the heliosphere. This indicates that the area associated with positive drag decreases over time, leading to a reduction in the skewness of its distribution.

On the other hand, the distribution of negative drag force starts with low skewness but becomes more skewed as time passes. It is interesting to note that the area associated with negative drag expands rapidly and eventually reaches a point, at roughly 40 hours, where the ratio of the positive and negative drag areas ($\mathcal{R}$) becomes constant. In Figure 4.10, the magnitude and the distribution of grid points for both negative and positive drag forces almost coincide in the d2, e2, and f2 histogram plots. This indicates that not only have their effective areas reached a balanced state with each other, but their magnitudes have also stabilized. This indicates that the CME and the SW achieves a balanced state after approximately 40 hours of propagation.This potentially explains the observed power law expansion of CMEs discussed in the previous section.

Conclusively, the dynamic interaction between CME and SW leads to inter-play between positive and negative drag forces, which in turn, results in the localized deformation of CME front. This deformation is highly dependent on the presence of SIR and its 3D structure. While both forces reach a balanced state over time, the combined drag force decreases but remains positive throughout the simulation of the undertaken cases. Therefore, the nature of drag force directly affects the morphology and kinematics of CME in the inner-heliosphere and indirectly affects the distribution of CME's thermodynamic properties and time of arrival.

4.5 Summary and Discussion

In this work, we presented the newly developed MHD-based CME model, SWASTi-CME. It incorporates two distinct representations of CMEs: the elliptic cone model and the flux rope model. The elliptic cone model portrays a non-magnetic cloud with a simplified geometric shape. In addition to considering the angular width, this model also includes the angular height, leading to a better representation of the CME structure. On the other hand, the flux rope model allows for the inclusion of all the major deformities of the CME structure in the corona. The description of the initiation mechanisms for the cone and flux rope models into the MHD domain at 0.1 AU is also provided. Once the initial properties of the CMEs are defined, they undergo propagation in conjunction with the ambient solar wind generated by the SWASTi-SW module [Mayank et al., 2022].

Using SWASTi-CME, we conducted a simulation case study for CR2165, corresponding to solar maxima and consisting of five CMEs, and CR2238, corresponding to solar minima and consisting of one CME. Within this case study, the SWASTi results were also compared with the OMNI observational data at the Sun-Earth L1 point. The evaluation demonstrates that the results achieved for the flux rope CMEs exhibit favorable agreement with the observations for both scenarios: multiple (CR2165) and single (CR2238) CME events. However, while the cone CMEs yield satisfactory results for CR2238, their performance is comparatively less impressive for CR2165. This discrepancy in results for CR2165 can be attributed to the assumption of homogeneous speed and the absence of tilt in the CME axis, as well as the simpler insertion technique in the cone model. One way to enhance the accuracy of the cone CME results would be to take a distribution of CME speed as compared to a homogeneous value along the CME structure and consider the tilt angle. Additionally, improving the insertion mechanism beyond the one described in equation 4.4 may further improve the results.

In addition to the CME results, the simulated properties of the ambient solar wind also demonstrated a good agreement with the observations. It is worth noting that beyond 0.3 AU, the CME transitions into an incoherent MHD structure [Owens et al., 2017a], highlighting the significance of accurately reconstructing both the ambient solar wind and the CME for a comprehensive assessment of CME dynamics. Considering the favorable performance of the flux rope CME and the ambient solar wind in comparison to the observations, it is reasonable to conclude that the SWASTi-CME model can be effectively utilized to investigate the interaction between a CME and ambient solar wind.

With the objective to investigate the influence of ambient solar wind conditions on CME evolution, we presented a setup of two cases: the *real* case and the *synthetic* case. The degree of uniformity in solar wind conditions is very high in synthetic case whereas, real case is the data-driven simulated background i.e., default run of SWASTi-CME. Both cases are described in detail in Section 4.3, including the CME tracing technique employed to isolate the complete 3D structure of the CME from the ambient solar wind. Using this setup of two cases, we presented an analysis on the impact of non-uniformity in the ambient solar wind conditions on CMEs during the CR2165 (near solar maxima) and CR2238 (near solar minima) periods, particularly focusing on HSSs and SIRs. This analysis of the interaction between the CME and solar wind has yielded several findings, which are discussed as follows:

- *Morphology*: An initial eastward movement of the CME was observed, indicating a deflection caused by the obstructive effect of spiral-shaped ambient solar wind streams propagating from west to east. The trajectory of the CME can be further influenced by the presence of high-density SIRs, resulting in a deflection along the streamline of the SIR and causing an eastward deviation. Furthermore, on investigating the expansion of CMEs, we noticed distinct behaviors between the CME flank within a HSS and the flank interacting with the SIR. The former underwent

over-expansion, while the latter remained under-expanded. These variations in expansion rates have the potential to induce changes in the density distribution of the CMEs. Additionally, the spatial variation in density, which is correlated with the solar wind speed and, consequently, the drag force, along the leading edges of the CMEs contributes to their deformation. Notably, in the presence of SIRs, characterized by denser regions with significant speed variations, this phenomenon becomes more pronounced. As a result of the diverse drag forces experienced by different regions of the CME front, some regions undergo radial displacement, being pushed rearward, while others experience slight advancement due to over-expansion.

- *Internal pressure*: The analysis of temporal evolution reveals notable trends in CME pressure distribution, including thermal and magnetic pressure. The findings indicate that an uniform background (synthetic case) leads to a more pronounced decline in CME pressure compared to a non-uniform background (real case). This suggests that higher anisotropy in the solar wind leads to higher pressure within the CME at 1 AU. Moreover, this disparity is particularly prominent during the early stages of CME propagation, specifically within the first 24 hours after crossing 21.5 $R_{\odot}$. Subsequently, the thermal pressure follows a power law decay (though not strictly) with a slope of -2.30$^{+0.54}_{-0.37}$ (-2.50$^{+0.23}_{-0.1}$), while the magnetic pressure demonstrates a similar power law decay with a slope of -2.37$^{+0.51}_{-0.24}$ (-2.24$^{+0.31}_{-0.28}$) for real case of CR2165 (CR2238). These findings provide valuable insights into the influence of anisotropy in the ambient solar wind on the pressure dynamics within CMEs.

- *Internal speed*: The distribution of CME speed displayed a gradual decrease over time. In the synthetic case, representing an isotropic background, the power law exponent was -0.02$^{+0.01}_{-0.01}$ (-0.02$^{+0.02}_{-0.02}$), while in the real case, representing an anisotropic background, of CR2165 (CR2238), the power law exponent was -0.1$^{+0.03}_{-0.02}$ (-0.06$^{+0.01}_{-0.01}$). Notably, the median speed of both CR2165 and CR2238 CMEs showed a more pronounced decline in the anisotropic solar wind conditions compared to the isotropic

conditions, which can be attributed to increased drag resulting from their interaction with the ambient solar wind. Furthermore, the speed reduction is more significant in CR2165 due to the presence of stronger SIRs along its path, leading to a more substantial deceleration effect. These findings emphasize the influence of solar wind anisotropy on CME dynamics, highlighting the role of SIRs and drag force in shaping CME speed profiles.

- *Internal density and temperature*: While both the real and synthetic case CMEs experience a decrease in median proton density over time, they display distinct patterns in the temporal evolution of the power law exponent observed for CR2165 and CR2238. This highlights the influence of ambient solar wind conditions on the distribution of CME density throughout their propagation in the simulation domain. Furthermore, the temperature of CMEs gradually decreases, with the CME in an isotropic solar wind demonstrating a significantly higher rate of decrement. The difference in the temporal evolution of the power law exponent between the anisotropic and isotropic backgrounds indicates that the cooling process may encounter hindrance due to the interaction with the ambient solar wind. This hindrance can be attributed to the CME encountering higher-density SIRs, leading to compression and inhibition of the CME's expansion and cooling process.

- *Total Volume*: The analysis of the temporal evolution of the total volume of CMEs revealed that CMEs expand at a greater rate in conditions of higher isotropy in the ambient solar wind. The presence of high-density SIRs in the real case CMEs led to the formation of a denser sheath region at the leading edge, impeding their expansion and resulting in a slower increase in volume compared to the synthetic case CMEs. This difference in expansion rates between the isotropic and anisotropic backgrounds increased over time until approximately 40 hours since entering the MHD domain. After this time, the expansion rates reached a near-constant value, following a strict power law with different exponents. Similar, two phase expansion of CME was also

observed by Scolini et al. [2022]. The real case CMEs exhibited exponent values of 3.03 for CR2165, which had stronger SIRs, and 3.09 for CR2238, which had weaker SIRs. The stronger ambient conditions, i.e. the presence of SIRs and highly anisotropic medium, resulted in lower power law exponents and consequently smaller total volumes.

Though the results indicate that total volume varies roughly in proportion to the cube of time, the expansion is not self-similar in the heliosphere. Previous studies have suggested that most CMEs tend to expand approximately self-similarly in the corona [Subramanian et al., 2014; Vourlidas et al., 2010]. However, a recent study by Braga et al. [2022], based on WISPR observations, demonstrated that while CMEs expand self-similarly in the corona, they start deforming at 0.1 AU due to the non-uniformity of solar wind speed. Similarly, findings from our simulation also align with this argument, showing that the deformation of the CME deviates its structure from self-similar expansion.

- *Drag Force*: The investigation into the temporal evolution and distribution of the drag force acting on the CME front revealed interesting findings. The interaction between the CME and SIR resulted in the imprinting of the SIR's structure on the CME front, leading to higher drag force values on CME font. The presence of ripple-like structures indicated the dominant ploughing effect during the initial hours of CME-SW interaction. Furthermore, the anisotropic nature of the ambient solar wind conditions resulted in an uneven distribution of drag force on the CME front, with some regions experiencing positive force while others experienced negative force. This resulted in an asymmetric deformation of the CME's leading edge. The distribution of drag force exhibited a left-skewed normal distribution for both negative and positive values. Although the negative drag force grew rapidly as the CME evolved in the heliosphere, it consistently remained approximately 10 times smaller than the positive drag force, resulting in a decelerating forward motion of

the CME.

In summary, our study has primarily focused on investigating the structural and thermodynamic effects of the ambient solar wind on CMEs in the heliosphere. It is important to emphasize that such changes in CME properties can also arise from interactions with other CMEs. The adopted distribution of magnetic field within the FRi3D model in the CME has been validated with in-situ signatures of CME. However, a comparison with the other common models like Lundquist [Lundquist, 1950] and Gold and Hoyle [Gold & Hoyle, 1960] would be a natural future step. Moreover, employing a cylindrical geometry to populate curved flux rope may lead to imbalance between positive and negative flux. A curved magnetic flux rope model, such as proposed by Singh et al. [2022] in which they used the toroidal flux model of Vandas & Romashets [2017], could address this issue. Interestingly, a recent investigation carried out by Davies et al. [2022] has demonstrated a decreasing orientation of the flux rope over time as the CME propagates. These intriguing aspects will be the central focus of our future endeavors, as we plan to conduct a dedicated analysis on the magnetic field profile of the flux rope and explore the interactions between multiple CMEs using the SWASTi-CME model.

Chapter 5

Solar Flare Prediction and Feature Selection

This chapter is structured based on the paper titled "Solar Flare Prediction and Feature Selection using Light Gradient Boosting Machine Algorithm" by P A Vysakh and Prateek Mayank [Vysakh & Mayank, 2023].

5.1 Data Collection and Preparation

5.1.1 SHARP HMI active region parameters

For our model, the dataset we adopted was the Space-weather HMI Active Region Patches [SHARP, Bobra et al., 2014]) data provided by SDO HMI (Solar Dynamics Observatory: Helioseismic and Magnetic Imager). In 2014, the SHARP data series was released, which includes maps in patches that cover automatically tracked magnetic concentrations throughout their lifetime [Bobra et al., 2014]. These patches identify the active regions (ARs) automatically and continuously calculate various summary parameters of ARs at a 12-minute cadence. We collected a total of 25 AR summary parameters provided by the SHARP module. The selection of the 25

parameters was based on the previous work done in Bobra et al. [2014]. The list of initially considered parameters characterises several features of solar active regions that have been linked to increased flare activity. These parameters include different types of indices, such as the total magnetic flux, the spatial field gradients, the vertical current density characteristics, current helicity, and a proxy for integrated free magnetic energy [Bobra et al., 2014]. Table 5.1 presents the initial list of parameters along with their corresponding equations and a brief description. These parameters are consistent with those used in Bobra et al. [2014]. We used SunPy python module [Community et al., 2015] to collect SHARP data using JSOC client. The data products used were *hmi.sharp.720s* and *cgem.lorentz*. The subsequent data series, as described in Sun [2019], estimates the Lorentz force in ARs based on vector magnetogram patches from the HMI. Both the SHARP and HMI data series were collected at a cadence of 1 hour.

5.1.2 GOES Flaring data

To define the training samples for the machine learning model, we searched for flares that occurred between January 2012 and December 2020. This time range extends the whole range in which the SHARP HMI data is available. We used SunPy module to collect flaring events from the Geostationary Operational Environmental Satellite (GOES) Xray Flux Catalog maintained by the National Centers for Environmental Information. In order to create the final dataset, each active region was uniquely identified by its NOAA AR number. This identifier facilitated the cross-matching of GOES data with HMI SHARP data. Specifically, for every event listed in the GOES catalogue, all observations corresponding to the same NOAA AR number were extracted from the HMI SHARP dataset. From this subset of observations, the one closest in time to the occurrence of the solar flare was designated as a positive event. This process was repeated for each flare within the GOES catalogue, thereby culminating in the formation of the comprehensive final dataset. It is important

to acknowledge that a small subset of events documented in the GOES catalogue was not present in the HMI SHARP catalog. Consequently, these observations were omitted during the assembly of the final dataset. After filtering out the samples without any observations in the HMI SHARP dataset, we ended up with 1846 B-Class flares, 3246 C-Class flares, 318 M-Class flares, and 23 X-Class flares. It should be noted that we consider all the flaring events irrespective of the AR it originates from, i.e. if an active region flares multiple times during its lifetime, we count each of them as separate events.

5.1.3 Flaring history parameters

Active regions being areas of rich magnetic activity on the surface on the Sun, it is a good assumption that an active region with a history of flare occurrences could hold a high probability for more flares happening. Thus, through understanding the

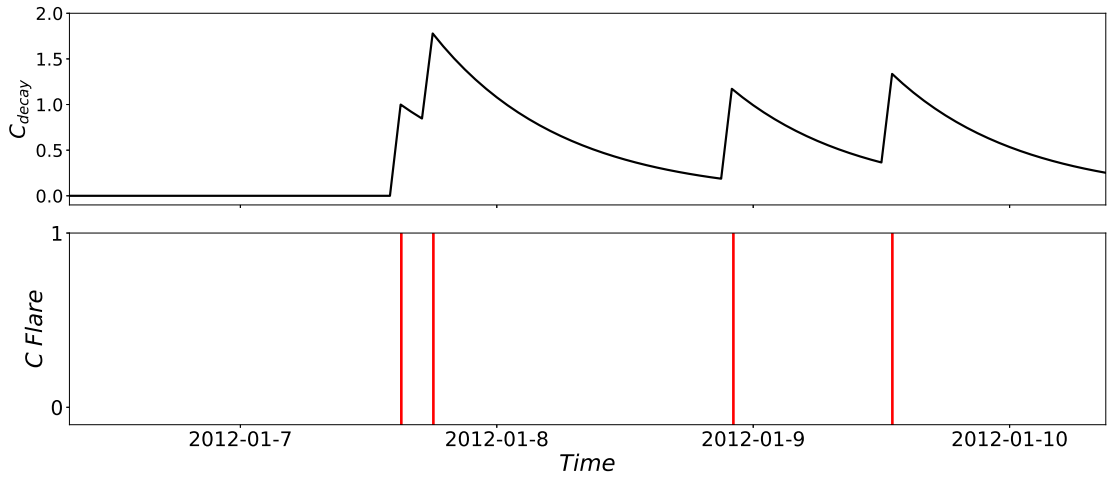

Figure 5.1: The plot of C_{decay} as a function of time. Comparing the top and bottom panels, we can see that when a flaring event occurs, the value increases and falls exponentially until the active region produces another flare. This plot corresponds to the NOAA AR 11393.

past flaring activity of an active region, we should be able to increase the ability to forecast flares [Falconer et al., 2012]. Based on the collected flaring data, we

made a framework of 12 flaring history parameters [Liu et al., 2019a] consisting of flare decay values and previous flare occurrences. These parameters will be able to encompass the history of each active region in terms of various levels of flaring activity, thus enabling us to study the contribution of history parameters in detail. Using the equations given in Jonas et al. [2018], time decay values were calculated for each individual active region. For a data sample in an AR, the decay values w.r.t C-class, M-class, and X-class are given by:

$$\mathrm{C}_{\mathrm{decay}}(\mathbf{t}) = \sum_{f_i \in F_C} exp\Big(- \frac{t - t(f_i)}{\tau} \Big) \quad , \tag{5.1}$$

$$\mathrm{M}_{\mathrm{decay}}(\mathbf{t}) = \sum_{f_i \in F_M} exp\Big(- \frac{t - t(f_i)}{\tau} \Big) \quad , \tag{5.2}$$

$$\mathrm{X}_{\mathrm{decay}}(\mathbf{t}) = \sum_{f_i \in F_X} exp\Big(- \frac{t - t(f_i)}{\tau} \Big) \quad , \tag{5.3}$$

here $F = F_C \cup F_M \cup F_X$,where F_k corresponds to the set of k class flares, and $t(f_i)$ corresponds to the time of occurrence of the flare f_i. The value of τ is fixed to be 12 as proposed by Jonas et al. [2018]. The nature of this decay function is depicted in Figure 5.1 with C_{decay} values of an active region. Apart from the time decay values w.r.t flare classes, we also calculate the energy decay values of an AR considering all flares, regardless of the type of flare that occurred before the sample time t. Here $E(f_i)$ corresponds to the magnitude of the flare f_i.

$$\mathrm{E}_{\mathrm{dec}}(\mathrm{x_t}) = \sum_{f_i \in F} E(f_i) exp\Big(- \frac{t - t(f_i)}{\tau} \Big) \quad , \tag{5.4}$$

$$\mathrm{logE}_{\mathrm{dec}}(\mathrm{x_t}) = \sum_{f_i \in F} \log(E(f_i)) exp\Big(- \frac{t - t(f_i)}{\tau} \Big) \quad . \tag{5.5}$$

The remaining seven parameters include flare history features of a data sample as

described in Nishizuka et al. [2017]. These features include Chist (Mhist, Xhist) storing the total number of C-Class (M-Class, X-Class) flares in the AR before the observation time, Chist1d (Mhist1d, Xhist1d) storing the flaring activity of each class during the 24 hours prior observation time, and finally Xmax1d storing maximum flare intensity 24 hours prior to the observation. Table 5.2 summarises all the flaring history parameters adopted in this model. As of now, we have 25 active region parameters and 12 flaring history parameters making a total of 37 features.

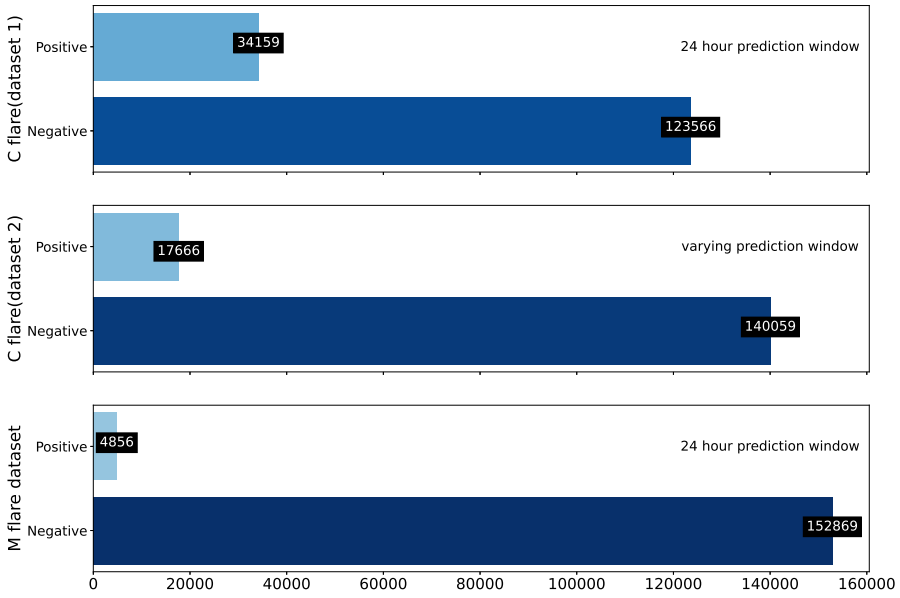

Figure 5.2: Positive and negative classes in 3 different datasets (≥C-Class with 24 hour prediction window, ≥C-Class with varying prediction window, and ≥M-Class with 24 hour prediction window).

5.1.4 Class imbalance problem

To obtain valuable insights into the robust predictive performance of the data, it is important to ensure the integrity of the data [Ahmadzadeh et al., 2019]. As we are taking the approach of point-in-time prediction, according to the study by Ahmadzadeh et al. [2019], one of the major factors that affect the performance of the model is the extensive class imbalance between positive and negative samples.

Table 5.1: SHARP active region parameters formula and description

Keyword	Formula	Description
TOTUSJH	$H_{c_{total}} \propto \sum \lvert B_z . J_z \rvert$	Total unsigned current helicity
TOTUSJZ	$J_{z_{total}} = \sum \lvert J_z \rvert dA$	Total unsigned vertical current
USFLUX	$\Phi = \sum \lvert B_z \rvert dA$	Total unsigned flux
AREA_ACR	Area = $\sum$Pixels	Area of strong field pixels in the active region
SAVNCPP	$J_{z_{sum}} \propto \left\lvert \sum^{B_z^+} J_z dA \right\rvert + \left\lvert \sum^{B_z^-} J_z dA \right\rvert$	Sum of the absolute values of the net current per polarity
TOTPOT	$\rho_{tot} \propto \sum \left(\vec{B}^{Obs} - \vec{B}^{Pot} \right)^2 dA$	Total photospheric magnetic free energy density
R_VALUE	$\Phi = \sum \lvert B_{LoS} \rvert$ dA within R mask	Sum of flux near polarity inversion line
TOTUBSQ	$F \propto \sum B^2$	Total magnitude of Lorentz force
ABSNJZH	$H_{c_{abs}} \propto \lvert \sum B_z . J_z \rvert$	Absolute value of the net current helicity
MEANPOT	$\overline{\rho} \propto \frac{1}{N} \sum \left(\vec{B}^{Obs} - \vec{B}^{Pot} \right)^2$	Mean photospheric magnetic free energy
MEANSHR	$\overline{\Gamma} = \frac{1}{N} \sum arccos \left(\frac{\vec{B}^{Obs} . \vec{B}^{Pot}}{\lvert B^{Obs} \rvert \lvert B^{Pot} \rvert} \right)$	Mean shear angle
SHRGT45	Area with Shear > 45° / Total Area	Area fraction with a shear angle higher than 45°
TOTFZ	$F_z \propto \sum \left(B_x^2 + B_y^2 - B_z^2 \right) dA$	Sum of z-component of Lorentz force
MEANGAM	$\overline{\gamma} = \frac{1}{N} \sum arctan \left(\frac{B_h}{B_z} \right)$	Mean angle of field from radial
TOTFY	$F_y \propto \sum B_y B_z dA$	Sum of y-component of Lorentz force
MEANGBT	$\overline{\lvert \nabla B_{tot} \rvert} = \frac{1}{N} \sum \sqrt{\left(\frac{\partial B}{\partial x} \right)^2 + \left(\frac{\partial B}{\partial y} \right)^2}$	Mean gradient of total field
MEANGBH	$\overline{\lvert \nabla B_h \rvert} = \frac{1}{N} \sum \sqrt{\left(\frac{\partial B_h}{\partial x} \right)^2 + \left(\frac{\partial B_h}{\partial y} \right)^2}$	Mean gradient of horizontal field
MEANJZD	$\overline{J_z} \propto \frac{1}{N}] \sum \left(\frac{\partial B_y}{\partial x} - \frac{\partial B_x}{\partial y} \right)$	Mean vertical current density
MEANGBZ	$\overline{\lvert \nabla B_z \rvert} = \frac{1}{N} \sum \sqrt{\left(\frac{\partial B_z}{\partial x} \right)^2 + \left(\frac{\partial B_z}{\partial y} \right)^2}$	Mean gradient of vertical field
EPSY	$\partial F_y \propto \frac{-\sum B_y B_z}{\sum B^2}$	Sum of y-component of normalised Lorentz force
EPSX	$\partial F_x \propto \frac{\sum B_x B_z}{\sum B^2}$	Sum of x-component of normalised Lorentz force
TOTFX	$F_x \propto -\sum B_x B_z dA$	Sum of x-component of Lorentz force
EPSZ	$\partial F_z \propto \frac{\sum B_x^2 + B_y^2 - B_z^2}{\sum B^2}$	Sum of z-component of normalised Lorentz force
MEANALP	$\alpha_{total} \propto \frac{\sum J_z . B_z}{\sum B_z^2}$	Mean characteristic twist parameter, α
MEANJZH	$\overline{H_c} \propto \frac{1}{N} \sum B_z . J_z$	Mean current helicity

Figure 5.2 shows the positive and negative samples in each dataset prepared. The figure clearly shows that the number of negatively sampled events far outnumber the positively sampled events. This imbalance becomes much more significant at datasets considering higher flare magnitudes. If this imbalance is not properly dealt with, the results and predictions can be misleading as the data is biased towards non-flaring events. There are various methods to deal with imbalanced problems. In this work, we use an oversampling technique, namely, Synthetic Minority Oversampling Technique (SMOTE). Normal oversampling techniques randomly duplicate examples in minority class without adding any new information to the set. SMOTE, as described in Chawla et al. [2002], works by selecting examples that are close in

Keyword	Formula	Description
Cdecay	$\text{Cdecay}(x_t) = \sum_{f_i \in F_C} e^{-\frac{t-t(f_i)}{\tau}}$	Time decay value based on the past C-class flares
Mdecay	$\text{Mdecay}(x_t) = \sum_{f_i \in F_M} e^{-\frac{t-t(f_i)}{\tau}}$	Time decay value based on the past M-class flares
Xdecay	$\text{Xdecay}(x_t) = \sum_{f_i \in F_X} e^{-\frac{t-t(f_i)}{\tau}}$	Time decay value based on the past X-class flares
Edecay	$\text{Edecay}(x_t) = \sum_{f_i \in F} E(f_i) e^{-\frac{t-t(f_i)}{\tau}}$	Time decay value determined using magnitudes of all past flares
logEdec	$\text{logEdec}(x_t) = \sum_{f_i \in F} \log(E(f_i)) e^{-\frac{t-t(f_i)}{\tau}}$	Time decay value determined using log-magnitudes of all past flares
Chist	-	Total number of C-class flares ever recorded in an AR
Mhist	-	Total number of M-class flares ever recorded in an AR
Xhist	-	Total number of X-class flares ever recorded in an AR
Chist1d	-	C-class flare activity in an AR over 24 hours
Mhist1d	-	M-class flare activity in an AR over 24 hours
Xhist1d	-	X-class flare activity in an AR over 24 hours
Xmax1d	-	Maximum X-ray intensity 24 hours before

Table 5.2: Flaring history parameters formulae and description

feature space and interpolating them to find new examples.

During the course of time, there were several modifications to the basic SMOTE algorithm changing the approach on how each selects samples from the minority class. A few of the most commonly used are Borderline SMOTE [Han et al., 2005], Borderline SMOTE SVM [Nguyen et al., 2011] and Adaptive Synthetic Sampling [He et al., 2008]. Trial runs of the whole flare prediction algorithm with these three variations were conducted separately, in which the Borderline SMOTE algorithm performed the best. Thus we have used the Borderline SMOTE method along with random undersampling [Chawla et al., 2002] to create the final required dataset. This will bring the ratio of flaring events to non-flaring events to a value around 0.6. This value was chosen by running a grid search on values from 0.1 to 0.9 and optimising the performance of the classifier.

5.1.5 Standardisation

As the features are of very different scales, the model could give higher preference to those features with higher numerical values. To prevent this, we standardise the values of each feature, bringing them to a comparable scale.

The following equation is used to calculate the standardised values for each feature. For n^{th} feature of the m^{th} data sample, the standardised value is given by:

$$s_n^m = \frac{v_n^m - \mu_n}{\sigma_n} \quad , \tag{5.6}$$

where v_n^m is the actual value of the n^{th} feature, and μ_n and σ_n are the mean and standard deviation of the n^{th} feature respectively.

5.2 Machine Learning Classifier

5.2.1 Labeling Algorithm

As our prediction model is a binary classifier, we define the flaring and non-flaring events as binary flags. First, we used the operational form of associations between active regions and solar flares to label the flares. While using the operational form, if an active region produces any flares within 24 hours after the sample time, it is classified as a positive class or flaring event, and if it does not flare within the given time, it is classified as a negative class or the non-flaring event. Secondly, we designed a new labelling algorithm taking into account the varying nature of solar activity throughout the cycle. The new algorithm divides the solar cycle into 12 parts, keeping flare occurrences equal in each and allotting each division a prediction window which varies logarithmically from 6 hours to 24 hours in the active and quiet periods of the solar cycle. Figure 5.3(a) and Figure 5.3(b) show how the prediction window varies and how it is allotted throughout the solar cycle.

For our model, we will be considering C-Class, M-Class, and X-Class flares as positive events and the rest as negative. Furthermore, in terms of flare magnitude, we

prepared two datasets such that the first one considers any flare with a magnitude greater than or equal to a C-Class flare to be positive and the second one such that any flare with a magnitude greater than or equal to an M-Class flare is considered positive. Due to high-class imbalance in the ≥M-Class dataset, only the operational form of labeling is adopted for the same. Thus we have three datasets: ≥C-Class dataset (24 hour prediction window), ≥C-Class dataset (varying prediction window) and ≥M-Class dataset (24 hour prediction window).

5.2.2 Light Gradient Boosting Machine Classifier

We use a LightGBM model as our classifier. LightGBM [Ke et al., 2017] is a highly efficient Gradient boosting decision tree (GBDT) algorithm developed by Microsoft Corporation in 2016. Compared to other GBDT algorithms like XGboost, LightGBM uses an optimised histogram-building method by down-sampling data and features using GOSS (Gradient Based One Side Sampling) and EFB (Exclusive Feature Bundling).

In contrast to its gradient-boosting counterparts, LightGBM's histogram building approach results in significant improvements in efficiency and forecasting ability. The algorithm discovers complex data patterns by concentrating on expanding leaf nodes that have the greatest impact on loss reduction, which is a significant advantage for our solar flare prediction task using HMI SHARP data. This choice of classifier perfectly complements the complex nature of solar flare predictors and triggers in our dataset. LightGBM is equipped to understand intricate relationships and distinctions thanks to the leaf-wise growth technique, which effectively decodes complex solar phenomena. Hyperparameters are used to further fine-tune the algorithm's performance, achieving a balance between computational needs and predictive power across various dataset sizes. Nevertheless, it is important to recognise the hindrances of the traditional level-wise growth approach from which LightGBM

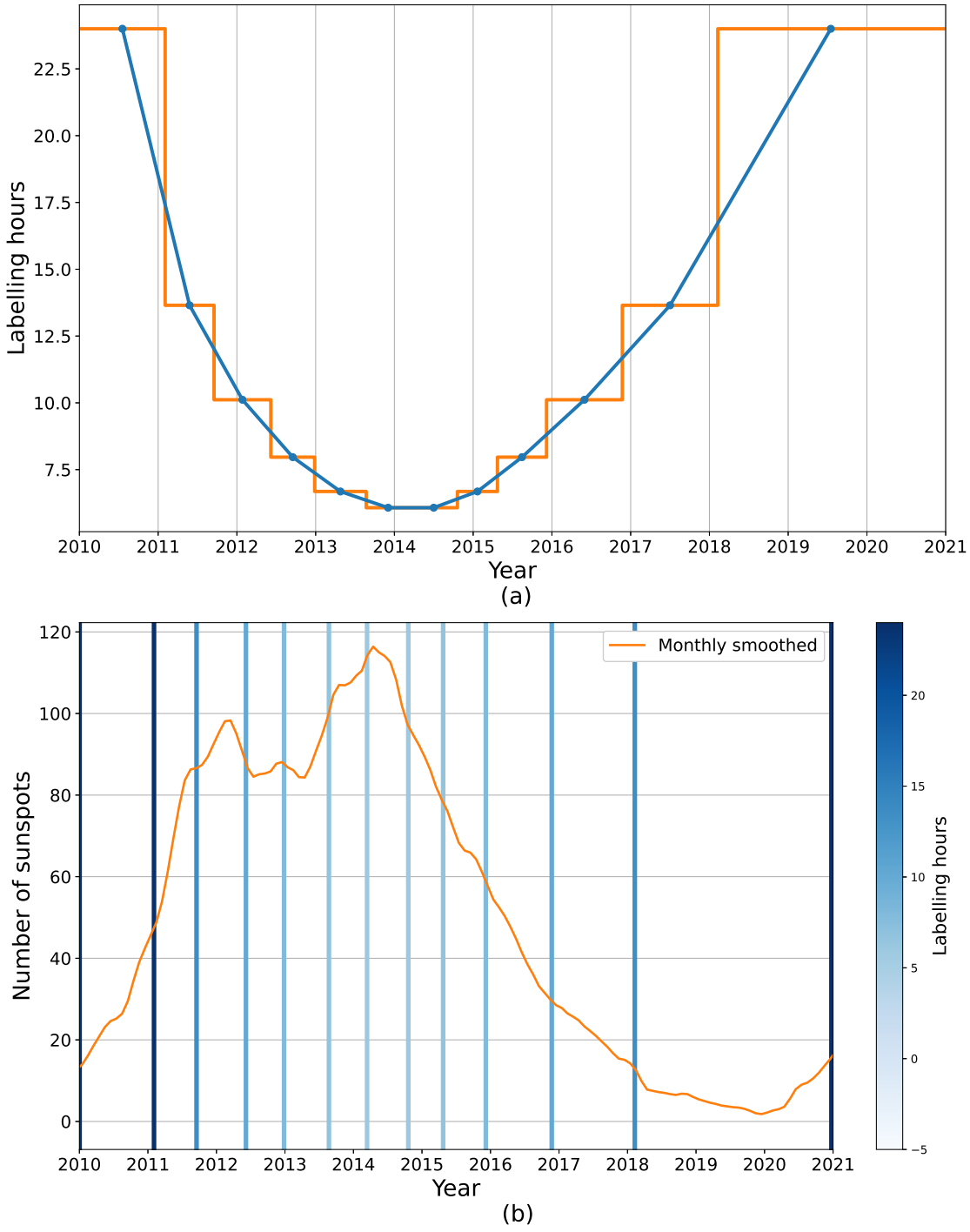

Figure 5.3: (a) Varying label prediction window (b) Divisions made throughout the solar cycle with color map displaying the prediction window.

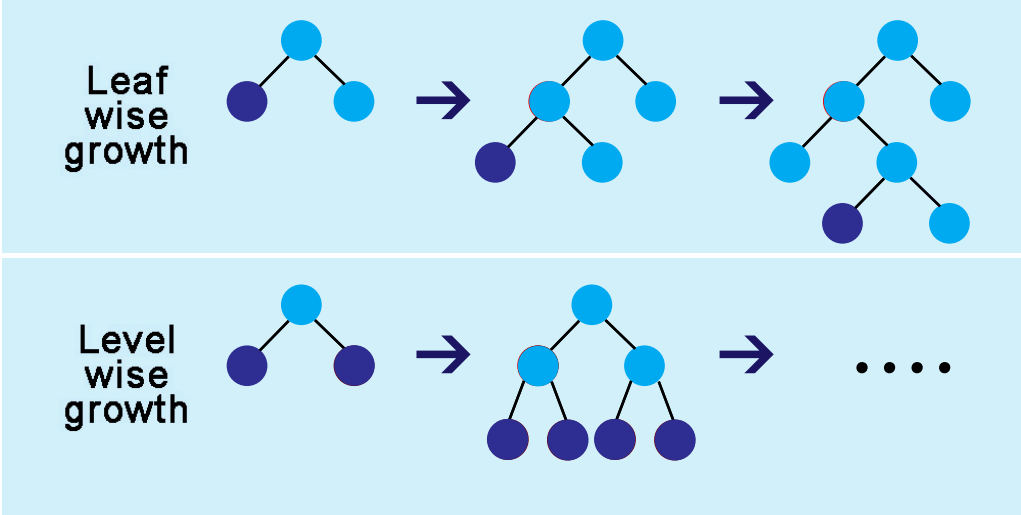

Figure 5.4: Leaf-wise and level-wise growths.

deviates. The primary distinction between leaf-wise and level-wise growth lies in how decision trees are constructed. In the leaf-wise approach, individual leaves at the end of the tree are allowed to grow independently, as opposed to the level-wise method, where growth occurs level by level sequentially. This difference has been visualised in Figure 5.4. Even though level-wise growth ensures a balanced tree structure and reduces overfitting, it might miss complex patterns in our data on solar activity. With its deeper trees and greater ability to capture complex interactions, LightGBM's adoption of the leaf-wise growth strategy presents a compelling alternative tailored to the intricacies of solar flare prediction. The appeal of LightGBM goes beyond its algorithmic innovation and includes its resource-conserving architecture. The algorithm uses gradient-based optimisation techniques like GOSS and EFB to speed up training and feature extraction, which is a significant benefit when dealing with a large dataset such as in the case of solar flare data.

The utilisation of LightGBM introduces a comprehensive array of hyperparameters, facilitating a nuanced configuration of the model. Within our study, the hyperparameters subject to tuning encompass the bagging fraction, learning rate, number

of leaves, L1 regularisation, and L2 regularisation (Ke et al., 2017). The bagging fraction assumes a pivotal role by governing the proportion of training data used in each iterative step, thereby contributing to the model's generalisation capability. Notably, the refinement of hyperparameters such as the number of leaves, and the imposition of L1 and L2 regularisation mechanisms collectively contribute to the model's regularisation process. The optimisation of these parameters is undertaken through an exhaustive grid search method aimed at eliciting the optimal configuration that maximises model performance, gauged through the TSS metric. The ranges considered for each parameter are bagging fraction ϵ $(0, 1)$, learning rate ϵ $(0.0001, 0.1)$, number of leaves ϵ $(2^4, 2^8)$, L1 ϵ $(0, 1)$ and L2 ϵ $(0, 1)$. Each parameter is sampled from a uniform prior in the given range. Even though this is not the best method in terms of efficiency, we chose this approach as it had a straightforward implementation and we were able to complete it within a reasonable time frame.

One of the parameters used in training the model is the loss function. We have used the focal loss as the chosen loss function for our model. As per Lin et al. [2017], the focal loss is a better choice for imbalanced problems than metrics like cross-entropy, as the former assigns more weight on easily misclassified labels and down-weight easily classified labels. For a binary classification problem, if $y \in \{\pm 1\}$ is the ground truth class and $p \in [0, 1]$ is the model's estimated probability for class $y = 1$, We could write the α-balanced variant of focal loss to be,

$$\mathrm{FL}(p_t) = -\alpha(1 - p_t)^{\gamma} \log(p_t) \quad , \tag{5.7}$$

$$\text{where, } p_t = \begin{cases} p & \text{if } y = 1 \\ 1 - p & \text{otherwise} \end{cases} \quad , \tag{5.8}$$

where t indicates the true class. This loss function is minimised over iterations to train the classification model. Optimising focusing parameter γ and weighing

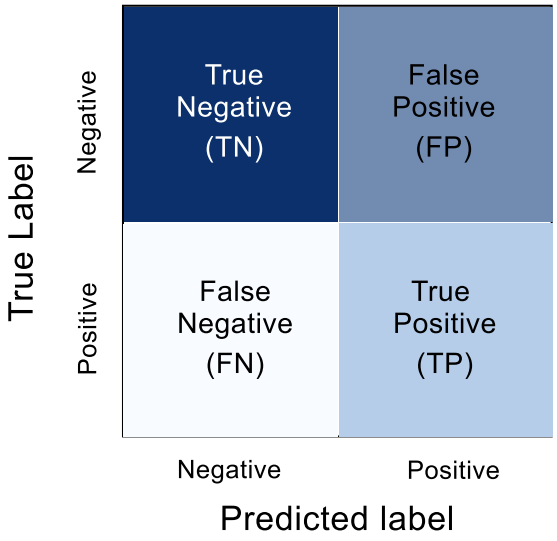

Figure 5.5: Confusion matrix.

parameter α lets the model perform better by assigning more weight to easily misclassified parameters. We set early stopping rounds parameter to be 20, to let the model stop training after a certain score in the validation set has been reached so as to avoid over-fitting.

5.2.3 Performance metrics

Being an imbalanced binary classification problem, most common metrics like accuracy would not act as a functional measure of the performance (He & Garcia [2009]). This is because the high accuracy could easily be achieved by only predicting the majority class, i.e. non-flaring class. A confusion matrix, as shown in Figure 5.5, can be used to represent the results of a binary classifier. The classifier's accurate predictions of flaring ARs are referred to as True Positives (TP), while incorrect predictions of flaring ARs are referred to as False Negatives (FN). Similarly, True negatives (TN) refer to accurate predictions of non-flaring ARs, and False positives (FP) refer to incorrect predictions of non-flaring ARs.

To statistically analyse the model results and compare with the observed data, we chose five metrices which are commonly used in the literature. Their expressions are following:

$$\text{Precision} = \frac{\text{TP}}{\text{TP} + \text{FP}} \quad , \tag{5.9}$$

$$\text{Recall} = \frac{\text{TP}}{\text{TP} + \text{FN}} \quad , \tag{5.10}$$

$$\text{HSS} = \frac{2(\text{TP} \times \text{TN} - \text{FP} \times \text{FN})}{(\text{TP} + \text{FN})(\text{FN} + \text{TN}) + (\text{TP} + \text{FP})(\text{FP} + \text{TN})} \quad , \tag{5.11}$$

$$\text{TSS} = \frac{\text{TP}}{\text{TP} + \text{FN}} - \frac{\text{FP}}{\text{TN} + \text{FP}} \quad , \tag{5.12}$$

$$\text{BACC} = \frac{1}{2}\left(\frac{\text{TP}}{\text{TP} + \text{FN}} + \frac{\text{TN}}{\text{TN} + \text{FP}}\right) \quad , \tag{5.13}$$

where, precision summarises the number of predicted positive classes that belong to the positive class, while recall summarises how well the positive class was predicted. HSS is Heidke Skill Score and measures the fractional improvement of the forecast over the standard forecast. TSS is True Statistical Score which is defined as the difference between the recall and false alarm rate. Even though HSS is useful, it changes despite the prediction success being held constant [Bloomfield et al., 2012], so it is suggested to use True Skill Statistic (TSS) as the measure of performance. Additionally, TSS is unbiased to class-imbalance ratio, thus making it the most useful measure for flare forecasting methods. We will also calculate the Balanced Accuracy (BACC) as it is a good measure for studying an imbalanced classification [He & Garcia, 2009]. Larger the TSS, HSS, or BACC, the better the performance of the model. Even though we will calculate all the mentioned metrics, we will focus more on increasing the True Skill Statistic as it provides a better measure in flare forecasting.

5.3 Results and Discussion

5.3.1 Model Evaluation

To find the best hyperparameters for our model, we perform a grid search in the parameter space to maximise the TSS score. We run the grid search for bagging fraction, learning rate, number of leaves, L1 regularisation, and L2 regularisation. Through trial runs, the best-boosting method for our dataset was found to be the Gradient Boosting Decision Tree (GBDT). Furthermore, we determined the optimal hyperparameters for our model are as follows: a learning rate of 0.01, a bagging fraction of 0.95, 146 leaves in the decision trees, L1 regularisation set at 0.74, and L2 regularisation set at 0.23.

As mentioned in Section 5.2.1, we prepared three datasets ($\geq$C-Class (24-hour prediction window), $\geq$C-Class (varying prediction window), $\geq$M-Class (24-hour prediction window)) to train our model. Each dataset was further divided into training, validation, and test sets. To ensure the unbiased nature of performance metrics, we need to make sure that the model performance is tested on a new dataset that it has not seen before. To ensure this, we divided the datasets such that all the samples collected from January 2012 to December 2014 were used to train the model, January 2015 to December 2016 were used as validation set to tune the model, and finally, samples from January 2017 to December 2020 were used to test the data. This division ensures the former statement and describes the real-world scenario for predicting solar flares.

Once the training, validation, and testing datasets are prepared, the LightGBM classifier is trained with the training dataset. Once the model is trained, a threshold moving approach is used to improve the model to deal with the imbalance in the data. For a binary prediction of flaring or non-flaring, a decision threshold is used to convert the predicted probability into a class label. The default value of 0.5

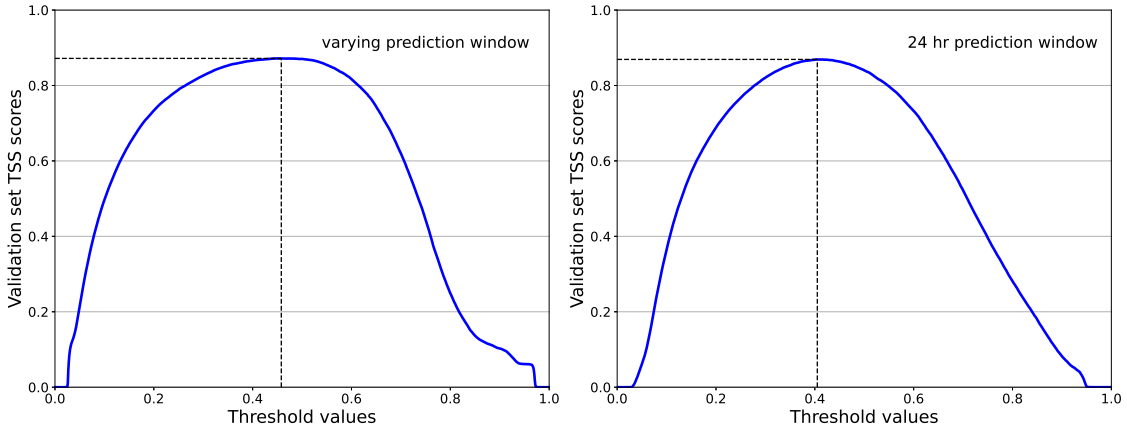

Figure 5.6: TSS score vs. threshold plot for a moving threshold for predicting C-class flares with varying prediction window and 24-hour prediction window.

may not represent the predicted probabilities accurately due to the skewness in the data. Hence, threshold moving is used in moving the decision threshold to an optimum value, reflecting the predicted probability in the right manner. The threshold moving is done using the training data set. Figure 5.6 and 5.7 display the TSS score against threshold plots for each dataset, using which the optimum threshold has been calculated for each dataset. For the C-class dataset with varying prediction window, the threshold is 0.461 (TSS score: 0.865); for the C-class dataset with 24-hour prediction window, the threshold is 0.410 (TSS score: 0.856) and for the M-Class dataset, the threshold is 0.372 (TSS score: 0.977). Once the best threshold is achieved, the previously mentioned hyperparameters (Section 5.2.2) are tuned using the validation set to achieve the best parameters for the model.

After calculating the threshold values for each dataset, we tested our model on the test set using all the parameters we calculated. All the performance metrics mentioned in the previous section were calculated to analyse the model. We calculated the score for two sets of features, only SHARP parameters and both SHARP and flaring history parameters. These scores are displayed in the Table 5.3. Upon conducting a comparative analysis of the scores within both scenarios, it becomes

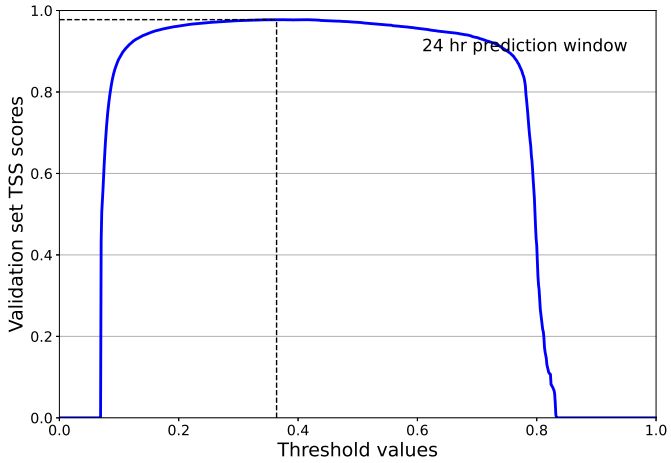

Figure 5.7: TSS score vs. threshold plot for moving threshold for predicting M-class flares with 24-hour prediction window.

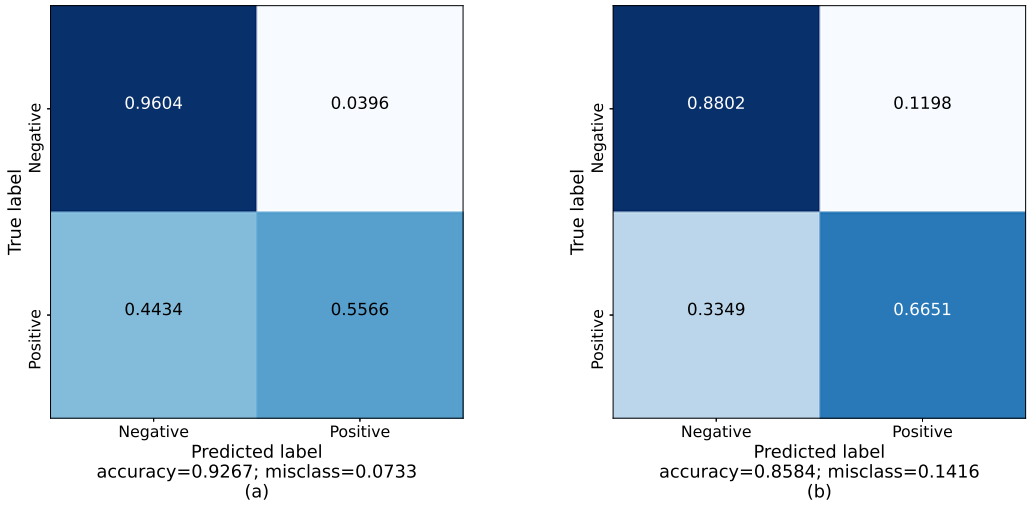

Figure 5.8: (a) Confusion matrix of test results using LightGBM model in the ≥C-Class dataset with varying prediction window; (b) Confusion matrix of test results using LightGBM model in ≥C-Class dataset with 24 hour prediction window.

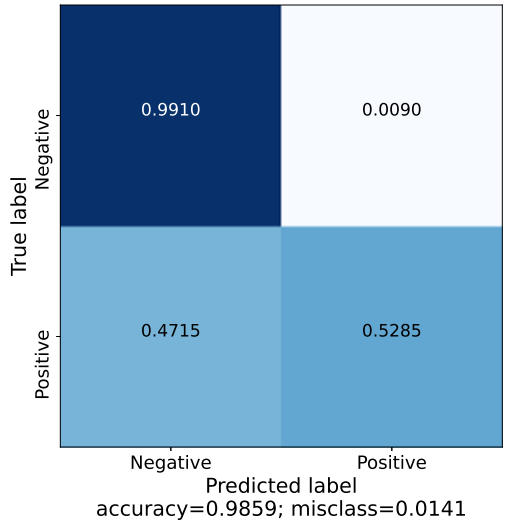

Figure 5.9: Confusion matrix of test results using LightGBM model in the ≥M-Class dataset with 24-hour prediction window.

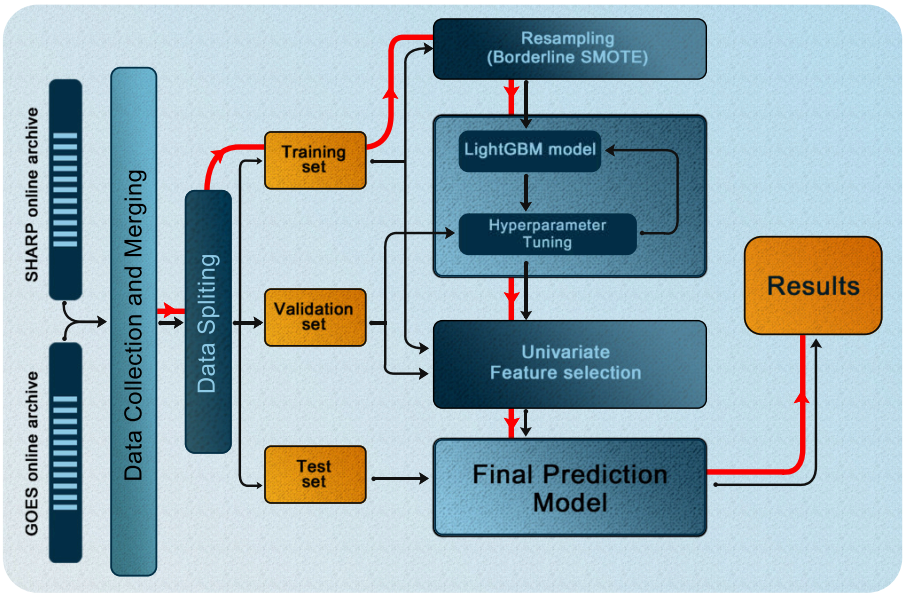

Figure 5.10: Flow chart of the model adopted. Starting from collection and processing solar data, the above diagram describes the steps taken throughout the chapter in a brief manner. Each block represents an important step in the adopted model. The red line indicates the order in which the model was executed and the black line shows how the data was distributed between steps.

evident that the incorporation of flaring history parameters has resulted in noteworthy enhancements across nearly all evaluated metrics, notably the TSS score. This substantiates the significance of integrating flaring history parameters and their instrumental role in improving the model performance. Along with the score, we have also provided the confusion matrix (Figure 5.8 and Figure 5.9) of the classification model on each dataset. Comparing the confusion matrices between varying and 24 hour prediction windows for ≥C-Class, we can see that the normalised true positive value for the 24-hour prediction window surpasses that of the varying prediction window, while conversely, the normalised true negative values exhibit higher proportions for the latter approach. This observation implies that the 24-hour prediction window proves more helpful for the model in handling the class imbalance, thereby enhancing its predictive capability for positive class instances (flaring events). Conversely, in the case of the varying prediction window, despite achieving a commendable 96% accuracy in predicting true negatives, its capacity to accurately identify positive labels stands at a relatively modest 55%. Shifting focus to the ≥M-Class dataset, it becomes apparent that the model achieves an impressive 99.1% accuracy in discerning non-flaring events, while its performance in predicting flaring events is substantially less satisfactory, amounting to a 52.8% accuracy. This outcome can be explained by the innate rarity of M-Class events, posing challenges for the model in effectively distinguishing between positive and negative instances. The whole workflow and the steps taken in the data analysis and model training part of this work, have been illustrated in the form of a flowchart in Figure 5.10. In the figure, each block represents an important step in the adopted model; the black lines represent how the data is distributed in different steps, and the red line represents the order in which the data analysis steps are implemented.

	Metric	≥C-Class(varying prediction window)	≥C-Class(24 hr prediction window)	≥M-Class(24 hr prediction window)
SHARP and flaring history parameters	Accuracy	0.92421	0.86982	0.98687
	Precision	0.54308	0.41357	0.42171
	Recall	0.57585	0.67212	0.52398
	ROC AUC	0.88703	0.88053	0.92618
	TSS	0.53173	0.56429	0.51597
	BACC	0.76586	0.78214	0.75799
	HSS	0.51731	0.44170	0.46012
SHARP parameters	Accuracy	0.91440	0.85773	0.97987
	Precision	0.48841	0.38504	0.26559
	Recall	0.56554	0.67062	0.47561
	ROC AUC	0.86081	0.86477	0.92951
	TSS	0.51165	0.54949	0.46107
	BACC	0.75583	0.77474	0.73053
	HSS	0.47729	0.41345	0.33084

Table 5.3: Flare prediction results of LightGBM model on different datasets.

5.3.2 Feature set evaluation

Not all features are important towards solar flare prediction [Bobra & Couvidat, 2015]. While some of them show high correlation with the output, for a few of the features, the inclusion of them in the feature could decrease the overall performance. Thus we use a univariate feature selection algorithm, using ANOVA F-value score to rank them. For ≥C-Class (24-hour prediction window) dataset (Figure 5.11), the Total unsigned current helicity feature is identified as having the highest F-score (TOTUSJH). Numerous studies have suggested a strong correlation between the accumulation of magnetic helicity and the occurrence of flares in active regions [Liu et al., 2023; Park et al., 2010]. Features like Total magnetic vertical current (TOTUSJZ), Total unsigned flux (USFLUX) are also among the high-ranked features for this dataset. From the flaring history parameters, CDEC was ranked in the top 3,

suggesting the time decay value of C flares in an active region shows high correlation towards a flaring event. It can also be seen that the history of C-flares is also ranked high. It can be noted that just considering the SHARP active region parameters, 11 out of the top 13 magnetic summary features selected matched with the top 13 magnetic summary features mentioned in Bobra et al. [2014]. These include TOTUSJH, TOTUSJZ, USFLUX, AREA_ACR, SAVNCPP, TOTPOT, R_VALUE TOTBSQ, ABSNJZH, MEANPOT, and MEANSHR. Thus our findings are consistent with published values in the literature.

For ≥C-Class (varying prediction window) dataset (Figure 5.12) an interesting trend is observed. Even though they display slightly different importance, all the first 12 features are the same as the first 12 features in the previous dataset. This shows that the basic dependence of different magnetic and flaring history features on flaring activity remains intact with the change in the prediction window. But a notable difference occurs in the importance of the CDEC parameter. Compared to the 24-hour prediction window, the varying prediction window shows higher relative importance towards the C flare decay value. This could have derived from the fact that, during high solar activity, the 24-hour prediction window could have included a higher number of samples even though they are from different C Class flares, thus reducing the importance of CDEC parameter. By the introduction of varying prediction windows at higher solar activity, only the samples corresponding to observed flare will contribute, thus letting the model learn it as an important feature for flare prediction.

For ≥M-Class (24 hour prediction window) dataset (Figure 5.13), the feature with the highest F-score is Absolute value of the net current helicity (ABSNJZH). Features like Total unsigned current helicity (TOTUSJH), Total magnetic vertical current (TOTUSJZ), and Sum of the modulus of the net current per polarity (SAVNNCPP) also are among highly ranked features for this dataset. From the flaring

history parameters, similar to C-Class prediction, time decay value of M flares in an active region (MDEC) shows high correlation towards an M Class flaring event. We also observe that apart from M Class flaring history parameters, CDEC and CHIS also show a higher importance towards the M Class flaring events. This could imply that an active region with C class flares occurring frequently is more prone to M class events.

In order to identify the optimal feature set, we have conducted an evaluation of performance metrics that are contingent upon the number of features utilised. This analysis entails arranging features in descending order with regard to their significance. The result can be seen in Figure 5.14, 5.15 and 5.16. This brings up an interesting property that not all the parameters are required to produce the best classifier. In the context of the ≥C-Class dataset, encompassing both variable and 24-hour prediction windows, noticeable trends emerge regarding feature selection. Initially, an ascent in scores is observed for 1 to 5 features, followed by a subsequent plateauing effect as additional features are incorporated. This phenomenon potentially underscores the pivotal contribution of the initial high-importance features towards predicting solar flaring activity. Conversely, the inclusion of less significant features appears to lead to a saturation of scores, indicating their comparatively diminished role in flare prediction. In the case of the ≥M-class dataset, a divergence in trends is evident across different performance metrics. Specifically, BACC and TSS, designed to address imbalanced datasets, exhibit a parallel trajectory, with scores peaking for 1 to 5 features and gradually diminishing thereafter. This trend implies that incorporating features beyond the most crucial ones not only stabilises but also reduces the predictive scores. This decline may stem from potential overfitting, as the model's complexity increases, leading to the incorporation of less relevant patterns from the less important features. While both the ≥C-Class and ≥M-Class datasets have undergone resampling to achieve comparable ratios, the

relative strength of this trend appears to be less pronounced in the former. This discrepancy may be attributed to the specific manner in which SMOTE algorithms perform the resampling process. SMOTE primarily operates by generating synthetic data points through interpolation between existing data vectors. Although this technique mitigates class imbalance concerns, it does not fundamentally alter the underlying distribution of parameters within the dataset. Given that events falling into the ≥M-Class category are inherently less frequent than those categorised as ≥C-Class, this results in a lower coverage of parameter space for the former class. Consequently, the model may encounter challenges in discerning and learning relevant patterns, particularly from the less prominent features within the dataset. In contrast to the other two metrics, the HSS demonstrates a distinct trajectory, implying varying influences of features and complexity on this metric itself.

In an attempt to elucidate the detectable dissimilarity in the importance of various features, we have undertaken the visualisation of feature importance distributions concerning both positive (flaring) and negative (non-flaring) labels. This visual representation is presented in Figures 5.17 and 5.18. Notably, for features attributed with heightened importance, a noticeable divergence in distribution peaks and spreads between the positive and negative labels is observed, thereby conferring distinctiveness to these features. Conversely, among features deemed less significant, a marked semblance in distribution patterns is discernible, indicative of their diminished discriminative capacity. This disparity in feature importance manifestation is particularly pronounced within the context of the M-Class dataset, wherein the broader distribution spread of certain features is evident. This phenomenon is particularly notable due to the scarcity and heightened magnitude of ≥M-class flares in contrast to ≥C-Class flares.

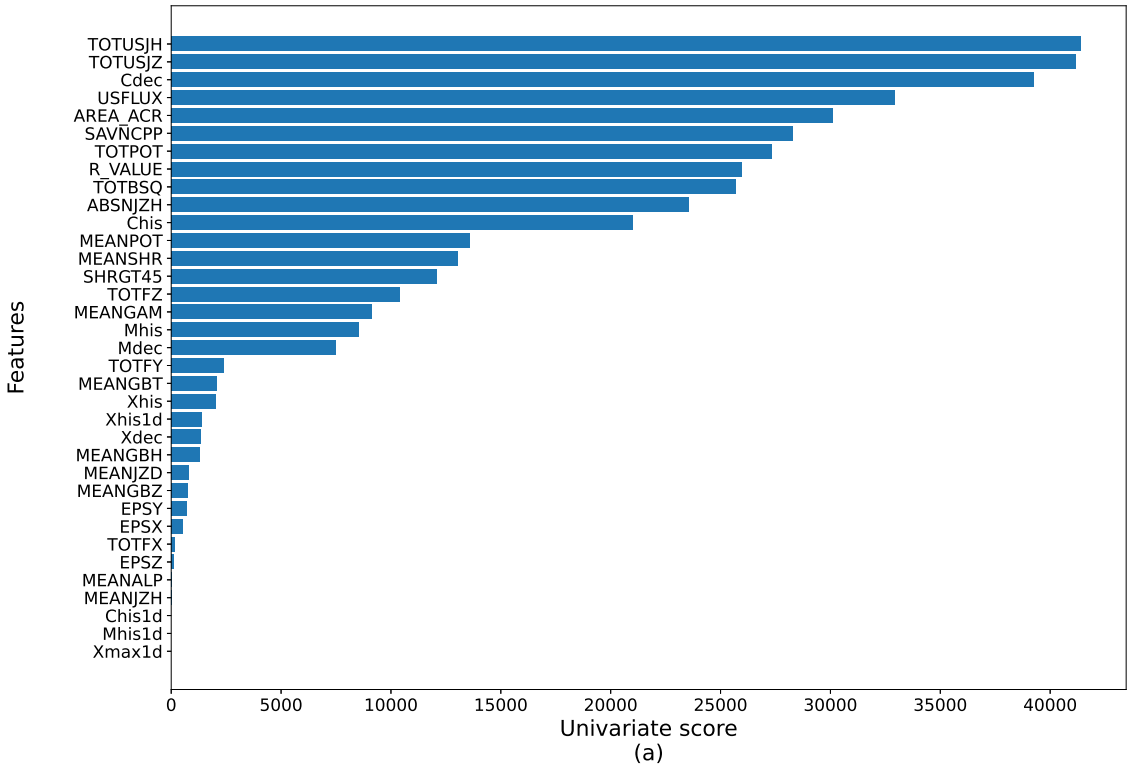

Figure 5.11: Univariate feature importance graph for predicting ≥C-class with 24 hour prediction window. The bar lengths indicate individual ANOVA F-value score.

Metric	≥C-Class(varying prediction window)	≥C-Class(24 hr prediction window)	≥M-Class(24 hr prediction window)
Accuracy	0.92055	0.89841	0.96987
Precision	0.52083	0.50001	0.22541
Recall	0.58531	0.63108	0.71869
ROC AUC	0.89077	0.88711	0.94186
TSS	0.53632	0.63057	0.69134
BACC	0.76816	0.80979	0.84567
HSS	0.50769	0.45664	0.33201

Table 5.4: Flare prediction results of LightGBM model using the highest scored parameters

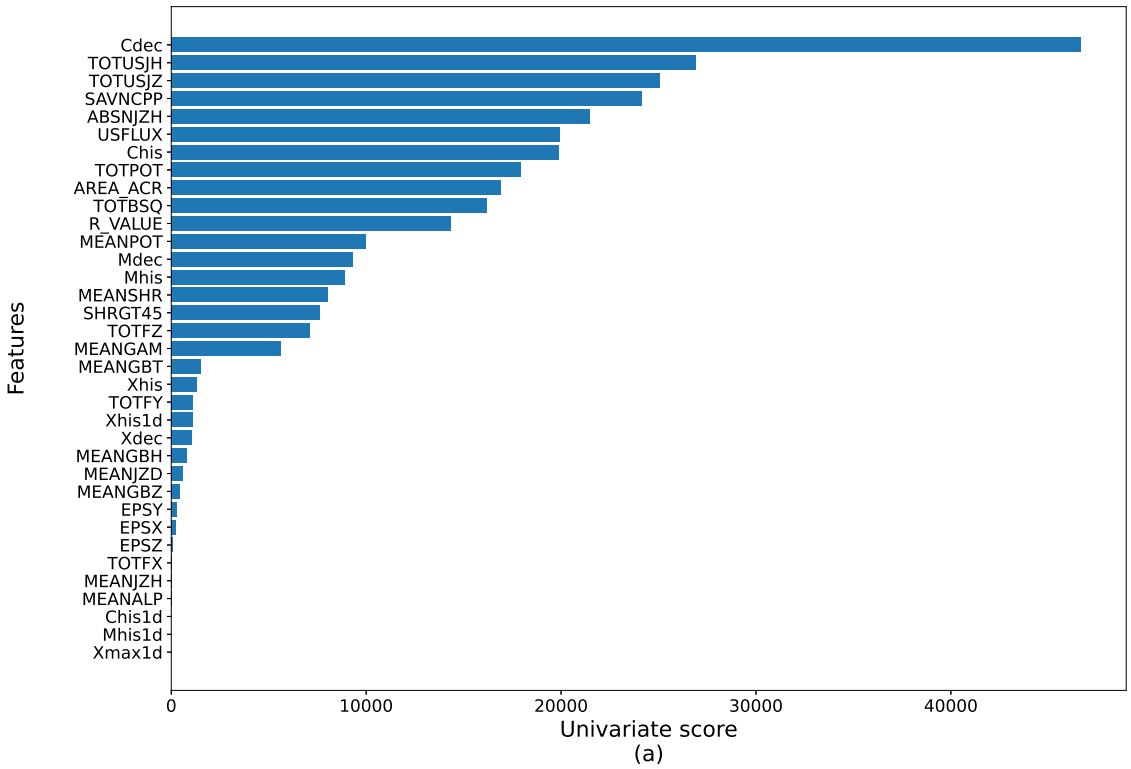

Figure 5.12: Univariate feature importance graph for predicting ≥C-class with varying prediction window. The bar lengths indicate individual ANOVA F-value score.

After the above analysis, we selected the best set of features as per data in Figures 5.14, 5.15, and 5.16. Based on the plots, we identified the optimal number of features around the highest TSS metric within each dataset. From the figures, it is clear that all three datasets displayed the highest TSS metric in between 3 - 5 sets of features. To have a more robust and general model and avoid having too few features leading to loss of information, a set of top five features was selected for each dataset.Subsequently, the classifier model was re-trained exclusively using these selected prominent features. The subsequent outcomes obtained utilising this refined feature subset are documented in Table 5.4. We have also plotted the confusion matrices (Figure 5.19 and 5.20) for the new subset of features for comparison. When comparing with Table 5.3, concerning the ≥C-Class dataset, consistent enhance-

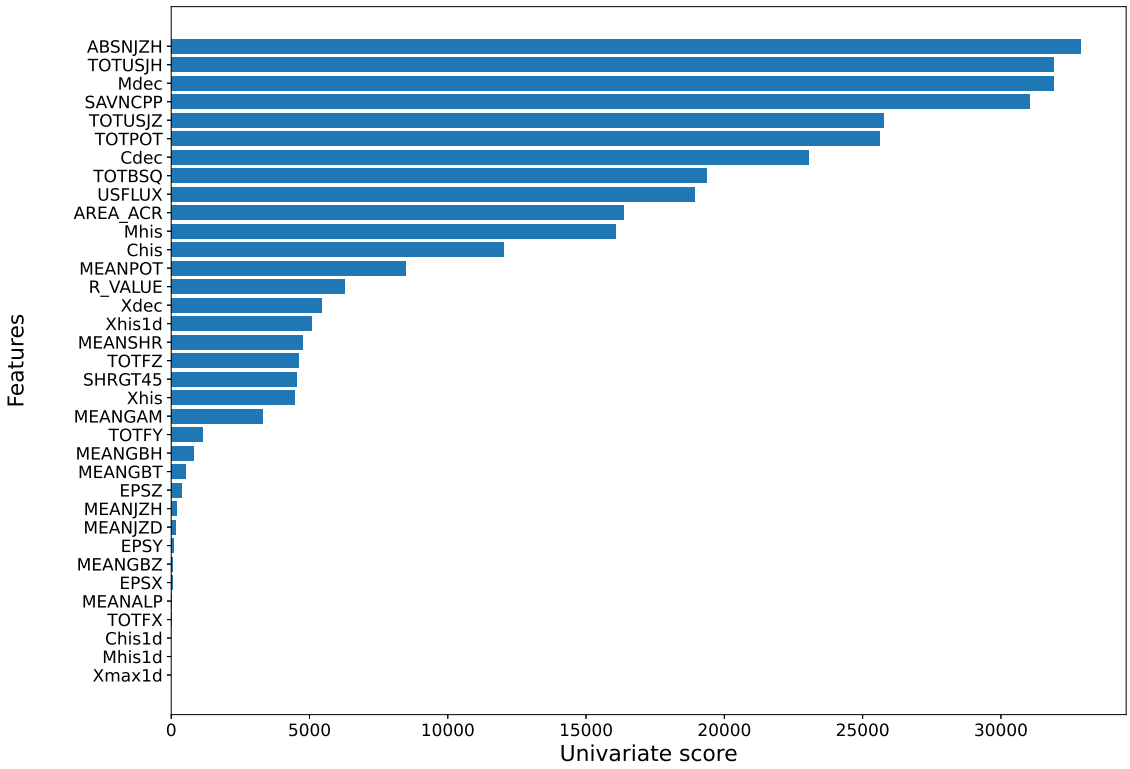

Figure 5.13: Univariate feature importance graph for predicting ≥M-class with 24 hour prediction window. The bar lengths indicate individual ANOVA F-value score.

ments in pivotal metrics, namely, TSS and BACC, are evident for both labeling algorithms. This observation underscores the efficacy of utilising a constrained feature subset, whereby improved predictive power is achieved in contrast to employing the complete set of features. Regarding the remaining metrics, precision, gauging the proportion of true positives among positive predictions, demonstrates better scores in the recent model for both scenarios. This outcome indicates the model's heightened success in accurately identifying positive instances. In terms of recall, which quantifies the fraction of correctly identified actual positives, a minor reduction is discernible in the recent model due to a slight elevation in False Negative values. As for the HSS metric, a marginal increase is noted in the 24-hour prediction window dataset, whereas a slight decrease is observed in the varying window dataset.

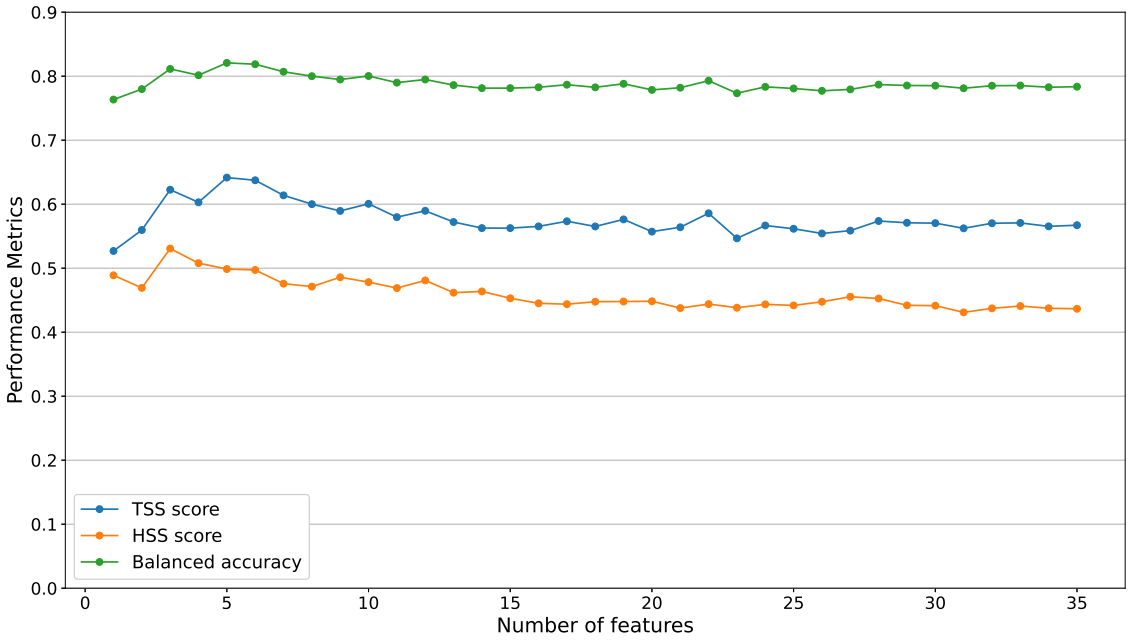

Figure 5.14: Performance metrics (TSS, HSS and BACC) as a function of number of features using LightGBM classifier for ≥C-Class with 24 hour prediction window dataset.

Given HSS's susceptibility to data imbalance, these trends inadequately represent model performance. Analysing the confusion matrices (Figure 5.19) in relation to its predecessor (Figure 5.8), it becomes evident that while a marginal decline in the accuracy of True Negatives is noticeable, the model exhibits a significantly enhanced capability to predict True Positives within both the varying prediction window and 24-hour prediction window datasets.

With regard to the ≥M-Class dataset, a notable finding is the significant increments in TSS and BACC metrics, which point to a noticeable improvement in model performance. Conversely, the metric of precision experiences a significant reduction, which can be attributed to the interplay between the scarcity of ≥M flares and a slight decrement in true negative values. This compound effect contributes to the observed decline in precision. Similar mechanisms are also evident in the context

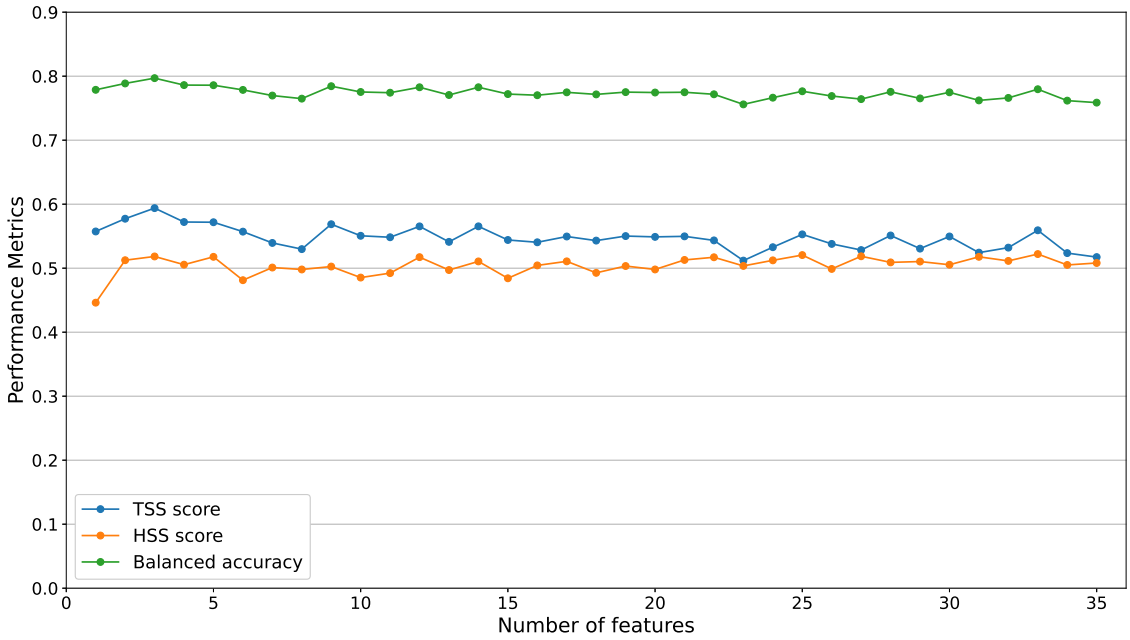

Figure 5.15: Performance metrics (TSS, HSS and BACC) as a function of number of features using LightGBM classifier for ≥C-Class with varying prediction window dataset.

of recall, where a marked increase is witnessed for the recent model. This phenomenon can be attributed to analogous underlying factors. The trend holds true for the Heidke Skill Score (HSS) metric as well, exhibiting a declining trajectory. It is imperative to emphasise that, during performance evaluation, metrics other than TSS and BACC should not be utilised due to their unsuited handling of data imbalance. Upon inspecting the confusion matrix, it becomes evident that the predictive capacity has notably improved, underscored by a significant enhancement in true positives.

5.3.3 Comparison with other similar works

We have also conducted a comparison of our results using the LightGBM model with existing studies that employed different methods, such as the Support Vector Machine (SVM) algorithm, Random Forest (RF), Long-Short Term Memory (LSTM),

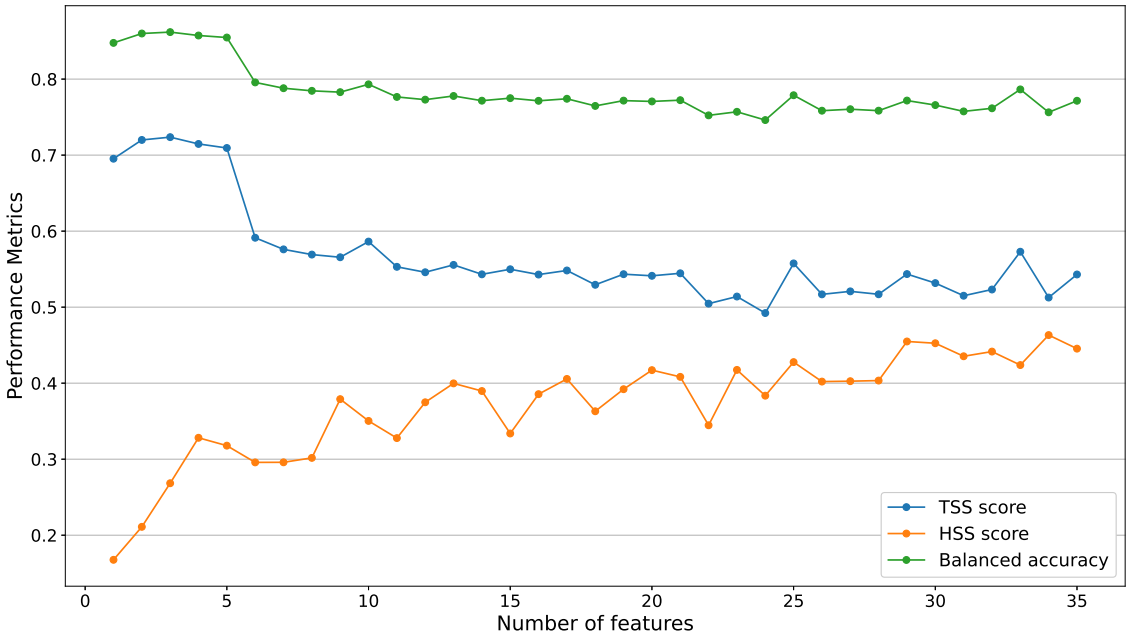

Figure 5.16: Performance metrics (TSS, HSS and BACC) as a function of number of features using LightGBM classifier for ≥M-Class with 24 prediction window dataset.

k-NN method, and Deep Flare Net (DeFN). Various studies have used diverse sets of scores or metrics to evaluate their findings. Given our aim to align our outcomes with related research, we have adopted the most commonly used evaluation measures: True Statistical Score (TSS) and Accuracy (Acc) for comparative analysis.

It is important to note that different studies in the literature have constructed datasets in varying ways, involving distinct time intervals for observations and analysis periods. Therefore, we have considered the most favourable outcomes achieved by these studies on their respective testing datasets for events of magnitude ≥M within a 24-hour period. While the presented analysis may not provide an exhaustive direct comparison of different solar flare forecasting models due to variations in data construction and analysis, our effort is to offer insights based on the chosen performance measures.

Among the available models, the Support Vector Machine (SVM) algorithm has been

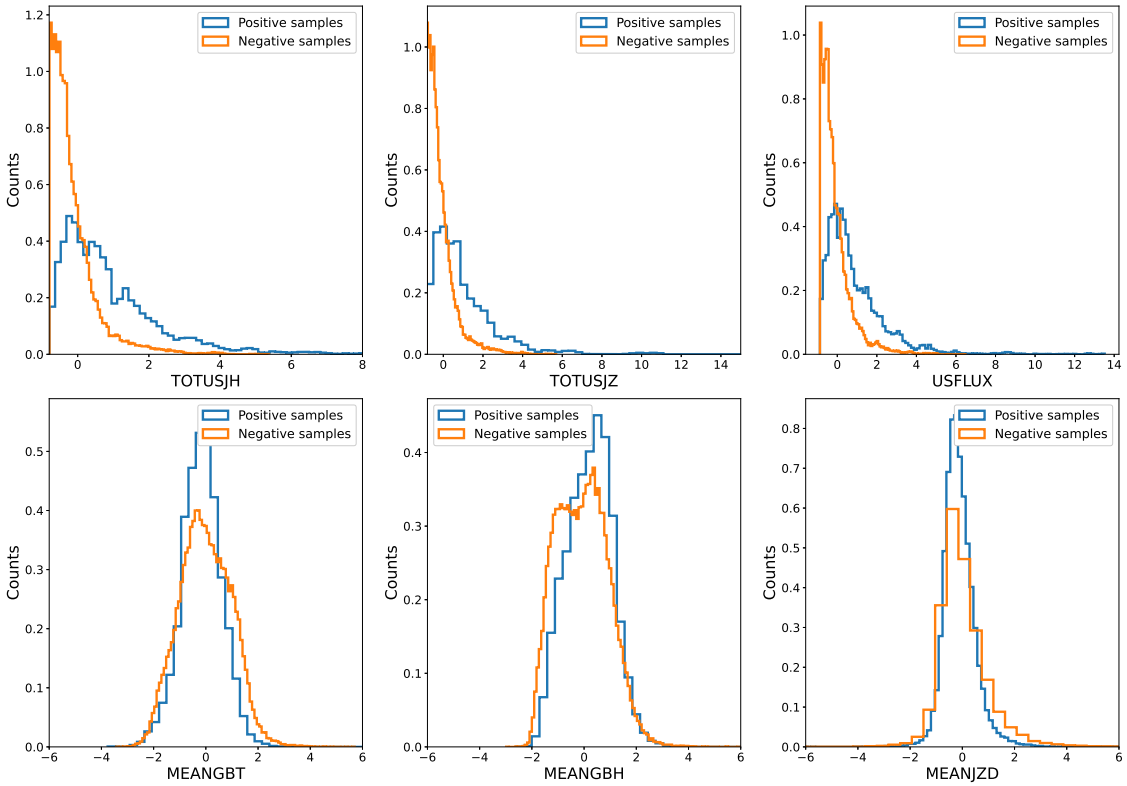

Figure 5.17: Histogram plot of various features in both positive and negative sample in dataset 1 (≥C-Class with 24 hour varying window). The top row contains the parameters from the selected set of parameters while the bottom row contains the rejected parameters.

widely used. Bobra & Couvidat [2015] used a method to select important factors and found that using 13 of these features, they got a TSS of 0.761 and Acc of 0.924. Nishizuka et al. [2017] also used the SVM algorithm, mixing vector magnetogram and UV brightening data to get a TSS of 0.87 and Acc of 0.988. Another study by Florios et al. [2018] used SVM too, and they used data over five years with 3-hour gaps to forecast ≥M flares, obtaining a TSS of 0.59 and Acc of 0.94. Additionally, Ribeiro & Gradvohl [2021] reported a TSS of 0.622 using SVM.

Some studies tried the Long Short-Term Memory (LSTM) network to predict whether an Active Region (AR) will produce a ≥M class flare within 24 hours. Liu et al.

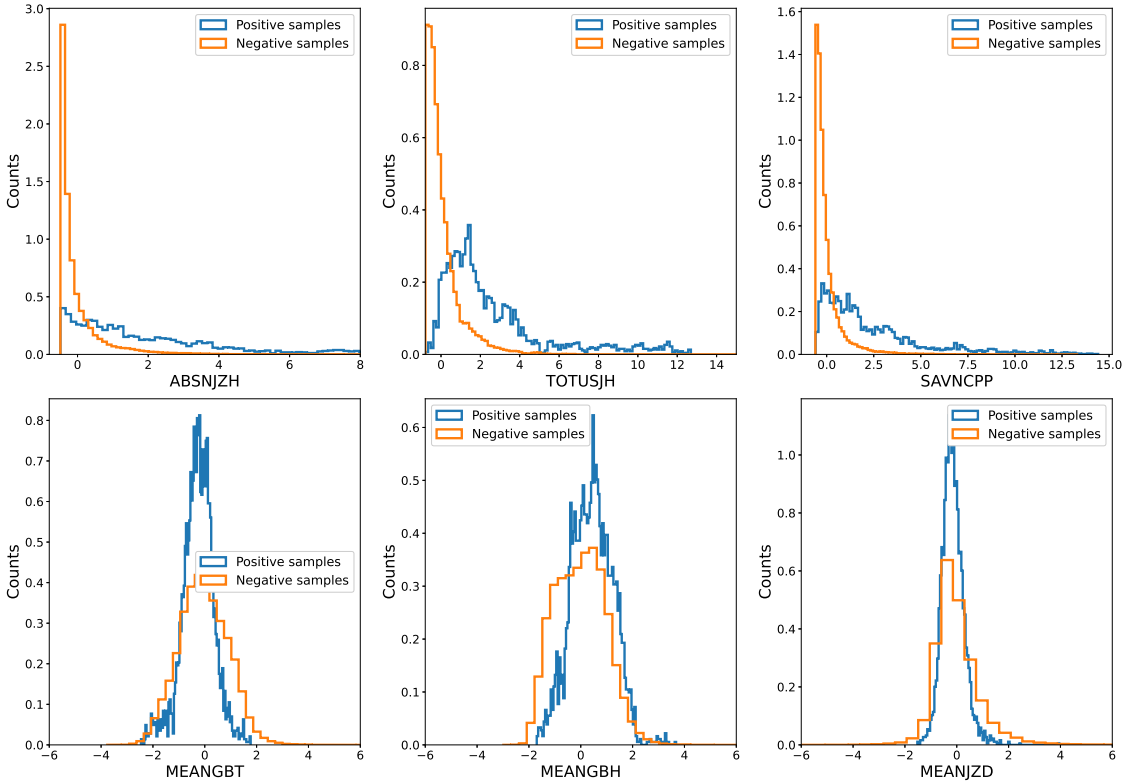

Figure 5.18: Histogram plot of various features in both positive and negative sample in dataset 2 (≥M-Class with 24 hour varying window). The top row contains the parameters from the selected set of parameters while the bottom row contains the rejected parameters.

[2019a] used this method, including 25 SHARP parameters and 15 flare history parameters, to achieve a TSS of 0.79 and Acc of 0.909.

The Random Forest (RF) algorithm has also been used for creating solar flare prediction models using machine learning. Florios et al. [2018] used RF with SDO/HMI SHARP data, getting a TSS of 0.74 and Acc of 0.93. Furthermore, Ribeiro & Gradvohl [2021] achieved a TSS of 0.63 for ≥M class solar flare prediction within 24 hours using RF.

Alongside SVM, Nishizuka et al. [2017] explored k-Nearest Neighbors (k-NN) with a TSS of 0.912 and Acc of 0.995, and Extremely Randomised Trees (ERT) with a TSS

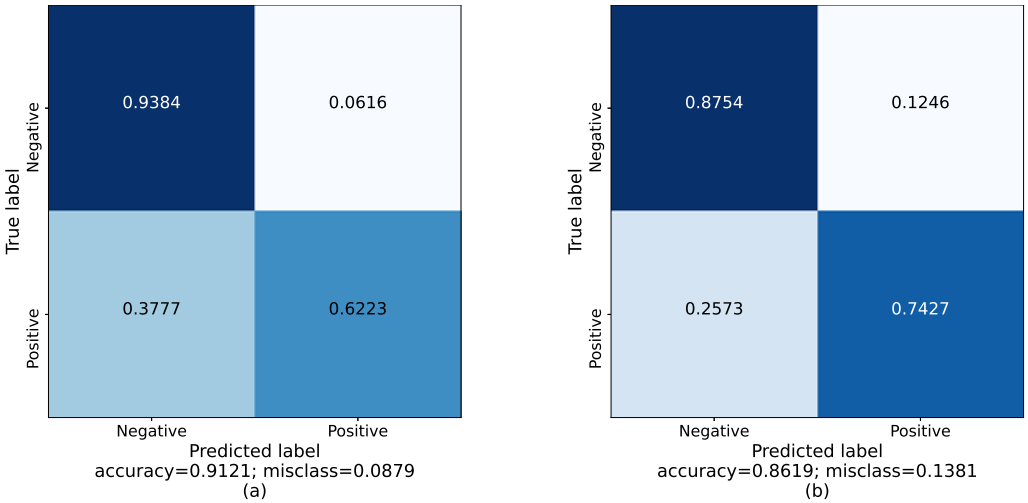

Figure 5.19: (a) Confusion matrix of test results using the highest scoring parameters in ≥C-Class dataset with varying prediction window; (b) Confusion matrix of test results using the highest scoring parameters in ≥C-Class dataset with 24 hour prediction window.

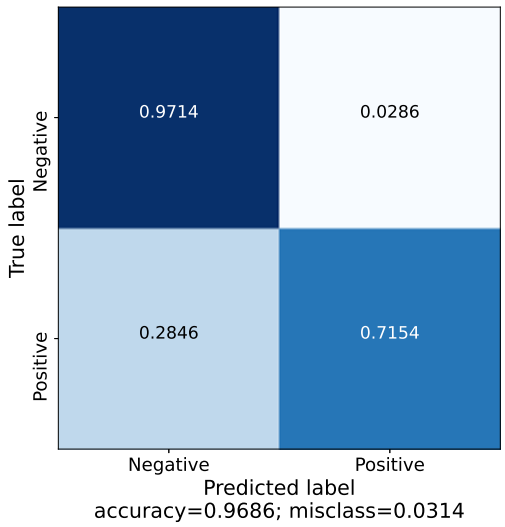

Figure 5.20: Confusion matrix of test results using the highest scoring parameters in ≥M-Class dataset with 24-hour prediction window.

of 0.71 and Acc of 0.990. Using 65 features, they found that k-NN performed better than ERT and SVM. Additionally, Nishizuka et al. [2018] used extra features like hot coronal brightening and data from SDO/AIA 131 Å and GOES X-ray emissions, to create the Deep Flare Net (DeFN) algorithm. This approach achieved a TSS of 0.802 and Acc of 0.858.

In our study, we used LightGBM and got a TSS of 0.69 and Acc of 0.970 by focusing on the top features. Similarly, Ribeiro & Gradvohl [2021] used LightGBM and got a TSS of 0.61. They also found that SVM, RF, and LightGBM gave similar TSS results.

To provide a complete picture of solar flare predictions using different methods, we used a modified Taylor diagram [Taylor, 2001]. This kind of diagram is often used to compare how well a model's forecasts match real observations. Usually, the Pearson correlation coefficient (cc) and standard deviation (std) between model's result and observation is considered. In this study, we have taken a similar approach but have used Acc and TSS values instead of cc and std.

Figure 5.21 illustrates a modified Taylor diagram presenting outcomes from distinct algorithms in comparable studies. The reference point, denoted by a black star, is set at TSS=1 and Acc=1. The distance of the marks from the center reflects their TSS value, while their position around the circle signifies their Acc value. The circles centered on the reference point indicate how closely the model outcomes resemble the ideal state of Acc=1 and TSS=1. The figure shows the results from those works in which both TSS and Acc were mentioned.

Models that are closer to the reference point, or essentially within smaller circles, exhibit stronger resemblance to Acc=1 and TSS=1. This can be a method to compare diverse model performances based on their best results. Interestingly, among the three works utilising SVM, they present notably different results, each lying in

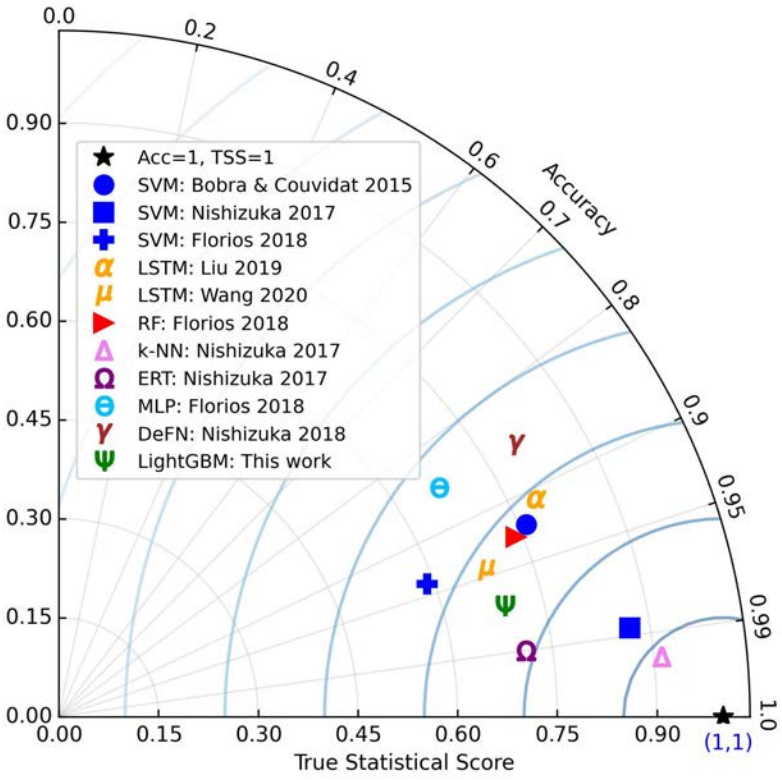

Figure 5.21: The picture depicts a modified Taylor diagram for comparing the results of solar flare prediction models using different machine learning algorithms. The radial distances from the center represent their TSS values and azimuthal positions are corresponding to Acc of their models. The position where TSS=1 and Acc=1 has been taken as the reference point for comparison.

distinct circles. Conversely, studies using LSTM demonstrate comparable outcomes, all positioned within the same circle at almost identical distances from the reference point.

Following this approach, our LightGBM-based model outperforms many prior studies, especially those utilising LSTM, RF, MLP, and DeFN. Notably, the results of Nishizuka et al. [2017] study showcase the highest performance. In this study, they employed k-NN, SVM, and ERT, with k-NN delivering the most favourable results.

The strong performance of the algorithms in Nishizuka et al. [2017] study could be

attributed to their use of a wide range of solar features. They employed a total of 65 features and demonstrated their relative importance for solar flare prediction. Their findings revealed that past flare activities, like the flare history in an Active Region (AR) and the highest X-ray intensity of the previous day, held the greatest significance. Following this, the configurations of magnetic neutral lines, unsigned magnetic flux, and the area of UV brightening were also considered highly important.

While their findings pointed to the greater significance of certain features compared to others, their results also indicated that employing all features might improve performance. In contrast, other studies have shown that utilising a more focused set of essential features could lead to equal or even better outcomes. For instance, Bobra & Couvidat [2015] explored a wide range of 25 parameters and found that using only four—total unsigned current helicity, total magnitude of the Lorentz force, total photospheric magnetic free energy density, and total unsigned vertical current—resulted in a TSS score similar to the combined top 13. Additionally, Liu et al. [2019a] demonstrated that using the 14-22 most important features, including both flare history and magnetic parameters, yielded superior performance compared to using all 40 features together (25 SHARP and 15 flare history). Our results also indicate that excluding less valuable features from the set could enhance the model's performance in predicting solar flares.

5.4 Summary and Conclusion

In this work, we used a gradient boosted decision tree classifier known as LightGBM to develop a machine learning model to predict solar flares based on observed magnetic and flaring history parameters. Using the data from SDO HMI SHARP data archive and GOES solar flare database, we prepared the final datasets for the machine learning model. Along with the 25 magnetic parameters, we also calculated 12 derived parameters to also account for the flaring history of that particular active

region. Solar flare prediction is the exact definition of an imbalanced classification problem in machine learning. This arises due to the fact that the number of non-flaring events or weak flare events (A and B class flares) far exceed the strong flares. This introduces an innate bias towards non flaring/weak flaring events while training a machine learning model. We used various techniques in preprocessing as well as in the classifier to address this issue. Borderline Synthetic Minority Over-sampling Technique (Borderline SMOTE) along with random undersampling was employed as a preprocessing step to get the ratio of the flaring and non-flaring events to be around 0.6. This reflected as an increase in the model performance thus was accepted as a part of the final classification pipeline.

For labeling the data as positive and negative samples, along with the commonly used operational algorithm we experimented with a varying labeling system which takes into account the varying levels of solar activity. Thus the model was trained and tested on three datasets: ≥C-class(varying prediction window), ≥C-Class (24 hour prediction window) and M-Class (24 hour prediction window). In the varying prediction window algorithm, the prediction window varies from 24 hours to 6 hours and then back to 24 hours while moving from the start to the end of solar cycle. This attains a minimum of 6 hours prediction window at solar maximum. While using the classifier on both the labeling methods with ≥C-Class dataset, the scores display an interesting trend where both 24 hour prediction window and the varying prediction window produce TSS scores very close to each other. This could be a result of the fact that as flares are more frequent during activity peak time, due to faster changes in magnetic activity, a 6 hr prediction window is sufficient in place of a 24 hour prediction window. But the varying prediction algorithm underachieves in the case of ≥M-Class, which can point to fact that, being a stronger class of flare, a constant 24 hour window is necessary to capture the changes in the magnetic properties as opposed to ≥C-class. It should be noted that the present study does

not extensively elaborate upon this case, as the utilisation of the varying prediction algorithm yielded notably low TSS scores, consequently rendering the algorithm inconsequential within the context of the examined scenario.

In addition to classification, we also performed feature importance study for all the magnetic and flaring history parameters. We used ANOVA F-value score to rank the features for all three datasets. Majority of the most important features aligned with already published results. While comparing varying and 24 hour prediction window datasets for C-Class flares, we observed a higher importance for C-Class flare decay value in varying prediction window dataset. This could be concluded as a result of the lower prediction window at solar maximum letting the model learn only the corresponding samples that affects the observed flare. Apart from this, both the datasets displayed the same top features even though the order was slightly different. For the M Class dataset, the feature importance is similar to that we see for C-Class, except for the fact that MDEC and MHIS showed a higher importance. To properly observe the importance of selecting the right features, we ran the classifier with only the top five features. This confirmed that if we remove the less useful features from the feature set, the model could display a better performance when it comes to flare prediction.

We also compared our results with other similar solar flare prediction models, assessing their relative performance through a Taylor diagram based on their optimal TSS and Acc values. Our LightGBM-based model demonstrated better performance over various other models, especially those employing LSTM, RF, MLP, and DeFN, when a limited but highly significant set of features was used. However, the models presented in Nishizuka et al. [2017] yielded better results than ours. Notably, they utilised a more extensive set of features—65 in total—compared to other models in the literature. Despite this, multiple studies, including our own, suggest that focusing on a subset of highly significant features can improve predictive accuracy.

This observation opens up an intriguing question regarding the optimal number of features for solar flare prediction: is a larger or smaller set more effective? To address this question comprehensively, further analysis involving model comparisons and in-depth feature selection assessments is required.

In the future, with more magnetic data of multiple solar cycles, we aim to improve the performance of the classifier as well as perform more comprehensive study on relative significance of features. During our trial runs, we noticed that instead of using consecutive time frames for training, validating, and testing datasets, if we randomly split the whole data into these datasets, the performance of the models is much better. Therefore, by using solar magnetic data from multiple cycles, we may achieve better accuracy with the solar flare prediction model.

Chapter 6

CME-CME Interaction: Ensemble Study

This chapter is structured based on the paper titled "Study of Evolution and Geo-effectiveness of CME-CME Interactions Using MHD Simulations with SWASTi Framework" by Prateek Mayank, Stefan Lotz, Bhargav Vaidya, Wageesh Mishra, and D. Chakrabarty [accepted for publication in ApJ].

When multiple CMEs erupt in quick succession, their interactions — known as CME-CME interactions — can significantly amplify their space weather effects. These interactions take place when a faster CME overtakes a slower one, resulting in a complex interplay between their shocks, magnetic fields, and plasma structures. Due to the inherent complexities and the limitations of observational and simplified analytical approaches, MHD ensemble simulations with realistic solar wind backgrounds and flux rope CMEs provide a valuable means to gain a comprehensive, global perspective. This chapter focuses on identifying global trends and understanding the impact of initial CME properties on the geo-effectiveness of CME-CME interactions using the SWASTi framework.

6.1 Numerical Models

To perform the ensemble study of CME-CME interactions within a realistic solar wind background, we utilized the Space Weather Adaptive SimulaTion framework [SWASTi; Mayank et al., 2022, 2023]. The three-dimensional physics-based models for solar wind and CMEs are described in the following subsections. Additionally, an empirical Dst relation, based on in-situ plasma properties, has been employed to analyze the geo-effectiveness of these energetic events. The relevant equations and comparisons with some specific events are presented in subsequent subsections.

6.1.1 Solar Wind Model

In order to simulate the background solar wind, we used observation based input from GONG magnetogram, which provides the magnetic field at solar surface. The fieldlines are then extrapolated to source surface using the potential field source surface [PFSS; Altschuler & Newkirk, 1969b] technique. Based on this extrapolation, the solar wind speed at the initial boundary of the MHD domain (V_{in}), located at 0.1 AU, is determined using a modified version of the Wang-Sheeley-Arge relation [WSA; Arge, 2003]:

$$V_{in} = v_1 + \frac{v_2}{(1+f_s)^{\frac{2}{9}}} \times \left(1.0 - 0.8\, exp\left(-\left(\frac{d}{w}\right)^{\beta}\right)\right)^3 \tag{6.1}$$

where, v_1, v_2, and β are parameters set at 250 km s^{-1}, 675 km s^{-1}, and 1.25, respectively. f_s represents the areal expansion factor of the flux tube, d is the minimum angular separation of the foot-point from the coronal hole boundary, and w is the median of d for field lines that extend to Earth's location. The initial density at 0.1 AU was estimated by equating the kinetic energy due to obtained WSA speed with that of the fast solar wind. Here we have assumed fast wind parameters as $n_{\rm fsw}$ = 200 cm^{-3} and speed $v_{\rm fsw}$ = 600 km s^{-1}. The temperature was determined based on constant thermal pressure of 6.0 nPa. The magnetic field was derived from a velocity-dependent empirical relation. For detailed methodology, readers can refer

to Section 2 of Mayank et al. [2022]. In this study, magnetic field strength ($B_{\rm fsw}$) associated with fast solar wind is assumed to be 300 nT at the MHD domain's initial boundary.

After setting the necessary parameters at 0.1 AU based on the semi-empirical coronal model, the time-dependent 3D ideal MHD equations were solved using the PLUTO code [Mignone et al., 2007a]. Computations were conducted on a uniform static grid in spherical coordinates, employing a finite volume method for the simulation. The set of conservative equations used in the MHD simulations is outlined in Mayank et al. [2022], with a specific heat ratio of 1.5 for to the solar wind plasma. The computational domain for the heliosphere extended from 0.1 AU to 2.1 AU radially (r), $\pm 60^\circ$ azimuthally (θ), and 0° to 360° meridionally (ϕ), structured on a grid resolution of $512 \times 61 \times 181$.

6.1.2 CME Model

To simulate magnetized CMEs, we employed the CME module of SWASTi framework [Mayank et al., 2023], which is based on the Flux Rope in 3D [FRi3D; Isavnin, 2016] model. This model incorporates the three-dimensional magnetic field configuration of a CME and accounts for major deformations to accurately reconstruct its global geometrical shape. In this study, the FRi3D model was used to construct the 3D magnetized shell of the CME at 0.1 AU, serving as the initial state for the MHD domain. The CME geometry forms a classic croissant-like shape anchored at both ends to the Sun in the beginning and then cut for non-hindrance eruption of the trailing CME.

Initially, the cross-section of the CME is assumed to be circular, with the radius varying in proportion to the heliocentric distance. The CME structure is populated with magnetic field lines that have a constant twist of two. In this work, the center of the CME footpoints was set at 0° latitude and 0° longitude. All CMEs had the

following fixed parameters: flattening = 0.5, pancaking = 0.6, chirality = -1, polarity = -1, half-width = 45°, and half-height = 22.5°. Other properties were varied in the ensemble study, with their exact values detailed in Section 6.2.

Once the FRi3D CME structure is formed with its leading edge at 0.1 AU, it is allowed to evolve in the MHD domain. The process of integrating the CME into the MHD domain involves gradually updating the boundary conditions to match the evolving CME structure, ensuring a smooth transition and accurate representation of the CME's impact on the surrounding solar wind. Overall, the use of flux rope CME model in this study provides a detailed and realistic simulation of CME-CME interactions, allowing for a comprehensive analysis of their evolution, and the influence of initial conditions on geo-effectiveness.

6.1.3 Dst Estimation

We use the pressure-corrected Dst index (Dst*) to quantify the geoeffectiveness of the simulated CME plasma cloud. Dst* estimates the storm time ring current strength without the influence of magnetopause and quiet time ring currents [O'Brien & McPherron, 2000]. There are many other indices that may be used to describe the coupling between solar wind and magnetosphere [see Lockwood, 2022, for a good summary] but since we are most interested in the kind of intense events that would arise from the effect of merged CMEs on the geomagnetic field, we feel that Dst is an appropriate proxy for this study. The intensity of a simulated storm will be quantified by the sum of the simulated Dst* over the duration of the event.

6.1.3.1 Empirical Relation

To quantify the geoeffectiveness of the CME-CME structure upon its arrival at 1 AU, we positioned virtual spacecraft within the simulation domain at 0° (along Sun-Earth line) and ±10° longitudes. These virtual spacecraft recorded the plasma properties in real-time with a 5-minute cadence. Based on these in-situ properties,

the Dst index at each time step was computed using the following empirical equations provided by O'Brien & McPherron [2000]:

$$\frac{dDst^*}{dt} = Q(t) - \frac{Dst^*}{\tau}, \tag{6.2}$$

$$Q = -4.4(VB_S - 0.5), \tag{6.3}$$

$$\tau = 2.4 \exp\left(\frac{9.74}{4.69 + VB_S}\right), \tag{6.4}$$

$$VB_S = \begin{cases} |VB_z| & \text{if } B_z < 0, \\ 0 & \text{if } B_z \geq 0. \end{cases} \tag{6.5}$$

$$Dst^* = Dst - b\sqrt{P_{dyn}} + c, \tag{6.6}$$

Here, Dst* represents the corrected Dst index, accounting for magnetopause current contamination, with constants $b = 7.26$ (nT/$\sqrt{nPa}$) and $c = 11$ (nT). The parameter Q (nT/hr) denotes the rate of energy injection into the ring current, while τ (hr) represents the decay time of the ring current, influenced by particle loss to the atmosphere. The variables V and P_{dyn} are the plasma speed and dynamic pressure, respectively, and B_z is the Z-component of the magnetic field in geocentric solar magnetospheric (GSM) coordinates. The considered units of $|VB_z|$ and P_{dyn} are mV/m and nPa, respectively. Dst* is used to perform time integration, and the model output Dst is calculated from Equation 6.6. Additionally, in order to convert the in-situ plasma properties into the Dst indices, an initial Dst value is required. Since we can't have observed initial Dst values for the ensemble simulations conducted in this work, we have taken this value to be 0 nT. However, the initial value of Dst doesn't effect the overall result.

6.1.3.2 Comparison with Observations

Although the efficiency of the above empirical Dst relation has been extensively demonstrated by O'Brien & McPherron [2000], we sought to verify its performance for significant geoeffective events in recent years. To test this relation, we compared the Dst values derived from the model with OMNI 1-hour data. Specifically, we examined CME events occurring during Carrington rotations (CR) 2165, 2194, and 2270, which included five interacting CMEs, two interacting CMEs, and one single CME, respectively. For these comparisons, the initial Dst values required for the model were set to match the observed Dst values at the initial time for CR.

Figure 6.1 presents the comparison between the modeled and observed Dst values. Subplots (a1) and (a2) depict the observed in-situ plasma properties at L1 (speed, density, and IMF B_z component). The estimated Dst, based on these values, is broadly accurate and captures most of the storm's features, such as the momentary rise in Dst due to a short-period northward IMF on June 1, 2023 (see Figure 6.1. a3). The onset of the initial phase of Dst and the duration of the main phase in the model output also match nicely for all three CRs. However, some finer structures are missed, such as the sudden commencement on August 18, 2017 (panel b), and the model shows some discrepancies in the magnitude of the storm's recovery phase.

The statistical results are promising, with Pearson correlation coefficient (cc) values ranging from 0.92 to 0.94 and root mean square error (rmse) values between 18 and 27 nT, corresponding to an error margin of roughly 9 to 17%. This strong agreement indicates that the empirical relation is reliable for comparative studies between events, which is the primary application in this work for comparing the Dst values across different ensemble cases.

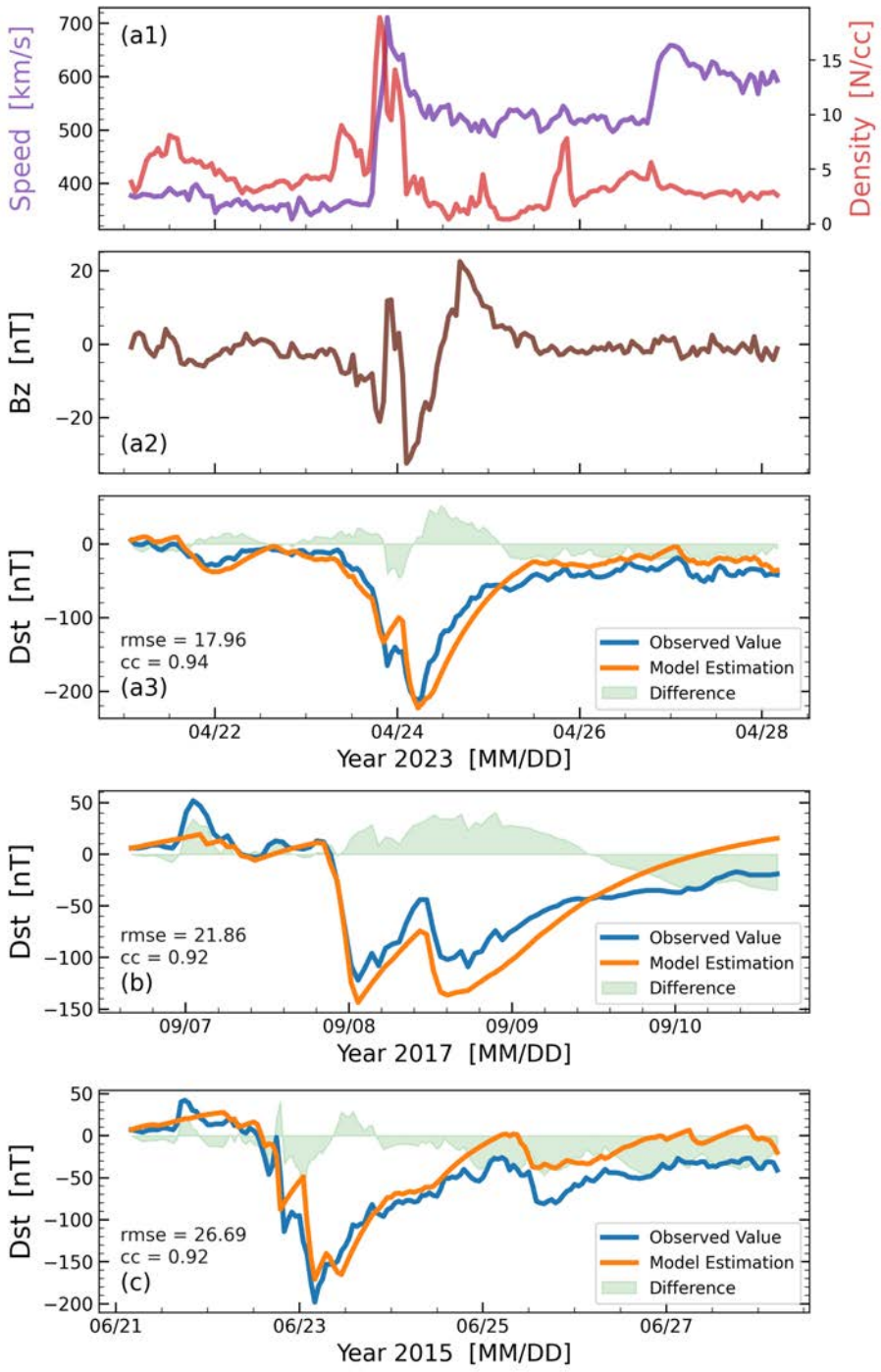

Figure 6.1: Comparison of observed Dst and the estimated values as described in equations (6.2)-(6.6). The top three panels show the observed solar wind speed, density, B_z, and Dst values for CR2270, along with the estimated Dst values and the error. The bottom two panels show the observed versus estimated Dst values for CR2194 and CR2165.

Table 6.1: CME initial properties of all the ensemble cases.

Case No.	Name	Vel_t ($10^3 kms^{-1}$)	Density ($10^{-18} kgm^{-3}$)	Magnetic Flux ($10^{12} Wb$)	Tilt (degree)
Case 0	Single CME	$v_t1 = 0.8$	$\rho1 = 3$	$\Phi_B1 = 7$	$\tau1 = 0$
Case 1	LSLDLF0	$v_t2 = 1$	$\rho2 = 1$	$\Phi_B2 = 5$	$\tau2 = 0$
Case 2	LSLDLF1	$v_t2 = 1$	$\rho2 = 1$	$\Phi_B2 = 5$	$\tau2 = 45$
Case 3	LSLDHF0	$v_t2 = 1$	$\rho2 = 1$	$\Phi_B2 = 9$	$\tau2 = 0$
Case 4	LSLDHF1	$v_t2 = 1$	$\rho2 = 1$	$\Phi_B2 = 9$	$\tau2 = 45$
Case 5	LSHDLF0	$v_t2 = 1$	$\rho2 = 5$	$\Phi_B2 = 5$	$\tau2 = 0$
Case 6	LSHDLF1	$v_t2 = 1$	$\rho2 = 5$	$\Phi_B2 = 5$	$\tau2 = 45$
Case 7	LSHDHF0	$v_t2 = 1$	$\rho2 = 5$	$\Phi_B2 = 9$	$\tau2 = 0$
Case 8	LSHDHF1	$v_t2 = 1$	$\rho2 = 5$	$\Phi_B2 = 9$	$\tau2 = 45$
Case 9	HSLDLF0	$v_t2 = 1.1$	$\rho2 = 1$	$\Phi_B2 = 5$	$\tau2 = 0$
Case 10	HSLDLF1	$v_t2 = 1.1$	$\rho2 = 1$	$\Phi_B2 = 5$	$\tau2 = 45$
Case 11	HSLDHF0	$v_t2 = 1.1$	$\rho2 = 1$	$\Phi_B2 = 9$	$\tau2 = 0$
Case 12	HSLDHF1	$v_t2 = 1.1$	$\rho2 = 1$	$\Phi_B2 = 9$	$\tau2 = 45$
Case 13	HSHDLF0	$v_t2 = 1.1$	$\rho2 = 5$	$\Phi_B2 = 5$	$\tau2 = 0$
Case 14	HSHDLF1	$v_t2 = 1.1$	$\rho2 = 5$	$\Phi_B2 = 5$	$\tau2 = 45$
Case 15	HSHDHF0	$v_t2 = 1.1$	$\rho2 = 5$	$\Phi_B2 = 9$	$\tau2 = 0$
Case 16	HSHDHF1	$v_t2 = 1.1$	$\rho2 = 5$	$\Phi_B2 = 9$	$\tau2 = 45$

6.2 Ensemble Cases

To investigate the evolution and geo-effectiveness of CME-CME interaction events, we conducted a series of simulations involving two interacting CMEs, with second CME having varying attributes. The primary objective was to understand how alterations in initial coronal properties — such as speed, density, and magnetic flux — affect their interaction, in-situ properties and the Dst index at 1AU. This focus is driven by the understanding that in-situ speed, density, and the southward magnetic field component play a pivotal role in determining the intensity of geomagnetic storms. Therefore, assessing the effects of these initial conditions at 1 AU is crucial. Moreover, recent research highlighting the significance of CME tilt in heliospheric evolution [Lugaz et al., 2013; Mayank et al., 2023] prompted us to also examine the

impact of relative tilt between interacting CMEs.

For this ensemble simulation, we selected the background solar wind conditions from the Carrington rotation (CR) 2270 period, corresponding to April 2023. This period was particularly significant due to an intense geomagnetic storm caused by a halo CME eruption. The Dst values of this CME have been discussed in Section 6.1.3.2, where the empirical Dst is compared with the observed values. In the simulation, the first CME (hereafter referred as CME1) was injected at the inner-boundary (0.1 AU) on 2023-05-12 3:00, with the second CME (hereafter referred as CME2) following 25 hours later. This schedule was optimised to ensure that the CME2 reaches 0.1 AU after the complete insertion of CME1 in the computational domain and they have significant interaction before reaching 1 AU.

Several studies have highlighted the influence of ambient solar wind on CME evolution [Mayank et al., 2023; Temmer et al., 2011; Wu et al., 2016]. To ascertain if similar impacts are present in CME-CME interactions, this study analyzes in-situ profiles at three different longitudinal positions: 0° and ±10°. Here, 0° corresponds to the Sun-Earth line, while -10° and +10° represent the eastern and western sides of the solar disk, respectively. Additionally, the projected trajectory allows the CME1 to interact with a stream interaction region (SIR), thereby enabling a detailed study of the potential impact of inhomogeneity in ambient solar wind.

To determine the optimal number of cases for the ensemble study, our objective was to select a sufficient number of cases to identify the trends in the properties while ensuring each case could be thoroughly analyzed. To examine the effects of speed, density, and magnetic flux, we varied these parameters for the CME2 while keeping the CME1's values constant. Specifically, for the CME2, we employed two sets of density and magnetic flux values, one set lower and another higher than the CME1's values. Furthermore, we chose two velocity values for the CME2, both higher than the first's and increasing incrementally, to guarantee their interaction before 1 AU.

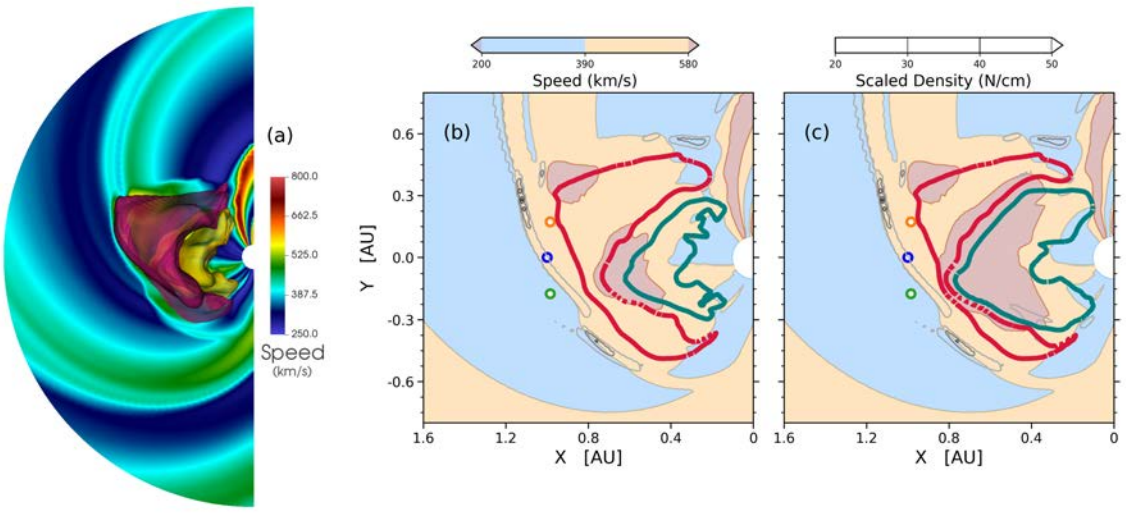

Figure 6.2: The subplot (a) demonstrates the traced 3D structures of leading and trailing CMEs with 2D snapshot of the solar wind speed in the equatorial plane. Subplots (b) and (c) show the traced boundary of CME structures for cases LSLDLF0 and LSHDLF0. Additionally, the three dots - blue, green and orange - represents the location of virtual spacecrafts at 0° and ±10°.

Regarding the relative tilt, two tilt angles were applied to the CME2 while the tilt of CME1 was kept constant. The overarching approach was to maintain consistent properties for the CME1 across all cases, thereby enabling a direct comparison with single CME1 simulation.

The specific values of the properties for the various cases are presented in Table 1. With two values for each of the four properties, the total number of cases in this ensemble study amounts to 16. The density of the CMEs was set of the order of 10^{-18} kgm^{-3} [Temmer et al., 2021], while the magnetic flux values were between 10^{12} - 10^{13} Wb [Scolini et al., 2020]. The CME apex speed values ranged approximately from 1300 to 1500 kms^{-1}, and the tilt values were 0° and 45°. To facilitate clear and easy reference during discussion, each case has been assigned a specific nomenclature. This naming convention consists of four elements: the first two letters denote low speed (LS)/high speed (HS) CME, followed by a pair of letters for low/high density

and magnetic flux, respectively. The final character in each case name denotes the tilt, with '0' representing no tilt and '1' indicating a 45° tilt. For example, the name 'HSHDLF1' corresponds to a case with higher speed, higher density, lower magnetic flux, and a 45° tilt of CME2 with respect to first. Additionally, a simulation of just the CME1 was conducted to serve as a basis for comparing all interaction cases, thereby highlighting the impact of such interactions on the front CME.

Figure 6.2 (a) presents a snapshot capturing the evolution of two interacting CMEs in the inner heliosphere, corresponding to the LSLDLF0 case as CME1 reaches 1 AU. It reveals 2D cross-section of the speed profile along the $r - \phi$ plane at 0° latitude, alongside 3D isosurfaces of CMEs. The background solar wind speed is depicted using a color map, with CME1 outlined in dark red and CME2 in a yellow-green hue. This image also illustrates the asymmetric expansion of CME1's leading edge, shaped by the variable speeds of the ambient solar wind streams.

Subplot 6.2(b) provides a detailed cut-out from 6.2(a), while subplot 6.2(c) is akin to 6.2(b) but represents the LSHDLF0 case. The red and teal colored contours represent the traced boundaries in the equatorial plane of the 3D CME structures shown in 6.2(a). These subplots showcase the filled contours for speed, as well as line contours for scaled density. The three dots at 1 AU mark the positions of virtual spacecrafts measuring in-situ plasma properties at 0° and ±10° longitudes. Notably, there is a fast stream at $\phi = -10°$, a slow-speed stream at $\phi = +10°$, with $\phi = 0°$ location approximately at the juncture of these streams. Due to which, the disparity in the expansion of CME1's flanks is apparent along these longitudes, with the top flank showing more pronounced expansion compared to the bottom flank. The SIR have higher density, as compared to fast or slow streams, making them more effective in compressing CME1 when CME2 approaches from behind, as depicted in subplot 6.2(c). Here, the intensified compression along -10° longitude is clearly visible.

It is important to emphasize that regions of high speed do not necessarily represent

shock structures but rather highlight areas where the speed exceeds 580 km/s. And on comparing the 6.2(b) and 6.2(c) subplots, the area of high speed region is much more in later case. In other words, strength of shock associated to CME2 is stronger for high density case. Additionally, the expansion of CME2 is also more in 6.2(c), leading to more compression of CME1. A more detailed analysis on the evolution of the CMEs in the heliosphere is discussed in the subsequent section.

6.3 Evolution in Heliosphere

One of the key aspects of CME-CME interaction is the change in their properties as they traverse the inner heliosphere. The nature and extent of this interaction play a critical role in determining their characteristics upon reaching Earth. These alterations directly affect space weather forecasting, underscoring the importance of understanding these dynamic processes. Through ensemble 3D MHD simulations with realistic solar wind conditions, we have sought to explore the following dynamics.

6.3.1 Shock Dynamics

The complex process of CME-CME interaction can be segmented into progressive phases based on the trailing shock associated with CME2. Lugaz et al. [2005] identified four distinct stages:

1. the shock propagates through the solar wind before reaching the rear of CME1,
2. upon impact, the shock advances inside CME1,
3. subsequently, the shock begins interacting with the sheath of CME1,
4. finally, the merging of the shocks commences.

All interaction scenarios evolve through these stages, and depending on the properties of the CMEs, the specific stage at which they arrive at 1 AU may vary.

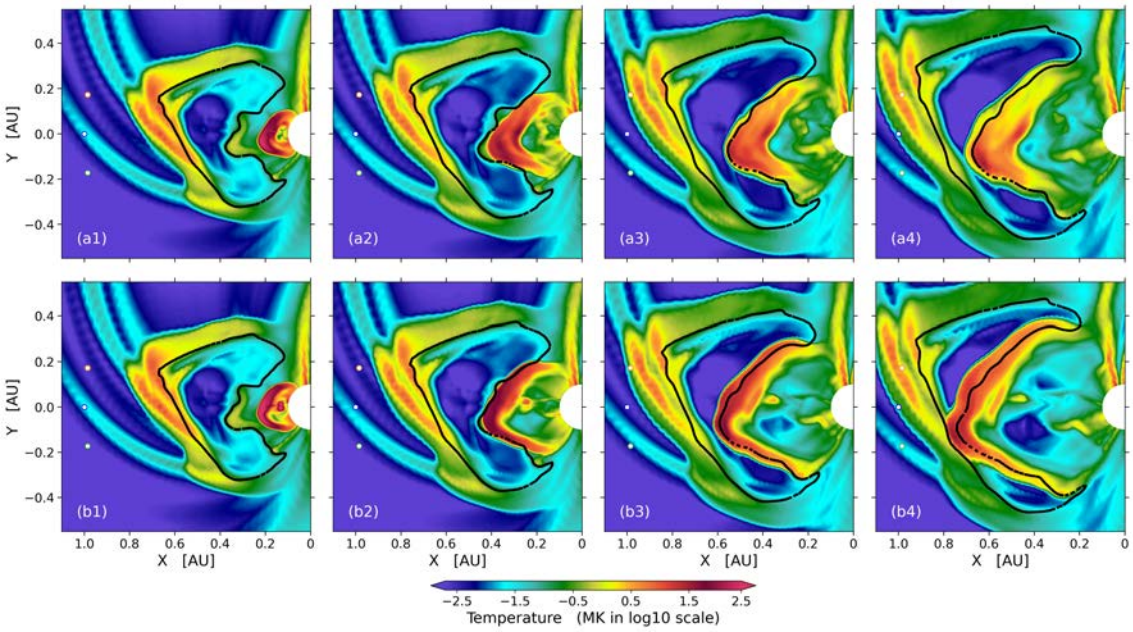

Figure 6.3: The subplots demonstrates the evolution of trailing shock in the inner-heliosphere for cases LSLDLF0 (a1-a4) and LSHDLF0 (b1-b4). The displayed colormap is corresponding to the plasma temperature in the logarithmic scale.

Figure 6.3 demonstrates these evolutionary stages. The subplots display the temperature profile in a logarithmic scale, emphasizing the sharp gradient of the shock associated with CME2. Subplots (a1) to (a4) pertain to the LSLDLF0 case, while subplots (b1) to (b4) relate to the LSHDLF0 case, each separated by a time interval of 6.65 hours. The only difference between the upper and lower rows is the density of CME2. Although initially similar, as time progresses, significant differences emerge. The interaction commences earlier in the HD case, with the trailing shock penetrating deeper into the leading magnetic cloud than in the LD case. As CME1 reaches 1 AU, the HD case nearly reaches stage 4, while the LD case has just entered stage 3. Notably, when different longitudes are considered, both cases exhibit varying stages at each location. Thus, depending on the portion of the CME-CME interaction structure encountering Earth, it may be at a different stage of evolution.

6.3.1.1 Non-uniform Shock Interaction

Most of the previous studies [Lugaz et al., 2017, and references therein] have focused on defining a single stage for the entire CME-CME interaction structure. However, given the relatively small scale of Earth's magnetosphere compared to the CME structure, examining the evolution of these stages at different longitudes is critical. For instance, the structures passing through the 1 AU locations marked by three dots in Figure 6.3 at 0° and ±10° longitudes are at different stages. The trailing shock does not extend to the sheath of CME1 along the -10° longitude in any of the cases. The radial evolution of this shock is greater along 0° and even more so along +10°, where it interacts with the sheath and merges with the first shock in some instances. The uneven evolution of these stages is primarily caused by the deformation of CME1 due to the ambient solar wind preceding it, particularly due to the SIR in front of it in these specific situations. This SIR positions the top flank of the CME predominantly within the fast solar wind stream, while the bottom flank experiences a significantly stronger anti-radial drag force. This dynamic results in an overexpansion of the upper flank and an underexpansion of the lower flank, as depicted in Figure 6.2.

This 4-stage evolution concept can be applied both globally across the entire structure and locally along different longitudes to study the progression of CME-CME interactions comprehensively. To facilitate a robust comparison of different cases with varying initial properties, it is crucial to identify both global and local stages. For this purpose, we utilized the concept of virtual spacecraft to observe the in-situ plasma conditions at the front and rear of CME1 along three longitudes (0°, and ±10°). Six comoving virtual spacecraft were positioned, with three at the rear and three at the front of CME1. Figure 6.4 displays the in-situ speed profiles collected by these spacecraft for the HSHDLF0 case. In the top subplot (6.4a), the solid lines represent data from the rear of CME1, while the dashed lines are from the front. At

the rear of CME1, the trailing shock arrives with a time difference of 1 hour between the ±10° longitudes, resulting in a similar speed jump along these longitudes due to the equivalent shock propagation time. However, at the front of CME1, the arrival time difference of the trailing shock between these longitudes is much larger. This is because the radial width of CME1 varies significantly between +10° and -10° longitudes, leading to an enhanced temporal gap in shock arrival. Furthermore, since the radial width is more along -10° shock travels a longer distance and loses more energy, resulting in a smaller speed jump compared to +10°.

6.3.1.2 Shock Propagation Duration

For comparison across all ensemble cases, we focused on the +10° longitude to study the properties of shock propagation. This approach examines the time it takes for the trailing shock to travel from the rear to the front of CME1, a duration primarily influenced by two factors: the radial width of CME1 and the strength of the trailing shock. Given that the CME1 properties remain consistent across all cases, the strength of the trailing shock emerges as the sole determinant of this duration. The bottom left and right subplots in Figure 6.4 illustrate the arrival and departure times of the trailing shock from the CME1 structure, revealing two distinct behaviors influenced by the initial density of CME2. The speed jump due to the shock was consistently higher in all HD cases compared to all LD cases. Although HD cases had similar arrival times, the sharpness of the shock was greatest in the HSHDHF case and least in the LSHDLF case. As the trailing shock reaches the front of CME1, the temporal differences between the cases become more pronounced, with the shock propagation duration for the strongest (HSHDHF0) and weakest (LSLDLF1) shock cases widening from 13.3 to 28.26 hours.

The trailing shock propagation time (Δ) for all ensemble cases is presented in Table 2. The duration is shortest for the HSHDHF case in both with and without rela-

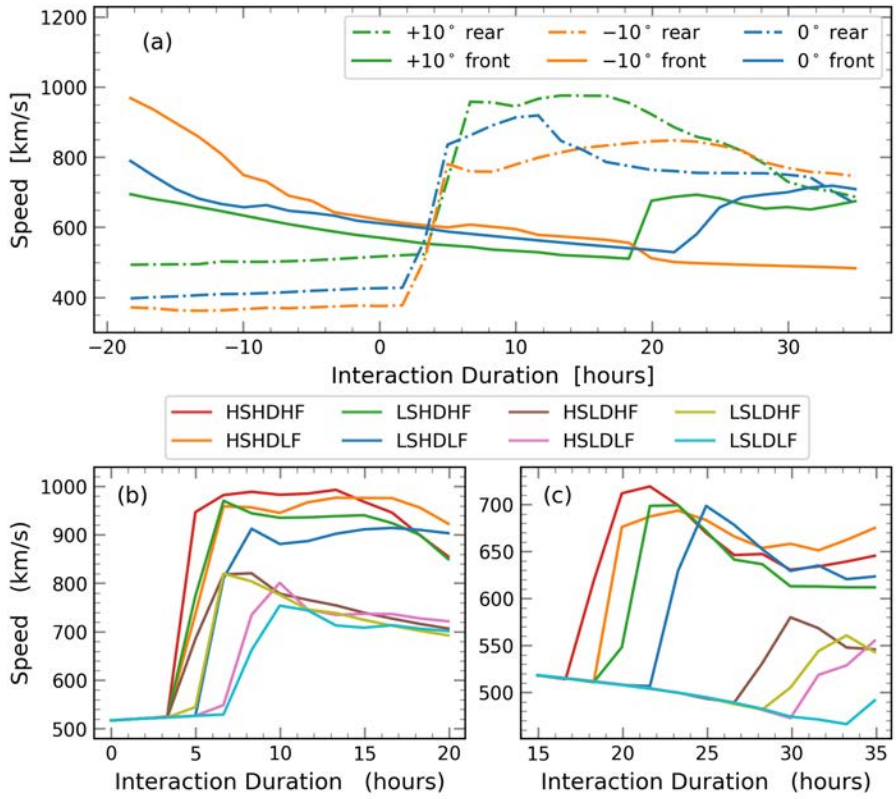

Figure 6.4: The arrival of trailing shock at the rear and front of CME1. Subplot (a) shows the result for HSHDLF0 case along 0° & ±10°. (b) depicts the speed variation at the rear of CME1, along -10°, for all cases with 0° tilt. Similarly (c) shows the speed at the front of CME1.

tive tilt scenarios, and progressively increases as the initial flux, speed, and density decrease, with the longest duration observed in the LSLDLF case. Cases with a higher initial density consistently exhibit shorter Δ values. Since this duration is directly correlated with shock strength, it suggests that higher density CMEs generate stronger shocks. Elevated density leads to an increase in internal pressure within the CME, which amplifies the pressure differential with the ambient solar wind. This, in turn, results in an accelerated rate of CME expansion. Moreover, greater momentum allows the CME to plow more effectively through the solar wind plasma, especially in the low-density environment of the preconditioned solar wind.

Table 6.2: Trailing shock propagation time inside CME1 for all ensemble cases.

Cases without Tilt	Δ (hr)	Cases with Tilt	Δ (hr)
HSHDHF	13.30	HSHDHF	16.62
HSHDLF	14.96	HSHDLF	16.62
LSHDHF	14.96	LSHDHF	18.28
LSHDLF	16.62	LSHDLF	19.95
HSLDHF	23.27	HSLDHF	24.93
HSLDLF	23.27	HSLDLF	24.93
LSLDHF	23.27	LSLDHF	24.93
LSLDLF	26.60	LSLDLF	28.26

Therefore, a combination of a faster expansion rate and more efficient plowing contributes to the observed trend. Furthermore, cases with 0° tilt consistently show smaller Δ values compared to those with 45° tilt. This could potentially be due to the preconditioned solar wind: CME2, having no relative tilt, follows the same trajectory as CME1 and encounters less drag force from the low-density solar wind swept by CME1. However, with non-zero relative tilt, the structure of CME2 does not completely align with the cleared path and faces greater resistance from the ambient solar wind, potentially leading to a reduction in shock strength.

6.3.1.3 Reverse Shock Formation

As the trailing shock progresses inside the first magnetic cloud, the rear CME begins colliding with the first. This collision starts in stage 2, where the trailing shock accelerates the rear of CME1. Depending on the advancement of the shock, the difference in speed between the rear of CME1 and the front of CME2 can exceed or fall below the local fast magnetosonic speed. When this speed is exceeded, the trailing CME pushes the plasma faster than the leading CME can smoothly adjust, leading to the formation of a shock wave directed towards CME2.

Fast reverse shocks associated with SIRs and their corresponding in-situ properties have been well studied [Kilpua et al., 2015; Oliveira, 2016]. However, their formation

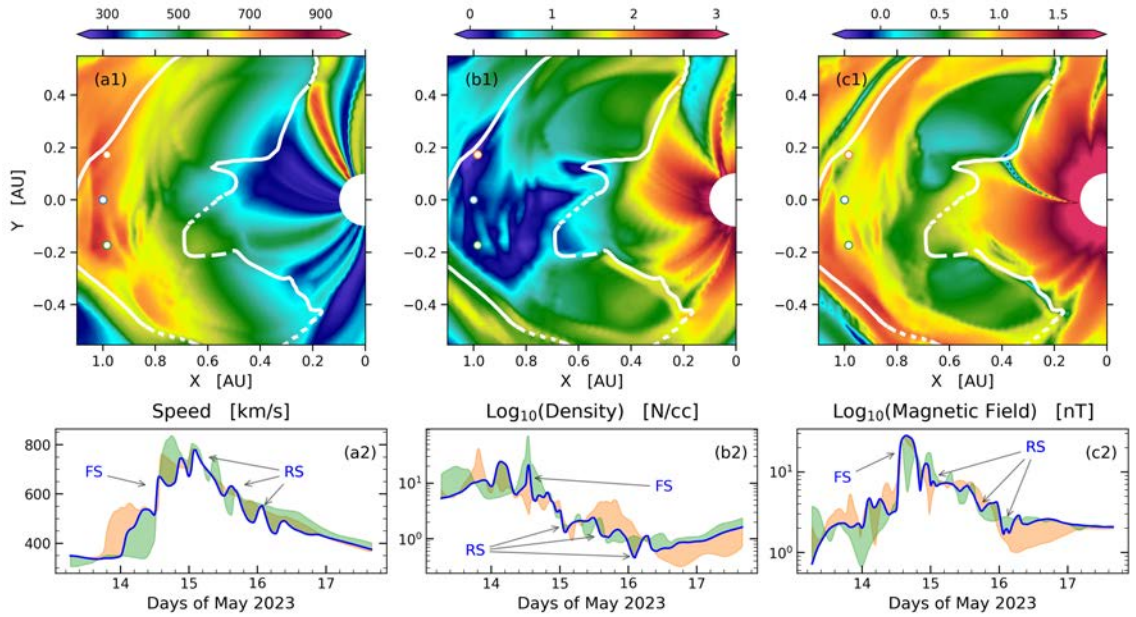

Figure 6.5: The picture showcases the reverse shocks propagation inside CME2 in the 2D snapshot of (a1) radial velocity in km/s, (b1) density in N/cc, and (c1) total magnetic field strength in nT. The density and magnetic field are plotted in logarithmic scale. The in-situ profile of virtual spacecraft are shown in (a2, b2 & c2), along with forward (FS) and reverse (RS) shocks.

due to CME-CME interaction has not been reported until very recently by Trotta et al. [2024] using Solar Orbiter observations. Similar in-situ features have also been observed through virtual spacecraft in our simulation. The bottom panel of Figure 6.5 (a2, b2 & c2) demonstrates the existence of fast reverse shocks. The characteristic feature of anti-correlation of plasma speed with magnetic field and density can also be seen. As this reverse fast-mode shock wave propagates anti-radially, it compresses the downstream plasma inside CME2, resulting in higher plasma density in the downstream region compared to the upstream region. Conversely, the effective plasma speed will be lower in the downstream region due to the anti-radial direction of the shock, leading to an anti-correlation between speed and density profiles.

Given the non-uniform interaction demonstrated in earlier sections, the deformation

of CME1 causes the collision to initiate in one or more localized areas rather than across the entire interface simultaneously. This non-uniformity leads to the generation of independent shock fronts in each of these areas. The interactions among these shocks can lead to complex dynamics, including the merging of shocks, the amplification or attenuation of wave fronts, and the formation of complex wave patterns. Figure 6.5 illustrates his complexity, showing the reverse shock's propagation in the rear magnetic cloud for the HSHDHF0 case. Inside CME2, a complex pattern of alternating compressed and rarefied zones is visible, manifesting as ripple-like structures in the in-situ plots. Such variations hold the potential to influence the duration of geomagnetic storms.

6.3.2 Impact on first CME

One of the crucial aspects of CME-CME interaction is the alteration in the properties of CMEs, particularly the first CME. This ensemble study, in which the first CME (CME1) remains constant while the second CME (CME2) varies across different cases, offers a unique approach to analyzing how CME1 is influenced by various CME2 scenarios. Drawing from previous studies [Shen et al., 2017, and references therein], our analysis primarily focuses on changes in total momentum, kinetic energy, magnetic energy, and radial extent of CME1 resulting from its interaction with CME2. The overarching approach is to examine the temporal evolution of impacts on CME1 caused by different CME2 scenarios. To facilitate this, we compared the simulations of a single first CME, case 0, with those from the ensemble cases, cases 1-16. The premise is that any observed changes in CME1 in cases 1-16, relative to the CME in case 0, are due to the influence of CME2.

6.3.2.1 Kinematics

The subplots (a1, a2, d1, and d2) of Figure 6.6 illustrate the percentage change in total radial momentum (TRM) of CME1, which is calculated using following

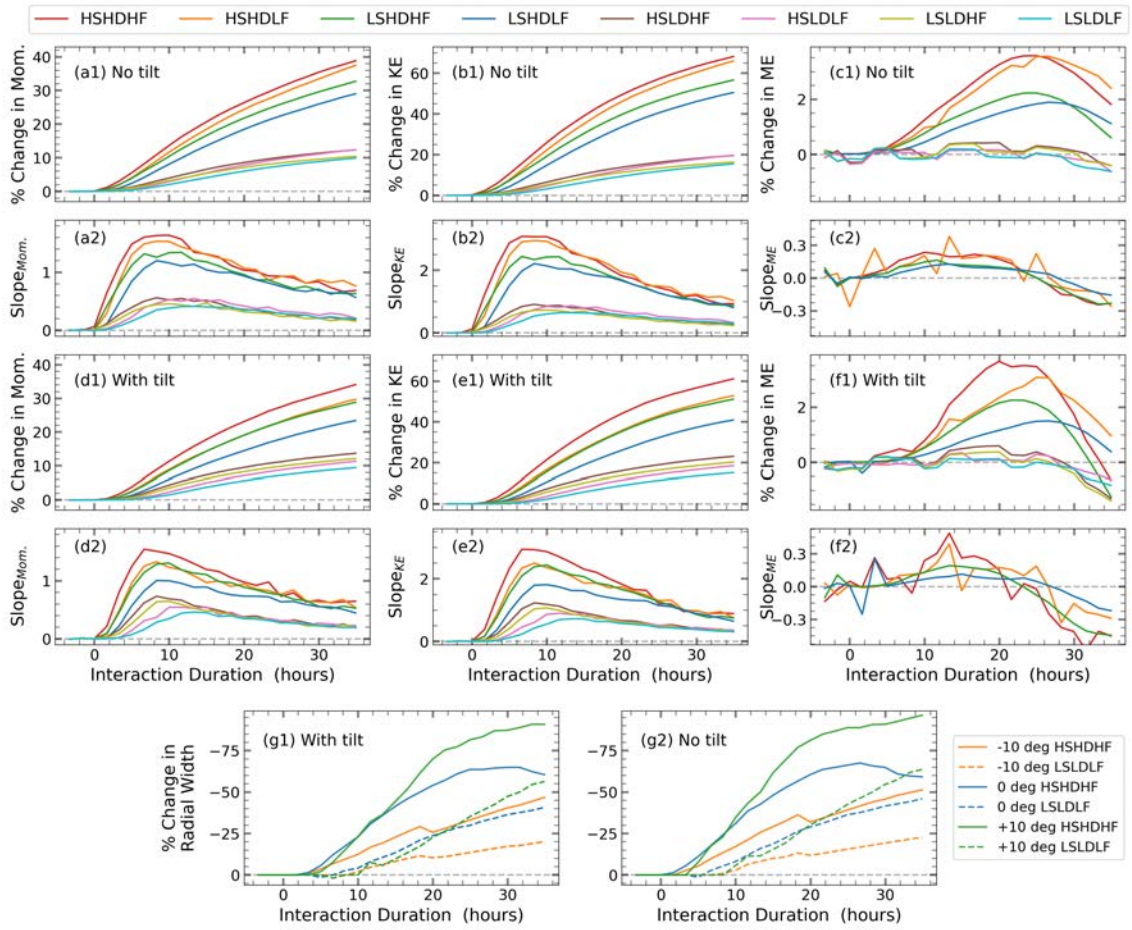

Figure 6.6: Subplots demonstrates the temporal evolution of change in the radial momentum, total kinetic energy, total magnetic energy and radial width of CME1 of cases 1-16, with respect to single CME case.

equations:

$$\%\,Change = 100 \times \left(\frac{TRM_i - TRM_0}{TRM_0} \right), \tag{6.7}$$

$$TRM = \sum_j \rho_j \, v_{r_j} \, dV_j \ . \tag{6.8}$$

Here, the subscript 'i' represents cases 1-16, while '0' denotes case 0. ρ_j, v_{r_j}, and dV_j are the mass density, radial velocity, and volume of the grid cell 'j', respectively. The TRM is the summation of the radial momentum at each grid cell. Based on the

slope of the momentum profile, we interpret the temporal evolution of momentum change in CME1 in two distinct phases: Rising Phase and Diminishing Phase.

The Rising Phase commences when the trailing shock from CME2 impacts the rear of CME1. During this phase, the effective total momentum of CME1 starts to increase due to the local velocity increase of CME1 plasma. As the shock propagates deeper into CME1, the total momentum continues to rise. This momentum increase of CME1 solely due to the trailing shock occurs very briefly (1-2 hours), followed by the collision of the trailing sheath and magnetic cloud with CME1. This collision initiates a substantial momentum exchange between the two CMEs. The high-velocity trailing CME2 exerts significant force on the slower-moving CME1, resulting in a notable increase in CME1's total momentum. During this phase, the rate of momentum increase (indicated by the slope of the momentum curve) achieve its highest value, reflecting the extent of direct and robust transfer of momentum from CME2 to CME1.

In the final Diminishing Phase, CME2 has transferred a considerable amount of its momentum to CME1, significantly reducing its own momentum. This momentum exchange decreases the relative speed between the two CMEs. Despite the reduction, CME2 still maintains a higher speed than CME1 and continues to push it forward, albeit with diminishing force. Consequently, the rate of change in momentum for CME1 gradually decreases, indicating that the interaction force is waning and the system is approaching a new equilibrium state.

The transition between phases is quite smooth, making it challenging to define rigid boundaries. Relatively speaking, the Rising Phase has an average duration of approximately 10 hours, after which the Diminishing Phase persists. The exact duration of this transition varies across different cases. For the HSHDHF case, the Diminishing Phase starts earliest, at roughly 7 hours, whereas for the LSLDLF case, it takes the longest time, approximately 13 hours. For cases with relative tilt

between CMEs, this transition period is slightly shorter compared to cases with no relative tilt.

The momentum gained by CME1, from the start of the interaction to the phase transition point and until the combined structure reaches 1 AU, also varies significantly with the initial conditions of CME2. The 8 cases shown in the subplots can be clustered into two groups: high-density (HD) and low-density (LD) cases. After 10 hours of interaction between CME1 and CME2, CME1 in HD cases gains approximately 5-15% more momentum, whereas in LD cases, it gains 1-5% more momentum. This momentum gain is slightly higher for cases with no relative tilt compared to cases with relative tilt. Moreover, the difference between the HD and LD cases is also more pronounced for no relative tilt cases.

As the CME-CME structure reaches 1 AU, starting from 25 hours, the difference in momentum gain between HD and LD cases becomes more pronounced. Since shock strength is inversely correlated with shock propagation time, which is shorter for high-density cases (see Table 6.2), these cases exhibit higher momentum gain. Additionally, CME2 in HD cases has more initial momentum to impart than in LD cases. After 30 hours of interaction, CME1 in HD cases demonstrates a 20-40% increase in momentum compared to 7-12% in LD scenarios. The gap between these two clusters of cases becomes 16% in the absence of relative tilt compared to 8% in the presence of tilt.

Since the total kinetic energy (KE $= 0.5\sum_j \rho_j, v_{r_j}^2, dV_j$) of a radially evolving CME1 is related to its total radial momentum, a similarity between the two is expected. The subplots (b1, b2, e1, and e2) of Figure 6.6 depict the temporal evolution of the percentage change in the KE of CME1 for cases 1-16 relative to case 0. These subplots closely resemble the momentum plots but indicate a greater gain. On average, the percentage gain in KE is about two-thirds greater than the percentage gain in momentum of CME1 due to the interaction process. As with momentum,

the eight cases can be clustered into two groups based on their initial density. The difference between these two groups is more pronounced in the absence of relative tilt (up to 25%) compared to scenarios with non-zero tilt (up to 18%). After 30 hours of interaction, CME1 gains up to 60% more kinetic energy in the HSHDHF case and up to 20% in the LSLDLF case due to the interaction with CME2.

6.3.2.2 Magnetic Energy

The evolution of total magnetic energy (ME) of CME1 differs significantly from the changes observed in momentum and kinetic energy. The subplots (c1, c2, f1, and f2) of Figure 6.6 showcases the temporal evolution of the percentage change in ME of CME1. These subplots reveal distinct behaviors based on the initial density of CME2. In low-density cases, the interaction has little to no effect on the ME of CME1. In contrast, high-density cases exhibit an initial increase in ME of approximately 1-3%, followed by a subsequent decrease. This pattern is consistent in both tilt and no-tilt scenarios, although the changes in ME occur more rapidly in the presence of relative tilt.

As the interaction begins, CME2 compresses CME1, potentially increasing the magnetic field strength and, consequently, the total magnetic energy if magnetic flux is conserved. Since CME1 and CME2 have the same chirality, this compression could also induce magnetic reconnection and other instabilities (e.g., tearing mode and plasmoid instabilities), dissipating magnetic fields and converting magnetic energy into kinetic and thermal energy. Despite significant compression even in the LSLDLF case, the gain in ME for low-density scenarios is almost negligible, suggesting the dissipation of magnetic field may happen even in weaker collisions.

In high-density cases, there is a noticeable increase in ME, implying that the rate of magnetic field strength enhancement due to compression initially exceeds the rate of magnetic dissipation. However, after approximately 25 hours of interaction, the

ME begins to decrease, indicating that the rate of compression diminishes while the rate of magnetic dissipation becomes dominant, leading to a reduction in the total magnetic energy of CME1.

Unlike momentum and kinetic energy profiles, ME profiles can be categorized into three groups: low-density (LD) cases, high-density high-flux (HDHF) cases, and high-density low-flux (HDLF) cases. Given the insignificant changes in ME for LD cases, their slopes are excluded from subplots (c2 and f2) to highlight the behavior of the remaining cases. Comparing HSHDHF (red) and HSHDLF (orange) cases, the initial rise in ME is greater for the HSHDHF case, but the subsequent decrease is also more rapid. After 30 hours of interaction, the effective ME is lower for the HSHDHF case. This trend is consistent when comparing LSHDHF to LSHDLF cases and across tilt and no-tilt scenarios. This suggests that a higher initial magnetic flux results in a greater initial gain in ME due to compression, followed by a more substantial decrease in ME due to magnetic dissipation.

6.3.2.3 Radial Extent

In the earlier sections, we demonstrated and discussed the non-uniform radial expansion of CME1 due to interactions with the solar wind from the front and CME2 from the rear (see Figures 6.2 and 6.3). We also noted in the last section that the only possible way of increasing the magnetic energy is the compression of CME1 due to CME2. Although multiple studies [Lugaz et al., 2013, 2017; Xiong et al., 2006] have examined the compression of the leading CME in CME-CME interactions, a quantitative analysis of the temporal evolution of this compression has not been performed.

Using the passive scalar tracing technique, we traced the CME1 structure and computed its compression along different longitudes. By placing virtual spacecraft at the front and rear of CME1, we could measure the radial difference between them,

thus determining the radial extent of CME1 along each longitude. Figure 6.6 (g1-g2) illustrates the percentage change in radial width of CME1 in ensemble cases (case 1-16) compared to the single CME (case 0), highlighting the evolution of compression in the leading CME due to CME-CME interaction. These measurements are shown for the HSHDHF (most intense) and LSLDLF (weakest) cases at three longitudes: -10°, 0°, and +10°.

At +10°, the HSHDHF1 case (with tilt) shows a significant decrease in radial width, reaching approximately 85% reduction over 30 hours. The rate of decrease is almost constant until 20 hours, after which it gradually slows. In contrast, the LSLDLF1 case shows a steady rate of decrease over 30 hours, resulting in around a 50% reduction. This substantial difference highlights the impact of high density, speed, and magnetic flux, with CME2 in the HSHDHF case exerting a much stronger compressive force on CME1.

Along -10°, the reduction in radial width for the HSHDHF1 case is around 40%, while for the LSLDLF1 case, it is about 20%. The absence of an SIR along this longitude means there is no significant obstruction to CME1's expansion from the front, resulting in less pronounced compression from the rear compared to the +10°longitude. Unlike at +10°, along this longitude, the rate of decrease is almost constant for both the HSHDHF and LSLDLF cases.

At 0°, the HSHDHF1 case exhibits a reduction of about 65% in radial width, compared to a 35% decrease in the LSLDLF1 case. The intermediate values at 0° suggest that the interaction between CME1 and CME2, influenced by the presence of the solar wind stream interaction region (SIR) ahead of CME1, is more significant here than at -10° but less than at +10°. Similar to +10°, the rate of decrease first remains constant and then decreases for the HSHDHF case, whereas it remains constant for the LSLDLF case.

The above-mentioned statistics were for cases having a 45° tilt between CMEs. In cases without tilt, the interaction starts slightly earlier, leading to faster and more pronounced compression. This difference due to tilt was more noticeable in cases where compression was higher. On average, the compression in cases without tilt was 5% more than in cases with tilt between CMEs. This indicates that the alignment of CME2 with CME1 can affect the efficiency of the compressive interaction. When comparing the overall effect of CME2's initial properties, it is evident that the HSHDHF case consistently results in greater compression of CME1 across all longitudes. The differences are most prominent along +10°, where the interaction is strongest due to the presence of the SIR, followed by 0° and then -10°.

6.3.3 Mixing of CMEs

In addition to the merging of shocks and alterations in CME properties, interactions between magnetic clouds can also lead to their merging. Multiple observational studies have suggested [Burlaga et al., 2002; Gopalswamy et al., 2001] and demonstrated [Liu et al., 2012; Lugaz et al., 2009; Temmer et al., 2012] the merging of magnetic clouds in the inner heliosphere during CME-CME interactions. However, the extent of plasma mixing between two interacting CMEs remains largely unknown. Particularly, a quantified study of this mixing and its dependence on other CME properties has not been conducted yet. Understanding this mixing is crucial, as it may influence the geoeffectiveness of CMEs, impacting the intensity and duration of geomagnetic storms.

6.3.3.1 Quantifying the Mixing of CMEs

To estimate the extent of plasma mixing between the leading and trailing CMEs, we utilized the CME tracer described in earlier sections to define the boundary of the CME structure. This approach is analogous to methods used in studying the mixing of astrophysical jets [e.g., see Walg et al., 2013]. To quantify this mixing,

we define a *mixing factor* ($\mathcal{M}$), which represents the absolute mass fractions within a specific grid cell. We set $\mathcal{M} = 0$ for the case of no mixing, where only CME1 material is present, and $\mathcal{M} = 2$ for the case where only CME2 material is present. We set $\mathcal{M} = 1$ in the case of maximum absolute mixing, meaning equal amounts of CME1 and CME2 constituents are present within the grid cell. In this scenario, the mass fraction of CME1 is equal to the mass fraction of CME2.

At a given time (t) and distance ($\mathbf{r}$), a tracer $\mathcal{T}(t, \mathbf{r})$ is advected by the flow and obtains values within the range $\mathcal{T}_{\rm min} \leq \mathcal{T}(t, \mathbf{r}) \leq \mathcal{T}_{\rm max}$. Here, $\mathcal{T}_{\rm min}$ corresponds to the absence of that CME within the cell, while $\mathcal{T}_{\rm max}$ corresponds to a cell purely containing the plasma of that CME. In this work, we have taken $\mathcal{T}_{\rm min} = 0.1$ and $\mathcal{T}_{\rm max} = 1.0$ for all CMEs. Given that a tracer value directly corresponds to the quantity of that CME, the mass fraction of CME1 (δ_1) within a grid cell can be expressed as follows:

$$\delta_1(t, r) = \left| \frac{\mathcal{T}_1(t, r) - \mathcal{T}_{\rm min}}{\mathcal{T}_{\rm max} - \mathcal{T}_{\rm min}} \right|. \tag{6.9}$$

Similarly, the mass fraction of CME2 (δ_2) can also be calculated. Furthermore, assuming that the mass fraction within a cell linearly scales with the amount of mixing, the mixing factor of the plasma of CME1 and CME2 in terms of their tracer values in a grid cell can be written as:

$$\mathcal{M} = 1 - \left(\frac{\mathcal{T}_1 - \mathcal{T}_2}{\mathcal{T}_1 + \mathcal{T}_2} \right). \tag{6.10}$$

6.3.3.2 Analysing the Mixing of CMEs

Figure 6.7 presents the 2D histogram of the calculated mixing factor values for all ensemble cases at the time when the merged structure reaches 1 AU. These values are computed for each grid cell within the computational domain and binned into eight uniform clusters, ranging from 0 to 2. A mixing factor of $\mathcal{M} = 1$ indicates the highest level of mixing (50%), meaning both CME1 and CME2 contribute equal

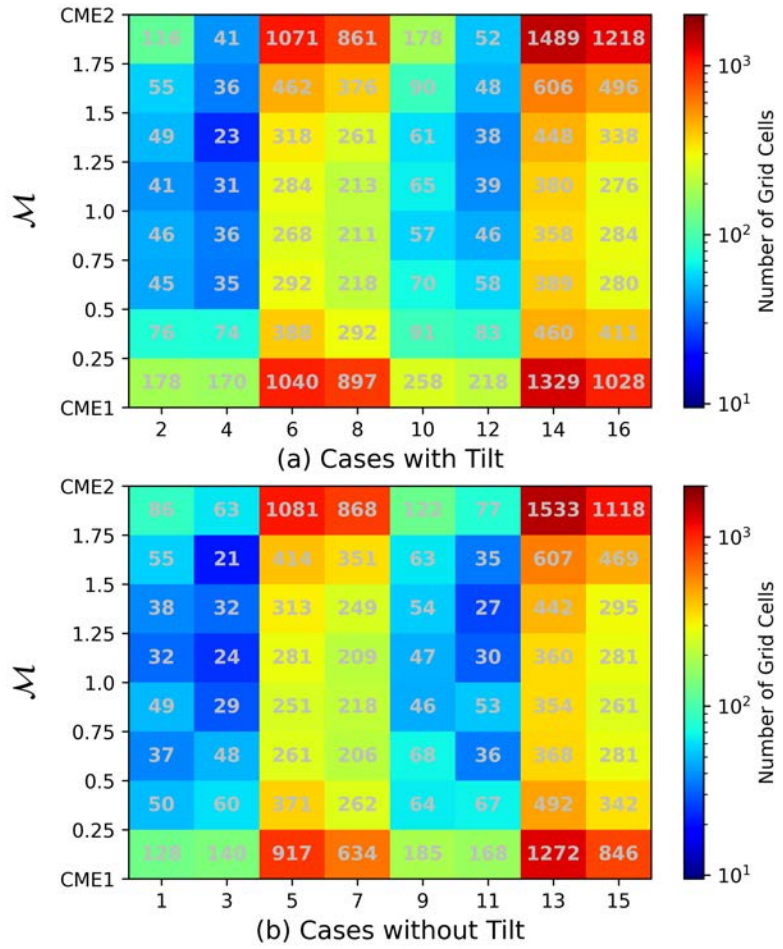

Figure 6.7: The subplots illustrate the amount of mixing between CME1 and CME2 upon the interacting structure's arrival at 1 AU. Subplot (a) shows the mixing factor ($\mathcal{M}$) for ensemble cases with a 45° relative tilt between the CMEs, along with the number of grid cells corresponding to each bin. Subplot (b) presents the results for cases without relative tilt between the CMEs.

amounts of plasma to that specific cell. The cases with and without relative tilt between the leading and trailing CMEs are plotted separately. The color of each block represents the number of grid cells associated with a specific amount of mixing (Y-axis) for each corresponding case (X-axis). For instance, in case 15, 261 grid cells have $\mathcal{M}$ values between 0.75 and 1 (see Figure 6.7(b)). In other words, a higher number of grid cells signifies a greater volume of mixing.

The most notable feature in these subplots corresponds to the high-density cases (5-8 and 13-16), which exhibit a significantly larger volume of mixing. As discussed earlier, these scenarios also demonstrated stronger CME shocks, higher momentum exchange, and greater radial compression. This trend is consistent in terms of the extent of mixing, where $\mathcal{M}$ values are several times higher in high-density cases as compared to low-density cases. High-speed cases (9-12 and 13-16) also consistently exhibit greater mixing compared to low-speed cases. Although the difference is not as big as in high versus low-density cases, the trend is evident across all bins of mixing factor.

Apart from these global trends, we also observed non-uniform mixing across the CME2 front. Similar to the non-uniform interaction between the back of CME1 and the front of CME2 discussed in earlier sections, the bottom flank exhibited higher mixing compared to the upper flank. This phenomenon is evident from the regions where interaction between CME1 and CME2 is stronger, resulting in higher mixing. This again highlights the impact of the inhomogeneous ambient solar wind, which causes non-uniform interaction and mixing of the interacting CMEs.

6.4 Geo-effectiveness

In the previous section, we discussed the evolution of CME-CME interactions and their impact on the kinematic, magnetic, and structural properties of CME1. From a geo-effectiveness perspective, it is crucial to understand how this evolution translates into in-situ properties at 1 AU. Specifically, we aim to determine how the interactions between two CMEs ultimately transform into plasma properties that will interact with the Earth's magnetosphere. To investigate this in depth, we placed three virtual spacecraft in our simulation at 0° and ±10° longitudes, as depicted in Figures 6.2 and 6.3.

The in-situ data measured by these three spacecraft at a 5-minute cadence, including

speed, density, and B_z profiles, are presented in the Appendix. The features observed in the evolution of CME1 and CME2 are reflected in their in-situ properties, which in turn lead to variations in the Dst profile. The next subsections delve into these changes in the Dst profile, focusing specifically on variations in the profile, the minimum Dst value, and the cumulative Dst.

6.4.1 Dst Variation

Figure 6.8 showcases the variations in Dst values across the 16 cases at three different longitudes: +10° (green), 0° (blue), and -10° (orange). Shaded regions depict the difference between the values at ±10° (green & orange) and 0° (blue). The plotted Dst values are computed based on the method described in Section 6.1.3. The analysis of these Dst profiles can be segmented into two distinct phases: the main phase and the recovery phase, which is divided by the global minimum in the Dst profile. The effects of the varying strengths of shocks, sheath regions, and CME1 are primarily manifested in the main phase. On the other hand, differences in the nature of the trailing CME are reflected in the recovery phase. The following discussion explores these significant impacts and their connections to the in-situ signatures.

6.4.1.1 Main Phase

The onset of the Dst main phase begins with the arrival of the first shock at 1 AU. Figure 6.8 illustrates the complex variations among the 16 cases, highlighting the different starting and ending times of the main phase. The onset time variation primarily depends on the ambient solar wind conditions, which remains constant across all cases, resulting in similar onset times for different cases at the same longitude. However, in scenarios where shock-shock interactions occur, deviations from the initial onset times are observed. Since the shock first impacts the spacecraft at +10° longitude and no shock-shock mergers occur at +10° in any of the cases, the main phase starting time is identical for the green profile across all cases. This

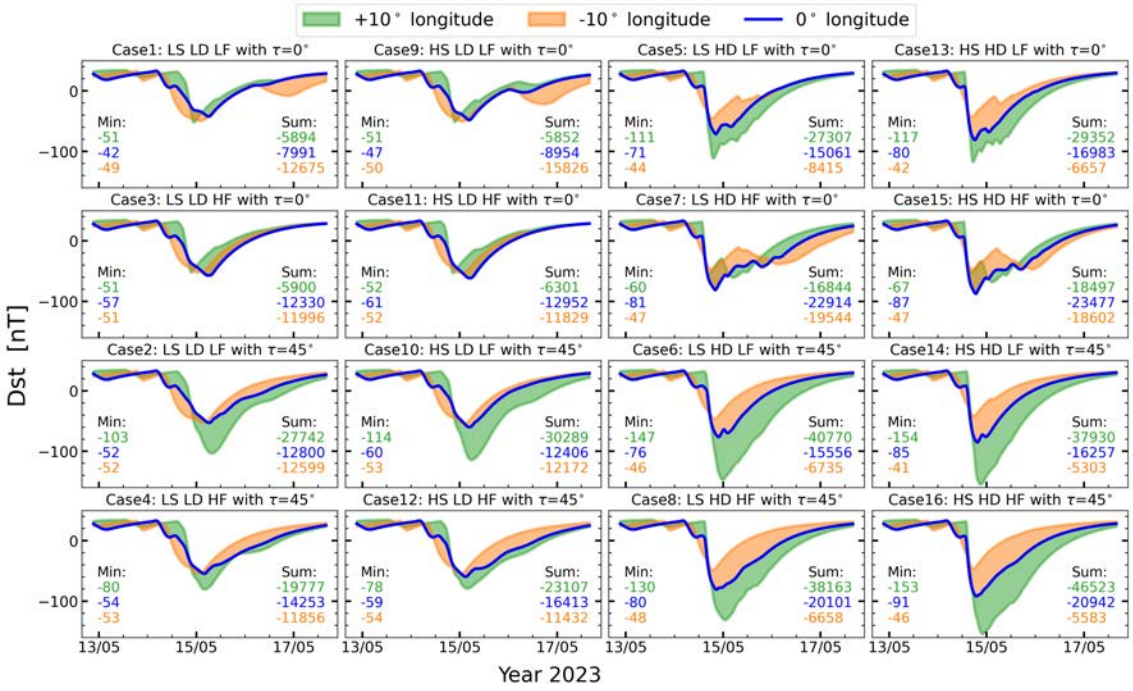

Figure 6.8: The Dst indices of all simulated cases in the ensemble, case 1-16, at three longitudes at 1AU.

timing aligns with the arrival of the first shock (∼20:00 hours on 13th May 2023).

Similar to the +10° longitude, the two shocks arrive sequentially at 0° longitude at 1 AU without merging in any of the cases. Both locations exhibit a two-dip profile, where the first dip is associated with the arrival of the first shock and the second dip begins with the arrival of the second shock. In the orange profile, the first Dst drop is very small (around 20:00 UT on 13/05) and recovers almost fully to the pre-storm level within a few hours, just before the second shock arrives at about 12:00 UT on 14/05. Depending on the strength of the second shock, the Dst value then drops again, reaching a minimum either more rapidly or gradually. A similar trend is observed for the blue profile, with the main difference being that the Dst recovers much less before the arrival of the second shock. This variation is primarily due to the B_z profiles at these two locations, as shown in Figure 6.9. In the orange

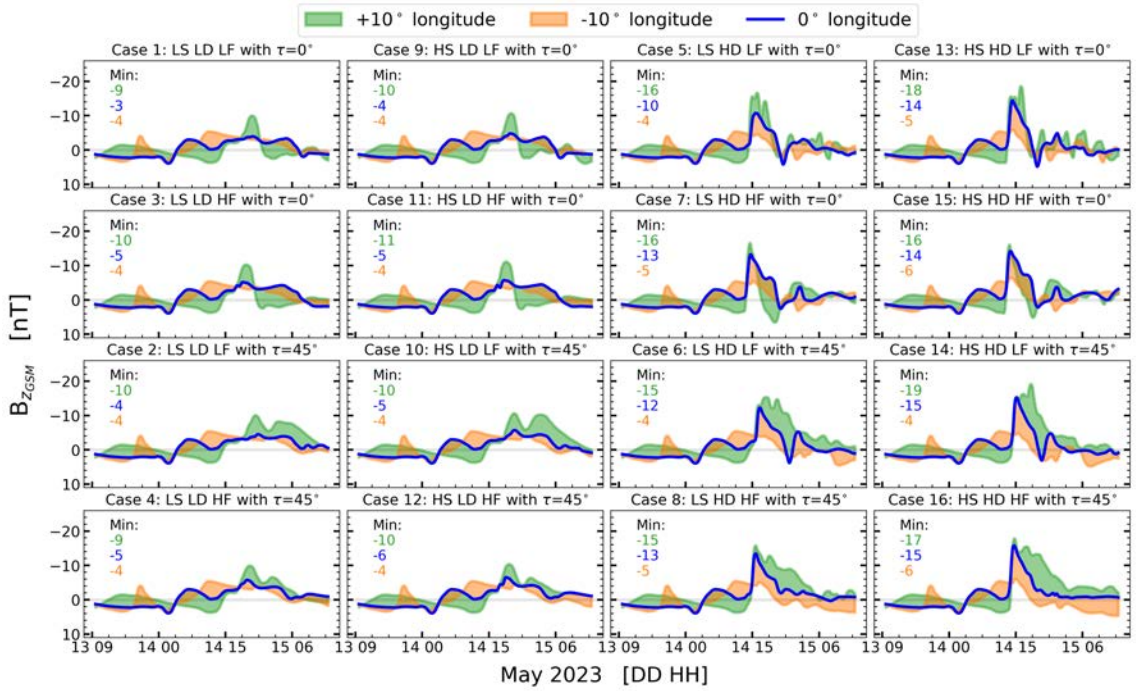

Figure 6.9: These subplots display the time series of in-situ southward magnetic field (B_z) measurements at 1 AU, captured at longitudes of -10 (orange), 0 (blue), and +10 (green) degrees, for all 16 ensemble cases.

profile, the negative B_z quickly ($\sim$ 4 hours) turns positive, whereas at 0° longitude, it remains negative for almost 7 hours.

Unlike the orange and blue profiles, the Dst main phase profiles at +10° show only a single dip in all cases. In low-density (LD) cases, this dip features two distinct slopes: an initial gradual decline followed by a sharper fall. For high-density (HD) cases, there is a single sharp decline to the global minimum, representing the shock-shock merger and indicating that the CME-CME interaction at this longitude is in its fourth stage. Despite the sharpest decline occurring at this location, the minimum Dst values do not always correspond to this longitude. Interestingly, this is especially not true for high-flux (HF) cases without tilt, where the initial magnetic flux of CME2 is greater. In these cases, the minimum Dst value is seen in

the blue profile rather than at +10°. Conversely, in low-flux (LF) cases without tilt, the minimum Dst value appears in the green (+10°) profile. This trend is intriguing because the interaction is most prominent along the +10° longitude. Yet, an increase in the initial magnetic flux of CME2 leads to higher Dst values along this longitude.

There are also some peculiar trends in the main phase corresponding to the initial properties of CME2. For instance, cases with and without relative tilt exhibit significant differences. In most cases, both the cumulative Dst and minimum Dst values are higher when there is a relative tilt between the CMEs compared to when there is none. The primary reason for this is the change in orientation of the magnetic field of CME2, which should ideally enhance the effect along -10° and decrease it along +10°, while remaining the same at 0°. However, due to the presence of solar wind and prolonged interaction with CME1, this trend deviates slightly from the ideal scenario. Figure 6.9 shows the B_z values for all cases, where the minimum B_z values exhibit a mixed trend along -10°, 0°, and +10° longitudes with changes in tilt. However, the cumulative duration of negative B_z is consistently longer for +10°. Additionally, another noticeable difference is in the slope of the Dst fall, which is steeper for HD cases compared to LD cases.

6.4.1.2 Recovery Phase

In an ideal single CME storm, the recovery phase is smooth and continuous, with the Dst index value generally increasing following an exponential trend and gradually returning to the pre-storm level (as in equation 6.4). Any deviations or additional fluctuations from this ideal trend can indicate the influence of second CME and subsequent solar wind. Among the 16 ensemble cases, some exhibited significant deviations, others showed minor variations, and a few had changes that were almost negligible.

The high-density (HD) cases exhibit significant deviations from the idealized sce-

nario of the Dst recovery phase. Notably, scenarios without relative tilt between CME1 and CME2 emphasize these deviations more clearly. In cases 5, 7, 13, and 15, a discontinuity is observed in the Dst index increase across all three profiles (orange, blue, and green), resulting in the formation of a recovery phase plateau. These interruptions, while not affecting the minimum Dst value, significantly prolong the overall recovery time, delaying the return to pre-storm Dst levels. The mentioned HD cases demonstrate notably longer recovery phases compared to their low-density (LD) counterparts. For instance, by May 16th, the Dst index had almost recovered to 0 nT for cases 3 and 11 (LDHF0), whereas for cases 7 and 15 (HDHF0), the Dst index remained near -50 nT.

The recovery phase plateau can be attributed to fluctuations in the southward magnetic field as southward IMF excursions drive the Dst down before recovery can resume. In the B_z profile (see Figure 6.9), such fluctuations are noticeable after approximately 18:00 hours on May 14th for HD cases without tilt. These fluctuations in the B_z profile are mirrored by similar, more pronounced fluctuations in the in-situ speed profile. As discussed in Section 6.3.1.3, these fluctuations result from the reverse shock formed by the collision of CME2 with CME1. The propagation of this reverse shock through CME2 creates complex patterns of alternating compressed and rarefied regions, leading to the ripples observed in the in-situ profiles. Consequently, these ripples extend the Dst recovery phase by forming a plateau, significantly delaying the return to pre-storm levels.

Apart from the major deviations from the idealized scenarios, many cases showcased minor or no deviations. For example, the blue profile in cases with tilt shows slight deviations; in cases 6 and 14, there is a break point, and in other cases, the profile does not increase smoothly but rather with some disruptions. Notably, there is no significant flipping in the B_z profile after reaching the global minimum in the Dst profile around May 15th for these cases. Interestingly, although there are a few

break points around May 15th in the speed profile, the absence of flipping in the B_z profile prevents the formation of any plateau. In other cases, such as 3 and 11, the blue profile closely follows the idealized scenario. Similarly, the orange profile exhibits an ideal recovery phase in almost all tilt cases. In these scenarios, there is neither directional flipping in the B_z profile nor any break points in the speed profile, resulting in a smooth, continuous function.

6.4.2 Minimum Dst Index

The minimum Dst value is arguably one of the most widely used parameters to define the severity of a geomagnetic storm. Therefore, it is essential to analyze the minimum Dst values of the simulated ensemble cases. To identify trends accurately, we have grouped the cases into pairs, where each pair differs by only one parameter: initial density, speed, flux, or tilt of CME2. This approach allows us to clearly analyze the effect of variations in these properties on the geo-effectiveness of CME-CME interactions.

Density. Figure 6.10 illustrates the minimum Dst values for low-density and high-density cases across three different longitudes: -10°, 0°, and +10°. The percentage differences (nearest integer of $100 \cdot \left[\frac{HD-LD}{LD}\right]$) between paired cases highlight some significant trends. At 0° (panel a2) and +10° (panel a3), high-density cases consistently show lower minimum Dst values compared to low-density cases, with percentage differences ranging from 42% to 70% at 0° and 18% to 129% at +10°. This indicates that higher initial densities tend to exacerbate the severity of geomagnetic storms at these longitudes. This trend seems intuitive since higher initial density in CME2 leads to a stronger trailing shock and higher in-situ speed and density, which in turn would lead to a lower Dst index. However, at -10° (panel a1), the trend is reversed; high-density cases exhibit higher minimum Dst values compared to low-density cases, with percentage differences ranging from -8% to -23%. Although

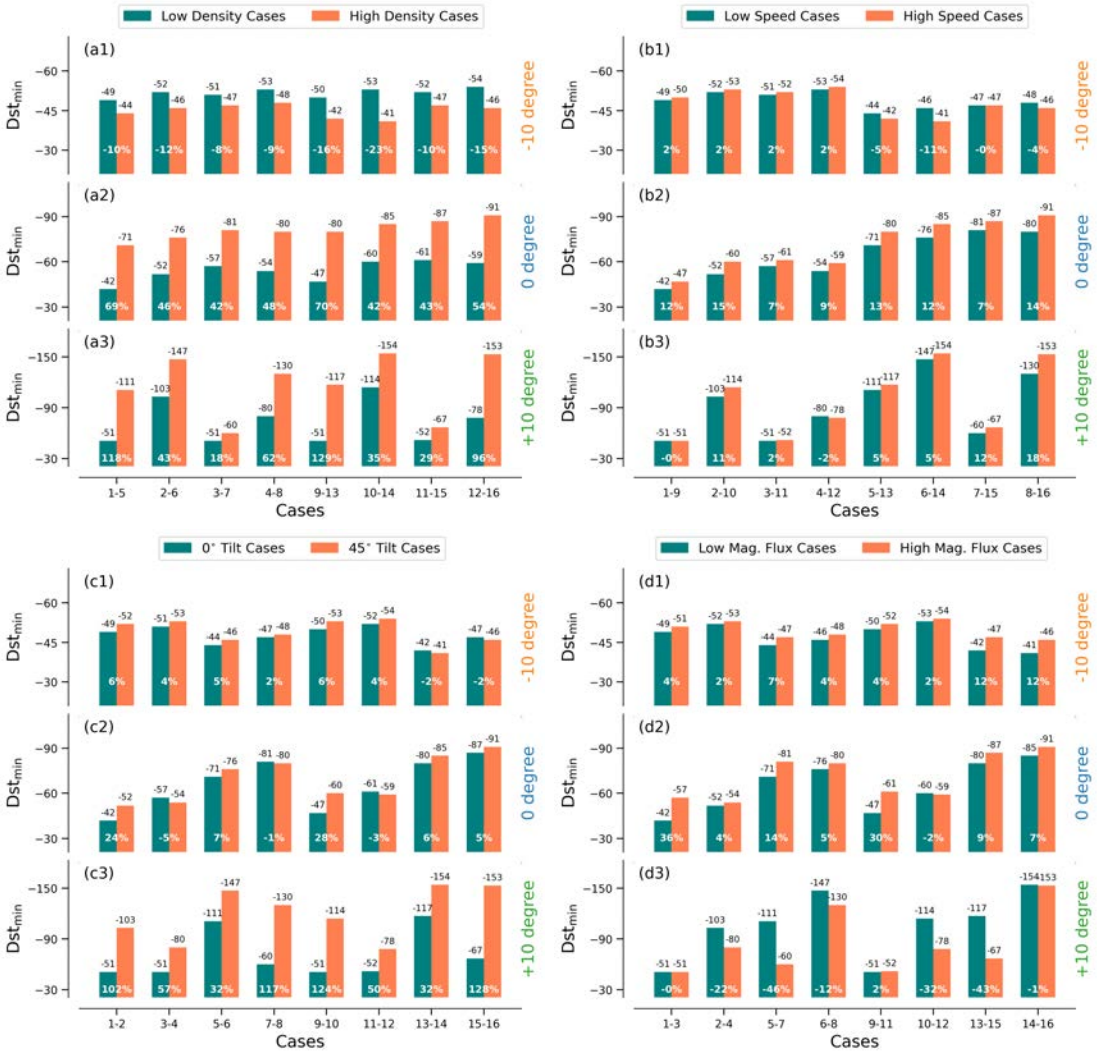

Figure 6.10: The histogram plots of the minimum Dst value corresponding to the change in initial density (a1-a3), speed (b1-b3), tilt (c1-c3) and magnetic flux (d1-d3), at three longitudes at 1AU.

there is a significant increase in in-situ speed at -10°, the in-situ density does not show a major increment, possibly because the trailing shock has to cover a much larger radial distance in an over-expanded region of CME1. Additionally, when this second shock arrived, the B_z profile was not in southward direction as it was along the 0° and +10° longitudes. Due to this combined in-situ configuration, the effective

Dst minimum became higher.

Speed. At -10° (panel b1), the differences between low-speed and high-speed cases are minimal, with percentage changes ranging from -11% to 2%. This suggests that initial speed has a relatively minor impact on the severity of geomagnetic storms along this over-expanded CME1 region. In contrast, at 0° (panel b2), high-speed cases consistently exhibit lower minimum Dst values compared to low-speed cases, with percentage differences ranging from 7% to 15% and an average change of 11%. This potentially indicates that higher initial speeds of CME2 results in a more geoeffective configuration at this longitude. At +10° (panel b3), the trend is less consistent (in 6 out of 8 cases), with percentage differences varying from -2% to 18% and an average change of 5%. Despite this variability, high-speed cases generally lead to lower minimum Dst values (in 18 out of 24 cases), suggesting a trend towards more severe storms with increased speeds. These findings demonstrate that while the influence of initial speed is significant at 0° and somewhat at +10°, it is relatively minor at -10°.

Tilt. Like initial density and speed, the effect of CME2 tilt on minimum Dst values also shows distinct patterns across the three longitudes. With an average percentage difference of 3%, ranging from -2% to 6%, the Dst minimum was lower for 6 out of 8 tilt cases along -10° longitude (panel c1). At 0° (panel c2), the tilt's effect is more varied, with percentage differences ranging from -5% to 28% and an average change of 7%, showing lower Dst minimum values for tilted cases in 5 out of 8 instances. The most pronounced effect is observed at +10° (panel c3), where the differences are consistent and substantial, ranging from 32% to 128% with an average decrease of 81%. This significant impact at +10° highlights how tilt in CME2, which alters the magnetic field orientation, can greatly intensify the geomagnetic storm along one direction. Ideally, the Dst minimum should have consistently increased in the opposite direction (+10°), but the non-uniform deformation of CME1 due

to inhomogeneous ambient solar wind causes the Dst values to deviate from this expected trend.

Magnetic Flux. The increase in the initial magnetic flux of a CME results in an increase in its magnetic field strength. In an ideal isolated flux rope scenario, this enhancement would typically lead to a lower Dst minimum upon the CME's interaction with Earth's magnetosphere. However, for CME-CME interactions in the presence of a realistic non-uniform ambient solar wind, the outcome can differ significantly. This is evident in the Figure 6.10. At -10° (panel d1), the differences between low and high magnetic flux cases are relatively minor, with percentage changes ranging from 2% to 12% and an average difference of 5%. This consistent trend of lower Dst minimum for higher initial magnetic flux suggests that magnetic flux does impact the severity of geomagnetic storms, albeit slightly at this location. At 0° (panel d2), the impact of magnetic flux is more pronounced, with percentage differences ranging from -2% to 36% and an average change of 13%. The trend is consistent, with one exception that has the lowest percentage change. Combining the results from -10° and 0°, the trend is clear: higher magnetic flux leads to lower Dst minimum values in 15 out of 16 cases. However, at +10° (panel d3), the trend is reversed in 7 out of 8 cases; high magnetic flux cases exhibit higher minimum Dst values compared to low magnetic flux cases, with percentage differences ranging from -46% to 2% and an average increase of -16%. It is important to emphasize that this trend reversal occurs along the longitude where the interaction has been strongest. This potentially indicates that higher magnetic flux in CME2 may lead to greater magnetic flux dissipation in strong CME-CME interaction regions, reducing the geo-effectiveness of CME-CME interactions at this longitude.

6.4.3 Cumulative Dst

The cumulative Dst value, representing the summation of the Dst index until it returns to pre-storm levels, is a critical parameter for comprehensively assessing the duration and overall impact of geomagnetic storms. Combined with the Dst minimum, this metric encapsulates both the intensity of the storm and its recovery characteristics, offering a more complete picture of the storm's effect on the Earth's magnetosphere. Similar to the previous subsection, we have used a pair-based analysis to identify trends in the effects of the initial properties of CME2.

Density. The histograms in Figure 6.11 illustrate the significant impact of initial density on the cumulative Dst values. Panel a1 shows the cumulative Dst index values for -10° longitude. The differences between low-density and high-density cases are substantial, with percentage changes ranging from -79% to 107% and an average change of -29%. This trend of higher initial densities resulting in lower cumulative Dst values is observed in 6 out of 8 cases, indicating a general reduction in geomagnetic impact at this longitude, consistent with the trend observed in the minimum Dst. At 0° (panel a2), high-density cases exhibit consistently higher cumulative Dst values compared to low-density cases, with percentage differences ranging from 33% to 246% and an average increase of 109%. At +10° (panel a3), the differences are even more pronounced, with percentage changes ranging from 28% to 2327% and an average increase of 731%. This increasing trend is observed in all 8 cases at 0° and +10°, underscoring the substantial enhancement in storm duration due to higher initial densities of CME2. These findings demonstrate that the initial density of CME2 plays a crucial role in determining the cumulative geomagnetic impact, with the most significant effects observed at 0° and +10°, and a complex behavior at -10°.

Speed. At -10° (panel b1), the cumulative Dst values show a wide range of percentage changes, from -46% to 47%, with an average change of -16%. This variability highlights that higher initial speeds tend to reduce the cumulative geomagnetic impact

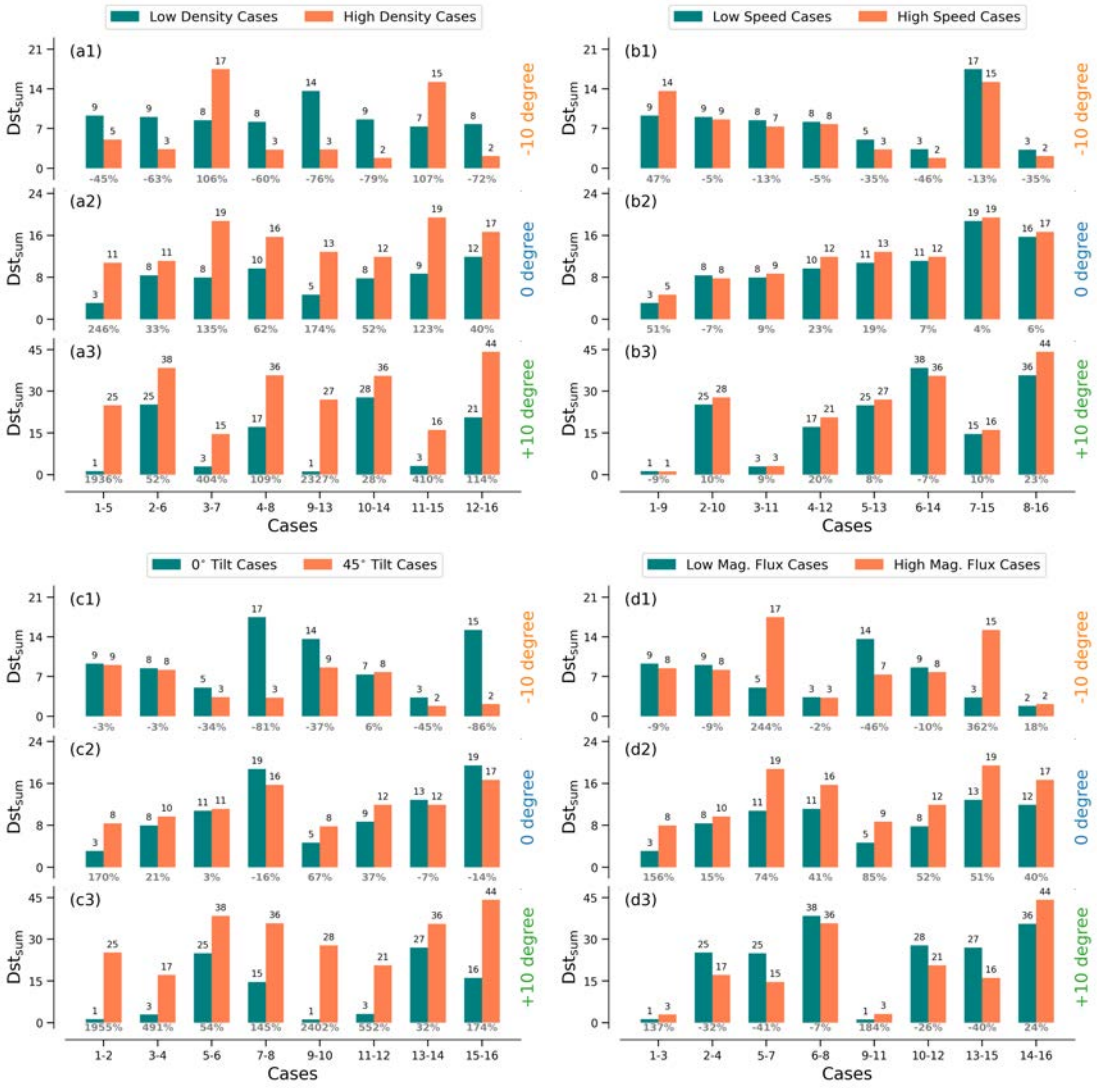

Figure 6.11: The histogram plots of the cumulative Dst values corresponding to the change in initial density (a1-a3), speed (b1-b3), tilt (c1-c3) and magnetic flux (d1-d3), at three longitudes at 1AU.

at this location, though the trend is opposite to what was observed in the minimum Dst, and the effect is not uniform. In contrast, at 0° (panel b2), the cumulative Dst values for high-speed cases exceed those of low-speed cases, with percentage changes spanning from -7% to 51% and an average increase of 16%. Here, 7 out of 8 cases follow this pattern, consistent with the trend observed in the minimum Dst. At

+10° (panel b3), the differences are more subtle, with percentage changes ranging from -9% to 23% and an average change of 9%. This pattern appears in 6 out of 8 cases, suggesting a mild tendency for higher speeds to amplify the cumulative Dst values. These observations indicate that the impact of CME2's initial speed on storm duration and intensity varies with longitude, showing enhancement at 0° and +10°, but reduction at -10°.

Tilt. The impact of tilt between CMEs shows a relatively more consistent trend. For -10°, the cumulative Dst values decrease, show mixed behavior at 0°, and increase at +10°. At -10° (panel c1), the high tilt cases have percentage changes ranging from -86% to 6%. This trend is observed in 7 out of 8 cases, with an average change of -36%, opposed to the general observation in minimum Dst. Moving to 0° (panel c2), the effect of tilt becomes inconsistent. Here, percentage changes vary from -16% to 170%, with an average change of 34%. The trend is followed in 5 out of 8 cases, indicating a mixed influence of tilt on cumulative geomagnetic impact, and is not as pronounced as at -10°. In contrast, at +10° (panel c3), the high tilt cases dramatically increase the cumulative Dst values, with percentage changes ranging from 32% to 2402% and an average increase of 697%. This overwhelming trend is observed in all 8 cases, highlighting a substantial enhancement in geomagnetic storm duration and intensity due to tilt at this longitude. This demonstrates that CME2's tilt has a variable influence on the cumulative geomagnetic impact, with a significant reduction at -10°, moderate variability at 0°, and immense enhancement at +10°.

Magnetic Flux. Among the three longitudes, only the cumulative Dst values at 0° show a consistent trend, while the ±10° longitudes exhibit mixed behavior with increasing magnetic flux of CME2. This inconsistency contrasts with the statistical trends observed in the minimum Dst. At -10° (panel d1), percentage changes range from -46% to 362%. Decreases are observed in 5 out of 8 cases, but the average

change is +56%, reflecting minor decrements and significant increments. Similarly, at +10° (panel d3), the results are highly variable, with percentage changes ranging from -41% to 184% and an average increase of 22%. Decreases occur in 5 cases, while increases are seen in 3 out of 8 cases. In contrast, at 0° (panel d2), the impact of higher magnetic flux is consistent and more pronounced, with percentage changes spanning from 15% to 156% and an average increase of 67%. This trend is observed in all 8 cases, indicating a strong correlation between increased magnetic flux and enhanced geomagnetic storm duration and intensity.

6.5 Summary

In this ensemble study, we utilized the SWASTi framework to conduct MHD simulations of 16 different scenarios of CME-CME interaction. The simulations employed a flux rope CME, propagating within data-driven realistic solar wind conditions. The chosen solar wind conditions correspond to Carrington rotation period 2270, with the projected trajectory of the CMEs passing through a solar wind stream interaction region (SIR). This unique setup implies that all CME-CME interactions in this study are significantly influenced by the in-path SIR, effectively making it a CME-CME-SIR interaction scenario. Below are brief discussions and conclusive remarks on the topics covered in this work:

Role of Solar Wind: Figure 6.2 clearly illustrates this situation and its implications. In all ensemble cases, the upper flank of CME1 over-expanded compared to the lower flank. This differential expansion occurs because the upper flank, situated along the fast stream, experiences greater pressure gradients, leading to more expansion and faster movement than the bottom flank. The inhomogeneity in the ambient solar wind results in an asymmetrical radial width of CME1. This variability makes the CME-CME collision non-uniform across the interaction surface.

Shock Evolution: We thoroughly investigated the dependency of shock evolution-

ary stages proposed by Lugaz et al. [2005] on the initial properties of CME2. Our study revealed that the evolution of these stages varied across different longitudes, primarily due to the non-uniform radial extension of CME1. This finding highlights that the shock-based classification of CME-CME interaction stages is not universally applicable to the entire structure but rather a localized phenomenon.

Impact on CME1: By comparing ensemble cases with the single CME1 simulation, we found some peculiar trends in the kinematic, magnetic, and structural properties:

- Kinematic: Due to the collision, CME1 gained 9-36% in radial momentum and 15-65% in kinetic energy by the time it reached 1 AU. Their temporal evolution showed similar patterns, with an initial rising phase lasting about 10 hours, followed by a diminishing phase. The amount of gain and the duration of the rising phase, were most influenced by CME2's initial density.

- Magnetic: CME1's magnetic properties showed less significant changes compared to its kinematic properties and followed a different evolution pattern. It increased by 1-3% only in high-density cases. We observed an initial increase in magnetic energy up to 20-25 hours, followed by a decrease due to magnetic field dissipation. This behavior is consistent with Koehn et al. [2022], given that the CMEs had the same chirality.

- Structural: The longitude (+10°), where CME1 interacted with both the SIR from the front and CME2 from behind, showed the highest compression – more than twice at longitude (-10°) without SIR interaction. This indicates that the SIR significantly enhances the leading CME's radial compression. Overall, CME2's initial density was observed to be a key factor in determining the interaction's impact on CME1.

Reverse Shock: Another noteworthy phenomenon observed in the CME-CME interaction was the formation of reverse shocks in cases of strong interaction. Similar

observations were reported by Lugaz et al. [2005] in their MHD simulation of two identical CMEs interacting in a simple axis-symmetric solar wind setup. Additionally, Trotta et al. [2024] recently observed such a reverse shock using Solar Orbiter data. We found that these shocks can originate from multiple locations due to the non-uniform interaction between CME1 and CME2 along different longitudes. As these reverse shocks propagate inside CME2, they create a complex pattern of alternating compressed and rarefied regions, causing ripples or fluctuations in the in-situ data (see Figure 6.4). These ripples influence the geo-effectiveness of the CME-CME structure, notably extending the overall recovery phase and delaying the return to pre-storm Dst levels.

Geo-effectiveness: We conducted a statistical study of the minimum and cumulative Dst index values for the ensemble cases to identify trends related to CME2's initial properties. Along the strong interaction region (+10°), the minimum Dst value decreased with increased initial density, tilt, and speed of CME2, with average changes of 66%, 81%, and 6%, respectively, indicating higher geo-effectiveness. Conversely, the minimum Dst value increased by an average of 19% with higher initial magnetic energy, suggesting greater magnetic dissipation and lower geo-effectiveness. Trends were less consistent at 0° and -10°. Overall, increase in CME2's any initial property mostly leads to stronger (72% of cases) and prolonged (63% of cases) storm.

It is important to emphasize that this ensemble study was conducted using an ideal MHD setup. Consequently, a quantitative study of magnetic dissipation in CME-CME interactions lies beyond the scope of this work. Additionally, the ambient solar wind conditions were consistent across all cases, introducing a bias towards specific ambient conditions. Therefore, the conclusions drawn are particularly relevant to the scenario of CME-CME-SIR interaction. We have also not considered the role of initial flux rope orientation (e.g., chirality and polarity) in this study, which can have considerable impact on geo-effectiveness [Koehn et al., 2022]. In our future work,

we aim to include non-ideal MHD effects to explore in greater depth, especially to investigate the formation of reverse shocks and their dependency on CME properties. This approach will provide a more comprehensive understanding of the underlying physical processes that can enhance the geo-effectiveness of CME-CME interaction events.

Chapter 7

Summary and Outlook

7.1 Thesis Summary

The study of space weather has gained increasing significance due to its potential impact on power grids, navigation systems, satellite operations, and the health of astronauts. Solar wind, coronal mass ejections (CMEs), and solar flares are the primary space weather drivers capable of causing disturbances on Earth. Understanding these drivers is crucial from two key perspectives: forecasting their impacts on Earth and comprehending their evolution and geo-effectiveness. Accurate forecasting is essential for mitigating the disruptions caused by space weather events, enabling timely warnings and protective measures to safeguard technological systems and infrastructure. Equally important is the need to understand the underlying mechanisms governing the evolution of these drivers as they propagate through the heliosphere. This deeper understanding not only enhances forecasting accuracy but also contributes to a broader knowledge of space weather dynamics and their potential long-term effects on Earth. In this thesis, we have studied space weather drivers with a dual focus on forecasting and understanding, specifically emphasizing the role of numerical modeling in the study of solar wind, CMEs, and solar flares.

In the first part of this thesis, an indigenous three-dimensional (3D) solar wind

model, SWASTi-SW, has been developed to compute plasma properties within the heliosphere. This work has also examined the parameters within the widely used Wang–Sheeley–Arge (WSA) relation and proposed a more generalized version of this empirical relation. The model has been rigorously validated against in-situ observations at 1 AU across multiple Carrington rotation periods, demonstrating its accuracy and reliability. Notably, the SWASTi-SW model is computationally efficient, requiring approximately 4-6 hours on a 48-core CPU to generate in-situ data at a 5-minute cadence, enabling solar wind forecasts more than 2 days in advance. Furthermore, this work has explored potential observations from the Solar Wind Ion Spectrometer subsystem of the Aditya Solar Wind Particle Experiment (ASPEX) payload aboard ADITYA-L1. The study has highlighted the multidirectional features of Stream Interaction Regions (SIRs), which can aid in developing a more robust automatic detection technique for SIRs.

With the solar wind background established, the next focus of this thesis was on developing and validating the CME module of the SWASTi framework (SWASTi-CME), incorporating both cone and flux rope CME models. The cone model has been enhanced with a more realistic approach, allowing for variable angular height and elliptical cross-sections, while the flux rope model uses the FRi3D technique to represent a magnetized structure with detailed parameters. The SWASTi-CME model is designed to efficiently estimate CME near-Earth arrival properties, typically requiring 5-7 hours on a 48-core CPU. This efficiency supports forecasts of CME impacts more than a day in advance. The study further presents a quantitative analysis of CME-solar wind interaction using this model. To account for ambient solar wind effects, two scenarios with varying solar wind conditions were established. The results indicate that ambient solar wind conditions significantly influence the trajectory, geometry, and internal properties of CMEs as they propagate through the inner heliosphere. Notably, CME volume follows a non-fractal power-law evolution,

transitioning to a balanced phase after approximately 40 hours of propagation.

The third work of this thesis involved developing a solar flare prediction model using the Light Gradient Boosting Machine (LightGBM) algorithm. Given the relatively limited application of LightGBM in solar flare prediction, this work not only developed the model but also conducted a comprehensive comparison of active-region (AR) features and flaring-history parameters to assess their effectiveness in forecasting accuracy. By employing a focused set of impactful features, the model achieved a true skill statistic (TSS) of 0.63 and an accuracy of 0.90 for predicting ≥C-Class flares within a 24-hour window, with even higher performance for ≥M-Class flares (TSS of 0.69 and accuracy of 0.97). The comparative study revealed that the LightGBM-based model outperformed several existing models, including those using Long-Short Term Memory (LSTM), Random Forest (RF), MultiLayer Perceptron (MLP), and Deep Flare Net (DeFN) techniques. However, it was noted that Nishizuka et al. [2017] achieved superior results using a broader set of features. Despite this, the findings of this study, along with several others, highlight the potential for improved prediction accuracy by concentrating on a smaller, more relevant set of features, challenging the notion that more features always lead to better results.

The final work of this thesis focused on CME-CME interactions, utilizing the SWASTi framework to conduct MHD simulations across 16 different scenarios under realistic solar wind conditions. This study explored how the initial properties of the interacting CMEs—such as magnetic flux, speed, density, and tilt—affect their dynamics and their combined impact on the Disturbance Storm Time (Dst) index. The study revealed that inhomogeneities in the ambient solar wind caused non-uniform radial widths in the leading CME (CME1) across different longitudes, even before its interaction with the trailing CME (CME2). This non-uniformity influenced the evolution of shocks and overall interaction dynamics, with high-density CMEs ad-

vancing through interaction stages more rapidly. The collision between CMEs led to a significant increase in the kinetic energy of CME1 by up to 60%, while its width reduced by up to 80%, with the impacts being more pronounced for higher-density cases. Additionally, this interaction resulted in the mixing of material from both CMEs, and in cases of strong collision, reverse shocks formed, further extending the duration of geomagnetic storms. The analysis showed that in 72% of the cases, increases in the initial properties of CME2 led to higher geo-effectiveness, with density and tilt being the most influential factors.

7.2 Thesis Outlook

By consolidating the results obtained from these works, this extensive study provides a suitable framework and valuable insights into the evolution and impact of space weather drivers. The work presented in this thesis hence has potential to be extended in several directions.

- **Operational Space Weather framework:** The SWASTi framework, developed and validated throughout this thesis, demonstrates significant potential as an operational tool for space weather forecasting. With its ability to accurately model solar wind, CMEs, and their interactions with the solar wind and each other, SWASTi offers a comprehensive approach to predicting space weather events. The solar wind module (SWASTi-SW) has proven its computational efficiency, forecasting solar wind properties more than 2 days in advance, while the CME module (SWASTi-CME) provides detailed insights into CME propagation, including complex interactions such as CME-CME collisions. As the next step, we are actively working on making SWASTi open-source, enabling the broader scientific community to access, refine, and apply this tool in operational space weather forecasting. This initiative aims to establish SWASTi as a valuable resource for both research and operational forecasting.

• **Solar wind impact on Geo-effectiveness of CME:** This thesis has demonstrated that the ambient solar wind significantly influences the arrival time, structural integrity, thermodynamic behavior, and magnetic properties of a CME. Building on this foundation, future work can leverage the developed SWASTi-CME model to further explore these interactions. Specifically, by integrating the resistive MHD module of the PLUTO code, it is possible to analyze the potential flux cancellation of a CME as it interacts with varying solar wind conditions. This approach could provide deeper insights into how different solar wind environments impact the ultimate geo-effectiveness of CMEs, including the potential weakening or strengthening of their magnetic fields before reaching Earth.

• **Robust automatic SIR detection algorithm:** The multi-directional observational capabilities of the ASPEX instrument aboard ADITYA-L1, combined with the characteristic latitudinal and longitudinal flow features of SIRs identified in this thesis, present a unique opportunity to develop a more reliable and robust SIR detection algorithm. By leveraging the comprehensive data collected from multiple directions, it is possible to refine our understanding of SIR signatures and enhance the accuracy of detection algorithms. Future work could focus on automating this detection process, enabling real-time identification of SIRs. Furthermore, integrating observations from other spacecraft, such as the Parker Solar Probe and Solar Orbiter, would significantly improve our understanding of the 3D properties of SIRs as they develop and evolve in the heliosphere.

• **Expansion of the SWASTi Framework to Study SEPs:** Building on the established models of solar wind and CME of the SWASTi framework, a promising future direction is its expansion to include the study of Solar Energetic Particles (SEPs). SEPs are high-energy particles emitted by the Sun during solar flares and CME-driven shocks. Integrating SEP modeling into the SWASTi framework would involve simulating the acceleration and propagation of these particles through the

heliosphere, accounting for their interactions with the solar wind magnetic fields. This expansion would allow for more comprehensive space weather forecasts, predicting not only the arrival of CMEs but also the associated SEP events.

- **Coordinated 3D Analysis with Multi-Vantage Observations:** The usage of solar wind and CME modeling capabilities of the SWASTi framework can be further enhanced through coordinated 3D studies using multi-vantage observations from missions like Parker Solar Probe (PSP), Solar Orbiter, and BepiColombo. These missions provide observations of solar transients at different radial distances, enabling an opportunity for comprehensive analysis of their 3D structure and evolution as they traverse them. Coordinated analysis of these observations with the 3D simulation using SWASTi framework could significantly improve their understanding. Additionally, the inclusion of even more detailed and diverse observations from upcoming missions like 4pi HeliOS [Raouafi et al., 2022] and Solaris [Hassler et al., 2023] will allow more insightful and refined synergistic study.

Looking ahead, the integration of hybrid machine learning and physics-based approaches presents a promising pathway for overcoming the current challenges in space weather forecasting. While physics-based models provide a robust framework grounded in the fundamental laws of nature, machine learning techniques offer the ability to rapidly analyze vast datasets, identify patterns, and make predictions with unprecedented speed and accuracy. By combining the strengths of both approaches, future space weather forecasting systems can achieve greater precision and reliability, adapting dynamically to new data and evolving conditions. This thesis has laid the groundwork for such advancements, and the continued development of hybrid models holds the potential to revolutionize our ability to predict and mitigate the impacts of space weather, ensuring the safety and resilience of our technological infrastructure in space and on Earth.

References

Ahmadzadeh, A., Hostetter, M., Aydin, B., et al. 2019, in 2019 IEEE international conference on big data (Big Data), Ieee, 1423–1431

Allen, J., Sauer, H., Frank, L., & Reiff, P. 1989, Effects of the March 1989 solar activity, Eos, Transactions American Geophysical Union, 70, 1479

Altschuler, M. D., Levine, R. H., Stix, M., & Harvey, J. 1977, High resolution mapping of the magnetic field of the solar corona, Solar Physics, 51, doi:10.1007/BF00216372

Altschuler, M. D., & Newkirk, G. 1969a, Magnetic fields and the structure of the solar corona - I: Methods of calculating coronal fields, Solar Physics, 9, doi:10.1007/BF00145734

Altschuler, M. D., & Newkirk, G. 1969b, Magnetic fields and the structure of the solar corona - I: Methods of calculating coronal fields, Solar Physics, 9, doi:10.1007/BF00145734

Alves, M. V., Echer, E., & Gonzalez, W. D. 2006, Geoeffectiveness of corotating interaction regions as measured by Dst index, Journal of Geophysical Research: Space Physics, 111, doi:10.1029/2005JA011379

Arge, C. N. 2003, Improved Method for Specifying Solar Wind Speed Near the Sun, AIP Conference Proceedings, 679, 190

Arge, C. N., Odstrcil, D., Pizzo, V. J., & Mayer, L. R. 2003, Improved Method for Specifying Solar Wind Speed Near the Sun, AIP Conference Proceedings, 679, 190

Arge, O. N., & Pizzo, V. J. 2000, Improvement in the prediction of solar wind conditions using near-real time solar magnetic field updates, Journal of Geophysical Research: Space Physics, 105, doi:10.1029/1999ja000262

Asvestari, E., Heinemann, S. G., Temmer, M., et al. 2019, Reconstructing Coronal Hole Areas With EUHFORIA and Adapted WSA Model: Optimizing the Model Parameters, Journal of Geophysical Research: Space Physics, 124, 8280

Belcher, & Davis, L. 1971, Large- amplitude Alfven waves in the interplanetary medium, 2, J Geophys Res, 76, doi:10.1029/ja076i016p03534

Belov, A., Eroshenko, E., Oleneva, V., Struminsky, A., & Yanke, V. 2001, What determines the magnitude of forbush decreases?, Advances in Space Research, 27, 625

Biondo, R., Pagano, P., Reale, F., & Bemporad, A. 2021, Tracing the ICME plasma with a MHD simulation, Astronomy and Astrophysics, 654, L3

Biondo, R., Bemporad, A., Pagano, P., et al. 2022, Connecting Solar Orbiter remote-sensing observations and Parker Solar Probe in situ measurements with a numerical MHD reconstruction of the Parker spiral, A&A, 668, A144

Bloomfield, D. S., Higgins, P. A., McAteer, R. J., & Gallagher, P. T. 2012, Toward reliable benchmarking of solar flare forecasting methods, The Astrophysical Journal Letters, 747, L41

Bobra, M. G., & Couvidat, S. 2015, Solar flare prediction using SDO/HMI vector

magnetic field data with a machine-learning algorithm, The Astrophysical Journal, 798, 135

Bobra, M. G., Sun, X., Hoeksema, J. T., et al. 2014, The Helioseismic and Magnetic Imager (HMI) vector magnetic field pipeline: SHARPs – Space-Weather HMI Active Region Patches, Solar Physics, 289, 3549–3578

Braga, C. R., Vourlidas, A., Liewer, P. C., et al. 2022, Coronal Mass Ejection Deformation at 0.1 au Observed by WISPR, The Astrophysical Journal, 938, 13

Brueckner, G. E., Howard, R. A., Koomen, M. J., et al. 1995, The Large Angle Spectroscopic Coronagraph (LASCO), Solar Physics, 162, 357

Burlaga, L. F., Plunkett, S. P., & Cyr, S. 2002, Successive CMEs and complex ejecta, Journal of Geophysical Research, 107, doi:10.1029/2001ja000255

Bussy-Virat, C. D., & Ridley, A. J. 2014, Predictions of the solar wind speed by the probability distribution function model, Space Weather, 12, doi:10.1002/2014SW001051

Caplan, R. M., Downs, C., Linker, J. A., & Mikic, Z. 2021, Variations in Finite-difference Potential Fields, The Astrophysical Journal, 915, doi:10.3847/1538-4357/abfd2f

Chawla, N. V., Bowyer, K. W., Hall, L. O., & Kegelmeyer, W. P. 2002, SMOTE: Synthetic Minority Over-sampling Technique, Journal of Artificial Intelligence Research, 16, 321–357

Chen, Y., Manchester, W. B., Hero, A. O., et al. 2019, Identifying solar flare precursors using time series of SDO/HMI Images and SHARP parameters, Space Weather, 17, 1404

Community, T. S., Mumford, S. J., Christe, S., et al. 2015, SunPy—Python for solar physics, Computational Science & Discovery, 8, 014009

Council, N. R. 2008, Severe Space Weather Events: Understanding Societal and Economic Impacts: A Workshop Report (National Academies Press), doi:10.17226/12507

Davies, E. L., Winslow, R. M., Scolini, C., et al. 2022, Multi-spacecraft Observations of the Evolution of Interplanetary Coronal Mass Ejections between 0.3 and 2.2 au: Conjunctions with the Juno Spacecraft, The Astrophysical Journal, 933, 127

Dumbović, M., Čalogović, J., Martinić, K., et al. 2021, Drag-Based Model (DBM) Tools for Forecast of Coronal Mass Ejection Arrival Time and Speed, Frontiers in Astronomy and Space Sciences, 8, doi:10.3389/fspas.2021.639986

Dumbović, M., Čalogović, J., Vršnak, B., et al. 2018, The Drag-based Ensemble Model (DBEM) for Coronal Mass Ejection Propagation, The Astrophysical Journal, 854, 180

Echer, E., Gonzalez, W., Guarnieri, F., Lago, A. D., & Vieira, L. 2005, Introduction to space weather, Advances in Space Research, 35, 855, fundamentals of Space Environment Science

Falconer, D. A., Moore, R. L., Barghouty, A. F., & Khazanov, I. 2012, Prior flaring as a complement to free magnetic energy for forecasting solar eruptions, The Astrophysical Journal, 757, 32

Feng, X., Yang, L., Xiang, C., et al. 2010, THREE-DIMENSIONAL SOLAR WIND MODELING FROM THE SUN TO EARTH BY A SIP-CESE MHD MODEL WITH A SIX-COMPONENT GRID, The Astrophysical Journal, 723, 300

Florios, K., Kontogiannis, I., Park, S.-H., et al. 2018, Forecasting solar flares using magnetogram-based predictors and machine learning, Solar Physics, 293, doi:10.1007/s11207-018-1250-4

Garcia, H. A. 1994, Temperature and emission measure from goes soft X-ray measurements, Solar Physics, 154, 275

Gary, G. A. 2001, Plasma beta above a solar active region: Rethinking the paradigm, Solar Physics, 203, doi:10.1023/A:1012722021820

Georgoulis, M. K., Nindos, A., & Zhang, H. 2019, The source and engine of coronal mass ejections, Philosophical Transactions of The Royal Society A, 377, 20180094

Gibson, S. E., & Low, B. C. 1998, A Time-dependent Three-dimensional Magnetohydrodynamic Model of the Coronal Mass Ejection, The Astrophysical Journal, 493, 460

Giri, G., Vaidya, B., Rossi, P., et al. 2022, Modelling X-shaped radio galaxies: Dynamical and emission signatures from the Back-flow model, Astronomy and Astrophysics, 662, A5

Goelzer, M. L., Schwadron, N. A., & Smith, C. W. 2014, An analysis of Alfvén radius based on sunspot number from 1749 to today, Journal of Geophysical Research: Space Physics, 119, doi:10.1002/2013JA019420

Gold, T., & Hoyle, F. 1960, On the Origin of Solar Flares, Monthly Notices of the Royal Astronomical Society, 120, 89

Gopalswamy, N., Akiyama, S., Yashiro, S., & Xie, H. 2017, A New Technique to Provide Realistic Input to CME Forecasting Models, Proceedings of the International Astronomical Union, 13, 258

Gopalswamy, N., Yashiro, S., & Akiyama, S. 2015, KINEMATIC AND ENERGETIC PROPERTIES OF THE 2012 MARCH 12 POLAR CORONAL MASS EJECTION, The Astrophysical Journal, 809, 106

Gopalswamy, N., Yashiro, S., Kaiser, M. L., Howard, R. A., & Bougeret, J.-L. 2001, Radio Signatures of Coronal Mass Ejection Interaction: Coronal Mass Ejection Cannibalism?, The Astrophysical Journal, 548, L91

Gosling, J. T., Asbridge, J. R., Bame, S. J., & Feldman, W. C. 1978, Solar wind stream interfaces, Journal of Geophysical Research: Space Physics, 83, 1401

Gosling, J. T., & Pizzo, V. J. 1999, Formation and Evolution of Corotating Interaction Regions and Their Three Dimensional Structure, Space Science Reviews, 89, 21

Gosling, J. T., & Riley, P. 1996, The acceleration of slow coronal mass ejections in the high-speed solar wind, Geophysical Research Letters, 23, 2867

Goyal, S. K., Kumar, P., Janardhan, P., et al. 2018, Aditya Solarwind Particle EXperiment (ASPEX) onboard the Aditya-L1 mission, Planetary and Space Science, 163, doi:10.1016/j.pss.2018.04.008

Hakamada, K. 1995, A simple method to compute spherical harmonic coefficients for the potential model of the coronal magnetic field, Solar Physics, 159, doi:10.1007/BF00733033

Han, H., Wang, W.-Y., & Mao, B.-H. 2005, in International conference on intelligent computing, Springer, 878–887

Hapgood, M., Liu, H., & Lugaz, N. 2022, SpaceX—Sailing Close to the Space Weather?, Space Weather, 20, doi:10.1029/2022sw003074

Harvey, J. T., Hill, F., Hubbard, R. G., et al. 1996, The Global Oscillation Network Group (GONG) Project, Science, 272, 1284

Hassler, D. M., Gibson, S. E., Newmark, J. S., et al. 2023, Solaris: A Focused Solar Polar Discovery-class Mission to achieve the Highest Priority Heliophysics Science Now, arXiv:2301.07647

He, H., Bai, Y., Garcia, E. A., & Li, S. 2008, in 2008 IEEE International Joint Conference on Neural Networks (IEEE World Congress on Computational Intelligence), 1322–1328

He, H., & Garcia, E. A. 2009, Learning from imbalanced data, IEEE Transactions on Knowledge and Data Engineering, 21, 1263

Heinemann, S. G., Temmer, M., Farrugia, C. J., et al. 2019, CME–HSS Interaction and Characteristics Tracked from Sun to Earth, Solar Physics, 294, doi:10.1007/s11207-019-1515-6

Hill, F. 2018, The Global Oscillation Network Group Facility—An Example of Research to Operations in Space Weather, Space Weather, 16, doi:10.1029/2018SW002001

Hinterreiter, J., Amerstorfer, T., Temmer, M., et al. 2021, Drag-Based CME Modeling With Heliospheric Images Incorporating Frontal Deformation: ELEvoHI 2.0, Space Weather, 19, doi:10.1029/2021sw002836

Holzknecht, L., Temmer, M., Dumbovic, M., et al. 2019, CME volume calculation from 3D GCS reconstruction, arXiv:1904.11418 [astro-ph, physics:physics], doi:10.48550/arXiv.1904.11418

Hosokawa, T., Hirano, S., Kuiper, R., et al. 2016, FORMATION OF MASSIVE

PRIMORDIAL STARS: INTERMITTENT UV FEEDBACK WITH EPISODIC MASS ACCRETION, The Astrophysical Journal, 824, 119

Howard, R. A., Moses, J. A., Vourlidas, A., et al. 2008, Sun Earth Connection Coronal and Heliospheric Investigation (SECCHI), Space Science Reviews, 136, doi:10.1007/s11214-008-9341-4

Hu, Q., Qiu, J., & Krucker, S. 2015, Magnetic field line lengths inside interplanetary magnetic flux ropes, Journal of Geophysical Research: Space Physics, 120, 5266

Huang, X., & Wang, H.-N. 2013, Solar flare prediction using highly stressed longitudinal magnetic field parameters, Research in Astronomy and Astrophysics, 13, 351

Hundhausen, A. J. 1979, Solar activity and the solar wind, Reviews of geophysics, 17, 2034

Isavnin, A. 2016, FRiED: A NOVEL THREE-DIMENSIONAL MODEL OF CORONAL MASS EJECTIONS, The Astrophysical Journal, 833, 267

Janvier, M., Winslow, R. M., Good, S., et al. 2019, Generic Magnetic Field Intensity Profiles of Interplanetary Coronal Mass Ejections at Mercury, Venus, and Earth From Superposed Epoch Analyses, Journal of Geophysical Research: Space Physics, 124, 812

Jiao, Z., Sun, H., Wang, X., et al. 2020, Solar flare intensity prediction with machine learning models, Space Weather, 18, doi:10.1029/2020sw002440

Jin, M., Manchester, W. B., , v., et al. 2017, DATA-CONSTRAINED CORONAL MASS EJECTIONS IN A GLOBAL MAGNETOHYDRODYNAMICS MODEL, The Astrophysical Journal, 834, 173

Jonas, E., Bobra, M., Shankar, V., Todd Hoeksema, J., & Recht, B. 2018, Flare prediction using photospheric and coronal image data, Solar Physics, 293, doi:10.1007/s11207-018-1258-9

Kay, C., & Nieves-Chinchilla, T. 2021, Modeling Interplanetary Expansion and Deformation of CMEs With ANTEATR-PARADE: Relative Contribution of Different Forces, Journal of Geophysical Research: Space Physics, 126, doi:10.1029/2020ja028911

Kay, C., Nieves-Chinchilla, T., Hofmeister, S. J., & Palmerio, E. 2022, Beyond Basic Drag in Interplanetary CME Modeling: Effects of Solar Wind Pileup and High-Speed Streams, Space Weather, 20, doi:10.1029/2022sw003165

Ke, G., Meng, Q., Finley, T., et al. 2017, Lightgbm: A highly efficient gradient boosting decision tree, Advances in neural information processing systems, 30

Kilpua, E., Lumme, E., Andréeová, K., Isavnin, A., & Koskinen, H. 2015, Properties and drivers of fast interplanetary shocks near the orbit of the Earth (1995–2013), Journal Of Geophysical Research: Space Physics, 120, 4112

Koehn, G. J., Desai, R. T., Davies, E. E., et al. 2022, Successive Interacting Coronal Mass Ejections: How to Create a Perfect Storm, The Astrophysical Journal, 941, 139

Li, R., & Zhu, J. 2013, Solar flare forecasting based on sequential sunspot data, Research in Astronomy and Astrophysics, 13, 1118

Lin, T.-Y., Goyal, P., Girshick, R., He, K., & Dollar, P. 2017, in Proceedings of the IEEE International Conference on Computer Vision (ICCV)

Lindsay, G. M., Luhmann, J. G., Russell, C. T., & Gosling, J. T. 1999, Relationships between coronal mass ejection speeds from coronagraph images and interplane-

tary characteristics of associated interplanetary coronal mass ejections, Journal of Geophysical Research: Space Physics, 104, 12515

Linker, J. A., Caplan, R. M., Downs, C., et al. 2017, The Open Flux Problem, The Astrophysical Journal, 848, 70

Liu, H., Liu, C., Wang, J. T. L., & Wang, H. 2019a, Predicting solar flares using a long short-term memory network, The Astrophysical Journal, 877, 121

Liu, J.-F., Li, F., Wan, J., & Yu, D.-R. 2017, Short-term solar flare prediction using multi-model integration method, Research in Astronomy and Astrophysics, 17, 034

Liu, Y., & Lin, H. 2008, Observational Test of Coronal Magnetic Field Models. I. Comparison with Potential Field Model, The Astrophysical Journal, 680, doi:10.1086/588645

Liu, Y., Richardson, J., & Belcher, J. 2005, A statistical study of the properties of interplanetary coronal mass ejections from 0.3 to 5.4AU, Planetary and Space Science, 53, 3

Liu, Y., Welsch, B. T., Valori, G., et al. 2023, Changes of magnetic energy and helicity in solar active regions from major flares, The Astrophysical Journal, 942, 27

Liu, Y.-S., Shen, F., & Yang, Y. 2019b, Numerical Simulation on the Propagation and Deflection of Fast Coronal Mass Ejections (CMEs) Interacting with a Corotating Interaction Region in Interplanetary Space, The Astrophysical Journal, 887, 150

Liu, Y. W., Luhmann, J. G., Möstl, C., et al. 2012, INTERACTIONS BETWEEN

CORONAL MASS EJECTIONS VIEWED IN COORDINATED IMAGING AND IN SITU OBSERVATIONS, The Astrophysical Journal Letters, 746, L15

Lockwood, M. 2022, Solar Wind—Magnetosphere Coupling Functions: Pitfalls, Limitations, and Applications, Space Weather, 20, e2021SW002989

Lugaz, N., Farrugia, C. J., Davies, J. C., et al. 2012, THE DEFLECTION OF THE TWO INTERACTING CORONAL MASS EJECTIONS OF 2010 MAY 23-24 AS REVEALED BY COMBINED IN SITU MEASUREMENTS AND HELIOSPHERIC IMAGING, The Astrophysical Journal, 759, 68

Lugaz, N., Farrugia, C. J., Manchester, W. B., & Schwadron, N. 2013, THE INTERACTION OF TWO CORONAL MASS EJECTIONS: INFLUENCE OF RELATIVE ORIENTATION, The Astrophysical journal, 778, 20

Lugaz, N., Manchester, W. B., & Gombosi, T. I. 2005, Numerical Simulation of the Interaction of Two Coronal Mass Ejections from Sun to Earth, The Astrophysical Journal, 634, 651

Lugaz, N., Temmer, M., Wang, Y., & Farrugia, C. J. 2017, The Interaction of Successive Coronal Mass Ejections: A Review, Solar Physics, 292, doi:10.1007/s11207-017-1091-6

Lugaz, N., Vourlidas, A., & Roussev, I. I. 2009, Deriving the radial distances of wide coronal mass ejections from elongation measurements in the heliosphere – application to CME-CME interaction, Annales Geophysicae, 27, 3479

Lundquist, S. 1950, Magnetohydrostatic fields, Ark. Fys., 2, 361

MacNeice, P., Jian, L. K., Antiochos, S. K., et al. 2018, Assessing the Quality of Models of the Ambient Solar Wind, Space Weather, 16, doi:10.1029/2018SW002040

Maharana, A., Isavnin, A., Scolini, C., et al. 2022, Implementation and validation of the FRi3D flux rope model in EUHFORIA, Advances in Space Research, 70, 1641

Majumdar, S., Patel, R., & Pant, V. 2022, On the Variation in the Volumetric Evolution of CMEs from the Inner to Outer Corona, The Astrophysical Journal, 929, 11

Manchester, W., Kilpua, E. K. J., Liu, Y. D., et al. 2017, The Physical Processes of CME/ICME Evolution, Space Science Reviews, 212, 1159

Manoharan, P. K. 2006, Evolution of Coronal Mass Ejections in the Inner Heliosphere: A Study Using White-Light and Scintillation Images, Solar Physics, 235, 345

Matthaeus, W. H. 2021, Sonic and Alfvenic Critical Point and the Solar Probe Mission: presentation to the Solar Probe Science and Technology Definition Team, arXiv (Cornell University), doi:10.48550/arxiv.2106.08450

Mayank, P., Vaidya, B., & Chakrabarty, D. 2022, SWASTi-SW: Space Weather Adaptive Simulation Framework for Solar Wind and Its Relevance to the Aditya-L1 Mission, The Astrophysical Journal Supplement Series, 262, 23

Mayank, P., Vaidya, B., Mishra, W., & Chakrabarty, D. 2023, SWASTi-CME: A Physics-based Model to Study Coronal Mass Ejection Evolution and Its Interaction with Solar Wind, The Astrophysical Journal Supplement Series, 270, 10

McComas, D. J., Elliott, H. A., Schwadron, N. A., et al. 2003, The three-dimensional solar wind around solar maximum, Geophysical Research Letters, 30, doi:10.1029/2003gl017136

McGregor, S. L., Hughes, W. J., Arge, C. N., & Owens, M. J. 2008, Analysis of the magnetic field discontinuity at the potential field source surface and Schatten Current Sheet interface in the Wang-Sheeley-Arge model, Journal of Geophysical Research: Space Physics, 113, n/a

McGregor, S. L., Hughes, W. J., Arge, C. N., Owens, M. J., & Odstrcil, D. 2011, The distribution of solar wind speeds during solar minimum: Calibration for numerical solar wind modeling constraints on the source of the slow solar wind, Journal of Geophysical Research: Space Physics, 116, doi:10.1029/2010JA015881

Mignone, A., Bodo, G., Massaglia, S., et al. 2007a, PLUTO: A Numerical Code for Computational Astrophysics, The Astrophysical Journal Supplement Series, 170, 228

Mignone, A., Bodo, G., Massaglia, S., et al. 2007b, PLUTO: A Numerical Code for Computational Astrophysics, The Astrophysical Journal Supplement Series, 170, doi:10.1086/513316

Mishra, W., Doshi, U., & Srivastava, N. 2021, Radial Sizes and Expansion Behavior of ICMEs in Solar Cycles 23 and 24, Frontiers in Astronomy and Space Sciences, 8, doi:10.3389/fspas.2021.713999

Mishra, W., & Srivastava, N. 2013, ESTIMATING THE ARRIVAL TIME OF EARTH-DIRECTED CORONAL MASS EJECTIONS AT IN SITU SPACECRAFT USING COR AND HI OBSERVATIONS FROM¡i¿STEREO¡/i¿, The Astrophysical Journal, 772, 70

Mishra, W., Srivastava, N., & Chakrabarty, D. 2014a, Evolution and Consequences of Interacting CMEs of 9–10 November 2012 Using STEREO/SECCHI and In Situ Observations, Solar Physics, 290, 527

Mishra, W., Srivastava, N., & Davies, J. A. 2014b, A COMPARISON OF RECONSTRUCTION METHODS FOR THE ESTIMATION OF CORONAL MASS EJECTIONS KINEMATICS BASED ON SECCHI/HI OBSERVATIONS, The Astrophysical Journal, 784, 135

Mishra, W., Srivastava, N., & Singh, T. 2015, Kinematics of interacting CMEs of 25 and 28 September 2012, J. Geophys. Res. Space Physics, 120, 10,221

Mukherjee, D., Bicknell, G. V., Wagner, A. Y., Sutherland, R. S., & Silk, J. 2018, Relativistic jet feedback – III. Feedback on gas discs, Monthly Notices of the Royal Astronomical Society, 479, 5544

Napoletano, G., Forte, R., Moro, D. D., et al. 2018, A probabilistic approach to the drag-based model, Journal of Space Weather and Space Climate, 8, A11

Narechania, N. M., Nikolić, L., Freret, L., Sterck, H. D., & Groth, C. P. T. 2021, An integrated data-driven solar wind – CME numerical framework for space weather forecasting, Journal of Space Weather and Space Climate, 11, 8

Nguyen, H. M., Cooper, E. W., & Kamei, K. 2011, Borderline over-sampling for imbalanced data classification, International Journal of Knowledge Engineering and Soft Data Paradigms, 3, 4

Nikolić, L. 2019, On Solutions of the PFSS Model With GONG Synoptic Maps for 2006–2018, Space Weather, 17, 1293, solves pfss using Spherical Harmonics

Nishizuka, N., Sugiura, K., Kubo, Y., Den, M., & Ishii, M. 2018, Deep Flare Net (DeFN) model for solar flare prediction, The Astrophysical Journal, 858, 113

Nishizuka, N., Sugiura, K., Kubo, Y., et al. 2017, Solar Flare Prediction Model with Three Machine-learning Algorithms using Ultraviolet Brightening and Vector Magnetograms, The Astrophysical Journal, 835, 156

O'Brien, T., & McPherron, R. L. 2000, Forecasting the ring current index Dst in real time, Journal of Atmospheric and Solar-Terrestrial Physics, 62, 1295

Odstrcil, D. 2003, Modeling 3-D solar wind structure, Advances in Space Research, 32, 497

Odstrcil, D., Riley, P., & Zhao, X. S. 2004, Numerical simulation of the 12 May 1997 interplanetary CME event, Journal of Geophysical Research, 109, doi:10.1029/2003ja010135

Oliveira, D. M. 2016, Magnetohydrodynamic Shocks in the Interplanetary Space: a Theoretical Review, Brazilian Journal of Physics, 47, 81

Owens, M. J., Lockwood, M., & Barnard, L. A. 2017a, Coronal mass ejections are not coherent magnetohydrodynamic structures, Scientific Reports, 7, doi:10.1038/s41598-017-04546-3

Owens, M. J., Riley, P., & Horbury, T. S. 2017b, Probabilistic Solar Wind and Geomagnetic Forecasting Using an Analogue Ensemble or "Similar Day" Approach, Solar Physics, 292, doi:10.1007/s11207-017-1090-7

Park, S.-h., Chae, J., & Wang, H. 2010, Productivity of solar flares and magnetic helicity injection in active regions, The Astrophysical Journal, 718, 43

Parker, E. N. 1958, Dynamics of the Interplanetary Gas and Magnetic Fields., The Astrophysical Journal, 128, 664

Pizzo, V. J. 1978, A three-dimensional model of corotating streams in the solar wind, 1. Theoretical foundations, Journal of Geophysical Research, 83, 5563

Poedts, S., van der Holst, B., Chattopadhyay, I., et al. 2003, in ESA Special Publication, Vol. 535, Solar Variability as an Input to the Earth's Environment, ed. A. Wilson, 603–612

Pomoell, J., & Poedts, S. 2018a, EUHFORIA: European heliospheric forecasting information asset, Journal of Space Weather and Space Climate, 8, A35

Pomoell, J., & Poedts, S. 2018b, EUHFORIA: European heliospheric forecasting information asset, Journal of Space Weather and Space Climate, 8, A35

Powell, K. K. G. 1994, An Approximate Riemann Solver for Magnetohydrodynamics (That Works More Than One Dimension), ICASE report, 94 - 24

Raghav, A., & Shaikh, Z. A. 2020, The pancaking of coronal mass ejections: an in situ attestation, Monthly Notices of the Royal Astronomical Society: Letters, 493, L16

Raouafi, N. E., Raouafi, N., Hoeksema, J. T., et al. 2022, in 44th COSPAR Scientific Assembly. Held 16-24 July, Vol. 44, 1530

Reiss, M. A., Temmer, M., Veronig, A. M., et al. 2016, Verification of high-speed solar wind stream forecasts using operational solar wind models, Space Weather, 14, doi:10.1002/2016SW001390

Ribeiro, F., & Gradvohl, A. 2021, Machine learning techniques applied to solar flares forecasting, Astronomy and Computing, 35, 100468

Richardson, I. G. 2018, Solar wind stream interaction regions throughout the heliosphere, Living Reviews in Solar Physics, 15, doi:10.1007/s41116-017-0011-z

Richardson, I. G., & Zhang, J. 2008, Multiple-step geomagnetic storms and their interplanetary drivers, Geophysical Research Letters, 35, doi:10.1029/2007gl032025

Richardson, I. G., Webb, D. F., Zhang, J., et al. 2006, Major geomagnetic storms generated by corotating interaction regions, Journal of Geophysical Research: Space Physics, 111, doi:10.1029/2005ja011476

Riley, P., Ben-Nun, M., Linker, J. A., Owens, M. J., & Horbury, T. S. 2017, Forecasting the properties of the solar wind using simple pattern recognition, Space Weather, 15, doi:10.1002/2016SW001589

Riley, P., & Crooker, N. U. 2004, Kinematic Treatment of Coronal Mass Ejection Evolution in the Solar Wind, The Astrophysical Journal, 600, 1035

Riley, P., & Issan, O. 2021, Using a Heliospheric Upwinding eXtrapolation Technique to Magnetically Connect Different Regions of the Heliosphere, Frontiers in Physics, 9, doi:10.3389/fphy.2021.679497

Riley, P., Linker, J. A., & Arge, C. N. 2015, On the role played by magnetic expansion factor in the prediction of solar wind speed, Space Weather, 13, 154

Riley, P., Linker, J. A., & Mikić, Z. 2001, An empirically-driven global MHD model of the solar corona and inner heliosphere, Journal of Geophysical Research: Space Physics, 106, 15889

Riley, P., Linker, J. A., Mikić, Z., et al. 2006, A Comparison between Global Solar Magnetohydrodynamic and Potential Field Source Surface Model Results, The Astrophysical Journal, 653, doi:10.1086/508565

Riley, P., & Lionello, R. 2011, Mapping Solar Wind Streams from the Sun to 1 AU: A Comparison of Techniques, Solar Physics, 270, 575

Rollett, T., Möstl, C., Isavnin, A., et al. 2016, ElEvoHI: A NOVEL CME PREDICTION TOOL FOR HELIOSPHERIC IMAGING COMBINING AN ELLIPTICAL FRONT WITH DRAG-BASED MODEL FITTING, The Astrophysical Journal, 824, 131

Rout, D., Chakrabarty, D., Janardhan, P., et al. 2017, Solar wind flow angle and geo-

effectiveness of corotating interaction regions: First results, Geophysical Research Letters, 44, doi:10.1002/2017GL073038

Sachdeva, N., Subramanian, P., Colaninno, R., & Vourlidas, A. 2015, CME PROPAGATION: WHERE DOES AERODYNAMIC DRAG "TAKE OVER"?, The Astrophysical Journal, 809, 158

Salman, T. M., Winslow, R. M., & Lugaz, N. 2020, Radial Evolution of Coronal Mass Ejections Between MESSENGER, ¡i¿Venus Express¡/i¿ , STEREO, and L1: Catalog and Analysis, Journal of Geophysical Research: Space Physics, 125, doi:10.1029/2019ja027084

Schatten, K. 1971, Current sheet magnetic model for the solar corona., Cosmical Electrodynamics, 2

Scherrer, P. H., Schou, J., Bush, R. I., et al. 2012, The Helioseismic and Magnetic Imager (HMI) Investigation for the Solar Dynamics Observatory (SDO), Solar Physics, 275, doi:10.1007/s11207-011-9834-2

Schrijver, C. J., & Derosa, M. L. 2003, Photospheric and heliospheric magnetic fields, Solar Physics, 212, doi:10.1023/A:1022908504100

Schwenn, R. 2006, Space Weather: The Solar Perspective, Living Reviews in Solar Physics, 3, doi:10.12942/lrsp-2006-2

Scolini, C., Dasso, S., Rodriguez, L., Zhukov, A. N., & Poedts, S. 2021, Exploring the radial evolution of interplanetary coronal mass ejections using EUHFORIA, Astronomy and Astrophysics, 649, A69

Scolini, C., Winslow, R. M., Lugaz, N., et al. 2022, Causes and Consequences of Magnetic Complexity Changes within Interplanetary Coronal Mass Ejections: A Statistical Study, The Astrophysical Journal, 927, 102

Scolini, C., Chané, E., Temmer, M., et al. 2020, CME–CME Interactions as Sources of CME Geoeffectiveness: The Formation of the Complex Ejecta and Intense Geomagnetic Storm in 2017 Early September, Astrophysical Journal Supplement Series, 247, 21

Shen, C., Wang, Y., Wang, S., et al. 2012a, Super-elastic collision of large-scale magnetized plasmoids in the heliosphere, Nature Physics, 8, 923–928

Shen, F., Wang, Y., Shen, C., & Feng, X. 2016, Turn on the super-elastic collision nature of coronal mass ejections through low approaching speed, Scientific Reports, 6, doi:10.1038/srep19576

Shen, F., Wang, Y., Shen, C., & Feng, X. 2017, On the Collision Nature of Two Coronal Mass Ejections: A Review, Solar Physics, 292, doi:10.1007/s11207-017-1129-9

Shen, F., Wu, S. T., Feng, X., & Wu, C.-C. 2012b, Acceleration and deceleration of coronal mass ejections during propagation and interaction, Journal of Geophysical Research: Space Physics, 117, doi:10.1029/2012ja017776

Shiota, D., & Kataoka, R. 2016, Magnetohydrodynamic simulation of interplanetary propagation of multiple coronal mass ejections with internal magnetic flux rope (SUSANOO-CME), Space Weather, 14, 56

Shiota, D., Kataoka, R., Miyoshi, Y., et al. 2014, Inner heliosphere MHD modeling system applicable to space weather forecasting for the other planets, Space Weather, 12, 187

Singh, T., Kim, T. K., Pogorelov, N. V., & Arge, C. N. 2022, Ensemble Simulations of the 2012 July 12 Coronal Mass Ejection with the Constant-turn Flux Rope Model, The Astrophysical Journal, 933, 123

Subramanian, P., Arunbabu, K. P., Vourlidas, A., & Mauriya, A. 2014, SELF-SIMILAR EXPANSION OF SOLAR CORONAL MASS EJECTIONS: IMPLICATIONS FOR LORENTZ SELF-FORCE DRIVING, The Astrophysical Journal, 790, 125

Sudar, D., Vršnak, B., Dumbović, M., Temmer, M., & Čalogović, J. 2022, Influence of the drag force on the leading edge of a coronal mass ejection, Astronomy and Astrophysics, 665, A142

Sun, X. 2019, The CGEM Lorentz Force Data from HMI Vector Magnetograms, arXiv:1405.7353

Tadesse, T., Wiegelmann, T., MacNeice, P. J., et al. 2014, A Comparison Between Nonlinear Force-Free Field and Potential Field Models Using Full-Disk SDO/HMI Magnetogram, Solar Physics, 289, doi:10.1007/s11207-013-0364-y

Taylor, K. E. 2001, Summarizing multiple aspects of model performance in a single diagram, Journal of Geophysical Research: Atmospheres, 106, 7183

Temmer, M., Rollett, T., Möstl, C., et al. 2011, INFLUENCE OF THE AMBIENT SOLAR WIND FLOW ON THE PROPAGATION BEHAVIOR OF INTERPLANETARY CORONAL MASS EJECTIONS, The Astrophysical Journal, 743, 101

Temmer, M., Vršnak, B., Amerstorfer, T., et al. 2012, CHARACTERISTICS OF KINEMATICS OF A CORONAL MASS EJECTION DURING THE 2010 AUGUST 1 CME–CME INTERACTION EVENT, The Astrophysical Journal, 749, 57

Temmer, M., Holzknecht, L., Dumbović, M., et al. 2021, Deriving CME Density From Remote Sensing Data and Comparison to In-Situ Measurements, Journal of Geophysical Research: Space Physics, 126, doi:10.1029/2020ja028380

Thernisien, A. 2011, IMPLEMENTATION OF THE GRADUATED CYLINDRICAL SHELL MODEL FOR THE THREE-DIMENSIONAL RECONSTRUCTION OF CORONAL MASS EJECTIONS, The Astrophysical Journal Supplement Series, 194, 33

Thompson, W. T. 2006, Coordinate systems for solar image data, Astronomy and Astrophysics, 449, doi:10.1051/0004-6361:20054262

Trotta, D., Dimmock, A., Blanco-Cano, X., et al. 2024, Observation of a Fully-formed Forward–Reverse Shock Pair Due to the Interaction Between Two Coronal Mass Ejections at 0.5 au, arXiv (Cornell University), doi:10.48550/arxiv.2404.17315

Tsurutani, B. T., Gonzalez, W. D., Gonzalez, A. L., et al. 2006, Corotating solar wind streams and recurrent geomagnetic activity: A review, Journal of Geophysical Research: Space Physics, 111, doi:10.1029/2005JA011273

Tóth, G., van der Holst, B., & Huang, Z. 2011, OBTAINING POTENTIAL FIELD SOLUTIONS WITH SPHERICAL HARMONICS AND FINITE DIFFERENCES, The Astrophysical Journal, 732, 102

Tóth, G., Sokolov, I. V., Gombosi, T. I., et al. 2005, Space weather modeling framework: A new tool for the space science community, Journal of Geophysical Research: Space Physics, 110, A12226

van Ballegooijen, A. A., Priest, E. R., & Mackay, D. H. 2000, Mean Field Model for the Formation of Filament Channels on the Sun, The Astrophysical Journal, 539, 983

van der Holst, B., Manchester, W. B., Frazin, R. A., et al. 2010, A DATA-DRIVEN, TWO-TEMPERATURE SOLAR WIND MODEL WITH ALFVÉN WAVES, The Astrophysical Journal, 725, 1373

Vandas, M., & Romashets, E. 2017, Magnetic cloud fit by uniform-twist toroidal flux ropes, Astronomy and Astrophysics, 608, A118

Verbeke, C., Pomoell, J., & Poedts, S. 2019, The evolution of coronal mass ejections in the inner heliosphere: Implementing the spheromak model with EUHFORIA, Astronomy and Astrophysics, 627, A111

Vourlidas, A., Howard, R. A., Esfandiari, E., et al. 2010, COMPREHENSIVE ANALYSIS OF CORONAL MASS EJECTION MASS AND ENERGY PROPERTIES OVER A FULL SOLAR CYCLE, The Astrophysical Journal, 722, 1522

Vršnak, B. 2006, Forces governing coronal mass ejections, Advances in Space Research, 38, 431–440

Vršnak, B., Vrbanec, D., Čalogović, J., & Žic, T. 2008, The role of aerodynamic drag in dynamics of coronal mass ejections, Proceedings of the International Astronomical Union, 4, 271

Vršnak, B., Žic, T., Vrbanec, D., et al. 2013, Propagation of Interplanetary Coronal Mass Ejections: The Drag-Based Model, Journal of Geophysical Research, 285, 295

Vysakh, P., & Mayank, P. 2023, Solar Flare Prediction and Feature Selection Using a Light-Gradient-Boosting Machine Algorithm, Solar Physics, 298, 137

Wagner, A. Y., Umemura, M., & Bicknell, G. V. 2013, ULTRAFAST OUTFLOWS: GALAXY-SCALE ACTIVE GALACTIC NUCLEUS FEEDBACK, The Astrophysical Journal, 763, L18

Walg, S., Achterberg, A., Markoff, S., Keppens, R., & Meliani, Z. 2013, Relativistic AGN jets I. The delicate interplay between jet structure, cocoon morphology and

jet-head propagation, Monthly Notices of the Royal Astronomical Society, 433, 1453

Wang, X., Chen, Y., Toth, G., et al. 2020, Predicting solar flares with machine learning: Investigating solar cycle dependence, The Astrophysical Journal, 895, 3

Wang, Y.-M. 2024, Coronal Holes, Footpoint Reconnection, and the Origin of the Slow (and Fast) Solar Wind, Solar physics, 299, doi:10.1007/s11207-024-02300-3

Webb, D. F., & Howard, T. A. 2012, Coronal Mass Ejections: Observations, Living Reviews in Solar Physics, 9, doi:10.12942/lrsp-2012-3

Wiegelmann, T., Petrie, G. J. D., & Riley, P. 2017, Coronal Magnetic Field Models, Space Science Reviews, 210, 249

Wilcox, J. M., & Ness, N. F. 1965, Quasi-stationary corotating structure in the interplanetary medium, Journal of geophysical research, 70, 5793

Winslow, R. M., Scolini, C., Lugaz, N., & Galvin, A. B. 2021, The Effect of Stream Interaction Regions on ICME Structures Observed in Longitudinal Conjunction, The Astrophysical Journal, 916, 40

Wu, C., Liou, K., Vourlidas, A., et al. 2016, Numerical simulation of multiple CME-driven shocks in the month of 2011 September, Journal of geophysical research. Space physics, 121, 1839

Xie, H. 2004, Cone model for halo CMEs: Application to space weather forecasting, Journal of Geophysical Research, 109, doi:10.1029/2003ja010226

Xiong, M., Zheng, H., Wang, Y., & Wang, S. 2006, Magnetohydrodynamic simulation of the interaction between interplanetary strong shock and magnetic cloud and its consequent geoeffectiveness, Journal of geophysical research, 111, doi:10.1029/2005ja011593

Zhang, J., Dere, K. P., Howard, R. A., & Vourlidas, A. 2004, A Study of the Kinematic Evolution of Coronal Mass Ejections, The Astrophysical Journal, 604, 420

Zhang, J., Richardson, I. G., & Webb, D. F. 2008a, Interplanetary origin of multiple-dip geomagnetic storms, Journal of Geophysical Research: Space Physics, 113, n/a

Zhang, Y., Sun, W., Feng, X. S., et al. 2008b, Statistical analysis of corotating interaction regions and their geoeffectiveness during solar cycle 23, Journal of Geophysical Research: Space Physics, 113, doi:10.1029/2008JA013095